

7-211
150569

CROSSFLOW STABILITY AND TRANSITION EXPERIMENTS IN A SWEEP-WING FLOW

p-286

by

J. Ray Dagenhart

Dissertation submitted to the Faculty
of the Virginia Polytechnic Institute and State University
in partial fulfillment of the requirements for the degree of
Doctor of Philosophy
in
Engineering Mechanics

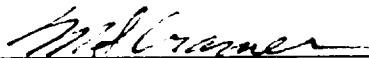
APPROVED:



Dr. W. S. Saric, Co-chairman



Dr. D. P. Telionis, Co-chairman



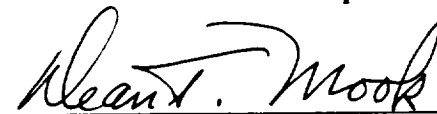
Dr. M. Cramer



Dr. W. Devenport



Dr. D. Frederick



Dr. D. T. Mook

December 1992

Blacksburg, Virginia

(NASA-TM-108650) CROSSFLOW
STABILITY AND TRANSITION
EXPERIMENTS IN A SWEEP-WING FLOW
Ph.D. Thesis (Virginia Polytechnic
Inst. and State Univ.) 286 p

N93-21819

Unclass

ABSTRACT

CROSSFLOW STABILITY AND TRANSITION EXPERIMENTS IN A SWEEP-WING FLOW

J. Ray Dagenhart

An experimental examination of crossflow instability and transition on a 45° swept wing is conducted in the Arizona State University Unsteady Wind Tunnel. The stationary-vortex pattern and transition location are visualized using both sublimating-chemical and liquid-crystal coatings. Extensive hot-wire measurements are conducted at several measurement stations across a single vortex track. The mean and travelling-wave disturbances are measured simultaneously. Stationary-crossflow disturbance profiles are determined by subtracting either a reference or a span-averaged velocity profile from the mean-velocity data. Mean, stationary-crossflow, and travelling-wave velocity data are presented as local boundary-layer profiles and as contour plots across a single stationary-crossflow vortex track. Disturbance-mode profiles and growth rates are determined. The experimental data are compared to predictions from linear stability theory.

Comparison of measured and predicted pressure distributions shows that a good approximation of infinite swept-wing flow is achieved. A fixed-wavelength vortex pattern is observed throughout the visualization range. The theoretically-predicted maximum-amplified vortex wavelength is found to be approximately 25% larger than the observed wavelength. Linear-stability computations for the dominant stationary-crossflow vortices show that the N-factors at transition ranged from 6.4 to 6.8.

The mean-velocity profiles vary slightly across the stationary-crossflow vortex at the first measurement station. The variation across the vortex increases with downstream distance until nearly all of the profiles become highly-distorted

S-shaped curves. Local stationary-crossflow disturbance profiles having either purely excess or deficit values develop at the upstream measurement stations. Further downstream the profiles take on crossover shapes not anticipated by the linear theory. The maximum streamwise stationary-crossflow velocity disturbances reach $\pm 20\%$ of the edge velocity just before transition. The travelling-wave disturbances have single lobes at the upstream measurement stations as expected, but further downstream double-lobed travelling-wave profiles develop. The maximum disturbance intensity remains quite low until just ahead of the transition location where it suddenly peaks at 0.7% of the edge velocity and then drops sharply. The travelling-wave intensity is always more than an order of magnitude lower than the stationary crossflow-vortex strength.

The mean streamwise-velocity contours are nearly flat and parallel to the model surface at the first measurement station. Further downstream, the contours rise up and begin to roll over like a wave breaking on the beach. The stationary-crossflow contours show that a plume of low-velocity fluid rises near the center of the wavelength while high-velocity regions develop near the surface at each end of the wavelength. There is no distinct pattern to the low-intensity travelling-wave contours until a short distance upstream of the transition location where the travelling-wave intensity suddenly peaks near the center of the vortex and then falls abruptly.

The experimental disturbance-mode profiles agree quite well with the predicted eigenfunctions for the forward measurement stations. At the later stations, the experimental mode profiles assume double-lobed shapes with maxima above and below the single maximum predicted by the linear theory. The experimental growth rates are found to be less than or equal to the predicted growth rates from the linear theory. Also, the experimental growth rate curve oscillates over the measurement range whereas the theoretically-predicted growth rates decrease monotonically.

ACKNOWLEDGMENTS

The author is sincerely grateful to Dr. William S. Saric for his invaluable advice, support, encouragement, and patience as the dissertation advisor. Special thanks go to Dr. Helen L. Reed who provided theoretical data for comparison with the experimental results and Dr. W. Pfenninger who continually provided technical insight and discussion throughout the project.

The author also thanks Dr. Demetri Telionis for acting as the examining committee co-chairman and Drs. Daniel Frederick, Dean T. Mook, Mark Cramer, and William Devenport for acting as members of the examining committee. Mr. W. D. Harvey and Dr. Stephen K. Robinson, my former and present branch heads at NASA Langley Research Center, gave necessary support and encouragement. Messrs. Jon Hoos, Marc Mousseux, Ronald Radeztsky, and Dan Clevenger provided important assistance and valuable discussion of the research at the Unsteady Wind Tunnel. Thanks are extended to Messrs. Harry L. Morgan and J. P. Stack of NASA Langley for assistance in computational and measurement aspects of the research. Finally, technical discussions with many members of the Experimental Flow Physics Branch contributed significantly to the work.

I am forever grateful to my parents, John and Anne Dagenhart, for their continuing support and encouragement throughout my educational career.

I also gratefully acknowledge the understanding, encouragement, and patience of my good friend, Malinda Knight.

Contents

ABSTRACT	ii
ACKNOWLEDGMENTS	iv
List of Tables	vii
List of Figures	ix
1 INTRODUCTION	1
1.1 Background	1
1.2 Instability Modes	4
1.3 Goals of the Present Investigation	4
1.4 Outline	5
2 REVIEW OF SWEEPED-WING FLOWS	7
2.1 Stability and Transition Prediction	7
2.2 Transition Experiments	10
2.3 Detailed Theory and Simulation	11
2.4 Stability Experiments	13
2.5 State of Present Knowledge	15
3 EXPERIMENTAL FACILITY	17
3.1 ASU Unsteady Wind Tunnel	17
3.2 New Test Section	19
4 MODEL AND LINER DESIGN	21
4.1 Airfoil Selection	21
4.1.1 Pressure Gradient Effects	21
4.1.2 Wind-Tunnel Wall Interference Effects	24
4.2 Stability Calculations	25
4.2.1 Stationary Crossflow Vortices	27
4.2.2 Tollmien-Schlichting Waves	29
4.2.3 Travelling Crossflow Vortices	30
4.2.4 Crossflow/Tollmien-Schlichting Interaction	32
4.3 Selection of the Experimental Test Condition	33
4.4 Reynolds Number Variation	34
4.5 Test-Section Liner Shape	34

5	EXPERIMENTAL RESULTS AND DISCUSSION	39
5.1	Freestream Flow Quality	39
5.2	Pressure Distributions	40
5.3	Flow Visualizations	41
5.4	Transition Locations	43
5.5	Boundary-Layer Spectra	44
5.6	Boundary-Layer Hot-Wire Surveys	45
5.6.1	Streamwise-Velocity Measurements	45
5.6.2	Spanwise Variation of Streamwise Velocity	48
5.6.3	Disturbance Profiles	49
5.6.4	Streamwise-Velocity Contour Plots	53
5.7	Experimental/Theoretical Comparisons	59
5.7.1	Theoretical Disturbance Profiles	60
5.7.2	Disturbance Profile Comparisons	62
5.7.3	Comparison of Experimental Streamwise Velocity-Contour Plots and Theoretical Vector Plots	64
5.7.4	Wavelength Comparison	66
5.7.5	Growth Rate Comparison	67
5.8	Experimental Results Summary	68
6	CONCLUSIONS	77
Appendix A	Relationships Between Coordinate Systems	247
Appendix B	Hot-Wire Signal Interpretation Procedure	251
Appendix C	Error Analysis	255
References		261

List of Tables

Table 1	Crossflow Stability Analysis Using SALLY Code for $\alpha = -4^\circ$ and $R_c = 3.81 \times 10^6$	82
Table 2	Transition Locations and Wavelengths from Naphthalene Flow Visualization.	82
Table 3	N-factors at Transition Computed Using the SALLY Code for $\alpha = -4^\circ$ and $R_c = 2.37 \times 10^6$, $(x/c)_T = 0.58$	83
Table 4	N-factors at Transition Computed Using the SALLY Code for $\alpha = -4^\circ$ and $R_c = 2.73 \times 10^6$, $(x/c)_T = 0.45$	83
Table 5	N-factors at Transition Computed Using the SALLY Code for $\alpha = -4^\circ$ and $R_c = 3.73 \times 10^6$, $(x/c)_T = 0.30$	84

List of Figures

Figure 1	Curved Streamlines over a Swept Wing.	85
Figure 2	Boundary-Layer Velocity Profiles on a Swept Wing.	86
Figure 3	Plan View of Arizona State University Unsteady Wind Tunnel (Dimensions in meters).	87
Figure 4	Photograph of New UWT Test Section With Liner Under Construction.	88
Figure 5	NLF(2)-0415 Airfoil.	89
Figure 6	NLF(2)-0415 Design Point Pressure Distribution at $\alpha = 0^\circ$ and $\delta_f = 0^\circ$ in Free Air.	90
Figure 7	NLF(2)-0415 Pressure Distribution for $\alpha = -4^\circ$ and $\delta_f = 0^\circ$ in Free Air.	91
Figure 8	NLF(2)-0415 Pressure Distribution for $\alpha = -2^\circ$ and $\delta_f = 0^\circ$ in Free Air.	92
Figure 9	NLF(2)-0415 Pressure Distribution for $\alpha = 2^\circ$ and $\delta_f = 0^\circ$ in Free Air.	93
Figure 10	NLF(2)-0415 Pressure Distribution for $\alpha = 4^\circ$ and $\delta_f = 0^\circ$ in Free Air.	94
Figure 11	NLF(2)-0415 Pressure Distribution for $\alpha = 0^\circ$ and $\delta_f = -20^\circ$ in Free Air.	95
Figure 12	NLF(2)-0415 Pressure Distribution for $\alpha = 0^\circ$ and $\delta_f = -10^\circ$ in Free Air.	96
Figure 13	NLF(2)-0415 Pressure Distribution for $\alpha = 0^\circ$ and $\delta_f = 10^\circ$ in Free Air.	97
Figure 14	NLF(2)-0415 Pressure Distribution for $\alpha = 0^\circ$ and $\delta_f = 20^\circ$ in Free Air.	98
Figure 15	NLF(2)-0415 Pressure Distribution for $\alpha = -4^\circ$ and $\delta_f = 0^\circ$ in UWT.	99
Figure 16	NLF(2)-0415 Pressure Distribution for $\alpha = -2^\circ$ and $\delta_f = 0^\circ$ in UWT.	100
Figure 17	NLF(2)-0415 Pressure Distribution for $\alpha = 0^\circ$ and $\delta_f = 0^\circ$ in UWT.	101
Figure 18	NLF(2)-0415 Pressure Distribution for $\alpha = 2^\circ$ and $\delta_f = 0^\circ$ in UWT.	102
Figure 19	NLF(2)-0415 Pressure Distribution for $\alpha = 4^\circ$ and $\delta_f = 0^\circ$ in UWT.	103
Figure 20	Local Spatial Growth Rates for Stationary Crossflow Vortices at $\alpha = -4^\circ$ and $\delta_f = 0^\circ$ in UWT, $R_c = 3.81 \times 10^6$	104
Figure 21	Local Spatial Growth Rates for Stationary Crossflow Vortices at $\alpha = -2^\circ$ and $\delta_f = 0^\circ$ in UWT, $R_c = 3.81 \times 10^6$	105

Figure 22	Local Spatial Growth Rates for Stationary Crossflow Vortices at $\alpha = 0^\circ$ and $\delta_f = 0^\circ$ in UWT, $R_c = 3.81 \times 10^6$	106
Figure 23	Local Spatial Growth Rates for Stationary Crossflow Vortices at $\alpha = 2^\circ$ and $\delta_f = 0^\circ$ in UWT, $R_c = 3.81 \times 10^6$	107
Figure 24	Local Spatial Growth Rates for Stationary Crossflow Vortices at $\alpha = 4^\circ$ and $\delta_f = 0^\circ$ in UWT, $R_c = 3.81 \times 10^6$	108
Figure 25	N-factors for Stationary Crossflow Vortices at $\alpha = -4^\circ$ and $\delta_f = 0^\circ$ in UWT, $R_c = 3.81 \times 10^6$	109
Figure 26	N-factors for Stationary Crossflow Vortices at $\alpha = -2^\circ$ and $\delta_f = 0^\circ$ in UWT, $R_c = 3.81 \times 10^6$	110
Figure 27	N-factors for Stationary Crossflow Vortices at $\alpha = 0^\circ$ and $\delta_f = 0^\circ$ in UWT, $R_c = 3.81 \times 10^6$	111
Figure 28	N-factors for Stationary Crossflow Vortices at $\alpha = 2^\circ$ and $\delta_f = 0^\circ$ in UWT, $R_c = 3.81 \times 10^6$	112
Figure 29	N-factors for Stationary Crossflow Vortices at $\alpha = 4^\circ$ and $\delta_f = 0^\circ$ in UWT, $R_c = 3.81 \times 10^6$	113
Figure 30	Maximum N-factors for Stationary Crossflow Vortices at $\alpha = -4^\circ$ and $\delta_f = 0^\circ$ in UWT, $R_c = 3.81 \times 10^6$	114
Figure 31	Maximum N-factors for Stationary Crossflow Vortices at $\alpha = -2^\circ$ and $\delta_f = 0^\circ$ in UWT, $R_c = 3.81 \times 10^6$	115
Figure 32	Maximum N-factors for Stationary Crossflow Vortices at $\alpha = 0^\circ$ and $\delta_f = 0^\circ$ in UWT, $R_c = 3.81 \times 10^6$	116
Figure 33	Maximum N-factors for Stationary Crossflow Vortices at $\alpha = 2^\circ$ and $\delta_f = 0^\circ$ in UWT, $R_c = 3.81 \times 10^6$	117
Figure 34	Maximum N-factors for Stationary Crossflow Vortices at $\alpha = 4^\circ$ and $\delta_f = 0^\circ$ in UWT, $R_c = 3.81 \times 10^6$	118
Figure 35	Maximum N-factors for Tollmien-Schlichting Waves for $\alpha = 0, 2,$ and 4° and $\delta_f = 0^\circ$ in UWT, $R_c = 3.81 \times 10^6$	119
Figure 36	Maximum N-factors for Stationary Crossflow Vortices at $\alpha = -4^\circ$ and $\delta_f = 0^\circ$ in UWT for a Range of Reynolds Numbers.	120
Figure 37	Streamline Traces of Wind-Tunnel End Liner on X_L-Z_L Plane.	121
Figure 38	Lateral Deflections of End-Liner Surface at Various Distances from Wing-Chord Plane.	122
Figure 39	End-Liner Contours in the Y_L-Z_L Plane at Various Longitudinal Positions.	123
Figure 40	Diagram of Wind-Tunnel Test Section with Swept-Wing Model and End Liners Installed.	124
Figure 41	Freestream Velocity Spectrum for $R_c = 3.27 \times 10^6$	125

Figure 42	Comparison of Measured and Predicted Model Pressure Coefficients at the Upper End of the Model, $\alpha = -4^\circ$. . .	126
Figure 43	Comparison of Measured and Predicted Model Pressure Coefficients at the Lower End of the Model, $\alpha = -4^\circ$. . .	127
Figure 44	Naphthalene Flow Visualization, $\alpha = -4^\circ$, $R_c = 1.93 \times 10^6$	128
Figure 45	Naphthalene Flow Visualization, $\alpha = -4^\circ$, $R_c = 2.19 \times 10^6$	129
Figure 46	Naphthalene Flow Visualization, $\alpha = -4^\circ$, $R_c = 2.40 \times 10^6$	130
Figure 47	Naphthalene Flow Visualization, $\alpha = -4^\circ$, $R_c = 2.73 \times 10^6$	131
Figure 48	Naphthalene Flow Visualization, $\alpha = -4^\circ$, $R_c = 3.27 \times 10^6$	132
Figure 49	Naphthalene Flow Visualization Showing Vortex Tracks in the Turbulent Regions.	133
Figure 50	Liquid-crystal Flow Visualization.	134
Figure 51	Transition Location Versus Reynolds Number.	135
Figure 52	Boundary-Layer Velocity Spectrum, $\alpha = -4^\circ$, $R_c = 2.62 \times 10^6$	136
Figure 53	Boundary-Layer Velocity Spectrum, $\alpha = -4^\circ$, $R_c = 2.82 \times 10^6$	137
Figure 54	Boundary-Layer Velocity Spectrum, $\alpha = -4^\circ$, $R_c = 2.92 \times 10^6$	138
Figure 55	Boundary-Layer Velocity Spectrum, $\alpha = -4^\circ$, $R_c = 3.28 \times 10^6$	139
Figure 56	Comparison of Measured and Predicted Boundary-Layer Velocity Spectra, $\alpha = -4^\circ$, $R_c = 2.92 \times 10^6$	140
Figure 57	Streamwise-Velocity Profiles at $x/c = 0.20$, $\alpha = -4^\circ$, $R_c = 2.37 \times 10^6$	141
Figure 58	Streamwise-Velocity Profiles at $x/c = 0.25$, $\alpha = -4^\circ$, $R_c = 2.37 \times 10^6$	142
Figure 59	Streamwise-Velocity Profiles at $x/c = 0.30$, $\alpha = -4^\circ$, $R_c = 2.37 \times 10^6$	143
Figure 60	Streamwise-Velocity Profiles at $x/c = 0.35$, $\alpha = -4^\circ$, $R_c = 2.37 \times 10^6$	144
Figure 61	Streamwise-Velocity Profiles at $x/c = 0.40$, $\alpha = -4^\circ$, $R_c = 2.37 \times 10^6$	145
Figure 62	Streamwise-Velocity Profiles at $x/c = 0.45$, $\alpha = -4^\circ$, $R_c = 2.37 \times 10^6$	146

Figure 63	Streamwise-Velocity Profiles at $x/c = 0.50$, $\alpha = -4^\circ$, $R_c = 2.37 \times 10^6$	147
Figure 64	Streamwise-Velocity Profiles at $x/c = 0.55$, $\alpha = -4^\circ$, $R_c = 2.37 \times 10^6$	148
Figure 65	Stationary Crossflow-Disturbance Velocity Profiles at $x/c = 0.20$, $\alpha = -4^\circ$, $R_c = 2.37 \times 10^6$ Obtained From $U_s - U_{s \text{ avg.}}$	149
Figure 66	Stationary Crossflow-Disturbance Velocity Profiles at $x/c = 0.25$, $\alpha = -4^\circ$, $R_c = 2.37 \times 10^6$ Obtained From $U_s - U_{s \text{ avg.}}$	150
Figure 67	Stationary Crossflow-Disturbance Velocity Profiles at $x/c = 0.30$, $\alpha = -4^\circ$, $R_c = 2.37 \times 10^6$ Obtained From $U_s - U_{s \text{ avg.}}$	151
Figure 68	Stationary Crossflow-Disturbance Velocity Profiles at $x/c = 0.35$, $\alpha = -4^\circ$, $R_c = 2.37 \times 10^6$ Obtained From $U_s - U_{s \text{ avg.}}$	152
Figure 69	Stationary Crossflow-Disturbance Velocity Profiles at $x/c = 0.40$, $\alpha = -4^\circ$, $R_c = 2.37 \times 10^6$ Obtained From $U_s - U_{s \text{ avg.}}$	153
Figure 70	Stationary Crossflow-Disturbance Velocity Profiles at $x/c = 0.45$, $\alpha = -4^\circ$, $R_c = 2.37 \times 10^6$ Obtained From $U_s - U_{s \text{ avg.}}$	154
Figure 71	Stationary Crossflow-Disturbance Velocity Profiles at $x/c = 0.50$, $\alpha = -4^\circ$, $R_c = 2.37 \times 10^6$ Obtained From $U_s - U_{s \text{ avg.}}$	155
Figure 72	Stationary Crossflow-Disturbance Velocity Profiles at $x/c = 0.55$, $\alpha = -4^\circ$, $R_c = 2.37 \times 10^6$ Obtained From $U_s - U_{s \text{ avg.}}$	156
Figure 73	Stationary Crossflow-Disturbance Velocity Profiles at $x/c = 0.20$, $\alpha = -4^\circ$, $R_c = 2.37 \times 10^6$ Obtained From $U_s - U_{s \text{ ref.}}$	157
Figure 74	Stationary Crossflow-Disturbance Velocity Profiles at $x/c = 0.25$, $\alpha = -4^\circ$, $R_c = 2.37 \times 10^6$ Obtained From $U_s - U_{s \text{ ref.}}$	158
Figure 75	Stationary Crossflow-Disturbance Velocity Profiles at $x/c = 0.30$, $\alpha = -4^\circ$, $R_c = 2.37 \times 10^6$ Obtained From $U_s - U_{s \text{ ref.}}$	159
Figure 76	Stationary Crossflow-Disturbance Velocity Profiles at $x/c = 0.35$, $\alpha = -4^\circ$, $R_c = 2.37 \times 10^6$ Obtained From $U_s - U_{s \text{ ref.}}$	160
Figure 77	Stationary Crossflow-Disturbance Velocity Profiles at $x/c = 0.40$, $\alpha = -4^\circ$, $R_c = 2.37 \times 10^6$ Obtained From $U_s - U_{s \text{ ref.}}$	161
Figure 78	Stationary Crossflow-Disturbance Velocity Profiles at $x/c = 0.45$, $\alpha = -4^\circ$, $R_c = 2.37 \times 10^6$ Obtained From $U_s - U_{s \text{ ref.}}$	162
Figure 79	Stationary Crossflow-Disturbance Velocity Profiles at $x/c = 0.50$, $\alpha = -4^\circ$, $R_c = 2.37 \times 10^6$ Obtained From $U_s - U_{s \text{ ref.}}$	163
Figure 80	Stationary Crossflow-Disturbance Velocity Profiles at $x/c = 0.55$, $\alpha = -4^\circ$, $R_c = 2.37 \times 10^6$ Obtained From $U_s - U_{s \text{ ref.}}$	164
Figure 81	Travelling Wave Disturbance Velocity Profiles for $f = 100$ Hz at $x/c = 0.20$, $\alpha = -4^\circ$, $R_c = 2.37 \times 10^6$	165
Figure 82	Travelling Wave Disturbance Velocity Profiles for $f = 100$ Hz at $x/c = 0.25$, $\alpha = -4^\circ$, $R_c = 2.37 \times 10^6$	166

Figure 83	Travelling Wave Disturbance Velocity Profiles for $f = 100$ Hz at $x/c = 0.30$, $\alpha = -4^\circ$, $R_c = 2.37 \times 10^6$	167
Figure 84	Travelling Wave Disturbance Velocity Profiles for $f = 100$ Hz at $x/c = 0.35$, $\alpha = -4^\circ$, $R_c = 2.37 \times 10^6$	168
Figure 85	Travelling Wave Disturbance Velocity Profiles for $f = 100$ Hz at $x/c = 0.40$, $\alpha = -4^\circ$, $R_c = 2.37 \times 10^6$	169
Figure 86	Travelling Wave Disturbance Velocity Profiles for $f = 100$ Hz at $x/c = 0.45$, $\alpha = -4^\circ$, $R_c = 2.37 \times 10^6$	170
Figure 87	Travelling Wave Disturbance Velocity Profiles for $f = 100$ Hz at $x/c = 0.50$, $\alpha = -4^\circ$, $R_c = 2.37 \times 10^6$	171
Figure 88	Travelling Wave Disturbance Velocity Profiles for $f = 100$ Hz at $x/c = 0.55$, $\alpha = -4^\circ$, $R_c = 2.37 \times 10^6$	172
Figure 89	Mean Streamwise-Velocity Contours at $x/c = 0.20$, $\alpha = -4^\circ$, $R_c = 2.37 \times 10^6$	173
Figure 90	Mean Streamwise-Velocity Contours at $x/c = 0.25$, $\alpha = -4^\circ$, $R_c = 2.37 \times 10^6$	174
Figure 91	Mean Streamwise-Velocity Contours at $x/c = 0.30$, $\alpha = -4^\circ$, $R_c = 2.37 \times 10^6$	175
Figure 92	Mean Streamwise-Velocity Contours at $x/c = 0.35$, $\alpha = -4^\circ$, $R_c = 2.37 \times 10^6$	176
Figure 93	Mean Streamwise-Velocity Contours at $x/c = 0.40$, $\alpha = -4^\circ$, $R_c = 2.37 \times 10^6$	177
Figure 94	Mean Streamwise-Velocity Contours at $x/c = 0.45$, $\alpha = -4^\circ$, $R_c = 2.37 \times 10^6$	178
Figure 95	Mean Streamwise-Velocity Contours at $x/c = 0.50$, $\alpha = -4^\circ$, $R_c = 2.37 \times 10^6$	179
Figure 96	Mean Streamwise-Velocity Contours at $x/c = 0.55$, $\alpha = -4^\circ$, $R_c = 2.37 \times 10^6$	180
Figure 97	Stationary Crossflow-Vortex Velocity Contours Obtained From $U_s - U_{s \text{ avg}}$ at $x/c = 0.20$, $\alpha = -4^\circ$, $R_c = 2.37 \times 10^6$	181
Figure 98	Stationary Crossflow-Vortex Velocity Contours Obtained From $U_s - U_{s \text{ avg}}$ at $x/c = 0.25$, $\alpha = -4^\circ$, $R_c = 2.37 \times 10^6$	182
Figure 99	Stationary Crossflow-Vortex Velocity Contours Obtained From $U_s - U_{s \text{ avg}}$ at $x/c = 0.30$, $\alpha = -4^\circ$, $R_c = 2.37 \times 10^6$	183
Figure 100	Stationary Crossflow-Vortex Velocity Contours Obtained From $U_s - U_{s \text{ avg}}$ at $x/c = 0.35$, $\alpha = -4^\circ$, $R_c = 2.37 \times 10^6$	184
Figure 101	Stationary Crossflow-Vortex Velocity Contours Obtained From $U_s - U_{s \text{ avg}}$ at $x/c = 0.40$, $\alpha = -4^\circ$, $R_c = 2.37 \times 10^6$	185
Figure 102	Stationary Crossflow-Vortex Velocity Contours Obtained From $U_s - U_{s \text{ avg}}$ at $x/c = 0.45$, $\alpha = -4^\circ$, $R_c = 2.37 \times 10^6$	186

Figure 103	Stationary Crossflow-Vortex Velocity Contours Obtained From $U_s - U_{s\text{ avg}}$ at $x/c = 0.50$, $\alpha = -4^\circ$, $R_c = 2.37 \times 10^6$..	187
Figure 104	Stationary Crossflow-Vortex Velocity Contours Obtained From $U_s - U_{s\text{ avg}}$ at $x/c = 0.55$, $\alpha = -4^\circ$, $R_c = 2.37 \times 10^6$..	188
Figure 105	Stationary Crossflow-Vortex Velocity Contours Obtained From $U_s - U_{s\text{ ref}}$ at $x/c = 0.20$, $\alpha = -4^\circ$, $R_c = 2.37 \times 10^6$..	189
Figure 106	Stationary Crossflow-Vortex Velocity Contours Obtained From $U_s - U_{s\text{ ref}}$ at $x/c = 0.25$, $\alpha = -4^\circ$, $R_c = 2.37 \times 10^6$..	190
Figure 107	Stationary Crossflow-Vortex Velocity Contours Obtained From $U_s - U_{s\text{ ref}}$ at $x/c = 0.30$, $\alpha = -4^\circ$, $R_c = 2.37 \times 10^6$..	191
Figure 108	Stationary Crossflow-Vortex Velocity Contours Obtained From $U_s - U_{s\text{ ref}}$ at $x/c = 0.35$, $\alpha = -4^\circ$, $R_c = 2.37 \times 10^6$..	192
Figure 109	Stationary Crossflow-Vortex Velocity Contours Obtained From $U_s - U_{s\text{ ref}}$ at $x/c = 0.40$, $\alpha = -4^\circ$, $R_c = 2.37 \times 10^6$..	193
Figure 110	Stationary Crossflow-Vortex Velocity Contours Obtained From $U_s - U_{s\text{ ref}}$ at $x/c = 0.45$, $\alpha = -4^\circ$, $R_c = 2.37 \times 10^6$..	194
Figure 111	Stationary Crossflow-Vortex Velocity Contours Obtained From $U_s - U_{s\text{ ref}}$ at $x/c = 0.50$, $\alpha = -4^\circ$, $R_c = 2.37 \times 10^6$..	195
Figure 112	Stationary Crossflow-Vortex Velocity Contours Obtained From $U_s - U_{s\text{ ref}}$ at $x/c = 0.55$, $\alpha = -4^\circ$, $R_c = 2.37 \times 10^6$..	196
Figure 113	Travelling-Wave RMS-Velocity Contours for $f = 100$ Hz at $x/c = 0.20$, $\alpha = -4^\circ$, $R_c = 2.37 \times 10^6$..	197
Figure 114	Travelling-Wave RMS-Velocity Contours for $f = 100$ Hz at $x/c = 0.25$, $\alpha = -4^\circ$, $R_c = 2.37 \times 10^6$..	198
Figure 115	Travelling-Wave RMS-Velocity Contours for $f = 100$ Hz at $x/c = 0.30$, $\alpha = -4^\circ$, $R_c = 2.37 \times 10^6$..	199
Figure 116	Travelling-Wave RMS-Velocity Contours for $f = 100$ Hz at $x/c = 0.35$, $\alpha = -4^\circ$, $R_c = 2.37 \times 10^6$..	200
Figure 117	Travelling-Wave RMS-Velocity Contours for $f = 100$ Hz at $x/c = 0.40$, $\alpha = -4^\circ$, $R_c = 2.37 \times 10^6$..	201
Figure 118	Travelling-Wave RMS-Velocity Contours for $f = 100$ Hz at $x/c = 0.45$, $\alpha = -4^\circ$, $R_c = 2.37 \times 10^6$..	202
Figure 119	Travelling-Wave RMS-Velocity Contours for $f = 100$ Hz at $x/c = 0.50$, $\alpha = -4^\circ$, $R_c = 2.37 \times 10^6$..	203
Figure 120	Travelling-Wave RMS-Velocity Contours for $f = 100$ Hz at $x/c = 0.55$, $\alpha = -4^\circ$, $R_c = 2.37 \times 10^6$..	204
Figure 121	Theoretical Mean Chordwise-Velocity Profiles, $\alpha_{\text{ref}} = -5^\circ$, $R_c = 2.37 \times 10^6$..	205
Figure 122	Theoretical Mean Spanwise-Velocity Profiles, $\alpha_{\text{ref}} = -5^\circ$, $R_c = 2.37 \times 10^6$..	206

Figure 123	Theoretical Stationary Crossflow-Disturbance Velocity Profiles (Chordwise Component), $\alpha_{ref} = -5^\circ$, $R_c = 2.37 \times 10^6$	207
Figure 124	Theoretical Stationary Crossflow-Disturbance Velocity Profiles (Surface-Normal Component), $\alpha_{ref} = -5^\circ$, $R_c = 2.37 \times 10^6$	208
Figure 125	Theoretical Stationary Crossflow-Disturbance Velocity Profiles (Spanwise Component), $\alpha_{ref} = -5^\circ$, $R_c = 2.37 \times 10^6$	209
Figure 126	Theoretical Mean Streamwise-Velocity Profiles, $\alpha_{ref} = -5^\circ$, $R_c = 2.37 \times 10^6$	210
Figure 127	Theoretical Mean Cross-stream Velocity Profiles, $\alpha_{ref} = -5^\circ$, $R_c = 2.37 \times 10^6$	211
Figure 128	Theoretical Stationary Crossflow-Disturbance Velocity Profiles (Streamwise Component), $\alpha_{ref} = -5^\circ$, $R_c = 2.37 \times 10^6$	212
Figure 129	Theoretical Stationary Crossflow-Disturbance Velocity Profiles (Cross-stream Component), $\alpha_{ref} = -5^\circ$, $R_c = 2.37 \times 10^6$	213
Figure 130	Theoretical Mean-Velocity Profiles Along the Vortex Axis, $\alpha_{ref} = -5^\circ$, $R_c = 2.37 \times 10^6$	214
Figure 131	Theoretical Mean-Velocity Profiles Perpendicular to the Vortex Axis, $\alpha_{ref} = -5^\circ$, $R_c = 2.37 \times 10^6$	215
Figure 132	Theoretical Stationary Crossflow-Disturbance Velocity Profiles Along the Vortex Axis, $\alpha_{ref} = -5^\circ$, $R_c = 2.37 \times 10^6$	216
Figure 133	Theoretical Stationary Crossflow-Disturbance Velocity Profiles Perpendicular to the Vortex Axis, $\alpha_{ref} = -5^\circ$, $R_c = 2.37 \times 10^6$	217
Figure 134	Theoretical Stationary Crossflow-Disturbance Velocity Vectors Across a Single Vortex Wavelength, $\alpha_{ref} = -5^\circ$, $R_c = 2.37 \times 10^6$	218
Figure 135	Theoretical Total Velocity Vectors (Disturbance Plus Mean Flow) Across a Single Vortex Wavelength, $\alpha_{ref} = -5^\circ$, $R_c = 2.37 \times 10^6$	219
Figure 136	Theoretical Total Velocity Vectors (Disturbance Plus Mean Flow) Across a Single Vortex Wavelength With Normal Velocity Components Scaled by a Factor of 100, $\alpha_{ref} = -5^\circ$, $R_c = 2.37 \times 10^6$	220

Figure 137	Comparison of Experimental Streamwise-Disturbance Velocity Profile Determined from $U_s - U_{s \text{ avg}}$ with Theoretical Eigenfunction, $x/c = 0.20$, $\alpha = -4^\circ$, $R_c = 2.37 \times 10^6$	221
Figure 138	Comparison of Experimental Streamwise-Disturbance Velocity Profile Determined from $U_s - U_{s \text{ avg}}$ with Theoretical Eigenfunction, $x/c = 0.25$, $\alpha = -4^\circ$, $R_c = 2.37 \times 10^6$	222
Figure 139	Comparison of Experimental Streamwise-Disturbance Velocity Profile Determined from $U_s - U_{s \text{ avg}}$ with Theoretical Eigenfunction, $x/c = 0.30$, $\alpha = -4^\circ$, $R_c = 2.37 \times 10^6$	223
Figure 140	Comparison of Experimental Streamwise-Disturbance Velocity Profile Determined from $U_s - U_{s \text{ avg}}$ with Theoretical Eigenfunction, $x/c = 0.35$, $\alpha = -4^\circ$, $R_c = 2.37 \times 10^6$	224
Figure 141	Comparison of Experimental Streamwise-Disturbance Velocity Profile Determined from $U_s - U_{s \text{ avg}}$ with Theoretical Eigenfunction, $x/c = 0.40$, $\alpha = -4^\circ$, $R_c = 2.37 \times 10^6$	225
Figure 142	Comparison of Experimental Streamwise-Disturbance Velocity Profile Determined from $U_s - U_{s \text{ avg}}$ with Theoretical Eigenfunction, $x/c = 0.45$, $\alpha = -4^\circ$, $R_c = 2.37 \times 10^6$	226
Figure 143	Comparison of Experimental Streamwise-Disturbance Velocity Profile Determined from $U_s - U_{s \text{ avg}}$ with Theoretical Eigenfunction, $x/c = 0.50$, $\alpha = -4^\circ$, $R_c = 2.37 \times 10^6$	227
Figure 144	Comparison of Experimental Streamwise-Disturbance Velocity Profile Determined from $U_s - U_{s \text{ avg}}$ with Theoretical Eigenfunction, $x/c = 0.55$, $\alpha = -4^\circ$, $R_c = 2.37 \times 10^6$	228
Figure 145	Comparison of Experimental Mean Streamwise-Velocity Contours with Theoretical Vortex Velocity-Vector Field, $x/c = 0.20$, $\alpha = -4^\circ$, $R_c = 2.37 \times 10^6$	229
Figure 146	Comparison of Experimental Mean Streamwise-Velocity Contours with Theoretical Vortex Velocity-Vector Field, $x/c = 0.25$, $\alpha = -4^\circ$, $R_c = 2.37 \times 10^6$	230
Figure 147	Comparison of Experimental Mean Streamwise-Velocity Contours with Theoretical Vortex Velocity-Vector Field, $x/c = 0.30$, $\alpha = -4^\circ$, $R_c = 2.37 \times 10^6$	231

Figure 148	Comparison of Experimental Mean Streamwise-Velocity Contours with Theoretical Vortex Velocity-Vector Field, $x/c = 0.35$, $\alpha = -4^\circ$, $R_c = 2.37 \times 10^6$	232
Figure 149	Comparison of Experimental Mean Streamwise-Velocity Contours with Theoretical Vortex Velocity-Vector Field, $x/c = 0.40$, $\alpha = -4^\circ$, $R_c = 2.37 \times 10^6$	233
Figure 150	Comparison of Experimental Mean Streamwise-Velocity Contours with Theoretical Vortex Velocity-Vector Field, $x/c = 0.45$, $\alpha = -4^\circ$, $R_c = 2.37 \times 10^6$	234
Figure 151	Comparison of Experimental Mean Streamwise-Velocity Contours with Theoretical Vortex Velocity-Vector Field, $x/c = 0.50$, $\alpha = -4^\circ$, $R_c = 2.37 \times 10^6$	235
Figure 152	Comparison of Experimental Mean Streamwise-Velocity Contours with Theoretical Vortex Velocity-Vector Field, $x/c = 0.55$, $\alpha = -4^\circ$, $R_c = 2.37 \times 10^6$	236
Figure 153	Comparison of Experimental Stationary Crossflow-Disturbance Velocity Contours with Theoretical Vortex Velocity-Vector Field, $x/c = 0.20$, $\alpha = -4^\circ$, $R_c = 2.37 \times 10^6$	237
Figure 154	Comparison of Experimental Stationary Crossflow-Disturbance Velocity Contours with Theoretical Vortex Velocity-Vector Field, $x/c = 0.25$, $\alpha = -4^\circ$, $R_c = 2.37 \times 10^6$	238
Figure 155	Comparison of Experimental Stationary Crossflow-Disturbance Velocity Contours with Theoretical Vortex Velocity-Vector Field, $x/c = 0.30$, $\alpha = -4^\circ$, $R_c = 2.37 \times 10^6$	239
Figure 156	Comparison of Experimental Stationary Crossflow-Disturbance Velocity Contours with Theoretical Vortex Velocity-Vector Field, $x/c = 0.35$, $\alpha = -4^\circ$, $R_c = 2.37 \times 10^6$	240
Figure 157	Comparison of Experimental Stationary Crossflow-Disturbance Velocity Contours with Theoretical Vortex Velocity-Vector Field, $x/c = 0.40$, $\alpha = -4^\circ$, $R_c = 2.37 \times 10^6$	241
Figure 158	Comparison of Experimental Stationary Crossflow-Disturbance Velocity Contours with Theoretical Vortex Velocity-Vector Field, $x/c = 0.45$, $\alpha = -4^\circ$, $R_c = 2.37 \times 10^6$	242

Figure 159	Comparison of Experimental Stationary Crossflow-Disturbance Velocity Contours with Theoretical Vortex Velocity-Vector Field, $x/c = 0.50$, $\alpha = -4^\circ$, $R_c =$ 2.37×10^6	243
Figure 160	Comparison of Experimental Stationary Crossflow-Disturbance Velocity Contours with Theoretical Vortex Velocity-Vector Field, $x/c = 0.55$, $\alpha = -4^\circ$, $R_c =$ 2.37×10^6	244
Figure 161	Comparison of Theoretical and Experimental Stationary Crossflow-Vortex Wavelengths, $\alpha = -4^\circ$, $R_c = 2.37 \times 10^6$. .	245
Figure 162	Comparison of Theoretical and Experimental Stationary Crossflow-Vortex Growth Rates, $\alpha = -4^\circ$, $R_c =$ 2.37×10^6	246
Figure A1	Coordinate System Relationships for a Swept Wing. . .	249
Figure A2	Left-Handed Coordinate Systems for a Swept Wing. . .	250

1 INTRODUCTION

1.1 Background

The flow over aircraft surfaces can be either laminar or turbulent. Laminar flow smoothly follows the airplane contours and produces much lower local skin-friction drag than the more chaotic turbulent flow. Often both laminar and turbulent flow regions are found on a given aircraft. The ratio of laminar/turbulent flow areas is highly dependent on the size, shape, surface finish, speed, and flight environment of the aircraft. The process of minimizing aircraft drag by maintaining laminar flow using active means such as suction, heating, or cooling is referred to as Laminar Flow Control (LFC). LFC technology is being considered for applications on new large transonic and supersonic transport aircraft. The goal of this effort is to reduce direct operating costs of new aircraft by reducing the drag and therefore the fuel consumed. This effort could take on increased significance if political situations produce fuel shortages as have occurred several times in the past. Adequate understanding of the boundary-layer transition process from laminar to turbulent flow lies at the heart of LFC technology. The present research effort is aimed at investigating an important component of the transition process on swept wings, namely, the development and growth of crossflow vortices.

The boundary-layer transition problem consists of three important phases — receptivity, linear disturbance amplification, and nonlinear interaction and breakdown (Reed and Saric, 1989). The Navier-Stokes equations are the appropriate model for all of these phases. However, techniques to solve these equations for the entire range of the transition problem are only now being developed. Most experimental and theoretical examinations until recently have focused on the second of the phases, namely, linear disturbance growth in a laminar boundary layer. For two-dimensional flows the experimental and theoretical investigations in this

linear regime are in general agreement and are considered to be conceptually well understood (Saric, 1992a). However, for three-dimensional flows, several important phenomena remain unresolved even for the linear stability phase (Reed and Saric, 1989). The resolution of these uncertainties has broad implications not only for linear stability analyses but also for the entire transition problem for three-dimensional flows.

Receptivity is the process by which disturbances in the external environment enter the boundary layer to begin the transition process (Morkovin, 1969). Examples of external disturbance mechanisms include freestream turbulence (with both vortical and acoustic components), wing surface irregularities and roughness, and surface vibrations. These small disturbances provide the initial-amplitude conditions for unstable waves.

The sensitivity of the laminar boundary layer to small-amplitude disturbances can be estimated by solving a set of linear disturbance equations obtained from the governing nonlinear Navier-Stokes equations (Schlichting, 1968). The best known example of this is the Orr-Sommerfeld equation for two-dimensional, incompressible Tollmien-Schlichting waves (Schlichting, 1968), but similar equations can be derived for more general three-dimensional, compressible flows. These linear equations are obtained by assuming that the complete flow field can be divided into a steady base flow and a disturbance or perturbation flow which varies both spatially and temporally. The base flow is assumed to be a known solution of the Navier-Stokes equations. By eliminating the known base flow solution from the complete problem, nonlinear disturbance equations result. The disturbance equations can be linearized by assuming that the input disturbances are small so that products of disturbance components are neglected. Thus, we obtain linear equations whose solutions can be superposed. These equations cover the second (or linear growth) phase of the transition problem. The disturbances

actually grow exponentially in time or space, but the linearity of the equations allows a Fourier decomposition of the problem by modes where each mode has its own characteristic frequency, wavelength, and wave orientation angle. The linear equations can be solved locally when the base flow solution is known by selecting two of the three characteristic variables (frequency, wavelength, and orientation). The local growth rate and the third of the characteristic variables are obtained from the linear equation solution. To estimate a transition location using the so-called e^N method of Smith and Van Ingen (Saric, 1992a) the local solutions to the linear equations must be integrated over the wing surface subject to some parameter constraint. The definition of the proper parameter constraint for the three-dimensional swept-wing flow problem is uncertain. Examples of the parameter-constraint relation which have been selected (often very arbitrarily) by various researchers include maximum local amplification rate, fixed wavelength, and fixed spanwise wavenumber. Widely different values for the integrated e^N solutions (and thus estimated transition locations) are obtained using the various constraint relations.

The nonlinear interaction and breakdown phase of the transition problem begins when the individual modes attain sufficient magnitude that products of the disturbance components can no longer be neglected as being small when compared to the base flow. At this stage the disturbances may have become so large that they begin to severely distort the base flow either spatially or temporally. These interaction processes are characterized by double exponential growth of the interacting modes (Saric, 1992a). Fortunately, this phase of the transition process usually occurs over a fairly short distance when compared to the total laminar flow run so that almost all of the pre-breakdown flow region can be approximated by the linear equations only.

1.2 Instability Modes

The laminar boundary layer on a swept wing has four fundamental instability modes — attachment-line, streamwise, crossflow, and centrifugal instabilities. These may exist independently or in combinations. The streamwise instability in a three-dimensional boundary layer is similar to the Tollmien-Schlichting waves in two-dimensional flows. Crossflow vortices arise as a result of a dynamic (or inviscid) instability of the inflectional crossflow velocity profile produced by the three-dimensionality of the mean flow field. Both of these instabilities are governed to first order by the Orr-Sommerfeld eigenvalue problem or its three-dimensional analog. This equation is obtained by assuming a separation of variables solution to the linearized Navier-Stokes disturbance equations. The results obtained are predictions of the local disturbance amplification rates subject to the constraints required by the separation of variables assumption. Görtler vortices may develop due to a centrifugal instability in the concave regions of a wing. Appropriate curvature terms must be included in the governing equations to account for this instability. The attachment-line instability problem may be significant on wings with large leading-edge radii. For the present experiment neither Görtler vortices nor attachment-line contamination are expected to be present. The most important effects are due to crossflow and Tollmien-Schlichting instabilities.

1.3 Goals of the Present Investigation

The goal of the present investigation is to isolate the crossflow instability of the three-dimensional flow over a 45° swept wing in such a way that it is independent of the other instabilities. This sweep angle is chosen because the crossflow instability has maximum strength at this angle. The wing consists of an NLF(2)-0415 airfoil which has its minimum pressure point for its design condition at $x/c = 0.71$ (Somers and Horstmann, 1985). The model is designed with a range

of two-dimensional angles of attack from -4° to $+4^\circ$ adjustable in steps of 1° . Contoured end liners are used in a closed-return 1.37 x 1.37 m wind-tunnel test section to simulate infinite swept-wing flow. When operated at $\alpha = -4^\circ$ the wing produces a long run of favorable streamwise pressure gradient which stabilizes the Tollmien-Schlichting waves while strongly amplifying crossflow vortices. The streamwise chord of 1.83 m allows the development of a relatively thick boundary layer (~ 2 to 4 mm in the measurement region) so that detailed velocity-profile measurements are possible in the region of crossflow-vortex development. Since the wing has a small leading-edge radius and the upper surface has no concave regions, attachment-line instability and Görtler vortices are not expected. Thus, this test condition allows the examination of the crossflow instability in isolation from the other three instability modes.

Naphthalene-sublimation and liquid-crystal flow-visualization studies are performed at several test conditions to determine both the extent of laminar flow and the stationary-vortex wavelengths. Detailed streamwise-velocity profiles are measured with hot-wire anemometers at several spanwise stations across a selected vortex track. The evolution of the vortex is analyzed over this single wavelength and compared with theoretical computations. Velocity profiles at the various spanwise locations and velocity contours across the vortex wavelength for both the mean and disturbance velocities are presented. Vector plots of the theoretical disturbance vortices are shown overlaid on the experimental velocity-contour plots. Experimental and theoretical growth rates and wavelengths are compared.

1.4 Outline

The research philosophy employed for this investigation consists of three steps — 1) use available computational methods to design the experiment, 2) conduct the experiment, and 3) compare the experimental results with computational

predictions. With the exception of the theoretical disturbance profiles introduced in Section 5.7.1 all computations presented are performed by the author.

Chapter 2 discusses and summarizes relevant research in swept-wing boundary-layer instabilities and transition. The experimental facility is described in Chapter 3. Wind tunnel dimensions and features which produce low-disturbance flow are discussed along with descriptions of the instrumentation, hot-wire traverse, and data acquisition systems. Chapter 4 gives details of the model and liner design. Extensive computations including linear stability analyses are performed for the highest possible test Reynolds number to insure, to the extent possible, that the proper parameter range is selected for the experiment. The relevant coordinate systems are introduced in Appendix A. The hot-wire data acquisition and analysis procedures are outlined in Appendix B. The experimental results are presented and discussed in Chapter 5. These data include model pressure distributions, flow-visualization photographs, boundary-layer spectra, and detailed hot-wire velocity profiles and contour plots. Comparisons of the experimental results to those from linear stability analyses for the exact test conditions are also shown. These comparisons require the introduction of computational results provided by other researchers. An analysis of the experimental measurement errors is discussed in Appendix C. Chapter 6 gives the conclusions.

2 REVIEW OF SWEEP-WING FLOWS

Reed and Saric (1989) give an excellent review of the stability of three-dimensional boundary layers. This Chapter basically follows their discussion for swept-wing flows and includes references since that time. Related material for the crossflow-vortex development on rotating disks, spheres, and cones is not included because of the differences in geometry from the swept-wing problem.

2.1 Stability and Transition Prediction

The principal motivation for the study of three-dimensional boundary layers is to understand the transition mechanisms on swept wings. The crossflow instability is first identified by Gray (1952) when he finds that high-speed swept wings have only minimal laminar flow even though unswept versions of the same wings have laminar flow back to approximately 60% chord. He uses sublimating-chemical coatings to visualize the stationary crossflow-vortex pattern in the short laminar flow region near the wing leading edge. These findings are subsequently verified by Owen and Randall (1952) and Stuart (1953). Owen and Randall introduce a crossflow Reynolds number (based on the maximum crossflow velocity and the boundary-layer height where the crossflow velocity is 10% of the maximum) and determine that the minimum critical crossflow Reynolds number near the leading edge of a swept wing is very low ($R_{cf\ crit} = 96$). This work is put on a firm footing both experimentally and theoretically in the classic paper of Gregory, Stuart, and Walker (1955), who establish the generality of the results for three-dimensional boundary layers and present the complete disturbance-state equations.

Brown and Sayre (1954), and Brown (1955, 1959) working under Pfenninger's direction (Pfenninger, 1977) are the first to integrate the three-dimensional disturbance equations. Brown obtained results in agreement with Gray (1952) and

Owen and Randall (1952), but, in addition, showed the potential of suction in controlling the crossflow instability on swept wings. Pfenninger and his coworkers examine suction LFC in a series of experiments — Pfenninger (1957); Bacon, Tucker, and Pfenninger (1959); Pfenninger and Bacon (1961); Gault (1960); and Boltz, Kenyon, and Allen (1960). They verify the achievement of full-chord laminar flow to a maximum chord Reynolds number of $R_c = 29 \times 10^6$. With this first successful swept-wing LFC program, Pfenninger and his group thus establish the foundation of future efforts in this area. See Pfenninger (1977) for a collection of references on LFC efforts.

Smith and Gamberoni (1956) and Van Ingen (1956) introduce the so-called e^N linear stability method by integrating the local growth rates to determine an overall amplification factor at transition for two-dimensional and axisymmetric flows. They find that transition occurs whenever the N-factor reaches about 10 (or a disturbance amplification of e^{10}). Many investigators including Jaffe et al. (1970); Mack (1975, 1977, 1984); Hefner and Bushnell (1979); Bushnell and Malik (1985); and Berry et al. (1987) verify that similar results apply for the crossflow instability on swept wings. Recent wind-tunnel transition studies which add to the N-factor transition data base include Arnal, Casalis, and Jullien (1990); Creel, Malik, and Beckwith (1990); and Bieler and Redeker (1990). Flight tests involving NLF-transition studies include Collier et al. (1989); Parikh et al. (1989); Collier et al. (1990); Obara et al. (1990); Lee, Wusk, and Obara (1990); Horstmann, Redeker, and Quast (1990); Waggoner et al. (1990); and Obara, Vijgen, and Lee (1991). Suction-LFC wind-tunnel transition experiments include Berry et al. (1990); Harvey, Harris, and Brooks (1990); Arnal, Jullien, and Casalis (1991); and flight tests with suction LFC include Maddalon et al. (1989); and Runyan et al. (1990). These N-factor transition studies are facilitated by the use of linear stability codes such as SALLY (Srokowski and Orzag, 1977), MARIA (Dagenhart, 1981),

COSAL (Malik and Orzag, 1981), (Malik, 1982), and Linear-X (Herbert, 1989). Arnal (1989), Saric (1989, 1992), Stetson (1989), Malik (1989), Poll (1989), and Arnal and Aupoix (1992) give general discussions of the applicability of the e^N -transition methods in three-dimensional flows.

The basic equations for the linear stability analysis of compressible parallel flows are derived by Lees and Lin (1946), Lin (1955), Dunn and Lin (1955), and Lees and Reshotko (1962) using small disturbance theory. Mack's numerical results (Mack, 1965a,b, 1969, 1975) have long been heralded as the state of the art in both compressible and incompressible parallel-stability analysis. Other investigations of the crossflow instability in compressible flows include Lekoudis (1979); Mack (1979, 1981); El-Hady (1980); Reed, Stuckert, and Balakumar (1989); and Balakumar and Reed (1990). These investigations show that compressibility reduces the local amplification rates and changes the most unstable wave orientation angles. The largest impact of this stabilizing influence, however, is on the streamwise instability while little effect is noted for the crossflow instability.

Nonparallel flow effects on the crossflow instability are considered by Padhye and Nayfeh (1981), Nayfeh (1980a,b), El-Hady (1980), and Reed and Nayfeh (1982). Malik and Poll (1984) and Reed (1988) find that the most highly amplified crossflow disturbances are travelling waves rather than stationary waves. Viken et al. (1989); Müller, Bippes, and Collier (1989); Collier and Malik (1990); and Lin and Reed (1992) investigate the influence of streamline and surface curvature on crossflow vortices. The interaction of various primary disturbance modes is considered by Lekoudis (1980); Fischer and Dallmann (1987); El-Hady (1988); and Bassom and Hall (1990a,b,c, 1991). Transition criteria other than the e^N -method are considered by Arnal, Coustols, and Juillen (1984); Arnal, Habiballah, and Coustols (1984); Arnal and Coustols (1984); Michel, Arnal, and Coustols (1985); Arnal, Coustols, and Jelliti (1985); Michel, Coustols, and Arnal

(1985); Arnal and Jullien (1987); and King (1991).

2.2 Transition Experiments

Many transition experiments involving both NLF and LFC in wind tunnels and flight are discussed in the previous section in relation to N-factor correlation studies. Several transition experiments such as Poll (1985), Michel et al. (1985), and Kohama, Ukaku, and Ohta (1987) deserve further discussion.

Poll (1985) studies the crossflow instability on a long cylinder at various sweep angles. He finds that increasing the yaw angle strongly destabilizes the flow producing both stationary and travelling-wave disturbances. The fixed disturbance pattern is visualized using either surface-evaporation or oil-flow techniques. These disturbances appear as regularly spaced streaks nearly parallel to the inviscid flow direction and end at a sawtooth transition line. The unsteady disturbances appear as high-frequency ($f \approx 1$ kHz) harmonic waves which reach amplitudes in excess of 20% of the local mean velocity before the laminar flow breaks down.

Michel et al. (1985) investigate the crossflow instability on a swept-airfoil model. Surface-visualization studies show the regularly spaced streamwise streaks and sawtooth transition pattern found by Poll (1985). Hot-wire probes are used to examine both the stationary vortex structure and unsteady wave motion. Based on their hot-wire studies Michel et al. conclude that the ratio of the spanwise wavelength to boundary-layer thickness is nearly constant at $\lambda/\delta = 4$. They also find a small spectral peak near 1 kHz which is attributed to the streamwise instability. Theoretical work included in the paper shows that the disturbance flow pattern consists of a layer of counter-rotating vortices with axes aligned approximately parallel to the local mean flow. But, when the mean flow is added to the disturbance pattern the vortices are no longer clearly visible.

Kohama et al. (1987) use hot-wire probes and smoke to examine the three-dimensional transition mechanism on a swept cylinder. A traveling-wave disturbance appears in the final stages of transition which is attributed to an inflectional secondary instability of the primary stationary crossflow vortices. The secondary instability consists of ringlike vortices surrounding the primary vortex. They conclude that the high-frequency waves detected by Poll (1985) are actually produced by the secondary instability mechanism.

2.3 Detailed Theory and Simulation

Several papers investigating the development and growth of crossflow vortices on swept wings using detailed theoretical and simulation techniques have appeared recently. Choudhari and Streett (1990) investigate the receptivity of three-dimensional and high-speed boundary layers to several instability mechanisms including crossflow vortices. They use both numerical and asymptotic procedures to develop quantitative predictions of the localized generation of boundary-layer disturbance waves. Both primary and secondary instability theories are applied by Fischer and Dallmann (1987, 1988, 1991) to generate theoretical results for comparison to the DFVLR swept flat plate experiments (Nitschke-Kowsky and Bippes, 1988; Bippes, 1989; Müller, 1989; Bippes and Müller, 1990). They use the Falkner-Skan-Cooke similarity profiles as a model of the undisturbed flow to find that the secondary-instability model yields good agreement with the experimental results especially the spatial distribution of the root-mean-square velocity fluctuations. Meyer and Kleiser (1988, 1989); Singer, Meyer, and Kleiser (1989); Meyer (1990); and Fischer (1991) use temporal simulations to investigate the non-linear stages of crossflow-vortex growth and the interaction between stationary and travelling crossflow vortices. They find generally good agreement between their numerical solutions and the DFVLR swept flat-plate experimental results. A pri-

mary stability analysis of the nonlinearly-distorted, horizontally-averaged velocity profiles shows stability characteristics similar to the undistorted basic flow.

Probably the most relevant computations are those which allow spatial evolution of the flow field especially for the nonlinear interaction problems where large distortions of the mean flow occur. However, these methods seem to suffer from the requirement to force fixed spanwise periodicity while the streamwise pattern is allowed to evolve naturally. Spalart (1989) solves the spatial Navier-Stokes equations for the case of swept Hiemenz flow to show the development of both stationary and travelling crossflow vortices with initial inputs consisting of either random noise, single disturbance waves, or wave packets. He finds disturbance amplification beginning at crossflow Reynolds numbers of $R_{cf} \approx 100$ and a smooth nonlinear saturation when the vortex strength reaches a few percent of the edge velocity. Also, preliminary evidence of a secondary instability is obtained. Reed and Lin (1987) and Lin (1992) conduct a direct numerical simulation of the flow over an infinite swept wing similar to that of the present experiment. In a very recent paper Malik and Li (1992) use both linear and nonlinear parabolized stability equations (See Herbert, 1991) to analyze the swept Hiemenz flow which approximates the flow near the attachment line of a swept wing. Their linear computations agree with the direct numerical simulations of Spalart (1989). They show a wall vorticity pattern which they conclude is remarkably similar to the experimental flow-visualization patterns seen near a swept-wing leading edge. The nonlinear growth rate initially agrees with the linear result, but further downstream it is found to drop below the linear growth rate and to oscillate with increasing downstream distance. When both stationary and travelling waves are used as initial conditions the travelling waves are shown to dominate even when the travelling wave is initially an order of magnitude smaller than the stationary vortex.

2.4 Stability Experiments

Detailed experimental investigations of the crossflow instability in three-dimensional boundary layers similar to those on swept wings have been conducted in two ways — with swept flat plates having a chordwise pressure gradient imposed by an associated wind-tunnel wall bump or with actual swept wings (or swept cylinders). Experiments using the flat plate technique include Saric and Yeates (1985); the DFVLR experiments of Bippes and coworkers (Nitschke-Kowsky, 1988; Nitschke-Kowsky and Bippes, 1988; Bippes, 1989; Müller, 1989,1990; Bippes and Müller, 1990; and Bippes, Müller, and Wagner, 1990); and Kachanov and Tarakykin (1989). The swept flat plate crossflow experiments offer the advantage of allowing easy hot-wire probe investigation over the flat model surface, but suffer from the lack of a properly-curved leading edge where the boundary-layer crossflow begins its development. Arnal and coworkers at ONERA (Arnal, Coustols, and Jullien, 1984; and Arnal and Jullien, 1987) conduct experiments of swept-wing or swept-cylinder models.

Arnal, Coustols, and Jullien (1984) find the mean velocity to exhibit a wavy pattern along the span due the presence of stationary crossflow vortices. The spanwise wavelength of this wavy pattern is found to correspond to the streamwise streaks observed in flow-visualization studies. The crossflow-vortex wavelength is shown to increase with downstream distance as some streaks observed in the flow visualizations coalesce while others vanish. The ratio of spanwise wavelength to local boundary-layer thickness remains approximately constant at $\lambda/\delta \approx 4$. Low-frequency travelling waves are observed which reach large amplitudes ($\pm 20\%$ of the local edge velocity) before transition to turbulence takes place. They conclude that both stationary and travelling crossflow waves constitute the primary instability of the flow on a swept wing. Arnal and Jullien (1987) investigate a swept-wing configuration with both negative and positive chordwise pressure

gradients. They find that when transition occurs in the accelerated-flow region that their crossflow transition criterion gives good results. In the mildly positive pressure gradient regions they find that interactions between crossflow vortices and Tollmien-Schlichting waves produce a complicated breakdown pattern which is not properly characterized by their crossflow transition criterion.

Saric and Yeates (1985) originate the technique of using contoured wall bumps to force a chordwise pressure gradient on a separate swept flat plate. This sets the foundation for detailed crossflow instability research which has been repeated by other investigators. They use the naphthalene flow-visualization technique to show a steady crossflow-vortex pattern with nearly equally-spaced streaks aligned approximately with the inviscid-flow direction. The wavelength of these streaks agrees quite well with the predictions from linear stability theory. Saric and Yeates use straight and slanted hot-wire probes to measure both streamwise- and crossflow-velocity profiles. The probes are moved along the model span (z -direction) at a fixed height (y) above the model surface for a range of locations using two different freestream velocities. Typical results show a steady vortex structure with vortex spacing half that predicted by the linear stability theory and shown by the surface flow-visualization studies. Reed (1988) uses her wave-interaction theory to show that the observed "wave doubling" is apparently due to a resonance between the dominant vortices predicted by the linear theory and other vortices of half that wavelength which are slightly amplified in the far upstream boundary layer. This wave-doubled pattern persists for a long distance down the flat plate without the subsequent appearance of harmonics. Unsteady disturbances are observed by Saric and Yeates but only in the transition region.

Nitschke-Kowsky (1988) and Nitschke-Kowsky and Bippes (1988) use oil coatings and naphthalene for flow flow-visualization studies on the swept flat plate. Flow velocities and surface shear disturbances are measured with hot-

wire and hot-film probes. They find a stationary crossflow-vortex pattern with the wavelength to boundary-layer thickness ratio of $\lambda/\delta \approx 4$ and travelling waves in a broad frequency band. The rms values for the travelling waves are modulated by the stationary vortex pattern indicating disturbance interaction. The wavelength of the stationary vortices and the frequencies of the travelling waves are found to be well predicted by the generalized Orr-Sommerfeld equation. Bippes (1989); Müller (1989, 1990); Bippes and Müller (1990); and Bippes, Müller, and Wagner (1990) find that stationary crossflow vortices dominate the instability pattern when the freestream disturbance level is low and that travelling waves tend to dominate in a high-disturbance environment. They find that when the swept plate is moved laterally in the open-jet wind-tunnel flow the stationary vortex pattern remains fixed and moves with the plate. The most amplified travelling-wave frequency is observed to differ between wind tunnels. Nonlinear effects are found to dominate although the linear theory adequately predicts the stationary vortex wavelengths and the travelling-wave frequency band.

Kachanov and Tarakykin (1989) duplicate the experiments of Saric and Yeates (1985) using identical swept flat plate and wall-bump geometries. They go on to demonstrate that streamwise slots with alternate suction and blowing can be used to artificially generate stationary crossflow vortices.

2.5 State of Present Knowledge

Detailed crossflow instability experiments are few in number, yet some significant observations are made. Both stationary and travelling crossflow waves are observed. The balance between stationary and travelling waves is shown to vary with external environmental conditions. Some evidence of nonlinear developments including disturbance interactions and disturbance-mode saturation is detected.

Theoretical and computational methods are currently being developed at a rapid pace. Benchmark experimental data sets are urgently needed for comparison with results from these new codes. Many questions about three-dimensional boundary-layer stability and transition remain to be answered. Why do stationary crossflow vortices seem to dominate in low-disturbance environments even though the existing theories indicate that the travelling waves are more highly amplified? Why do the stationary vortex flow patterns observed in different environments vary? That is, why do some studies show a fixed stationary vortex pattern throughout the flow and others show an evolving vortex pattern with vortices occasionally merging or vanishing? How does one accurately compute disturbance growth rates and transition locations for engineering applications? What are the effects of compressibility, curvature, nonparallelism, and nonlinearity on disturbance evolution? How does three-dimensional-flow transition compare and contrast with the situation in two-dimensional-flow? Information about the transition process is extremely important for the design of aircraft ranging from subsonic transports to hypersonic space vehicles. Understanding the instability mechanisms to be controlled by LFC systems is central to their design and optimization.

3 EXPERIMENTAL FACILITY

3.1 ASU Unsteady Wind Tunnel

The experiments are conducted in the Arizona State University Unsteady Wind Tunnel (UWT). The wind tunnel was originally located at the National Bureau of Standards and was reconstructed at Arizona State during 1984 to 1988 (Saric, 1992b).

The tunnel is a low-turbulence, closed-return facility that is equipped with a 1.4 x 1.4 x 5 m test section, in which oscillatory flows of air can be generated for the study of unsteady problems in low-speed aerodynamics. It can also be operated as a conventional low-turbulence wind tunnel with a steady speed range of 1 m/s to 36 m/s that is controlled to within 0.1%. A schematic plan view of the tunnel is shown in Figure 3. The facility is powered by a 150 hp variable speed DC motor and a single-stage axial blower.

The UWT is actually a major modification of the original NBS facility. A new motor drive with the capability of continuous speed variation over a 1:20 range was purchased. In order to improve the flow quality, the entire length of the facility is extended by 5 m. On the return leg of the tunnel, the diffuser is extended to obtain better pressure recovery and to minimize large-scale fluctuations. The leg just upstream of the fan is internally contoured with rigid foam. The contour is shaped to provide a smooth contraction and a smooth square-to-circular transition at the fan entrance. A large screen is added to the old diffuser to recover a stall and a nacelle is added to the fan motor. Another screen is added downstream of the diffuser splitter plates. Steel turning vanes with a 50 mm chord, spaced every 40 mm, are placed in each corner of the tunnel.

On the test length, the contraction cone is redesigned by using a fifth-degree polynomial with a L/D of 1.25 and a contraction ratio of 5.33. It is fabricated from

3.2 mm thick steel sheet. The primary duct has seven screens that are uniformly spaced at 230 mm. The first five screens have an open area ratio of 0.70 and the last two have an open area ratio of 0.65. This last set of screens are seamless and have dimensions of 2.74 x 3.66 m with 0.165 mm diameter stainless steel wire on a 30 wire/inch mesh. Aluminum honeycomb, with a 6.35 mm cell size and a L/D of 12, is located upstream of the screens. This helps to lower the turbulence levels to less than 0.02% (high pass at 2 Hz) over the entire velocity range.

Both the test section and the fan housing are completely vibration isolated from the rest of the tunnel by means of isolated concrete foundations and flexible couplings. The test section is easily removable and each major project has its own test section. The interior of the return section is contoured with a wooden frame, window screens, and urethane foam in order to provide a smooth contraction and a square-to-circular transition before the fan.

Static and dynamic pressure measurements are made with a 1000 torr and a 10 torr, temperature-compensated transducers, MKS type 390HA-0100SP05. These are interfaced with 14-bit, MKS type 270B Signal Conditioners. Powerful real time data-processing capabilities are provided by a MASSCOMP 5600 and a DEC 5000 Model 200 with output via floppy disk, printer, CRT display, and digital plotting. The super mini-computers control the experiment and the data acquisition. They are built around a real-time UNIX operating system and are the state-of-the-art in data acquisition and computing. All static and instantaneous flying hot-wire calibrations, mean-flow measurements, proximeter calibration, 3-D traverse control, conditional sampling, freestream turbulence and boundary-layer disturbance measurements are interfaced into the data-acquisition system. The MASSCOMP 5600 Data-Acquisition System has a 32-bit CPU, floating-point processor with accelerator, *Aurora* Graphics subsystem with processor, 8 Mb RAM, 71 Mb hard disk, 45 Mb tape cartridge, 16-channel 1 MHz A/D converter with

programmable gain, 8-channel 500 kHz D/A converter, IEEE-488 bus, *Ethernet* (XNS) connection, and associated display terminals and output devices. Each DEC Station 5000 Model 200 has a 32-bit RISC 25 MHz CPU, 16 Mb RAM, 330 Mb hard disk, 5 Mb/sec SCSI bus, *Ethernet* (XNS), and associated display terminals. The facility has a 2-D Laser Doppler Anemometer system and a low-noise hot-wire anemometer system to measure simultaneously two velocity components in the neighborhood of model surfaces. Signal analysis devices include 2 computer-controlled differential filter amplifiers, 3 differential amplifiers, a dual phase-lock amplifier, a function generator, an 8-channel oscilloscope, a single-channel spectrum analyzer, fourth-order band-pass filters, and 2 tracking filters. A three-dimensional traverse system is included in the facility. The x-traverse guide rods are mounted exterior to the test section parallel to the tunnel side walls. A slotted, moveable plastic panel permits the insertion of the hot-wing strut through the tunnel side wall. The traverse system has total travel limits of 3700 mm, 100 mm, and 300 mm in the x-, y-, and z-directions, respectively, where x is in the freestream flow direction, y is normal to the wing-chord plane, and z spans the tunnel. The data-acquisition system automatically moves the probe within the boundary layer for each set of measurements after an initial manual alignment. The x-traverse is driven by stepping motors through a chain drive with a minimum step size of 286 μm . The y- and z-traverses are operated by precision lead screws (2.54 mm lead, 1.8° per step) which give minimum steps of 13 μm .

Further details of the wind tunnel, data-acquisition system, and operating conditions of the UWT are discussed in Saric, Takagi, and Mousseux (1988)[9] and Saric (1992b).

3.2 New Test Section

An entirely new test section was designed and fabricated for these experiments

in the UWT. Figure 4 shows a photograph of the new test section with the liner under construction. It is fully interchangeable with the existing test section. The 45° swept-wing model which weighs approximately 500 kilograms is supported by a thrust bearing mounted to the floor of the new test section. With the model weight supported on the thrust bearing, the two-dimensional model angle of attack can be easily changed from -4 to $+4^\circ$ in steps of 1° . Contoured endliners must be fabricated and installed inside the test section for each angle of attack. Once the system of model and endliners are installed in the new test section, the entire unit replaces the existing test section. This allows alternate tests of the crossflow experiment and other experiments in the UWT without disrupting the attachment and alignment of the model in the test section.

4 MODEL AND LINER DESIGN

Chapter 4 gives the design procedure for the experiment. The expected pressure distributions on the selected airfoil in free air and on the swept wing in the UWT including wind-tunnel wall-interference effects are shown. Linear stability analyses for stationary and travelling crossflow waves and Tollmien-Schlichting waves at the maximum chord Reynolds number are performed. The experimental test condition is selected. A test-section liner shape to simulate infinite swept-wing flow is presented.

4.1 Airfoil Selection

In order to investigate crossflow-vortex development and growth in isolation from other boundary-layer instabilities it is necessary to design or select an experimental configuration which strongly amplifies the crossflow vortices while keeping the other instabilities subcritical. The NLF(2)-0415 airfoil (Somers and Horstmann, 1985) is designed as a low-drag wing to be used on a commuter aircraft with unswept wings. It has a relatively small leading-edge radius and no concave regions on its upper surface. The NLF(2)-0415 airfoil shape and pressure distribution for the design angle of attack of 0° are shown in Figures 5 and 6. The minimum pressure point on the upper surface at this condition is at 0.71 chord. The decreasing pressure from the stagnation point back to the minimum pressure point is intended to maintain laminar flow on the unswept wing by minimizing the Tollmien-Schlichting instability.

4.1.1 Pressure Gradient Effects

As discussed earlier in Chapter 2, positive or negative pressure gradients act to generate boundary-layer crossflow on a swept wing. For the present application on a 45° swept wing, the NLF(2)-0415 airfoil when operated at a small negative

angle of attack, functions as a nearly ideal crossflow generator. Its relatively small leading-edge radius eliminates the attachment-line instability mechanism for the range of Reynolds numbers achievable in the UWT. The Görtler instability is not present since there are no concave regions on the upper surface. And, the negative pressure gradient on the upper surface keeps the Tollmien-Schlichting instability subcritical back to $x/c = 0.71$ for angles of attack at or below the design angle of attack of 0° .

Figures 7–10 show the NLF(2)-0415 airfoil pressure distributions predicted using the Eppler airfoil code (Eppler and Somers, 1980) for angles of attack of -4° , -2° , 2° , and 4° , respectively. These computations neglect viscous effects and assume that the airfoil is operating in free air, i.e., no wind-tunnel wall interference is present. Note that for $\alpha = -4^\circ$, -2° , and 0° the minimum pressure point on the upper surface is located at about $x/c = 0.71$. Beyond $x/c = 0.71$ the pressure recovers gradually at first and then more strongly to a value somewhat greater than the freestream static pressure ($C_p > 0$) for all of the angles of attack shown in Figures 6–10. For positive angles of attack the minimum pressure point shifts far forward to $x/c < 0.02$. For $\alpha = 2^\circ$ the pressure recovery is very gradual back to $x/c = 0.30$ followed by a slight acceleration to a second pressure minimum at $x/c = 0.71$. For $\alpha = 4^\circ$ a relatively strong pressure recovery follows the pressure minimum and a nearly flat pressure region is observed over the middle portion of the airfoil.

This shift in the pressure distribution with angle of attack has important implications for the strength of the boundary-layer crossflow generated in the leading-edge region. The strength of the crossflow varies with the magnitude of the pressure gradient, the extent of the pressure-gradient region, and the local boundary-layer thickness. The leading-edge crossflow is driven most strongly by the strong negative pressure gradients for the positive angles of attack, but since the extent

of the negative-pressure-gradient region is quite small and the boundary layer is very thin near the leading edge, very little boundary-layer crossflow is actually generated. Furthermore, for the positive angles of attack the positive pressure gradient which follows the pressure minimum overcomes the initial leading-edge crossflow to drive the crossflow in the opposite direction. This positive pressure gradient also accelerates the development of Tollmien-Schlichting waves. For the negative angles of attack, the negative pressure gradient in the leading-edge region is a somewhat weaker crossflow driver, but the negative pressure gradient region ($0 \leq x/c \leq 0.71$) is much larger. Thus, as the angle of attack decreases from 4° to -4° the leading-edge crossflow increases in strength. This indicates that the desired crossflow-dominated test condition is achieved at $\alpha = -4^\circ$. Interaction between Tollmien-Schlichting waves and crossflow vortices generated in the pressure recovery region is possible for $\alpha = 4^\circ$. Quantitative computational results to support these statements are presented in the following section.

Figures 6–10 show that a considerable range of pressure distributions is achievable by varying the model angle of attack. To insure even more flexibility in the pressure distributions the model is also equipped with a 20% chord trailing-edge flap. Figures 11–14 show typical effects of the 20% chord flap for the nominal design angle of attack of 0° and a range of flap-deflection angles from -20° to 20° . Using this flap-deflection range, the airfoil lift is changed from a negative value for $\delta_f = -20^\circ$ to a large positive value at $\delta_f = 20^\circ$ with corresponding upper surface pressure gradients which vary from mildly negative to strongly positive. However, these calculations neglect viscous effects to yield some very strong positive pressure gradients which are probably not physically achievable in the wind tunnel. But, they indicate that changes in the angle of attack and flap-deflection angles can be used together to achieve a large range of pressure gradient conditions on the upper surface.

4.1.2 Wind-Tunnel Wall Interference Effects

The large model-chord length of 1.83 m is selected to permit the examination of the crossflow-vortex development in a relatively thick (2 to 4 mm) boundary layer. However, wind-tunnel wall interference effects are expected when a 1.83 m chord model is installed in a 1.37 m square test section. To eliminate the influence of the walls on the model pressure distribution, the model could be surrounded by a four-wall test-section liner which follows streamline paths in free air flow. At each end of the swept wing, the liner would have to follow the curved streamlines as shown in Figure 1. And on the walls opposite the airfoil surfaces the liner would have to bulge to accommodate the flow over the wing shape. However, contoured top and bottom wall shapes make visual observation of the model during testing very difficult.

For the present experiment, a two-wall liner design was selected. In this approach the wind-tunnel walls opposite the wing upper and lower surfaces are not contoured to match the free-air streamlines but are simply left flat. The presence of the flat walls must, however, be accounted for in the design of the end-liner shapes and in the data interpretation. To accomplish this, a two-dimensional airfoil code (MCARF) which includes wind-tunnel wall effects (Stevens, Goradia, and Braden, 1971) was modified for 45° swept-wing flow. The influence of the flat tunnel walls on the pressure distribution is shown in Figures 15–19 for angles of attack of –4, –2, 0, 2, and 4°, respectively. Note that the influence of the flat walls on the airfoil pressure distributions is not negligible. But, the qualitative features of the pressure distributions remain the same when the wall interference is included. Negative angles of attack still produce gradual accelerations of the flow to the minimum pressure point at $x/c = 0.71$ while positive angles of attack give a rapid drop to minimum pressure near the leading edge followed by pressure recovery to a nearly constant level in the midchord region. The required end-liner shapes

to achieve quasi-infinite swept-wing flow will be discussed in a later section.

4.2 Stability Calculations

Extensive stability calculations were conducted prior to any experiments in order to determine the appropriate parameter range for this study. Two boundary-layer stability codes — MARIA (Dagenhart, 1981) and SALLY (Srokowski and Orszag, 1977) are used to predict the performance of the experimental configuration to assure, to the extent possible, that the experimental parameter range covers the physical phenomena of interest. Both of these codes use mean laminar boundary-layer profiles computed using the Cebeci swept and tapered wing boundary-layer code (Kaups and Cebeci, 1977) with pressure boundary conditions such as those shown in Figures 15–19. The MARIA code analyzes the stationary crossflow instability subject to the constraint of constant crossflow-vortex wavelength. It does not actually solve the crossflow eigenvalue problem discussed earlier in Chapter 2, but estimates the local spatial growth rates from a range of known solutions to the Orr-Sommerfeld equation for crossflow velocity profiles. The SALLY code, on the other hand, can analyze either the crossflow or Tollmien-Schlichting instabilities with a variety of constraint conditions. In the SALLY code, the crossflow instability is not limited to stationary vortices; travelling crossflow modes are also permissible.

The boundary-layer stability analysis methods are strictly only eigenvalue solvers which give local disturbance growth rates. The e^N method of transition prediction employs the integrated amplification factors (N-factors) as functions of location on the wing as given by

$$N(x/c) = \int_{(x/c)_0}^{(x/c)} -\alpha_i d(x/c) \quad (1)$$

where the local spatial amplification rate, α_i , indicates amplification whenever $\alpha_i < 0$. The values of α_i are determined by applying the eigenvalue solver at numerous locations along a streamline for various instability Fourier components. Each Fourier component is specified by its frequency and the eigenvalue solution must be constrained by some parameter(s) to make the integral of Equation 1 physically meaningful. As mentioned in Chapters 1 and 2, this constraint parameter is often selected in an apparently arbitrary fashion. In this dissertation the fixed wavelength constraint is used for crossflow vortices while the maximum amplification constraint is employed for Tollmien-Schlichting wave calculations. At this point, the constant wavelength constraint for crossflow is simply an assumption; however, a full justification for this selection based on the experimental observations will be presented later in Chapter 5. Since this investigation is aimed at the examination of crossflow vortices in the absence of primary Tollmien-Schlichting waves, it is critical that the strength of the Tollmien-Schlichting instability not be underestimated. Hence, the selection of the maximum amplification constraint for Tollmien-Schlichting waves.

The factor, A/A_0 , represents the amplification from the neutral point, $(x/c)_0$, back to an arbitrary location, (x/c) , and is obtained as

$$\frac{A}{A_0} = e^{N(x/c)} \quad (2)$$

for each disturbance component. The maximum N-factor, N_{max} , for each wavelength is obtained by continuing the integration in Equation 1 to the end of the amplification range as

$$N_{max} = \int_{(x/c)_0}^{(x/c)_e} -\alpha_i d(x/c) \quad (3)$$

where $(x/c)_e$ indicates the end of the amplification region. The amplification region may end for several possible reasons — because the second neutral point is

reached or because transition is forced by some other factor such as a laminar separation. The maximum amplification over the entire crossflow zone ($0 \leq x/c \leq 0.71$) is given by

$$\left(\frac{A}{A_0}\right)_{max} = e^{N_{max}} \quad (4)$$

or, equivalently, the natural logarithm of the amplification ratio is given by

$$\ln\left(\frac{A}{A_0}\right)_{max} = N_{max} \quad (5)$$

which is, of course, still a function of the disturbance component wavelength.

4.2.1 Stationary Crossflow Vortices

Figures 20–34 show predicted stationary crossflow-vortex growth rates, local amplification factors (N-factors), and maximum amplification factors (N_{max}) computed using the MARIA code (Dagenhart, 1981) for the 45° swept wing installed in UWT at angles of attack ranging from -4° to 4° . The growth rates are normalized with respect to the chord length. Travelling crossflow vortices which are more highly amplified than stationary vortices are considered in a later section. Emphasis here is placed on the stationary vortices because they arise due to surface roughness effects which seem likely to dominate on practical wing surfaces operated in low-disturbance wind-tunnel or flight environments (See Bippes and Müller, 1990). These computations set an upper bound on the stationary crossflow-vortex amplification ratios by assuming that laminar flow is maintained back to the beginning of the strong pressure recovery region at $x/c = 0.71$ for the highest achievable chord Reynolds number of 3.81×10^6 . Of course, the amplification of crossflow vortices may cause boundary-layer transition before $x/c = 0.71$ for this or even lower Reynolds numbers.

The local spatial growth rate is shown for each angle of attack in Figures 20–24. The data are plotted for a range of wavelengths for each case with the

ratio of wavelength to chord indicated in the key. Note that the distribution of local amplification is considerably different for the five cases. Short-wavelength disturbances are amplified over a fairly narrow range near the leading edge while the amplification region for the longer wavelengths begins further downstream and continues back to the beginning of the strong pressure recovery at $x/c = 0.71$. In all cases, the maximum local amplification occurs in the leading-edge region ($x/c < 0.10$) and it is of similar magnitude. Downstream of the leading-edge region ($x/c > 0.10$) the amplification rates vary considerably from case to case. For $\alpha = -4^\circ$ the growth rates for intermediate wavelengths level off at a plateau slightly greater than half the initial short-wavelength amplification peak. As α increases from -4° this plateau level decreases until it disappears completely at $\alpha = 2^\circ$. For $\alpha = 2^\circ$ and 4° the amplification region divides into two crossflow regions. At $\alpha = 2^\circ$ both of these crossflow regions are associated with mean flow accelerations, the first in the leading-edge region and the second in the slight acceleration region from $x/c = 0.20$ back to $x/c = 0.71$ (see Figure 18). For $\alpha = 4^\circ$ the two crossflow regions are associated with pressure gradients of opposite sign (see Figure 19) with the mean boundary-layer crossflow going in opposite directions. The first region corresponds to the leading-edge negative pressure gradient (and inboard crossflow) while the other is associated with the relatively strong positive pressure gradient following the early pressure minimum at $x/c = 0.02$ (outboard crossflow). Thus, the crossflow instability pattern changes progressively as the angle of attack is increased from $\alpha = -4^\circ$ where fairly strong crossflow amplification continues following the initial crossflow surge to a complete reversal of the crossflow direction when $\alpha = 4^\circ$.

Figures 25–29 show N-factors obtained by applying Equation 1 for the five angles of attack. The $N(x/c)$ values are shown as functions of location on the wing for various wavelength to chord ratios which are indicated in the key.

N_{\max} values obtained by continuing the integration of Equation 3 over the entire crossflow region ($0 \leq x/c \leq 0.71$) are displayed in Figures 30–34 as functions of the wavelength for each angle of attack. Short-wavelength disturbances are shown to begin amplification in the thin boundary-layer near the leading edge, reach maximum amplification in the range $0.10 < x/c < 0.30$, then decay back to initial intensity levels. Mid- and long-wavelength vortices begin amplification further downstream from the leading edge and continue to grow back to beginning of the strong pressure recovery at $x/c = 0.71$. The maximum stationary crossflow amplification decreases progressively as the angle of attack is increased from $\alpha = -4^\circ$ to $\alpha = 2^\circ$. The N_{\max} curves peak at 15, 9.5, 4.4, 0.5 for $\alpha = -4, -2, 0,$ and 2° , respectively. For $\alpha = 4^\circ$ the leading-edge crossflow is negligible and the pressure recovery crossflow is fairly weak ($N_{\max} = 2.3$). These results indicate that significant stationary crossflow amplification should occur for $\alpha = -4$ and -2° , moderate crossflow at $\alpha = 0^\circ$, and only minimal amplification for $\alpha \geq 2^\circ$.

Previous correlations between computed stationary crossflow amplification factors and experimental transition locations in low-disturbance wind tunnels indicate that N_{\max} at transition is about 7 (Dagenhart, 1981). Thus, selecting either $\alpha = -4$ or -2° should insure sufficient crossflow amplification to cause transition on the wing at the highest Reynolds number, $R_c = 3.81 \times 10^6$. In fact, crossflow-generated transition should occur well ahead of the pressure minimum at $x/c = 0.71$ in the more extreme case ($\alpha = -4^\circ$) and move progressively back toward the pressure minimum as Reynolds number is decreased. This will be discussed in greater detail in a later section.

4.2.2 Tollmien-Schlichting Waves

Significant stationary crossflow-vortex amplification is predicted in the previous section for the selected configuration when $\alpha = -4^\circ$ or -2° . The experimental goal is to examine crossflow-vortex amplification and breakdown in the absence

of Tollmien-Schlichting waves. Figure 35 shows the maximum N-factors for TS amplification predicted by the SALLY code as functions of frequency for angles of attack of $\alpha = 0^\circ$, 2° , and 4° . The maximum-amplification-rate constraint (envelope method) is employed for these computations. In this method the wave orientation angle is allowed to float freely while the code searches for the maximum amplification rate. Examination of the computational results indicates that at least two peaks in the local amplification rate solutions are possible, one near $\psi = 0^\circ$ and the other near $\psi = 40^\circ$. The rough nature of the N-factor curves in Figure 35 is probably due to the code switching back and forth between these two possible solutions.

Figure 35 shows large TS amplification for $\alpha = 4^\circ$, much weaker disturbance growth for $\alpha = 2^\circ$, minimal amplification at $\alpha = 0^\circ$, and no amplification is found for negative angles of attack. The large TS amplification for $\alpha = 4^\circ$ is easily anticipated from the pressure distribution shown in Figure 19. The relatively strong positive pressure gradient in the region $0.02 < x/c < 0.18$ strongly excites TS waves. For $\alpha = 2^\circ$ much less TS amplification results from the weaker positive pressure gradient in the region $0.02 < x/c < 0.10$ (see Figure 18). For $\alpha = 0^\circ$ the flow accelerates (negative pressure gradient) all the way back to $x/c = 0.71$ and as a result Figure 35 shows minimal TS amplification. For $\alpha = -4$ and -2° Figures 15 and 16 show that fairly strong flow accelerations continue back to $x/c = 0.71$ preventing any TS amplification. Thus, $\alpha = -4$ and -2° produce the desired flow conditions — strong crossflow amplification with no Tollmien-Schlichting wave growth.

4.2.3 Travelling Crossflow Vortices

Travelling crossflow vortices are examined theoretically for $\alpha = -4^\circ$ at the maximum Reynolds number, $R_c = 3.81 \times 10^6$, using the SALLY stability code subject to the constraint of fixed vortex wavelength. Table 1 summarizes the predicted N_{\max} values for a range of frequencies and wavelengths where the

local amplification rates are integrated using Equation 3 over the entire crossflow region $0 \leq x/c \leq 0.71$. The local amplification rates, integrated N-factors, and total amplification values for these cases vary in a manner similar to the MARIA code results shown in Figures 20, 25, and 30. The frequencies investigated range from -50 Hz to 500 Hz and include stationary vortices ($f = 0$) as a subset. The negative frequency waves may be physically possible and simply correspond to waves that travel in the direction opposite to the direction of the wave-number vector. The orientation of the wave-number vector is shown in Appendix A.

Table 1 shows that the most amplified wavelength varies slightly with frequency but in all cases lies in the range $0.004 \leq \lambda/c \leq 0.006$. This slight adjustment of the maximum-amplification wavelength is probably due to local pressure gradient effects and is not considered to be particularly significant. The stationary vortex results are very similar to those obtained with the MARIA code. The wavelength having maximum total amplification for both codes is $\lambda/c = 0.004$, but the maximum N-factor from the SALLY code is lower — $N_{\max} = 13.1$ as compared to $N_{\max} = 15.0$ from MARIA. This is not surprising since the MARIA code does not actually solve the boundary-layer-stability eigenvalue problem, but only estimates the amplification rates from known solutions. On the other hand, the maximum predicted N-factor for all cases investigated is $N = 17.3$ for travelling crossflow waves with $f = 200$ Hz and $\lambda/c = 0.005$. Thus, the travelling crossflow vortices are predicted to be considerably more amplified (by the factor $e^{4.2} = e^{17.3}/e^{13.1} = 66.7$) than the stationary waves. Of course, the actual vortex strength depends not only on the amplification factor, but also, the external disturbance inputs. That is, the receptivity portion of the transition process is equally important in the vortex development, growth, and eventual breakdown. The moving vortices are driven by time-varying sound and vorticity fluctuations in the freestream whereas local surface roughness and discontinuities are most important for stationary

vortices. The balance between these two types of disturbance inputs is critical to developments in the transition process.

4.2.4 Crossflow/Tollmien-Schlichting Interaction

The oft-stated goal of the present experiment is to examine crossflow-vortex development and growth in the absence of Tollmien-Schlichting waves. However, the results of the previous sections indicate two test conditions where the interaction between crossflow vortices and TS waves may be fruitfully pursued. The most promising of these conditions is at $\alpha = 0^\circ$ where moderate crossflow amplification and weak TS waves are predicted. The other possible interaction condition exists at $\alpha = 4^\circ$ where very strong TS waves and weak pressure-recovery crossflow should coexist. These instability estimates are, of course, independent of any such interaction effects themselves since they are computed using linear stability methods.

Figure 32 shows that for $\alpha = 0^\circ$ the maximum amplified stationary crossflow is $N_{\max} = 4.6$ while Figure 35 shows that the TS amplification peaks at $N_{\max} = 3$. The presence of the moderate-strength crossflow vortices may sufficiently distort the mean flow velocity profiles so as to produce enhanced TS wave amplification and early breakdown to turbulence. If, however, these disturbance intensities are insufficient to generate mode interaction, then the disturbance intensities can be increased by one of two methods. The simplest way to increase the interaction is to increase the Reynolds number which will increase the strength of both fundamental instabilities. However, this is probably not possible in the UWT since the calculations presented are for $U_\infty = 35$ m/sec which is near the tunnel speed limit. The other alternative is to boost the disturbance intensities by the selective use of two-dimensional and three-dimensional roughness elements. This is similar to the use of vibrating ribbons to introduce disturbances into flat-plate TS instability experiments.

4.3 Selection of the Experimental Test Condition

In previous sections of Chapter 4, we have discussed the airfoil selection process, wind-tunnel wall interference effects, and boundary-layer stability analysis. The NLF(2)-0415 airfoil is selected as a strong crossflow generator with minimal TS wave amplification. The interference effects of installing a large wing model in the UWT are demonstrated to be nonnegligible, but these effects do not change the basic character of the pressure distributions, and, therefore, do not change the expected instability characteristics. The stationary crossflow instability is found to be strong for $\alpha = -4$ and -2° , but to get progressively weaker as the angle of attack is increased. For $\alpha = 2^\circ$ the crossflow instability essentially disappears and only a fairly weak pressure recovery crossflow region is found for $\alpha = 4^\circ$. The Tollmien-Schlichting instability is determined to be very strong at $\alpha = 4^\circ$ and to get progressively weaker as the angle of attack is reduced. This instability is predicted to be totally absent for angles of attack less than zero. Travelling crossflow vortices are examined for $\alpha = -4^\circ$ where it was shown that the travelling waves are more amplified than stationary vortices by a factor of 66.7. It is now appropriate to select the test point for the crossflow-dominated transition experiment.

The selected test point is at $\alpha = -4^\circ$. This condition has the strongest crossflow instability and no Tollmien-Schlichting wave amplification. This allows the isolated examination of crossflow-vortex development and growth. In addition, with the predicted crossflow being very strong at this angle of attack, the Reynolds number can be reduced from the maximum to achieve a range of test conditions where crossflow-induced transition is likely. The effect of Reynolds number variation on the crossflow instability is examined in the next section. And, the final section of Chapter 4 illustrates the wind-tunnel liner shape required to achieve quasi-infinite swept-wing flow.

4.4 Reynolds Number Variation

Figure 37 shows the effect of decreasing Reynolds number on the strength of the stationary crossflow instability as computed using the MARIA code. The peak of the maximum N-factor curve is seen to decrease from $N_{\max} = 15$ to $N_{\max} = 8.5$ as the Reynolds number is reduced from $R_c = 3.81 \times 10^6$ to 2.00×10^6 . The peak N-factor is reduced approximately in proportion to the Reynolds number reduction; however, this corresponds to a nearly 700 fold reduction in the total amplification. Thus, a very large range for the crossflow-vortex strength can be achieved simply by varying the test Reynolds number for the selected test condition of $\alpha = -4^\circ$.

4.5 Test-Section Liner Shape

The pressure distributions and boundary-layer stability predictions in the previous sections are computed with the assumption that the flow could be approximated as that on an infinite swept wing (i.e., no spanwise pressure gradients). The infinite swept wing produces a three-dimensional boundary layer due to the combined effects of wing sweep and chordwise pressure gradient, but the boundary-layer profiles and stability parameters are invariant along lines of constant chord. This ideal situation is not possible if a swept wing is installed in a wind tunnel with flat sides on all four walls. With a large-chord model installed in a flat-walled wind-tunnel, pressure-interference effects will produce a highly three-dimensional pressure pattern and, therefore, a highly three-dimensional boundary-layer instability and transition pattern. To obtain a flow field which is invariant along lines of constant chord one must employ contoured wind-tunnel liners. In the most idealized case, all four walls of the wind tunnel would be contoured to follow stream-surface shapes for an infinite swept wing in free air. For the present application of a large-chord model installed in the UWT, the less restrictive approach of contouring only the end liners is adopted. For this approach to be successful,

the interference due to the flat side walls adjacent to the upper and lower wing surfaces must be properly taken into account. In Section 4.1.2, these effects are considered by employing a modified version of the MCARF two-dimensional airfoil code (Stevens, Goradia, and Braden, 1971) which includes the effects of wind-tunnel side walls by modeling both the wing and tunnel walls by singularity distributions.

Figures 37–39 show various contour lines on the end liners designed for the NLF(2)-0415 airfoil when operated at an angle of attack of $\alpha = -4^\circ$ in the UWT. Figure 40 shows a schematic diagram of the model and liners installed in UWT. These lines are computed using a modified version of a code called TRACES which was written by Morgan to use output from the MCARF code. The TRACES code is modified to include a constant velocity component along the span of the 45° swept wing (i.e., the infinite swept-wing approximation). Twenty-five streamline tracks are computed for the end liners, but for clarity of presentation, only six are shown in Figure 37. The lines are projected in Figure 37 onto the x_L - z_L tunnel-liner coordinate plane. The model leading edge is located at $x_L/c = 1.0$ which is one chord length downstream of the liner origin. The trailing edge of the model is located at $x_L/c = 2.0$. The streamlines shown include lines near each flat side wall ($z_{L0}/c = 0.306$ and -0.417), lines just above and below the wing surface ($z_{L0}/c = 0.0$ and 0.028), and lines intermediate between the model and the tunnel walls ($z_{L0} = \pm 0.139$). Note that the streamlines near the walls are nearly flat as required by the presence of the flat tunnel wall. The other streamlines curve and bulge as they pass the model location. The approximate model shape is discernible from the separation of the streamlines around the model. The negative model angle of attack is indicated by the downward curve of the streamlines just ahead of the model leading edge.

Figure 38 shows the lateral deflections of the end liner required to follow the

curved streamlines over the swept wing. Again twenty-five streamline paths are computed, but only six are shown for clarity. The lines all begin with an initial deflection of zero at the liner origin and gradually curve as the model leading edge is approached. In the neighborhood of the model the streamlines curve more sharply as they pass through regions of strong pressure gradient. Note that the streamlines nearest to the wing surface ($z_{L0}/c = 0.0$ and 0.028) which both had zero lateral deflection at the liner origin are separated at the trailing edge by about $0.02 c$ (38 mm). This offset of the streamlines is due to the lift of the wing which causes the upper and lower surface streamlines to deflect different amounts as they pass over the model. The total thickness of liner material can be seen from Figure 38 to be just under $0.11 c$ (0.2 m). The liner contours on the two ends of the swept-wing model must, of course, be complementary so that a positive deflection on one wall corresponds to a negative deflection on the other wall. To accommodate these contours in the end liners the initial liner thickness is taken to be 0.127 m on each end. This leaves about 38 mm of spare material on one end of the model with slightly less than 25 mm minimum thickness on the other end.

Figure 39 shows another view of the liner surface shape. Here surface lines in the y_L-z_L plane are shown for various longitudinal positions along the liner. At the liner origin ($x_L/c = 0.0$) the contour is flat and the deflection is taken to be zero. At the model leading edge ($x_L/c = 1.0$) the liner is deflected to negative y_L values over the upper surface side of the model ($z_L > 0$) and a portion of the lower surface side. The liner lateral deflection is purely negative for the upper surface and purely positive for the lower surface side of the model at the midchord position ($x_L/c = 1.5$). Note that there is an abrupt jump in the liner contour from the upper to lower surfaces of the model at this location. The jump occurs through the model location itself. This jump or discontinuity continues into the wake region ($x_L > 2.0$) due to the lift on the model.

A schematic view of the model and end liners installed in the UWT is shown in Figure 40. The model is mounted with the wing chord plane vertical and the contoured liners located on the floor and ceiling of the test section. The contraction section of the tunnel is equipped with fairings which go from the existing contraction contours to an initial liner depth of 0.127 m at the entrance of the test section. The contraction fairings are each cut from a single large slab of styrofoam material. The end liners are manufactured by laminating 51 mm x 152 mm x 1.22 m (2 in x 6 in x 4 ft) pieces of styrofoam material into blocks to form the required liner thickness. The surface contour is then cut into each laminate block using a heated-wire apparatus. This process results in a faceted shape to the liners when all of the laminate blocks are assembled into the complete liner. Figure 4 is a photograph of the composite liner during installation in the new UWT test section. To complete the liner construction the styrofoam block surface is sanded lightly to remove the facets and the surface is covered with a thin layer of heat-shrink plastic film.

5 EXPERIMENTAL RESULTS AND DISCUSSION

The experimental results are presented, analyzed, and compared with predictions from the linear stability theory in Chapter 5. Appendix B outlines the hot-wire signal interpretation procedure. Measured wing pressure distributions are given. The stationary-crossflow vortex pattern and the transition line are visualized with sublimating-chemical and liquid-crystal surface coatings. Freestream and boundary-layer velocity spectra are shown. Velocity profiles and contour plots are given for the extensive hot-wire measurements taken across a single stationary-crossflow vortex track from $x/c = 0.20$ to 0.55 at $R_c = 2.37 \times 10^6$ and $\alpha = -4^\circ$. These data include the mean-velocity, stationary crossflow-disturbance velocity, and narrow band-pass travelling-wave velocity components in the stream-wise direction. Theoretical stationary-crossflow disturbance-velocity data supplied by Reed (Fuciarelli and Reed, 1992) are presented and transformed to various coordinate systems for comparison with the experimental results. Theoretical velocity-vector plots are shown overlaid on the experimental velocity-contours plots. Observed stationary-crossflow vortex wavelengths and growth rates are compared to theoretical predictions.

5.1 Freestream Flow Quality

The Unsteady Wind Tunnel is designed to operate as either an unsteady wind tunnel or as a conventional low-turbulence tunnel. The tunnel is equipped with an aluminum-honeycomb mesh and seven turbulence damping screens which limits the freestream turbulence level to less than $0.04\% U_\infty$ in the low-turbulence mode. For the present experiment the large-chord model and associated end liners add disturbances which increase the background turbulence level somewhat but it generally remains less than $0.09\% U_\infty$ which is still excellent flow quality

for the crossflow experiments. A typical freestream velocity spectrum measured with a hot wire for $R_c = 2.66 \times 10^6$ is shown in Figure 41. Most of the freestream disturbance energy is concentrated at low frequencies. Above 10 Hz the energy rolls off with increasing frequency out to about 100 Hz where the spectrum drops below the electronic noise.

5.2 Pressure Distributions

Figures 42 and 43 show the measured wing-pressure distributions on the upper surface. These data are measured for three different freestream velocities and the three sets of data are almost indistinguishable. The pressure taps are located in streamwise rows with one row near the top end of the model and the other row near the bottom end. The data presented here are the swept-wing pressure coefficients (C_{p3}) which differ from the airfoil pressure coefficients (C_p) given in Chapter 4 by the square of the cosine of the sweep angle as

$$C_{p3} = \frac{p - p_\infty}{\frac{1}{2}\rho U_\infty^2} = C_p \cos^2 \Lambda$$

where p is the local surface pressure, p_∞ , ρ , and U_∞ are the freestream pressure, density, and velocity, respectively. For the top end of the model the measured pressure distribution is in general agreement with the predicted curve, but the theoretical pressure distribution slightly underestimates the measurements over the whole model (Figure 42). The underestimate is largest in the region $0.05 < x/c < 0.40$. Examination of the top end liner contour indicates that the liner is slightly thinner near the model leading edge than designed which probably accounts for the under prediction of the pressure in this region. At the lower end of the model, the experimental pressure distribution is well predicted back to about $x/c = 0.25$, but the pressure minimum near $x/c = 0.7$ is under predicted (Figure 43). This may occur because the test section floor is inclined to offset normal tunnel-wall boundary layer growth on all four tunnel walls. Both the top and bottom rows of

pressure taps are located within 5 to 15 cm of the liner surfaces which probably exaggerates the influence of liner contour errors as compared to the impact felt in the majority of the flow field. Since the measured pressure distributions differ only slightly from the predicted distributions, it appears that in the central portion of the test region a reasonable approximation of infinite swept-wing flow has been established. The freestream and boundary-layer hot-wire measurements confirm this.

5.3 Flow Visualizations

A naphthalene/trichlorotrifluoroethane spray is used to place a white sublimating coating over the black model surface. The naphthalene sublimates faster in regions of high shear allowing the visualization of the stationary crossflow vortices and clearly indicating the transition location. Figures 44–48 show naphthalene visualization photographs for $\alpha = -4^\circ$ and chord Reynolds numbers ranging from $R_c = 1.93 \times 10^6$ to $R_c = 3.27 \times 10^6$. The flow is from left to right on the Figures with fractions of chord indicated by the markings at 10 percent chord intervals. In each figure the naphthalene coating is absent over approximately the first 15% of chord due to the high laminar shear stress in this region. From approximately $x/c = 0.15$ back to the jagged transition line the stationary crossflow-vortex pattern is clearly evident. The vortex spacing is determined by counting the number of light and dark streak pairs over a 10 cm length. The wavelength is observed to remain constant over the model at each test condition. This observation is in agreement with the findings of Saric and Yeates (1985). In contrast to the results obtained by Arnal and Juillen (1987) no vortex dropouts or other adjustments to the vortex spacing are observed. The laminar region is terminated in each case at a jagged transition line produced by overlapping turbulent wedges. Table 2 shows the average transition location and measured vortex spacing as a function of the chord Reynolds number. The transition location is estimated from the photographs as

the average of the beginning and ending locations of the turbulent wedges. Figure 49 shows a closeup photograph of a heavy coating of naphthalene for $R_c = 2.65 \times 10^6$ where the stationary crossflow-vortex traces can be seen to continue into the turbulent wedge regions.

In addition to naphthalene, liquid-crystal coatings are also employed to visualize the crossflow-vortex streaks and transition pattern. Figure 50 shows an example of a green liquid-crystal flow-visualization photograph. The black and white view shown does not adequately demonstrate the patterns which are visible in a color image. The stationary crossflow vortices are visible as alternating green and black streaks and the transition location is indicated by an abrupt shift to a deep blue. However, this technique proved less satisfactory than the naphthalene visualization. The crossflow streaks and the transition location are less obvious in the liquid-crystal photographs than in the naphthalene visualizations. Perhaps the relatively low shear stress in the present application limits the utility of the liquid-crystal technique. Similar results were obtained when these studies were repeated in a cooperative program with Reda using his technique (Reda, 1988).

The repeatability of the transition pattern is investigated by marking the jagged transition line on the model with a felt-tipped pen following a naphthalene flow-visualization run. The naphthalene visualizations are repeated at the same Reynolds number after several days, during successive tunnel entries, and even after the screens are removed, cleaned, and reinstalled with virtually identical transition patterns observed. The visualization is also repeated with liquid crystals and again, essentially identical transition patterns are observed. This indicates that the stationary vortex traces and the transition pattern are dominated by small-scale surface roughness effects which are not significantly influenced by the two different flow-visualization techniques or the facility condition. Indeed, Bippes and Müller (1990) find that when they move their flat-plate model laterally in the open-

jet test section the vortex-streak and transition patterns remain fixed and move with the plate.

5.4 Transition Locations

Boundary-layer transition locations are determined by several methods including interpretations of hot-film and hot-wire voltage signals and sublimating-chemical flow visualizations. The transition locations are determined from the flow-visualization photographs by the abrupt shift in sublimation rate of the naphthalene coating due to turbulence-induced shear stress increases. The sharp change from the streaked naphthalene pattern to black background thus marks the transition location. The rms voltage responses of the hot-film gages are plotted as functions of the Reynolds number. The point on the curve where the slope increases abruptly with increasing Reynolds number is taken as the transition point. For the boundary-layer hot-wire probes the onset of abrupt voltage spikes in the time-dependent voltage signal is taken as the transition indicator. Thus, all of these methods indicate the beginning of the transition process with the hot wires and hot-film gages providing local transition measurements and the flow visualization giving a global view of the transition pattern.

Figure 51 is a summary plot of transition measurements on the swept wing versus chord Reynolds number for $\alpha = -4^\circ$. A transition band is indicated for the naphthalene flow-visualization results. The beginning of the band indicates the origin of the most forward turbulent wedge and the end of the band is the location where the wedges merge. Points are shown for hot-wire transition measurements at $x/c = 0.4$ and for hot-film transition measurements at several locations. Thus, the naphthalene flow-visualization technique is calibrated. For chord Reynolds numbers greater than 2.3×10^6 the transition location is observed to be ahead of

the pressure minimum at $x/c = 0.7$. For these Reynolds numbers the transition process is presumed to be completely crossflow dominated.

5.5 Boundary-Layer Spectra

Figures 52–55 show the rms velocity spectra for a hot wire located within the boundary layer at $x/c = 0.4$, as the chord Reynolds number is increased from $R_c = 2.62$ to 3.28×10^6 . This Reynolds number range is selected since transition is expected to occur in the neighborhood of $x/c = 0.4$ as seen from Figure 51. In Figure 52, an amplified-response band is noted near the blade-passing frequency, f_{bp} . As the Reynolds number increases in Figures 53 and 54, the response band near f_{bp} broadens and a second, higher-frequency amplified band emerges. For this test condition, f_{bp} is approximately equal to the maximum amplified crossflow frequency, $f_{cf \max}$. These frequencies fall within the lower-frequency amplified band. The higher-frequency band corresponds to approximately $2 f_{cf \max}$. In addition, the blade plus stator passing frequency, f_{bps} , and $2 f_{bp}$, are in the higher-frequency band. Figure 55 shows the spectrum for $R_c = 3.28 \times 10^6$ which is in the turbulent flow region. Here the spectrum is flattened with similar energy levels at all frequencies out to 500 Hz. A comparison between the predicted crossflow frequency response and the measured spectrum is shown in Figure 56. The lower-frequency response band corresponds to a portion of the predicted moving crossflow-vortex amplification range near f_{bp} . The higher-frequency response band is located at the extreme upper end of the predicted amplified-frequency range where the predicted amplitude rapidly decreases with increasing frequency. Bippes and Müller (1990) observe travelling crossflow waves which tend to dominate the flows in relatively high-disturbance tunnel environments. They find that stationary crossflow vortices predominate in low-disturbance tunnels. Saric and Yeates (1985) do not observe travelling crossflow vortices. However, they do observe a stationary wavelength spectrum with a

broad peak near the theoretically-predicted maximum-amplified wavelength and an additional sharp peak at half the predicted wavelength. Reed (1988) is able to explain this development as a parametric resonance between the primary crossflow vortices which develop relatively far downstream and vortices of half this wavelength which are slightly amplified in the thin upstream boundary layer.

5.6 Boundary-Layer Hot-Wire Surveys

5.6.1 Streamwise-Velocity Measurements

Constant-temperature hot-wire anemometers are used to make detailed mean streamwise-velocity-profile measurements across a single stationary crossflow vortex for $\alpha = -4^\circ$ and $R_c = 2.37 \times 10^6$. The measurements are made at intervals of $\Delta(x/c) = 0.05$ from $x/c = 0.20$ to $x/c = 0.55$ using two hot-wire elements. A single hot-wire probe is located inside the boundary layer while a second single-wire probe is located in the freestream. Both wires are oriented parallel to the model surface and perpendicular to the freestream velocity vector. The ratio of the velocity indications from the two anemometers yields the streamwise boundary-layer velocity ratio. The hot-wire calibration and data reduction procedure is given in Appendix B. The experimental error analysis is given in Appendix C. Figure 20 shows that the stationary crossflow vortices become unstable at $x/c = 0.05$ while Figure 51 shows that the average transition line lies at approximately $x/c = 0.58$. Thus, the measurement locations cover a large portion of the unstable crossflow region from slightly downstream of the first neutral point to just ahead of the transition location.

A high-shear vortex track (i.e., dark streak) on the model is marked with a soft felt-tipped pen following a sublimating chemical flow-visualization study. The beginning point of the track is arbitrarily chosen to be the midspan location for $x/c = 0.20$. For most locations the measurements are made at seven spanwise

locations across the vortex along lines parallel to the leading edge of the 45° swept wing. These seven profiles represent six steps across the vortex with the first and seventh profiles expected to be essentially the same. The spanwise measurement locations are separated by intervals of $\Delta s = 1.6$ mm. The spanwise step size is dictated by the unit steps in the downstream and lateral directions and the desire to make an integral number of steps across the vortex. This can be demonstrated as follows. Figure 47 shows that the stationary-vortex tracks lie at an angle of approximately $\theta_v = 5^\circ$ with respect to the freestream direction. Then, lines parallel to the leading edge cut across the vortex tracks at an angle of approximately $\theta_M = \Lambda - \theta_v = 40^\circ$ where Λ is the wing sweep angle. Now, the wavelength measured parallel to the leading edge can be obtained as $\lambda_{45} = \lambda / \cos(\theta_M)$. Table 2 indicates that for $R_c = 2.37 \times 10^6$ the wavelength to chord ratio is approximately $\lambda/c = 0.004$ or $\lambda = 7.32$ mm. Thus, $\lambda_{45} = 9.5$ mm.

Both the mean and fluctuating velocity components are measured simultaneously by separating the anemometer output signals into DC and AC components. The AC component is quite small and can not be measured accurately in its raw state. It is measured by blocking the DC component of the signal, amplifying the remaining fluctuating signal, narrow bandpass filtering at $f = 100$ Hz, and amplifying again before the computer analog to digital (A/D) converter measures the signal. The amplifier gains are then divided out to obtain the final fluctuating signal values. The selected central frequency of $f = 100$ Hz is chosen since it is near the maximum amplified frequency for travelling crossflow vortices as indicated both by computations and experimental hot-wire spectra.

The motion of the hot-wire probe inside the boundary layer is controlled by the data-acquisition computer after the initial position is set by hand. This initial alignment is accomplished by locating the hot-wire probe above the intersection of the marked vortex track and the local fractional chord line. The starting

point for each boundary-layer survey station is set in this fashion. During the data-acquisition procedure, the experimenter has to actively observe the hot-wire AC signals on an oscilloscope, adjust the amplifier gain settings to assure maximum signal strength with overranging the instruments, and stop the traverse mechanism before the probe collides with the model surface. The data-acquisition computer measures the anemometer voltages and moves to the next point only after acceptance of the data by the experimenter.

The velocity data are presented in Figures 57–120 in two forms — as velocity profiles at several spanwise stations across the crossflow vortex and as velocity contours over the 45° spanwise measurement cuts. Figures 57–64 show the actual velocity ratio values obtained from the hot-wire data reduction procedure outlined in Appendix B. The height above the wing surface is determined by extrapolating the velocity data to a zero value at the surface for each profile. The presence of the stationary crossflow vortex is indicated in Figures 65–72 by subtracting the average value of the streamwise velocity from the local profile values. The resultant disturbance velocity profiles show the excess or deficit of velocity produced by the stationary vortex. An alternate representation of the stationary crossflow-vortex disturbance intensity is given in Figures 73–80 where reference computed velocity profiles are subtracted from the local velocity measurements. In both of these representations, the velocity difference is made nondimensional by dividing by the local boundary-layer edge velocity magnitude. Thus, the plots represent local disturbance intensity values, but, since the boundary-layer edge velocity increases slightly from $x/c = 0.20$ to 0.55 the velocity ratios are scaled down by a small amount as x/c increases. The root-mean-square velocity profiles for $f = 100$ Hz travelling waves are given in Figures 81–88. The velocity values are again nondimensionalized by the local boundary-layer edge velocity. Contour plots of the mean streamwise velocity across the vortex are shown in

Figures 89–96. Stationary vortex velocity contours are plotted in Figures 97–104 for $U_{s\text{ avg}}$ removed and in Figures 105–112 for $U_{s\text{ ref}}$ removed. Figures 113–120 show rms intensity contours for $f = 100$ Hz.

5.6.2 Spanwise Variation of Streamwise Velocity

Figure 57 shows that the mean-velocity profiles across the vortex are very similar in shape at $x/c = 0.20$, but there is already some variation in fullness of the profiles due the presence of the stationary crossflow vortex. As the stationary vortex grows in strength in the downstream direction so does the variation in the velocity profiles across the vortex. At $x/c = 0.35$ (Figure 60) some profiles have developed distinct inflectional shapes while other profiles remain rather full. Figure 64 shows that at $x/c = 0.55$, only a short distance ahead of the breakdown region, that all six velocity profiles have taken on a distorted inflectional shape and several profiles are severely distorted into S-shaped profiles. It may be expected that these highly distorted streamwise-velocity profiles will respond very differently to streamwise or secondary instabilities than would the undisturbed profiles. More discussion will appear on this later.

It was noted earlier that for each fractional chord location, the first velocity-profile measurement is centered on the dark (high-shear) vortex track marked with the felt-tipped pen. In examining Figures 57–64 it is evident that for the minimum measurement height the initial profile is very near the smallest velocity ratio and thus the highest surface shear at each station except at $x/c = 0.20$, 0.50, and 0.55. At these stations the maximum shear location appears to be approximately 2 or 3 mm away from the initial profile location. It was noted earlier that the flow-visualization patterns are highly repeatable given matching Reynolds numbers. However, lateral shifts of the whole vortex pattern by a small fraction of a wavelength are not unexpected. The deviation of the initial profile from the maximum shear location at $x/c = 0.20$, 0.50, and 0.55 could be due to a small shift

in the vortex pattern or to a small lateral misalignment (~ 2 to 3 mm) of the traverse rig at the beginning of the measurements. The influence of this misalignment at the beginning of the measurement region will be evident in results to follow.

5.6.3 Disturbance Profiles

Figures 65–72 show the stationary crossflow-disturbance velocity profiles determined by subtracting the average streamwise-velocity ratio at a given height from the measured velocity ratio at each location. The abscissa scale is chosen to keep the local velocity scales essentially the same for each chordwise station. As noted previously, the local boundary-layer edge velocity, which is used as a reference value, increases slightly from $x/c = 0.20$ to $x/c = 0.55$ so that the disturbance velocity ratios are scaled down slightly with this nondimensionalization as x/c is increased. For the crossflow instability, the disturbance vortex axes are nearly streamwise and the primary disturbance-vortex components in a streamwise coordinate system are the v - and w -velocity components. The perturbation in the streamwise direction (u -component) is a secondary effect due to the convection arising from the v - and w -velocity components. However, the streamwise component (U -component) of the boundary-layer velocity has a large gradient in the direction perpendicular to the wing surface (dU/dy) which when combined with small convective v - and w -velocity components produces a large secondary streamwise-velocity perturbation. This streamwise-velocity perturbation is the one shown in Figures 65–72 and later in Figures 73–80. It is to be expected that over a single vortex wavelength, these perturbation velocity profiles will exhibit either excesses or deficits from the mean, depending on the lateral location in the streamwise vortex. Over that portion of the vortex where the v - and w -velocity components convect the high-momentum flow from the outer portion of the boundary layer toward the surface the local profile should have an excess (or bulging) shape. On the other hand, when the vortex-velocity components convect

low-momentum flow away from the surface the local profile is expected to have a deficit shape.

Note that in Figures 65 and 67 only five velocity profiles are measured. Nonetheless, it is apparent in Figure 65 that some of the local disturbance profiles show excess velocities while others show deficit velocities as expected. However, the profiles in Figure 65 have two unexpected features. First, the disturbance profiles do not approach zero for large values of the height, y , above the wing surface. This is due to temperature drift effects in the Unsteady Wind Tunnel. The UWT has no temperature control; the test temperature is governed by the ambient temperature in the wind-tunnel building (which is cooled by an electrical air-conditioning unit) and, more importantly, by the power input to the wind-tunnel fan. To eliminate this effect for the other measurement stations the tunnel was run in a preheat mode for 30 to 45 minutes before acquiring boundary-layer disturbance data. This preheat time is used each day to verify instrumentation connections, filter settings, and so forth. The second anomalous aspect of the profiles in Figure 65 is the bulge in excess and deficit velocities below about $y = 0.5$ mm. These bulges are unexpected and are almost as large as the maximum disturbance intensities found for $y \approx 1.2$ mm. The presence of these velocity perturbations is traced to residue left behind by cleaning the model with alcohol and supposedly lint-free cloths. This contamination had not been noted earlier during the preliminary velocity-profile measurements probably because single velocity-profile measurements were generally made following a flow-visualization study in which the model surface was effectively cleaned by the trichlorotrifluoroethane solvent used with the naphthalene. The model cleaning procedure was modified to a two-step procedure — cleaning first with alcohol and then with distilled water. A single velocity-profile measurement at $x/c = 0.20$ confirmed that the residue problem was solved, but the complete set of velocity

profiles at $x/c = 0.20$ were not measured again due to lack of sufficient time. The data at all subsequent measurement stations are taken following the two-step model cleaning process and no further contamination problems are encountered.

Examination of Figures 65–72 shows that the maximum disturbance intensity of the stationary crossflow vortex grows progressively from $x/c = 0.20$ back to $x/c = 0.55$. At $x/c = 0.20$ the profiles show either excess or deficit velocities only. But by $x/c = 0.35$ some of the disturbance profiles have taken on definite crossover shapes. These crossover profiles have both excess and deficit velocity regions. At the last measurement station ($x/c = 0.55$) the maximum disturbance intensity exceeds 20% of the edge velocity and all of the profiles have taken on highly distorted shapes. The nature and significance of these crossover profiles will be discussed further in the following section where the disturbance velocities are displayed as contour plots.

Figures 73–80 show stationary crossflow-disturbance profiles obtained by a different procedure. Here local theoretical velocities are subtracted from the measured profiles to yield the local disturbance vortex intensities. Note that the angle of attack for the reference case is taken as $\alpha = -5^\circ$ rather than the actual angle of attack $\alpha = -4^\circ$. This adjustment in the theoretical angle of attack is required because the theoretical profiles for $\alpha = -4^\circ$ are obviously fuller than the experimentally measured profiles. The reason for this discrepancy is uncertain, but it may arise from a slight flow angularity in the UWT test section or a minor misalignment of the model mounting bearing.

The stationary crossflow profiles in Figures 73–80 agree in general trends with those shown in Figures 65–72. In both cases, the maximum disturbance intensity grows progressively with increasing x/c , definite crossover profiles develop by $x/c = 0.35$, and at $x/c = 0.55$ all profiles are highly distorted. However, there are some slight differences between removing the average velocity profile and

the theoretical velocity profile from the measured data. These differences arise because the averaged profiles from the experiment include flow history effects produced by the presence of the stationary crossflow vortices within the boundary layer while the theoretical profiles completely neglect this effect. The most notable of the differences in the two sets of profiles is observed by comparing Figures 65 and 73 for $x/c = 0.20$. In Figure 73, the influence of the surface contamination discussed earlier produces velocity deficits in all profiles for $y < 0.5$ mm. In Figure 65, this deficit effect is included in the averaged profile and as a result the disturbance profiles are not biased toward a deficit condition. Of course, this deficit effect is an experimental error which would have been removed completely by retaking the data at $x/c = 0.20$ if time had allowed. Other notable, and experimentally more significant, differences are observed for $x/c > 0.45$ where flow history effects become more pronounced. This effect will be shown more clearly in the disturbance-velocity contour plots which are shown later.

Root-mean-square velocity profiles for travelling waves are shown in Figures 81–88. As mentioned previously, these data are measured simultaneously with the mean velocity by splitting the hot-wire anemometer signal into mean and fluctuating components. The fluctuating component is amplified, narrow bandpass filtered, and amplified again before recording with the UWT A/D converter system. The selected central frequency for the narrow bandpass filter is $f = 100$ Hz which is near the frequency of maximum amplification according to both experimental and theoretical considerations. Again, these data are plotted with an abscissa scale which is essentially unchanged over the range of measurement locations. This allows for easy visual examination of the disturbance amplification with increasing x/c . For travelling crossflow waves rms averaged profiles of the streamwise velocity are expected to yield profiles with a single maximum and, of course, only positive values. Furthermore, in the absence of nonlinear distortions due to

the stationary crossflow vortices or the presence of some other travelling waves in the same frequency range the rms velocity profiles are expected to be identical at each spanwise location.

For the first two measurement stations ($x/c = 0.20$ and 0.25 , Figures 81 and 82) the disturbance intensities are quite small and the velocity profiles have essentially the same shape at all spanwise locations across the stationary crossflow vortex. Here the rms streamwise-velocity profiles have a single lobe (or maximum) as expected for travelling crossflow vortices. By $x/c = 0.30$ the shapes of the travelling-wave velocity profiles have begun to distort, but the profiles continue to have single-lobed shapes. This distortion of the profile shape may arise from the development of other travelling-wave disturbance modes of the same frequency, but different direction of travel, or the nonlinear distortion of travelling-crossflow waves by the strong stationary crossflow-vortex layer. For $x/c > 0.40$ (Figures 85–88) definite double-lobed travelling-wave disturbance velocity profiles are apparent at some spanwise locations across the stationary crossflow vortex. Between $x/c = 0.40$ and 0.50 the travelling waves grow considerably in strength. However, from $x/c = 0.50$ to 0.55 the largest amplitudes decrease by greater than a factor of two. Note that even at their maximum intensity, the travelling waves are quite small as compared to the strength of the stationary crossflow vortex (i.e., only 3.5% as large). Thus, it appears that the travelling waves which initially have very low amplitude, grow and distort considerably for $0.40 < x/c < 0.50$, and then decay for $x/c > 0.50$. The nature of the distortion of the travelling waves due to the stationary crossflow vortices will be more apparent when viewed as contour plots in the following section.

5.6.4 Streamwise-Velocity Contour Plots

Contour plots of the mean velocity, stationary crossflow-disturbance intensities, and the travelling-wave disturbances are given in Figures 89–120. These

plots show the various experimentally-determined quantities plotted on a grid which is 4 mm deep in the y (or surface normal) coordinate and stretches 9.5 mm along a 45° swept line parallel to the wing leading edge. As mentioned previously, the spanwise coordinate cuts across the stationary crossflow-vortex tracks at an approximately 40° angle and the stationary-vortex wavelength along a line parallel to the leading edge is $\lambda_{45} = 9.5$ mm. The abscissa is taken as $z_\lambda = -(z_m - z_{m0})/\lambda_{45}$ and is a local coordinate with $z_\lambda = 0$ on the marked stationary-vortex track and $z_\lambda > 0$ the direction of spanwise motion of the hot-wire probe. With this coordinate selection, the abscissa actually runs in the direction opposite to the model spanwise coordinate, z_m . The plots show the situation an observer would see when looking upstream from the hot-wire probe location. These data are plotted for $0.20 \leq x/c \leq 0.55$ in increments of $\Delta(x/c) = 0.05$. For $x/c = 0.20$ and 0.30 , the data are not measured across the full crossflow-vortex wavelength. But, for the other stations, these data are shown for a full stationary crossflow-vortex wavelength. For each boundary-layer station all velocities are made nondimensional by dividing by the local streamwise boundary-layer edge velocity. Since the edge velocity increases by about 10% from $x/c = 0.20$ to 0.55 the actual velocities are scaled down by this factor.

Figures 89–96 show the mean streamwise boundary-layer velocity ratio, $\frac{U}{U_{*c}}$, in the tunnel coordinate frame. In the absence of stationary crossflow-disturbance vortices, the velocity contours are expected to be flat and parallel to the wing surface. Figure 89 shows that the mean-velocity contours at $x/c = 0.20$ are, indeed, nearly flat and parallel to the wing surface. But, some influence of the stationary crossflow vortex is already present at this forward location with the contour levels somewhat wavy and inclined slightly toward the surface for increasing values of z_λ . The waviness of the contours increases with x/c until the contours obviously bulge upward at approximately the middle of the wavelength

for $x/c = 0.35$ (Figure 92). This upward bulge of the contours corresponds to low-momentum fluid being swept upward from the wing surface by the stationary crossflow vortex. The bulge continues to grow as x/c increases until the contours actually begin to roll over like a breaking wave for $x/c \geq 0.50$ (Figures 95 and 96).

This mean-velocity contour pattern is consistent with expectations for boundary-layer flow with imbedded stationary crossflow vortices which will be illustrated more fully in the next section. The flow-visualization photographs (Figures 44–48) show that the crossflow-vortex axes are aligned almost parallel to the freestream velocity vector. The instability produces a layer of counter-rotating disturbance vortices which combine with the mean boundary-layer crossflow to yield a layer of crossflow vortices all with the same rotational direction (co-rotating pattern). The flow field is illustrated more fully later in Section 5.7.1. This pattern develops because the flow is most unstable to the crossflow instability at some small angle to the pure crossflow direction (Dagenhart, 1981). The mean-velocity profile in the most unstable crossflow direction has a crossover shape with flow streaming in the crossflow direction near the wing surface, but in the opposite direction further out from the surface (Gregory, Stuart, and Walker, 1955). When this crossover velocity profile is combined with the counter-rotating disturbance vortices, it reinforces the strength of one of the pair of vortices while cancelling the other. This produces the observed velocity field with flow streaming in the crossflow direction near the wing (z_λ -direction) while the flow in the outer part of the boundary layer flows in the opposite direction. Hence, the breaking-wave pattern seen in Figures 95 and 96.

As previously noted, the initial velocity profile at each measurement station is intended to be on the line of maximum shear as determined by the flow-visualization study. But, since the measurements are made over many days of wind-tunnel testing, it is not unexpected that small shifts (~ 2 to 3 mm) in

the location of the stationary vortex pattern might occur. Such shifts in the vortex pattern can be deduced from the mean streamwise velocity-contour plots (Figures 89–96). The maximum surface shear stress location is determined qualitatively by observing the crowding of streamwise-velocity contours near the wing surface. Figures 95 and 96 show that the maximum shear stress point appears to have shifted by 1.5 to 3 mm in the z_λ -direction. This shift will be even more obvious in the stationary-vortex velocity field which follows.

Stationary crossflow-vortex velocity contours are plotted in Figures 97–104 and 85–92. The first set of contours corresponds to disturbance velocities determined by subtracting the theoretical mean-velocity values from the measured velocities. The second set of disturbance velocity contours are computed by removing the averaged mean-velocity profile from the local measured velocities. In each case the disturbance velocity values are nondimensionalized by the local boundary-layer edge velocity which increases slightly from $x/c = 0.20$ to 0.55 . The range of contour levels up to $\pm 0.20 U_{s_e}$ are used for all measurement locations for easy data comparisons. The two sets of contours agree in general shape and levels of the velocity contours. Some relatively small differences can be noted for $x/c = 0.50$ and 0.55 where the averaged mean-velocity profile is distorted by the presence of the stationary crossflow vortex, but the theoretical profiles ignore this effect. Thus, the following discussion of the evolution of the stationary crossflow-disturbance velocity contours applies equally well to either set of Figures.

The expected stationary crossflow-disturbance velocity pattern has excess velocities at the extremes of the plotting field ($z_\lambda = 0$ and 1) and deficit velocities near the middle of the field ($z_\lambda = 0.5$). This is because the initial velocity profile ($z_\lambda = 0$) is measured at the supposed maximum shear point which should correspond to high-momentum fluid being swept toward the wing surface. This situation should, of course, recur one full wavelength away ($z_\lambda = 1$). Velocity deficits

should occur where the stationary crossflow vortex sweeps flow away from the surface ($z_\lambda = 0.5$). Figures 97 and 105 show that at $x/c = 0.20$ the presence of the stationary crossflow vortices is already detectable with velocity variations exceeding $\pm 0.02 U_{s\theta}$. The expected velocity pattern is not evident for $x/c = 0.20$ or 0.25 (Figures 97–98 and 105–106), but it emerges for $x/c = 0.30$ (Figures 99 and 107). The periodicity of the velocity perturbations is clearly evident for $0.35 \leq x/c \leq 0.55$ (Figures 100–104 and 108–112). For $x/c = 0.35, 0.40,$ and 0.45 the excess velocities occur at the ends of the measurement zone and the deficits in the middle as expected. For $x/c = 0.50$ and 0.55 the peak excess velocities are shifted in the $+z_\lambda$ -direction by approximately 2 mm. This seems to correspond to and is consistent with the observed shift in the maximum shear stress location as discussed previously.

The stationary crossflow-disturbance velocities are quite small at the beginning of the measurement region ($x/c = 0.20$). The disturbances grow progressively larger with increasing x/c back to $x/c = 0.50$ until they exceed $\pm 0.20 U_{s\theta}$. From $x/c = 0.50$ to 0.55 the deficit velocities continue to increase in intensity, but the velocity excesses drop sharply. This decrease in excess velocity intensity seems surprising since the linear stability analysis presented earlier (see Figure 20) shows that the stationary crossflow-disturbance vortices should be amplified all the way back to the pressure minimum at $x/c = 0.71$. For the present case ($R_c = 2.37 \times 10^6$) the average transition line is determined by the flow-visualization studies to be at approximately $x/c = 0.58$ (see Figure 51 and Table 2). It may be that between $x/c = 0.50$ and 0.55 energy is being extracted from the stationary crossflow vortices and pumped into some other disturbance mode such as the secondary instability mode.

Figures 113–120 show contour plots of the temporal rms velocities of travelling waves with $f = 100$ Hz for $x/c = 0.20$ to 0.55 . These velocities are again made

nondimensional by dividing by the local boundary-layer edge velocity. It was indicated earlier that $f = 100$ Hz corresponds to a peak in both the measured and theoretical boundary-layer velocity spectra. The rms values measured are quite small with the maximum values being approximately $0.7\% U_{s_e}$. The same contour levels are used for all the plots so that the disturbance levels can be readily compared. In the absence of complicating factors such as nonlinear interaction with stationary crossflow vortices or the presence of other travelling waves in the same frequency range, the rms velocity contours are expected to be flat and parallel to the wing surface.

The travelling-wave intensities are essentially zero for $0.20 \leq x/c \leq 0.30$ (Figures 113–115). For $x/c = 0.35$ and 0.40 the peak disturbance amplitudes range from about 0.07% to $0.1\% U_{s_e}$ (Figures 116 and 117) and the contour lines are very roughly parallel to the wing surface, as anticipated for undistorted travelling-crossflow waves. The disturbance velocity profiles shown earlier in Figures 83 and 84 for these locations also have the expected single-lobed shapes. By $x/c = 0.40$ (Figure 118) definite closed-contour shapes have developed. This corresponds to the development of double-lobed disturbance profiles (Figure 86). Between $x/c = 0.45$ and 0.50 the travelling wave disturbance strength grows dramatically with the maximum rms intensity reaching $0.7\% U_{s_e}$. The disturbance intensity also departs strongly from the ideal of equal distribution along the span to peak sharply near the center of the vortex wavelength. Perhaps significantly, Figure 63 shows that near the middle of the measurement zone that the streamwise-velocity profile takes on a distinctly distorted S-shape. From $x/c = 0.50$ to 0.55 the strength of the travelling waves drops precipitously (Figure 120) and the maximum contour levels shift location. The sharp drop in travelling-wave intensity occurs even though the streamwise mean-velocity profiles continue to develop ever more distorted S-shaped profiles (Figure 64). This is in the same region where the stationary

crossflow vortices are observed to decrease in strength although the decrease is not so pronounced in the stationary vortex case. As mentioned previously, in the region from $x/c = 0.50$ to 0.55 energy may be transferred to other high-frequency modes which lead to laminar flow breakdown in the neighborhood of $x/c = 0.58$. The nonuniform nature of the rms disturbances along the span seems to indicate that the travelling waves detected may not be travelling crossflow vortices, but some other travelling waves in the same frequency range (possibly Tollmien-Schlichting waves generated at the locations of the S-shaped mean-velocity profiles).

5.7 Experimental/Theoretical Comparisons

In the previous sections, experimental velocity profiles and contours are shown along a single vortex track on the 45° swept wing for $\alpha = -4^\circ$ at $R_c = 2.37 \times 10^6$. Both mean and disturbance velocities extracted from the mean data are given. In this section, those experimental data and other results obtained from them are compared to linear stability theory predictions supplied by Reed using her theoretical code (Fuciarelli and Reed, 1992). This theoretical code is used because it gives both growth rates and disturbance eigenfunction profiles whereas the MARIA (Dagenhart, 1981) and SALLY (Srokowski and Orszag, 1977) codes employed earlier give only growth rates. The mean-velocity profiles supplied to Reed and shown below were computed using the method of Kaups and Cebeci (1977). As mentioned previously, theoretical data for $\alpha = -5^\circ$ are used for this comparison because these data seem to yield a better match to the experimental data which are measured at a nominal angle of attack of $\alpha = -4^\circ$. A small flow angularity in the UWT test section or a slight misalignment of the model could account for this difference.

5.7.1 Theoretical Disturbance Profiles

Figures 121 and 122 show the mean-velocity profiles at the experimental measurement stations computed using the method of Kaups and Cebeci (1977). The velocity components are given in a model-oriented coordinate system (x_m, y_m, z_m) with x_m perpendicular to the wing leading edge, y_m normal to the wing-chord plane, and z_m parallel to the wing leading edge (See Appendix A). Note that the spanwise velocities, W_m/U_{t_e} are taken to be negative. This occurs because Reed chooses to use a left-handed coordinate system so that the crossflow wave numbers are both positive. The experimental data presented in the previous sections are shown from the perspective of the hot-wire measurement probe looking upstream. This constitutes essentially a conversion of the experimental coordinate frame into a left-handed system. Thus, the experimental and theoretical data can be compared directly. Stationary crossflow-instability eigenfunctions are shown in Figures 123–125 for each of the coordinate directions. The computations are for a fixed wavelength of $\lambda = 7$ mm which essentially matches the experimentally observed wavelength of $\lambda/c = 0.004$ or $\lambda = 7.3$ mm. The profiles are scaled to match the experimentally-determined maximum streamwise-disturbance amplitudes at each measurement station. This is permissible, of course, since linear stability theory predicts the actual disturbance intensity only to within a multiplicative constant. The phase relationships between the velocity components are not shown in the figures, although they are critically important to the determination of the spatial velocity field of the instability waves. Note also that in the model-oriented coordinate frame, the disturbance velocities in the chordwise direction, u_m , and the spanwise direction, w_m , are of the same order while the normal-velocity component, v_m , is an order of magnitude smaller.

For comparison with the experimental data the velocity profiles given in Figures 121–125 must be rotated about the y -axis to two other coordinate reference

frames. One of these frames, the streamwise frame, (x_s, y_s, z_s) , is oriented with x_s parallel to the freestream-velocity vector and y_s perpendicular to the wing-chord plane while in the other frame, the wave-oriented frame, (x_w, y_w, z_w) , x_w is along the vortex axis and z_w is parallel to the wavenumber vector. Of course, y_m , y_s , and y_w are all parallel. The experimental measurements are made in the streamwise coordinate frame, (u_s, y_s, z_s) . The theoretical vortex flow pattern in the wave-oriented frame, (x_w, y_w, z_w) , will be superposed onto the experimental data plots. The relationships between these coordinate frames are given in Appendix A.

The mean flow velocity components in the (x_s, y_s, z_s) frame are shown in Figures 126 and 127. In this coordinate frame (See Appendix A), the cross-stream mean velocities, W_s , are considerably smaller than the streamwise velocities, U_s . Likewise the cross-stream disturbance velocities, w_s , are much smaller than the streamwise-disturbance velocities, u_s (See Figures 128 and 129). Figures 130–133 show the mean- and disturbance-velocity components in the wave-oriented coordinate frame. Here both the mean and disturbance velocity components in the z_w direction are an order of magnitude smaller than the respective velocities components along the vortex axis. In this frame, w_w is the same order of magnitude as $v_w = v_m$. Thus, in both the wave-oriented and streamwise-oriented coordinate frames the velocities along the x-axes are much larger than the velocity components in the other two directions.

The nature of the disturbance-vortex flow is illustrated in Figures 134–136. A vector plot of (v_w, w_w) , across a single vortex wavelength is shown in Figure 134 in the wave-oriented coordinate frame. The vectors are the projections of the disturbance-velocity vectors onto the y_w – z_w plane. The disturbance is seen to consist of a pair of counter-rotating vortices within a single wavelength. The vortex cells are skewed so that a central counterclockwise-rotating vortex is bordered on each side by a portion of the alternate clockwise-rotating vortices. In Figure

135 the mean plus disturbance velocity vectors, $(v_w, w_w + W_w)$ are plotted over a single wavelength. Here the mean normal velocity, V_w , which is quite small has been neglected. Note that the mean velocity, W_w (See Figure 131) completely dominates the vector field masking the presence of any disturbance vorticity. The presence of the disturbance vorticity can be illustrated by arbitrarily scaling the v_w velocities by a factor of 100. This is shown in Figure 136 where it is apparent that the mean plus disturbance flows combine to produce a single counterclockwise-rotating vortex per wavelength. That is, the total flow consisting of disturbances superposed on a base flow contains a layer of co-rotating vortices.

5.7.2 Disturbance Profile Comparisons

Experimental stationary crossflow-disturbance profiles (from $U_s - U_{s \text{ avg}}$) are compared with the linear-theory eigenfunction magnitudes in Figures 137–144. In each case the streamwise-disturbance velocity profiles are shown. Similar results are found using the experimental profiles determined from $U_s - U_{s \text{ ref}}$ (Figures 73–80) but these are not shown. The experimental profiles are determined by taking the spatial rms of the individual profiles (Figures 65–72) across the stationary vortex. This procedure is the spatial analog for a stationary wave of taking the temporal rms of a travelling wave. All of the profiles are plotted on the same abscissa scale (made nondimensional by reference to the local boundary-layer edge velocity) for easy visual comparison of the disturbance growth with distance along the wing. The theoretical eigenfunctions which have only a single lobe (See Figure 128) are scaled to match the peak experimental amplitude at each measurement location.

At $x/c = 0.20$ (Figure 137) the theoretical and experimental profiles are of similar shape in the region of the maximum amplitude near $y = 1$ mm, but the two curves diverge in the near-surface region and in the outer flow. As mentioned previously the measured profiles at this location are thought to contain

experimental errors which are rectified for the remaining measurements. The near-surface results are affected by a lint-contaminated surface and the outer flow measurements are affected by tunnel-temperature drift. For $x/c = 0.25, 0.30, 0.35,$ and 0.40 (Figures 138–141) the experimental and theoretical profiles are of similar single-lobed shapes. However, the point of maximum disturbance intensity is slightly higher in the boundary layer for the theoretical eigenfunctions than for the experimental profiles.

For $x/c = 0.45$ and beyond (Figures 142–144) the experimental profiles take on double-lobed shapes which contrast with the single-lobed theoretical eigenfunctions. The point of maximum disturbance strength for the theoretical profiles lies between the two maxima of the experimental profiles. Recall from the earlier discussion that for $x/c = 0.45$ and beyond, the local experimental disturbance profiles take on crossover shapes which are not anticipated from the linear theory. This is evident in the local profile plots of Figures 70–72 and 78–80 as well as the disturbance velocity-contour plots of Figures 102–104 and 110–112. Figures 94–96 show that the mean streamwise-velocity contours for $0.60 < U_s/U_{s_e} < 0.90$ rise sharply from the model surface and begin to roll over. That this is due to the presence of the stationary crossflow vortex will become evident in the next section.

Thus, there is general agreement between the shapes of the experimental disturbance velocity profiles and the theoretical eigenfunctions up to about $x/c = 0.40$ where the rms intensity of the stationary vortices is about 7% of U_s . But for $x/c = 0.45$ onward, the presence of the stationary crossflow vortices distorts the experimental disturbance profiles into double-lobed shapes not predicted by the linear theory. This does not necessarily mean that nonlinear effects are present, even though the stationary disturbance intensities ($\pm 20\% U_s$ at $x/c = 0.50$) are well beyond the small perturbation limits assumed in the linear theory. In fact, the observed effects may simply be due to flow history. That is, the strong stationary

crossflow vortices continually lift low-speed fluid up from the surface and push high-speed fluid downward so that the flow wraps around the vortex axis. More will be shown on this point in the next section.

5.7.3 Comparison of Experimental Streamwise Velocity-Contour Plots and Theoretical Vector Plots

Figures 145–152 show theoretical velocity vectors superposed on the experimental streamwise velocity-contour plots. Theoretical velocity vectors are superposed on the stationary crossflow-disturbance velocity-contour plots in Figures 153–160. The velocity vectors in these figures have v_w scaled up by a factor of 100 (as in Figure 136) so as to illustrate the presence of the stationary crossflow vortex.

Recall that the experimental procedure outlined in Section 5.6.1 called for the experimental profile measurements to be made at various spanwise locations across a single stationary crossflow vortex. To accomplish this a single dark vortex track is traced on the model with a felt-tipped pen following a flow-visualization run. For each fractional chord location the hot-wire probe is manually centered above this trace. After the initial manual setup, the traverse motion is computer controlled in both normal and spanwise steps. The dark vortex track in the flow-visualization study corresponds to high-shear path under the stationary crossflow-vortex pattern. Thus, this procedure should assure that the measurement locations move in steps from a high-shear region through minimum shear and back to high shear again. However, the experimental situation is not quite this simple. The entire flow-visualization pattern is found to be highly repeatable even months apart. The pattern repeats in detail down to the jagged transition line and the individual vortex tracks. But, the vortex wavelength is only $\lambda = 7.3$ mm so that small errors in the manual alignment of the traverse system or even very small shifts in the location of the vortex track can impact the relative location of the maximum shear. Exami-

nation of the streamwise-velocity plots in Figures 89–96 shows that the maximum shear point (judged here by how closely the velocity contours are bunched) is not always located at $z_\lambda = 0$. To account for this effect the maximum shear point in both the experimental and theoretical flow patterns is determined. The phase of the theoretical flow pattern is then shifted to align the maximum–shear points in the theoretical and experimental flows.

Examination of Figures 145–152 shows that the variations of the mean streamwise-velocity contours over the vortex wavelength can be anticipated from the vector plots. The streamwise-velocity contours spread out when the velocity vectors are directed away from the surface and they crowd together whenever the velocity vectors point toward the surface. In particular, near the surface, the streamwise-velocity contours approach each other to produce the high surface shear (i.e., large dU/dy) when the velocity vectors are directed downward. Low surface shear (i.e., small dU/dy) results when the velocity vectors are directed upward and the contour lines spread out.

Figures 153–160 show that the qualitative features of the streamwise-disturbance velocity-contour plots can also be anticipated from the velocity-vector field. A plume of low-speed fluid is observed in regions where the velocity vectors are directed sharply outward from the model surface. Concentrations of high-speed fluid near the model surface are found in regions where the velocity vectors are directed sharply toward the surface. Furthermore, both the low- and high-speed regions are skewed in a counterclockwise pattern consistent with the theoretical velocity-vector pattern. It should be noted here that flow history effects are not expected to produce qualitative differences between the contour and vector plots as found in the disturbance profile and eigenfunction comparisons performed above.

Thus, when the maximum shear points of the experimental and theoretic-

cal data are matched the qualitative features of the flow variables are consistent with expectations gleaned from the velocity-vector field. In particular, both the streamwise-velocity contours and the stationary crossflow-disturbance velocity contours distort in patterns consistent with the presence of a single counterclockwise-rotating vortex. This pattern of qualitative agreement between the theoretical and experimental flow fields persists throughout the measurement region from $x/c = 0.20$ to $x/c = 0.55$ in contrast to the disturbance profile and eigenfunction comparisons which diverge for $x/c > 0.45$.

5.7.4 Wavelength Comparison

Tables 3–5 show the results of crossflow-stability calculations performed using the SALLY code (Srokowski and Orzag, 1977) subject to the constraint of constant vortex wavelength. As mentioned previously, the naphthalene flow-visualization photographs show constant crossflow-vortex wavelengths over the entire region for a given Reynolds number. The calculations are begun at the neutral point and continued back to the average transition location as indicated in Table 2. Tables 3–5 correspond to chord Reynolds numbers of 2.37×10^6 , 2.73×10^6 and 3.73×10^6 , respectively. For all three test conditions the most amplified frequency is nonzero. The maximum amplified frequency increases with Reynolds number from $f_{cf \max} = 100$ Hz at $R_c = 2.37 \times 10^6$ to $f_{cf \max} = 300$ Hz at the maximum chord Reynolds number. The maximum N-factor at transition is found to be about 9.1 at the lower Reynolds number and about 8.5 for the higher Reynolds numbers. These results agree with earlier calibrations of the crossflow stability problem as indicated by Dagenhart (1981). It should be noted that surface and streamline curvature effects have not been considered in this analysis, but this may not be significant since both the surface and streamline curvatures are small over most of the unstable flow region. The wavelength of maximum stationary crossflow-vortex amplification is plotted in Figure 161 where it is compared to

the experimental observations given in Table 2. The experimental and theoretical curves have similar trends with wavelength decreasing as chord Reynolds number increases, but the theoretically-predicted wavelengths are approximately 25% larger than those observed experimentally. This discrepancy may arise because the crossflow-vortex pattern (having a constant wavelength over the entire wing) is established well forward on the wing where the boundary layer is relatively thin. Swept flat-plate experiments generally have shown closer agreement between the theoretically most-amplified wavelength and the observed wavelength than have swept-wing studies. Perhaps the blunter nose of the swept wing is an important factor in establishing the smaller wavelength.

5.7.5 Growth Rate Comparison

The stationary crossflow-vortex growth rate is estimated by numerically differentiating the amplitude data shown in Section 5.7.2. There are several possible choices for the disturbance amplitude function such as

$$A_1(x) = u_{s \max}(x) \quad (7)$$

or,

$$A_2(x) = \frac{1}{y_{\max}} \int_0^{y_{\max}} u_s(x, y) dy \quad (8)$$

or,

$$A_3(x) = \sqrt{\frac{1}{y_{\max}} \int_0^{y_{\max}} (u_s(x, y))^2 dy} \quad (9)$$

The simplest choice is given in Equation 6 where the amplitude function is taken as the maximum of the streamwise-velocity disturbance profiles as shown in Figures 137–144. The second choice given in Equation 7 is to use the average of the streamwise-disturbance velocity over the thickness of the boundary layer to represent the disturbance amplitude. A third possibility is to use the rms

value of the disturbance profile as in Equation 8. Then the growth rate (made dimensionless by referring to the chord length) is computed as

$$\sigma_i = \frac{1}{A_i} \frac{dA_i}{d\left(\frac{x}{c}\right)} \quad (10)$$

where i is 1, 2 or 3. If values from the smooth theoretical eigenfunctions shown in Figures 137–144 are substituted in Equations 6–9 the resulting growth rates are essentially the same irrespective of the choice of the amplitude function.

Figure 162 shows the various growth rate estimates obtained from the experimental disturbance profiles compared to theoretical predictions from the MARIA code (Dagenhart, 1981) and from Reed's computations (Fuciarelli and Reed, 1992). The experimental growth rates are computed from both the profiles shown in Figures 137–144 and from similar data determined from $U_s - U_{s, \text{ref}}$. The theoretical growth rates peak ahead of the first measurement station at $x/c = 0.2$ and decrease approximately linearly over the measurement zone from $0.2 \leq x/c \leq 0.55$ with the two codes predicting slightly different values. In contrast, the several experimental growth rate curves have a distinct up and down pattern over the measurement range and the experimental growth rates are all at or below the level of the theoretical estimates. This may be due to nonlinear saturation of the stationary crossflow vortices. The several experimental growth rate curves differ considerably at each measurement station. The variations in growth rate estimated with the various amplitude functions appear to be a measure of the roughness of the experimental profiles since the smooth theoretical profiles yield essentially the same growth rate estimate, no matter which amplitude function is employed.

5.8 Experimental Results Summary

This chapter gives the results of an experimental examination of crossflow instability and transition on a 45° swept wing in the Arizona State University

Unsteady Wind Tunnel. The model employs an NLF(2)-0415 airfoil in a swept-wing configuration which acts as a nearly ideal crossflow generator. The resulting favorable (i.e., negative) pressure gradient back to the minimum pressure point at $x/c = 0.71$ eliminates the Tollmien-Schlichting instability while strongly exciting the crossflow instability. Thus, the crossflow instability is examined in a crossflow-dominated flow.

Hot-wire spectra measured in the freestream indicate that the large swept-wing model and liner system increase the turbulence intensity to about $0.09\% U_\infty$. Although this is larger than the empty-tunnel turbulence intensity of $0.04\% U_\infty$ it still provides excellent flow quality for the examination of crossflow instability and transition. Most of the freestream disturbance energy is found to be concentrated at low frequencies with no sharp spikes in the spectra due to fan noise.

The pressure distribution is measured along two rows near the ends of the model span. Comparison of measured and predicted pressure distributions shows that a good approximation of infinite swept-wing flow is achieved. Minor discrepancies between the pressure distributions are noted in two locations, but, these differences are considered to be insignificant.

The stationary vortex pattern and transition are visualized using both sublimating-chemical and liquid-crystal coatings. The two visualizations methods give similar results, but the sublimating-chemical method is more extensively used because of better contrast in the images and easier cleanup. Both the vortex streak pattern and transition pattern are found to be highly repeatable even months apart. A fixed-wavelength vortex pattern is observed throughout the visualization range $0.15 \leq x/c \leq 0.80$. No vortex dropouts or other adjustments to the wavelength are observed. The transition line which is formed by overlapping turbulent wedges originating on various vortex lines is found to be very jagged. The transition location is determined from the flow-visualization photographs as

the midpoint between the transition wedge origins and the limit where the wedges merge.

Transition locations are also determined using surface-mounted hot-film gages and hot-wire probes at fixed locations in the boundary-layer. Transition at the gage or probe location is detected as the flow Reynolds number is gradually increased. Transition is assumed to have taken place at the point where the rms voltage output of the hot-film gage abruptly increases. The first detection of turbulent bursts in the hot-wire signal are considered as the indicator of transition. The transition locations determined using hot-film and hot-wire detectors fall within the transition band determined by the flow visualization. The average transition location is found to move from $x/c = 0.80$ for the lowest test Reynolds number of $R_c = 1.92 \times 10^6$ to $x/c = 0.30$ for the highest Reynolds number of $R_c = 3.81 \times 10^6$. Linear-stability computations indicate that the maximum N-factors at transition range from 8.5 to 9.1 in agreement with previous calibrations of the linear-stability method. However, the stationary crossflow-vortex N-factors ranged only from 6.4 to 6.8 at transition.

A limited number of boundary-layer spectra are measured with hot-wire probes. At low Reynolds numbers, the spectra are found to be dominated by low-frequency oscillations. As the Reynolds number is increased, a band of amplified frequencies within the theoretically-predicted travelling crossflow range is found near the blade-pass frequency. A second amplified-frequency band with frequencies roughly twice those in the first band appear for even higher Reynolds numbers. Further increases of the Reynolds number lead to transition to turbulence and an approximately flat spectrum out to the measurement cutoff frequency. The first of the amplified bands was initially thought to represent travelling-crossflow waves, but subsequent measurements across a single stationary crossflow vortex tend to discredit this conclusion.

The most extensive measurements are made as hot-wire surveys across a single stationary-crossflow vortex for $\alpha = -4^\circ$ and $R_c = 2.37 \times 10^6$. A dark stationary-vortex track is marked on the model surface with a felt-tipped pen following a flow-visualization run. Both mean- and rms-velocity profiles are measured at several spanwise locations across the vortex track for $x/c = 0.2, 0.25, 0.30, 0.35, 0.40, 0.45, 0.50,$ and 0.55 . For this test condition, the transition to turbulence took place at $x/c = 0.58$ which is just downstream of the last measurement station. The travelling-wave component is narrow bandpass filtered at $f = 100$ Hz and the gain boosted twice before measurement with the UWT analog/digital converter system. Local stationary crossflow-disturbance profiles are determined from the measured mean-velocity data in two ways — by subtracting either a theoretical mean-velocity profile or by subtracting a span-averaged profile from the mean-velocity data. The boundary-layer survey data are presented as local-velocity profiles or displayed as contour plots across the vortex.

The mean-velocity profiles are found to vary slightly across the stationary-vortex path even at the first measurement station at $x/c = 0.20$. The variation across the stationary vortex increases with downstream distance until distinctly S-shaped profiles develop near the center of the measurement range for $x/c > 0.45$. The mean-profile distortion continues to grow with downstream distance until all the profiles have pronounced S-shapes. For the forward measurement locations the local stationary-vortex disturbance profiles have single-lobed shapes with either purely excess or deficit velocities as expected from theoretical considerations. But, for $x/c \geq 0.45$ the local stationary-vortex disturbance profiles take on distinct crossover shapes not anticipated by the linear theory. The maximum stationary-vortex disturbance intensities reach levels of $\pm 20\% U_{s_e}$ at $x/c = 0.50$ before decreasing slightly at $x/c = 0.55$. The travelling-wave rms profiles at the forward locations have single-lobed shapes as expected from linear theory, but

develop double-lobed shapes for $x/c \geq 0.45$ which are not predicted by the linear theory. The maximum rms intensity reaches only 0.7% U_{s_0} which is more than an order of magnitude smaller than the stationary-vortex disturbances.

The streamwise components of mean-velocity, stationary crossflow-vortex disturbance velocity, and rms travelling-wave disturbance intensity are all plotted as isoline contours across a single stationary-crossflow vortex at the various measurement stations. The mean streamwise-velocity contours are shown to be essentially flat and parallel to the model surface at the beginning of the measurement range at $x/c = 0.20$. As x/c increases, the contours are seen to rise near the middle of the measurement span and to descend near the ends of the measurement span. For $x/c = 0.50$ and 0.55 , the streamwise-velocity contours in the outer portion of the boundary layer actually begin to roll over under the continuing action of the stationary-crossflow vortex.

The stationary crossflow-disturbance velocity contours determined by the two methods show qualitative agreement throughout the measurement range. At the forward measurement stations ($x/c = 0.20$ and 0.25) the stationary-crossflow vortex is weak and the disturbance-velocity contours showed very little distinctive pattern. For measurements at $x/c = 0.30, 0.35,$ and 0.40 , a distinct disturbance velocity pattern emerges with an area of deficit velocity developing near the middle of the measurement span and excess velocity regions evolving at each end of the measurement span. For the last two measurement stations ($x/c = 0.50$ and 0.55), the locations of the maximum excess disturbance velocities shift from the ends of the measurement span by approximately $\lambda/4$ toward the wing root. This shift may have occurred due to a misalignment of the traverse mechanism by approximately 2 mm in the spanwise direction or the entire vortex pattern may have shifted by $\lambda/4$. In any event, the pattern of alternate excess and deficit velocity regions established at the more forward measurement stations continues to develop with

the velocity perturbations reaching $\pm 20\% U_{s\infty}$ before transition. Furthermore, the deficit and excess velocity regions distort in a pattern similar to that of the mean streamwise-velocity contours with the low-velocity region beginning to roll up and over the high-velocity zones.

The travelling-wave disturbances are extremely weak and no distinct pattern emerges until $x/c = 0.40$ where rms velocity contours develop, which are approximately parallel to the wing surface as expected from the linear stability theory for travelling-crossflow waves. But, at $x/c = 0.45$, definite regions with closed contours of the travelling-wave disturbance velocity develop. Between the $x/c = 0.45$ and 0.50 the travelling-wave rms intensity increases dramatically with a pronounced peak near the middle of the measurement span. The maximum rms intensity, however, reaches only $0.7\% U_{s\infty}$ which is still more than an order of magnitude smaller than the stationary-vortex strength. Between $x/c = 0.50$ and 0.55 the travelling-wave disturbance intensity decreases abruptly perhaps because some other instability mechanism drains off energy as the transition to turbulence is approached at $x/c = 0.58$.

The experimental results are compared with predictions from the linear stability theory. The stationary crossflow-disturbance eigenfunctions are supplied in the model-oriented coordinate frame and are rotated to two other relevant coordinate frames for comparison with the experimental observations. The disturbance velocities are measured in a streamwise coordinate frame with the x-axis parallel to the freestream velocity vector. The theoretical velocity vectors in a wave-oriented reference frame are superposed on the streamwise velocity-contour plots. Experimental disturbance-velocity profiles are computed as the spatial root-mean-square of the local profiles across the vortex wavelength for comparison with the theoretical eigenfunctions. The stationary crossflow-vortex wavelengths observed with flow-visualization techniques are compared with the theoretically-

predicted maximum-amplified wavelengths. Growth rates are determined from the experimental disturbance functions by numerically differentiating the experimental data at the several measurement stations.

Since the linear stability theory gives the disturbance velocities only to within a multiplicative constant the theoretical eigenfunctions are scaled to match the maximum experimental disturbance intensities. The theoretical u_s -eigenfunctions at all locations have zero values at the wing surface, single-lobed profiles with maxima inside the boundary layer, and values asymptotically approaching zero as $y \rightarrow \infty$. The experimental streamwise-velocity disturbance functions are found to have single-lobed shapes very similar to those predicted by the linear stability theory for $0.20 \leq x/c \leq 0.40$. The maxima of the theoretical eigenfunctions are, on average, located a little further from the wing surface than the experimental disturbance maxima. For $x/c \geq 0.45$ the experimental disturbance functions take on double-lobed shapes with the peak disturbance intensity exceeding 7% U_s . This change in experimental profile shape is evidently due to the continuing action of the stationary crossflow vortex causing a rollover of flow within the vortex. For $x/c \geq 0.45$ the theoretical eigenfunction maximum occurs between the two maxima observed in the experimental data. The theoretical velocity-vector plots when superposed on the experimental data show qualitative agreement with the observed flow features throughout the measurement range. The theoretically-predicted wavelengths of maximum amplification are found to be approximately 25% larger than the wavelengths observed in the flow-visualization studies. This is probably due to the fact that the fixed stationary vortex wavelength is established well forward on the model where the boundary-layer is still relatively thin. Swept flat-plate experiments generally have shown closer agreement between the theoretically most-amplified wavelength and the observed wavelength than have swept-wing studies. Perhaps the blunter nose of the swept wing is an important

factor in establishing the smaller wavelength. Three different measures of the experimental disturbance growth rate are found to yield similar trends which differ from the theoretically-predicted growth rates. The experimental growth rates are at or below the theoretically-predicted levels over the measurement range. Also, the experimental growth rates develop a distinct up and down pattern over the measurement range whereas the theoretical growth rates decrease approximately linearly over the measurement range.

6 CONCLUSIONS

An experimental configuration is designed and constructed to permit the examination of a whole range of problems associated with the development, growth, and breakdown of crossflow vortices in a swept-wing flow. Careful control of the model and wind-tunnel geometries creates a benchmark experimental setup for the study of swept-wing flows. The range of problems which can be addressed with this experimental configuration include the investigation of crossflow-vortex growth and development in a crossflow-dominated flow, the interaction of crossflow vortices with Tollmien-Schlichting waves, surface-roughness effects on crossflow-disturbance receptivity, and crossflow-vortex breakdown mechanisms.

In the present investigation, we focus largely on the first of these possible research problems. In particular, a small negative angle of attack is selected so that the resulting favorable (i.e., negative) pressure gradient eliminates primary Tollmien-Schlichting waves while strongly amplifying the crossflow vortices. The bulk of the measurements taken at a chord Reynolds number of $R_c = 2.37 \times 10^6$ consists of extensive hot-wire probe surveys across a single stationary vortex track. Both steady and narrow-bandpass travelling-wave disturbance velocities are determined in steps across the vortex track at fractional chord locations ranging from just downstream of the neutral stability point to just ahead of the transition location. The data are presented as local velocity-profile plots and as isoline contour plots across the stationary vortex. The experimental results are compared with theoretical eigenfunction shapes, growth rates, and vector velocity plots.

The following conclusions are drawn:

1. The transition location is determined using surface-mounted hot-film gages, boundary-layer hot-wire probes, and flow visualization in the range from $x/c =$

0.80 at the minimum test Reynolds number of $R_c = 1.92 \times 10^6$ to $x/c = 0.30$ at the maximum Reynolds number of $R_c = 3.81 \times 10^6$. The local Reynolds number at transition varies across the range $1.14 \times 10^6 \leq R_{x \text{ tr}} \leq 1.54 \times 10^6$ which indicates that some roughness effects may be important.

2. The maximum theoretical crossflow N-factors for travelling crossflow vortices at transition range from 8.5 to 9.1 in agreement with previous calibrations of the linear stability method. However, the corresponding N-factors for the dominant stationary-crossflow vortices are in the range from 6.4 to 6.8.

3. The boundary-layer hot-wire spectra are observed to contain mostly low-frequency oscillations at the lower test Reynolds numbers. With increasing Reynolds number, two bands of amplified frequencies are observed. The first of these bands is near the blade-pass frequency and within the range of amplified travelling-crossflow waves predicted by the linear theory. The second amplified-frequency band falls at approximately twice the blade-pass frequency and at the upper frequency limit of the band of amplified travelling-crossflow waves. The travelling waves in the first frequency band are thought not to be travelling-crossflow waves, but perhaps Tollmien-Schlichting waves generated locally in the highly distorted mean flow.

4. The measured mean-velocity profiles show slight variations across the stationary-vortex track even at the first measurement station at $x/c = 0.20$. The variations across the vortex grow with downstream distance until distinct S-shaped profiles are observed near the middle of the measurement span at $x/c = 0.45$. By $x/c = 0.55$ the measured profiles all the way across the stationary vortex have taken on highly-distorted S-shapes.

5. The local stationary-vortex disturbance profiles have single-lobed shapes with either purely excess or deficit velocities at the forward measurement stations as expected from theoretical considerations. But, for $x/c \geq 0.45$ the local stationary

disturbance profiles take on distinct crossover shapes not anticipated by the linear theory. The maximum stationary-vortex disturbance intensities reach levels of $\pm 20\%$ of the local boundary-layer edge velocity just before transition.

6. The travelling-wave rms profiles at the forward locations have single-lobed shapes as expected from linear theory, but develop double-lobed shapes for $x/c \geq 0.45$ which are not predicted by the linear theory. The travelling-wave rms disturbance intensity peaks at 0.7% of the local boundary-layer edge velocity which is more than an order of magnitude smaller than the strength of the stationary crossflow vortex.

7. The mean streamwise-velocity contours are shown to be approximately flat and parallel to the model surface at $x/c = 0.20$, but by $x/c = 0.50$ to 0.55 the velocity contours in the outer portion of the boundary-layer actually begin to roll over under the continuing action of the stationary-crossflow vortex.

8. The stationary crossflow-vortex disturbances have little influence at the forward measurement stations but by $x/c = 0.30$ a distinctive pattern forms with a plume of low-velocity fluid rising from the model surface near the middle of the measurement span and concentrations of high-velocity fluid near the wing surface at the ends of the measurement span. For $x/c = 0.50$ and 0.55 the excess and deficit velocities reach maximum intensities of $\pm 20\%$ of the local boundary-layer edge velocity, but the established flow pattern shifted approximately one fourth of the wavelength toward the wing root. This shift is thought to be due either to a slight misalignment of the traverse mechanism or to a small shift in whole stationary crossflow-vortex pattern.

9. The travelling-wave disturbances are found to be very weak with no significant pattern evident until $x/c = 0.45$ where closed-contour isolines appear. These closed-contour isolines differ from the flat contours expected from linear stability theory. The travelling-wave disturbance intensity peaks strongly near the

middle of the measurement span at $x/c = 0.50$ and then abruptly decreases. The travelling-wave disturbance energy may be transferred to some other instability mechanism as the transition location at $x/c = 0.58$ is approached.

10. The experimental streamwise disturbance-velocity functions are found to have single-lobed shapes very similar to those predicted by linear stability theory for $0.20 \leq x/c \leq 0.40$. The maxima of the theoretical eigenfunctions are located slightly higher in the boundary-layer than are the experimental maxima. For $x/c \geq 0.45$ the experimental disturbance functions take on double-lobed shapes. The theoretical eigenfunction maximum is located at a height between the two experimental maxima. The rms-disturbance strength at the breakpoint between the single- and double-lobed experimental profiles is about 7% of the local boundary-layer edge velocity.

11. Qualitative agreement with the experimentally-observed flow features is obtained throughout the measurement range when theoretical velocity-vector plots are superposed onto the experimental contour plots.

12. The theoretically-predicted wavelengths of maximum amplification are found to be approximately 25% larger than the wavelengths observed in the flow-visualization studies. This is probably due to the fact that the fixed stationary-vortex wavelength is established well forward on the model where the boundary-layer is still relatively thin. Perhaps the swept-wing nose-radius is an important factor in establishing the smaller vortex wavelengths since swept flat plate experiments generally have closer agreement between theoretical and observed wavelengths.

13. Three different measures of the experimental growth rate are found to yield similar trends which differ with the theoretically-predicted growth rates. The experimental growth rates are found to be at or below the theoretical values. Also, the experimental growth rates develop a distinct up and down pattern over the

measurement range whereas the theoretical growth rates decrease approximately linearly with downstream distance over the measurement space.

Thus, the present investigation contributes to an improved understanding of the physics of the crossflow instability in a swept-wing flow. The stationary crossflow vortices which are highly sensitive to small-scale surface roughness effects dominate the disturbance flow field and the transition process even though traveling waves are more amplified according to the linear stability theory. The features of the observed flow field evolve from qualitative agreement with expectations from the linear stability theory for the forward measurement stations to highly-distorted profiles with marked differences between the observations and the theoretical predictions. A benchmark experimental data set for the crossflow instability is generated for comparison with results from advanced computational codes currently under development.

Table 1 Crossflow Stability Analysis Using SALLY Code for $\alpha = -4^\circ$ and $R_c = 3.81 \times 10^6$.

Frequency, f	N_{max}							
	Wavelength, λ/c							
	0.002	0.003	0.004	0.005	0.006	0.007	0.008	0.009
-100.0	4.8	10.1	11.2	10.0	8.7	7.3	6.1	5.1
-50.0	4.9	10.7	13.1	12.6	11.6	10.4	9.3	8.3
0.0	5.1	10.9	14.5	14.6	13.8	12.8	11.7	10.7
100.0	5.2	10.6	15.4	16.0	15.5	14.6	13.5	12.4
200.0	5.2	9.4	15.6	17.3	17.2	16.4	15.3	13.8
300.0	5.2	8.2	13.8	16.2	16.6	15.8	14.6	12.9
500.0	4.8	6.2	7.3	7.6	7.2	6.5	5.3	4.4

Table 2 Transition Locations and Wavelengths from Naphthalene Flow Visualization.

Reynolds Number, $R_c \times 10^{-6}$	Transition Location, $(x/c)_T$	Wavelength, λ/c
1.92	0.78	0.0050
2.19	0.73	
2.37	0.58	0.0040
2.73	0.45	0.0034
3.27	0.33	0.0029
3.73	0.30	0.0024

Table 3 N-factors at Transition Computed Using the SALLY
Code for $\alpha = -4^\circ$ and $R_c = 2.37 \times 10^6$, $(\lambda/c)_T = 0.58$.

Frequency, f	N_T						
	Wavelength, λ/c						
	0.004	0.005	0.0055	0.006	0.007	0.008	0.009
0.0	6.2	6.8	6.8	6.7	6.2	5.6	4.5
50.0		8.2		8.5	8.2		6.6
100.0		8.3		9.1	9.1	7.8	7.4
150.0		7.2		8.4	8.6	8.5	7.1
200.0		5.3		6.3	6.9	6.8	5.5
300.0		2.8		2.6	2.4	1.9	1.1

Table 4 N-factors at Transition Computed Using the SALLY
Code for $\alpha = -4^\circ$ and $R_c = 2.73 \times 10^6$, $(\lambda/c)_T = 0.45$.

Frequency, f	N_T						
	Wavelength, λ/c						
	0.003	0.004	0.005	0.0055	0.006	0.007	0.008
0.0	4.7	6.5	6.2		5.6	5.0	4.3
50.0		7.3	7.6	7.4	7.2	6.6	
100.0		7.6	8.3	8.2	8.1	7.6	
150.0		7.3	8.5	8.5	8.5	7.9	
200.0		6.4	8.0	8.1	8.2	7.7	
300.0		4.7	5.2	5.3	5.5	5.3	
400.0		3.3	3.0	2.9	2.5	2.2	

Table 5 N-factors at Transition Computed Using the SALLY Code for $\alpha = -4^\circ$ and $R_c = 3.73 \times 10^6$, $(\lambda/c)_T = 0.30$.

Frequency, f	N_T						
	Wavelength, λ/c						
	0.0025	0.003	0.004	0.0045	0.005	0.006	0.007
0.	6.1	6.4	6.0	5.5	5.0	4.1	3.3
50.0		7.0	6.8	6.4	5.9		
100.0		7.4	7.5	7.2	6.7		
150.0		7.6	8.1	7.8	7.3		
200.0		7.7	8.4	8.2	7.8		
300.0		7.2	8.5	8.4	8.0		
400.0		6.4	7.8	7.8	7.3		
500.0		5.6	6.2		5.9		

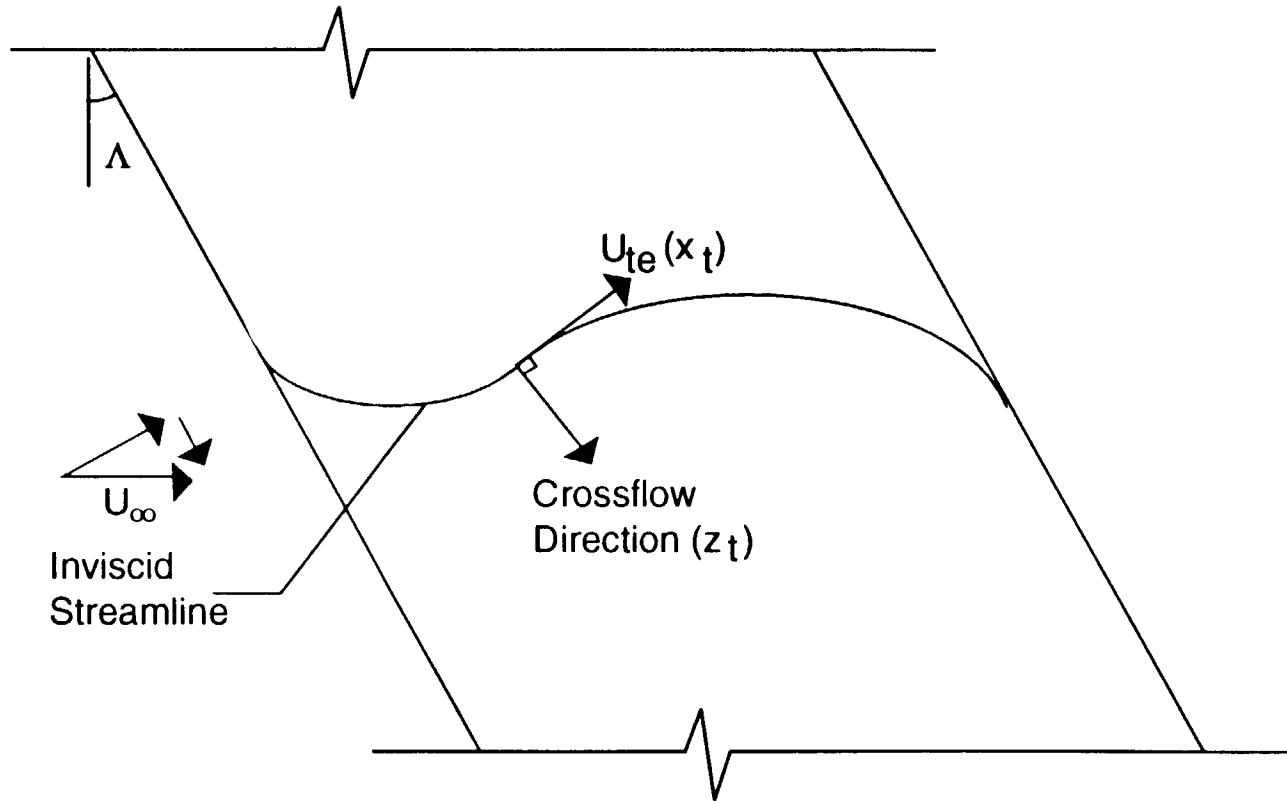


Figure 1. Curved Streamlines over a Swept Wing.

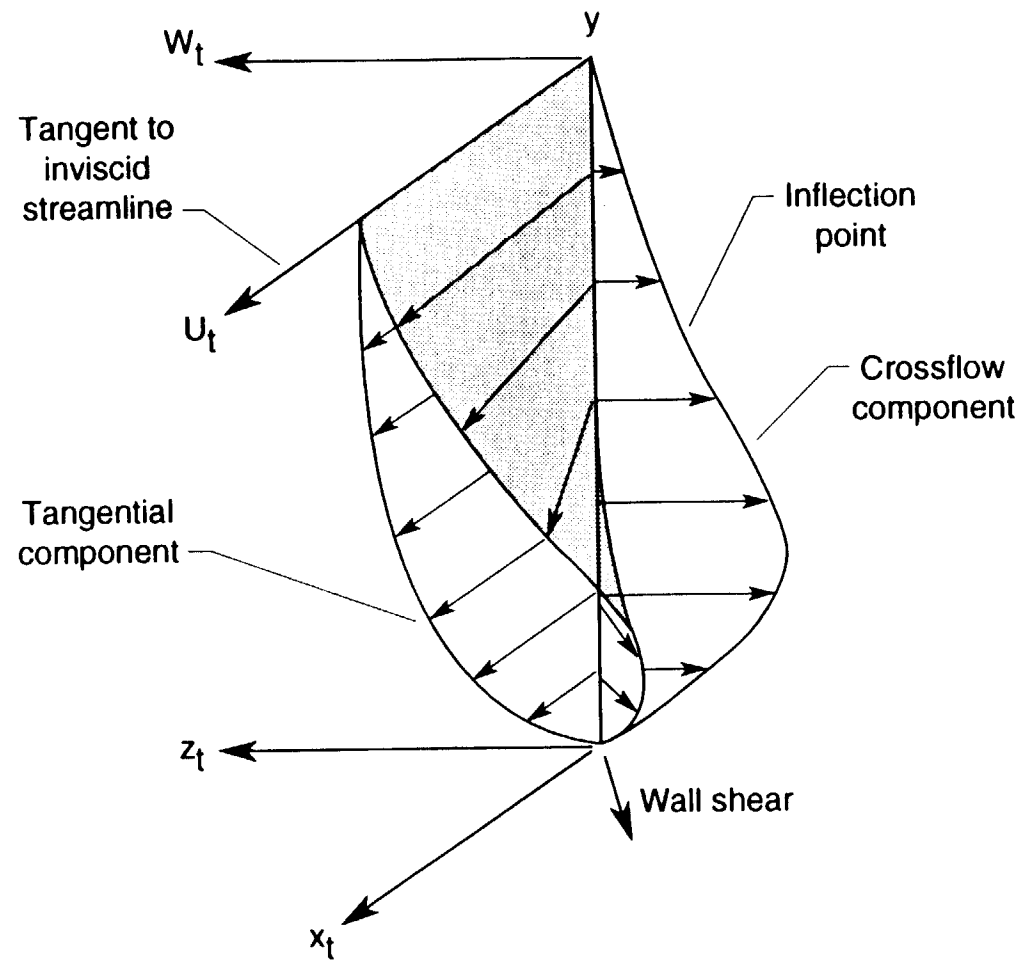


Figure 2. Boundary-Layer Velocity Profiles on a Swept Wing.

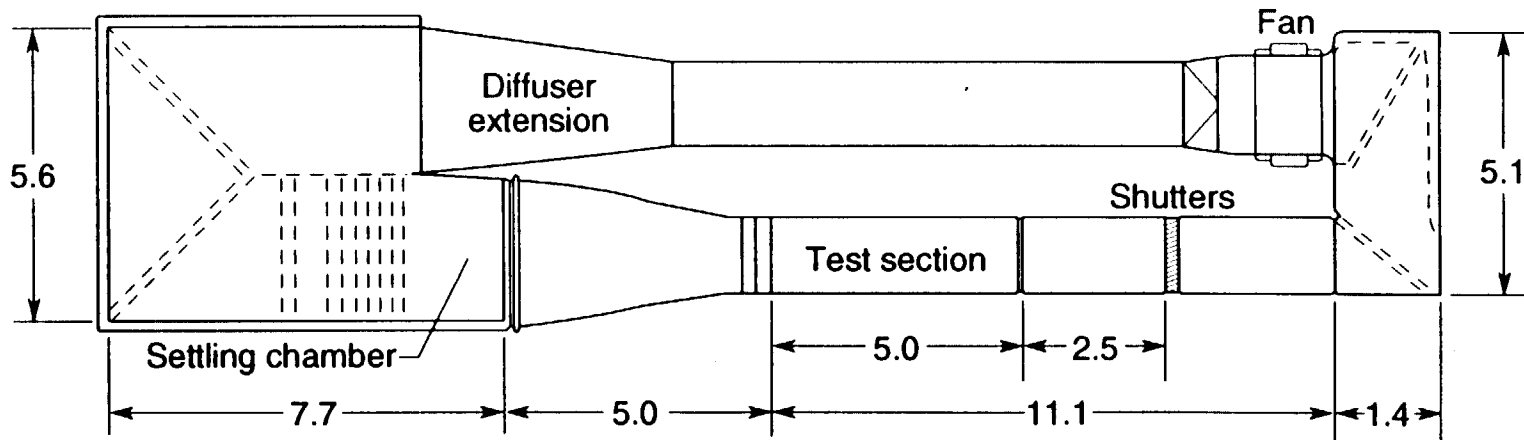


Figure 3. Plan View of Arizona State University Unsteady Wind Tunnel (Dimensions in meters).

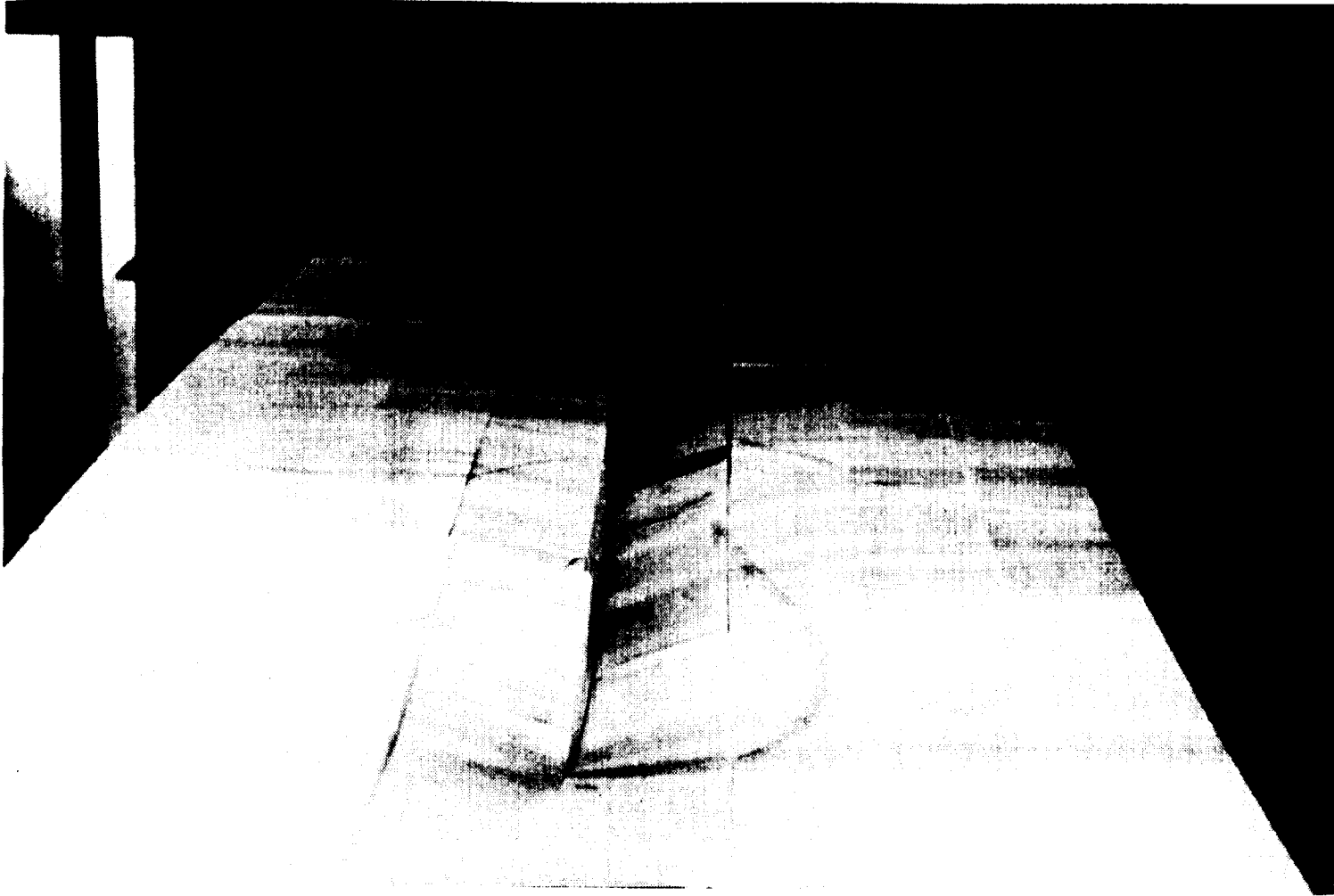


Figure 4. Photograph of New UWT Test Section With Liner Under Construction.

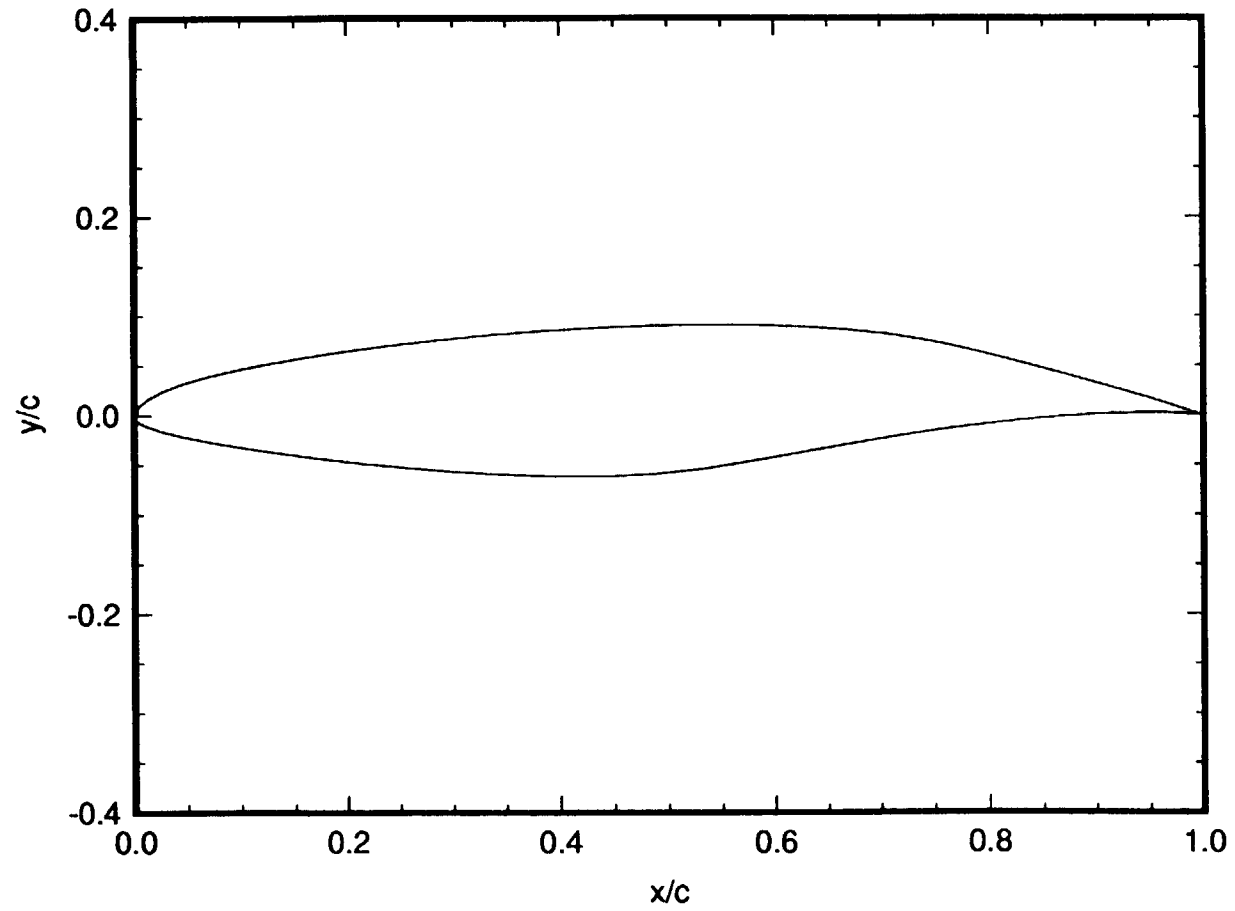


Figure 5. NLF(2)-0415 Airfoil.

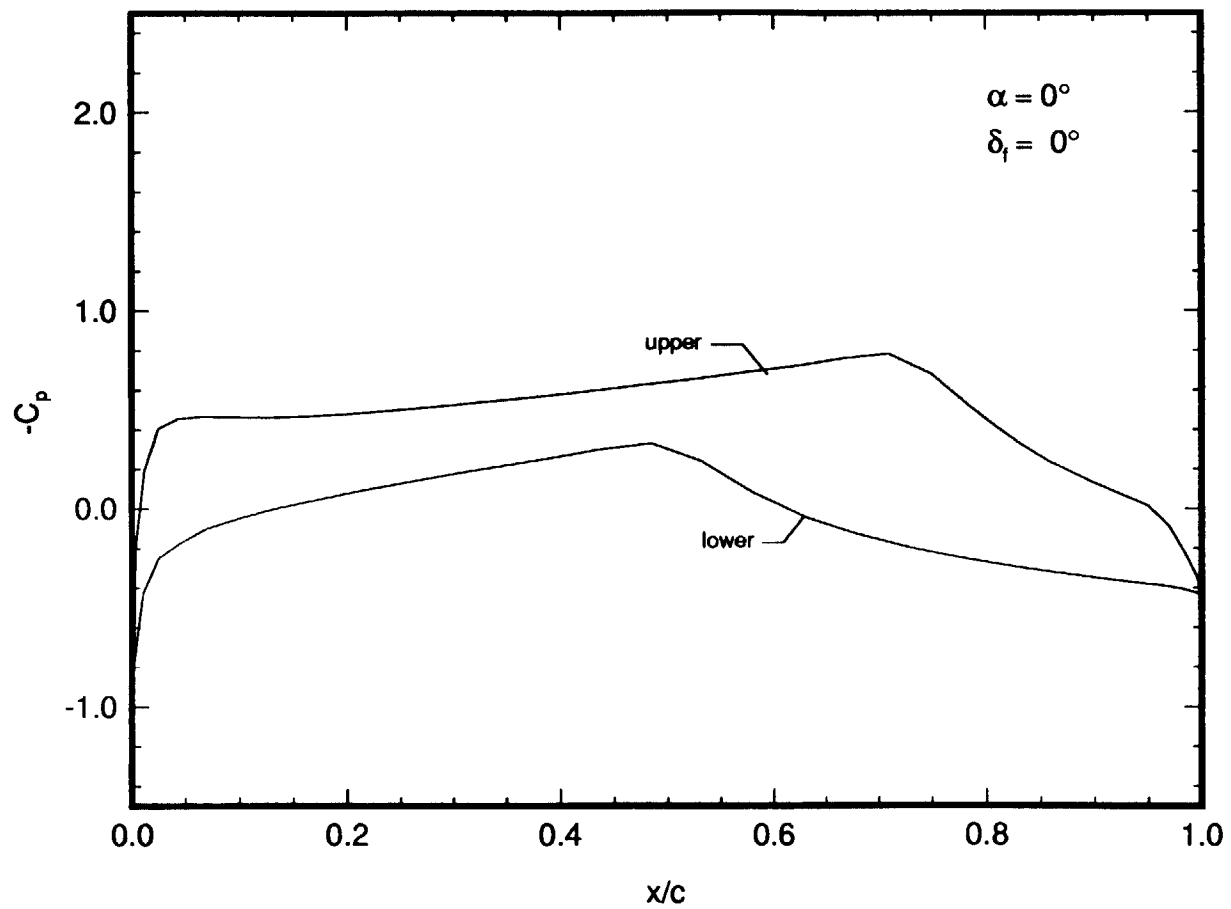


Figure 6. NLF(2)-0415 Design Point Pressure Distribution at $\alpha = 0^\circ$ and $\delta_f = 0^\circ$ in Free Air.

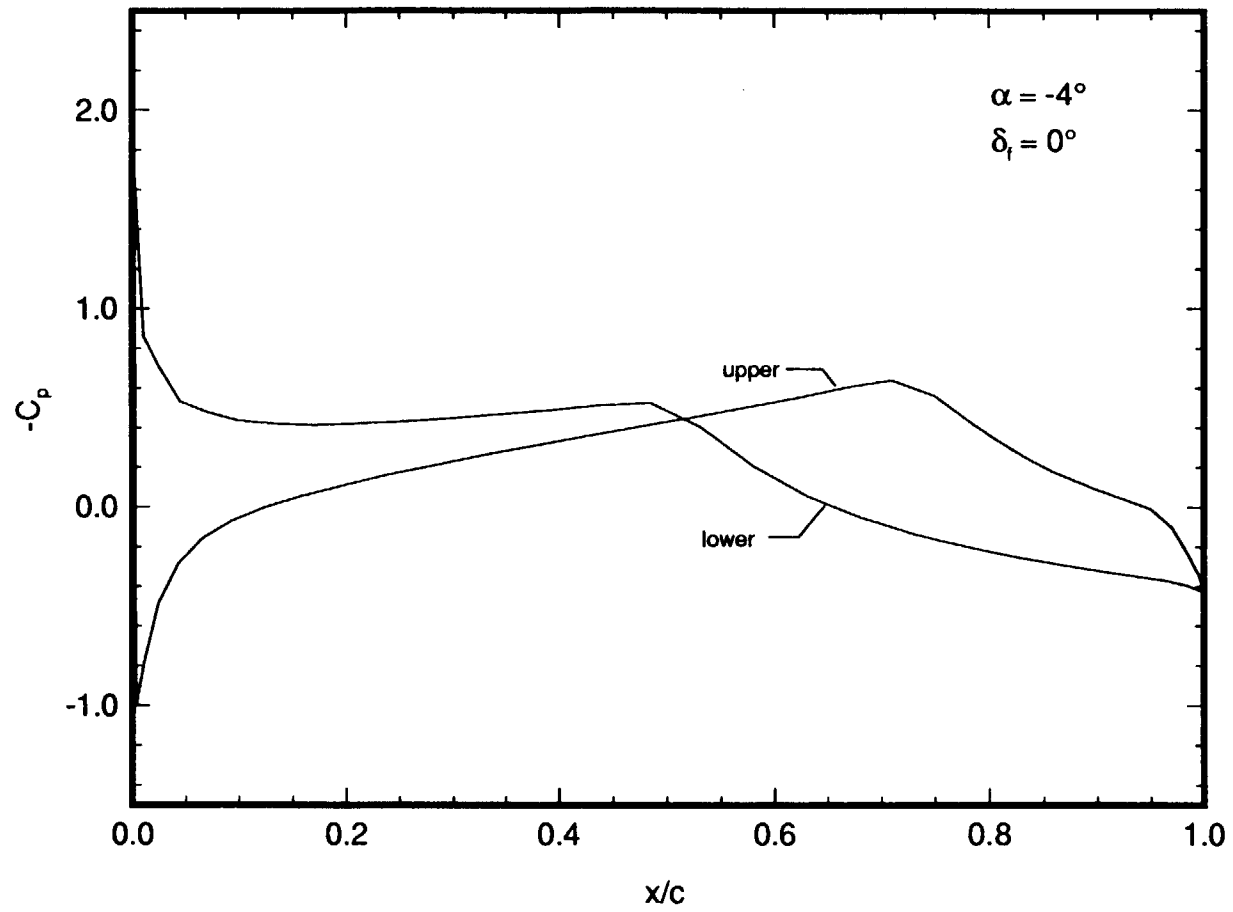


Figure 7. NLF(2)-0415 Pressure Distribution for $\alpha = -4^\circ$ and $\delta_f = 0^\circ$ in Free Air.

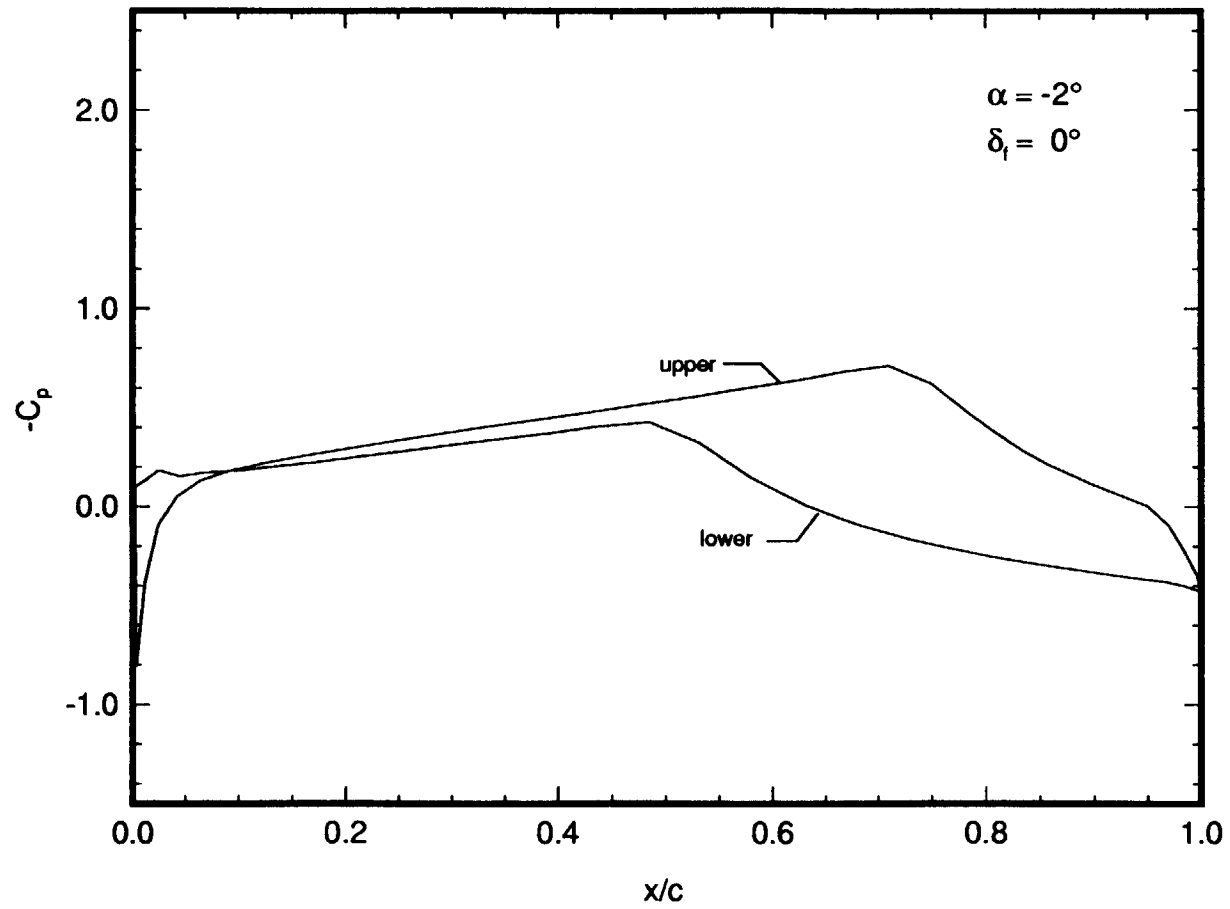


Figure 8. NLF(2)-0415 Pressure Distribution for $\alpha = -2^\circ$ and $\delta_f = 0^\circ$ in Free Air.

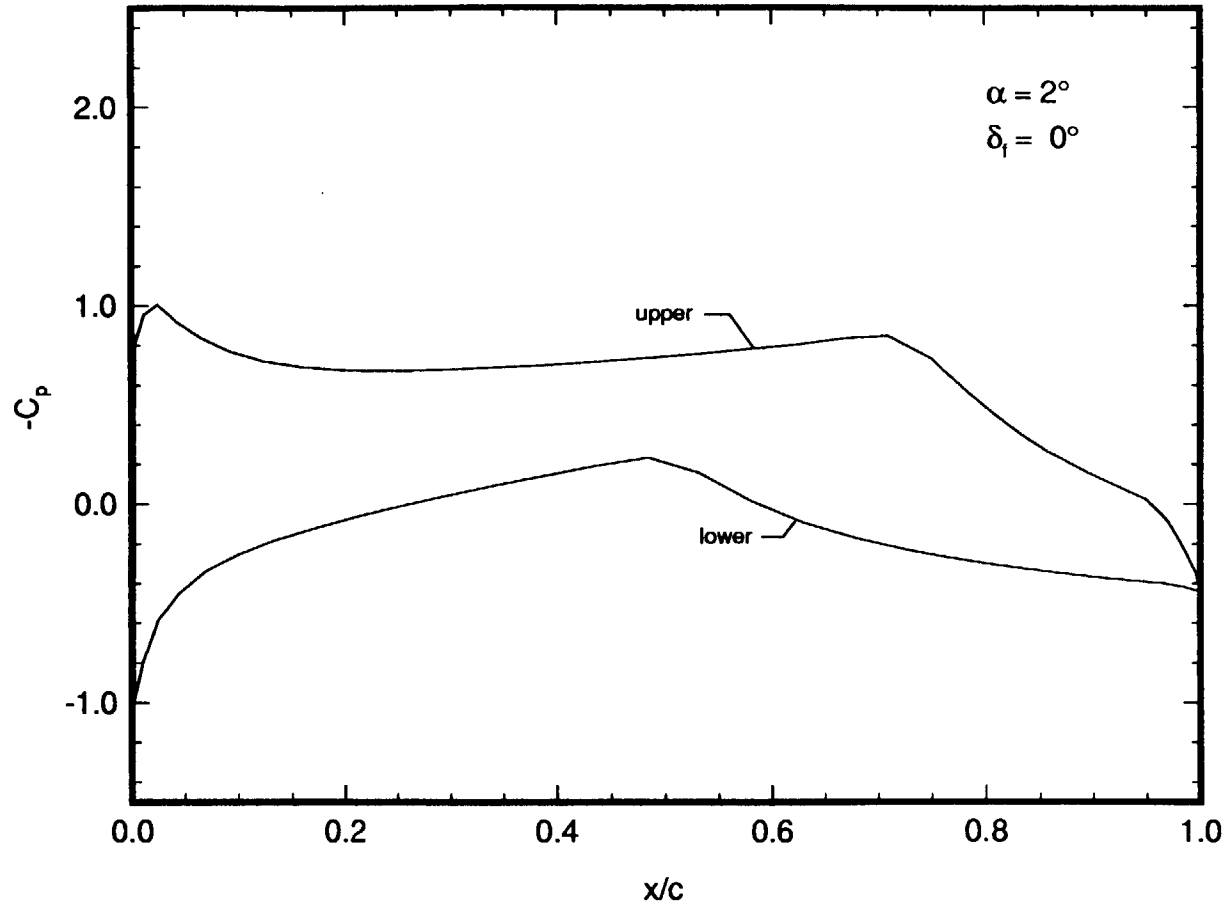


Figure 9. NLF(2)-0415 Pressure Distribution for $\alpha = 2^\circ$ and $\delta_f = 0^\circ$ in Free Air.

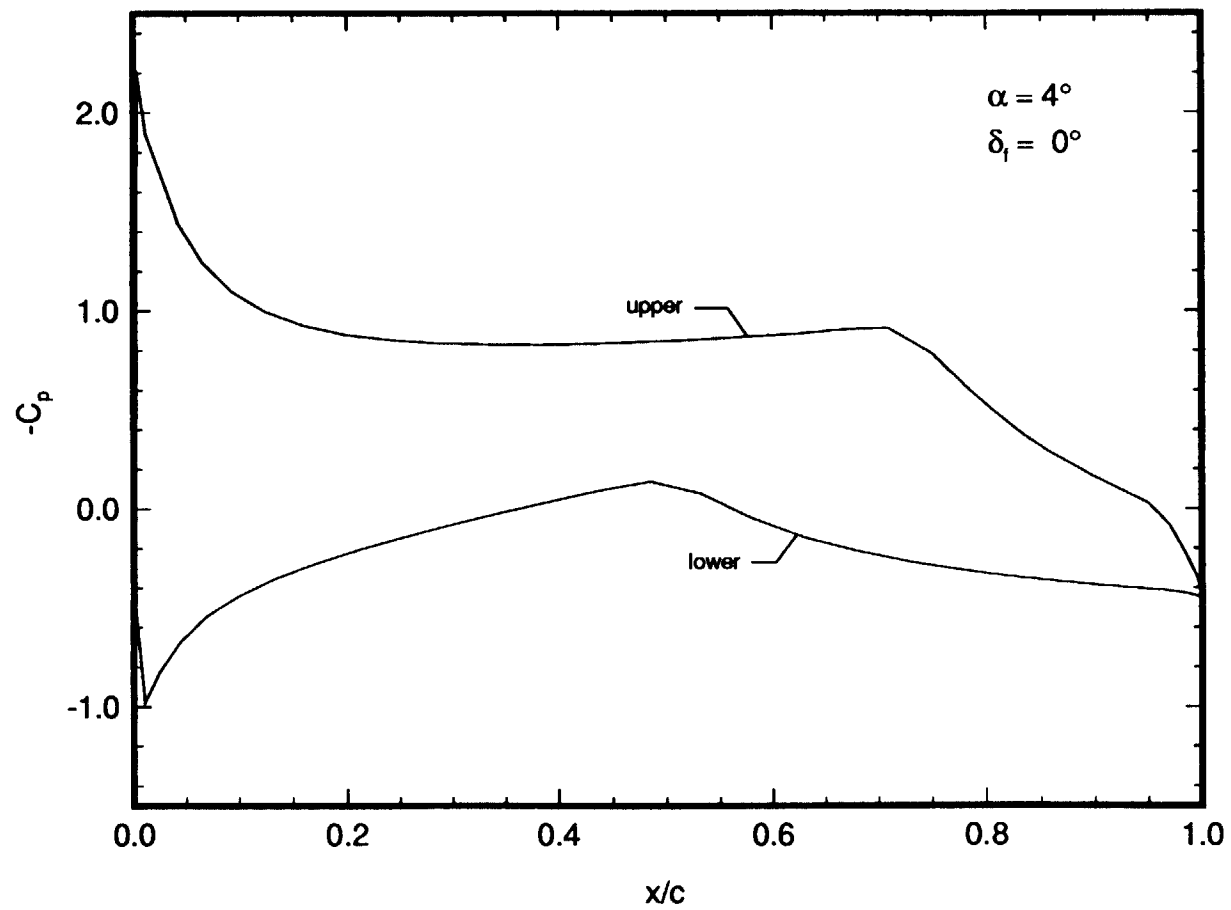


Figure 10. NLF(2)-0415 Pressure Distribution for $\alpha = 4^\circ$ and $\delta_f = 0^\circ$ in Free Air.

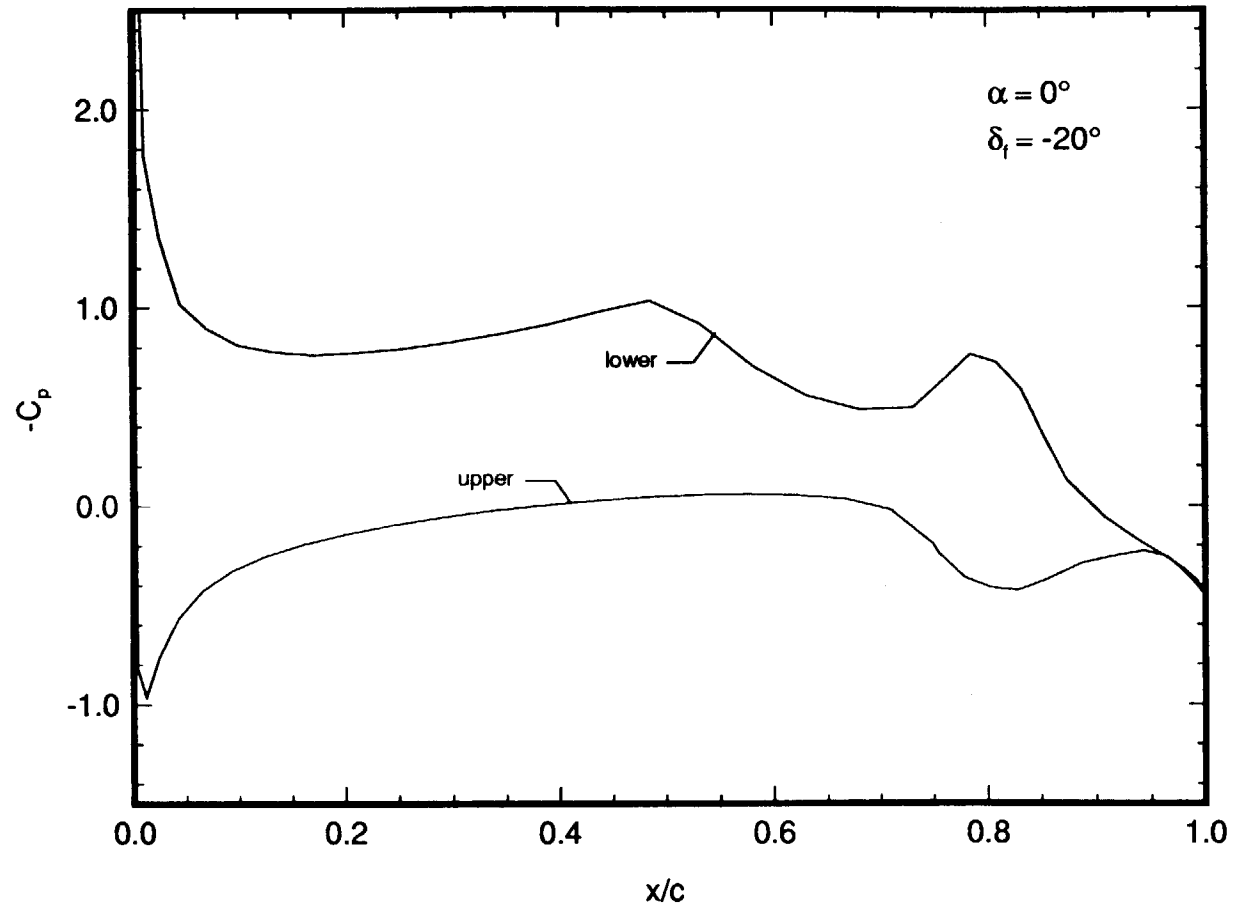


Figure 11. NLF(2)-0415 Pressure Distribution for $\alpha = 0^\circ$ and $\delta_f = -20^\circ$ in Free Air.

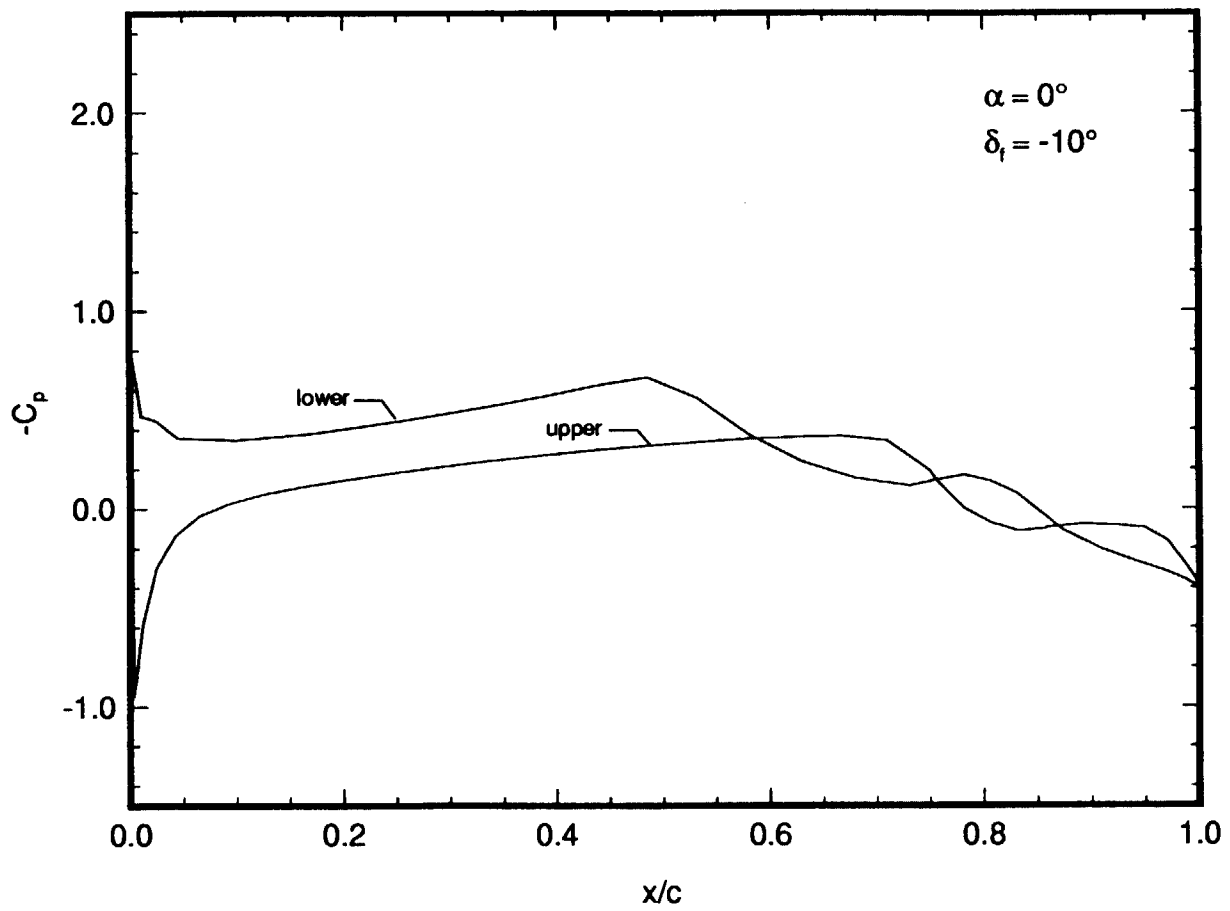


Figure 12. NLF(2)-0415 Pressure Distribution for $\alpha = 0^\circ$ and $\delta_f = -10^\circ$ in Free Air.

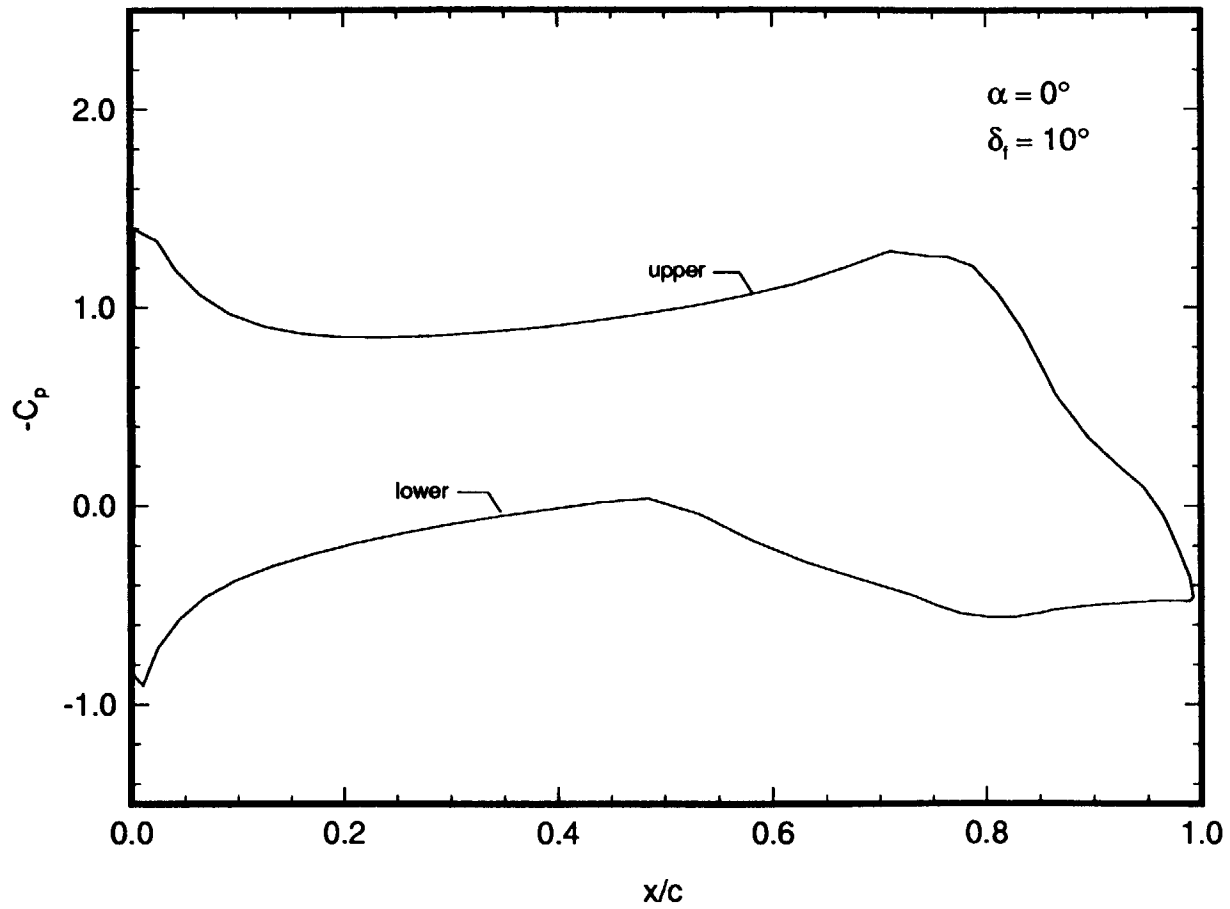


Figure 13. NLF(2)-0415 Pressure Distribution for $\alpha = 0^\circ$ and $\delta_f = 10^\circ$ in Free Air.

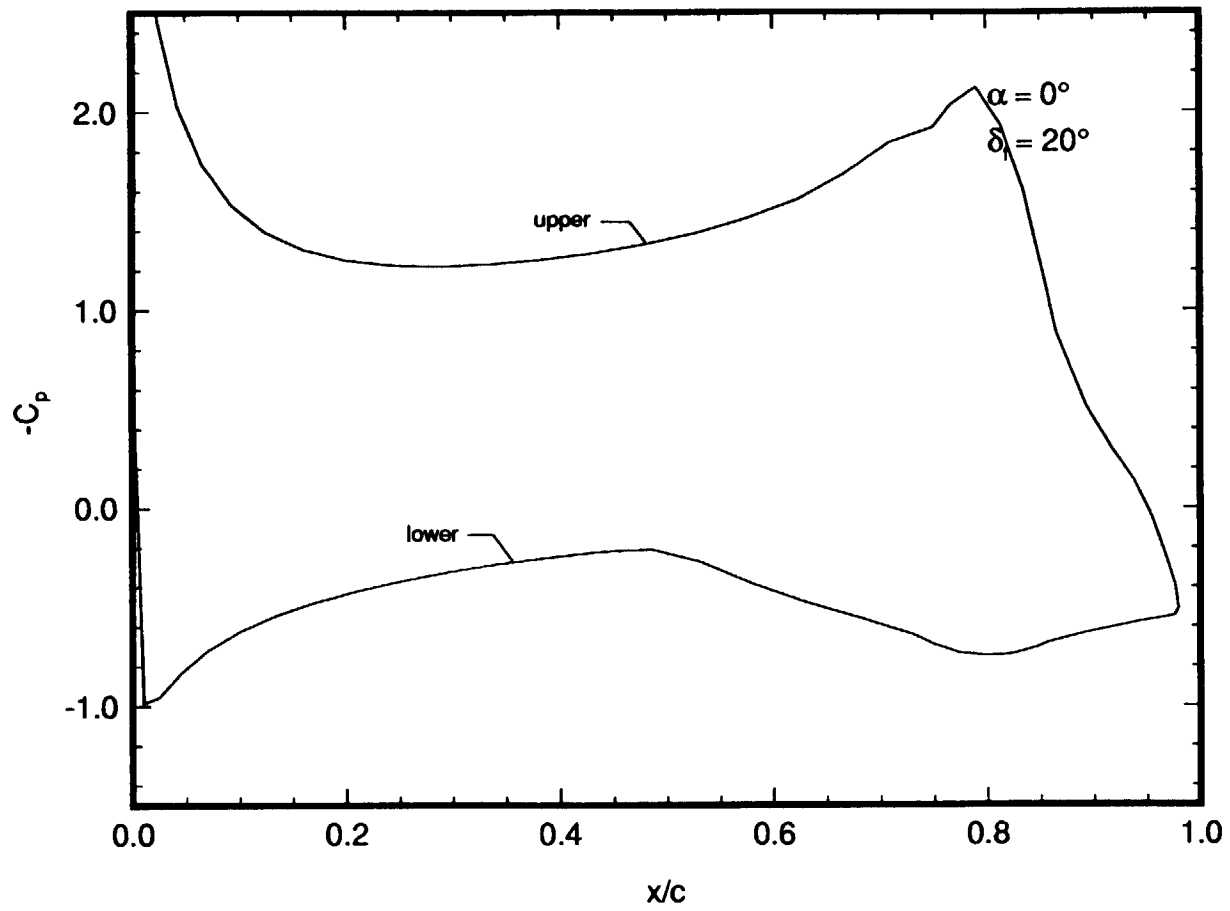


Figure 14. NLF(2)-0415 Pressure Distribution for $\alpha = 0^\circ$ and $\delta_f = 20^\circ$ in Free Air.

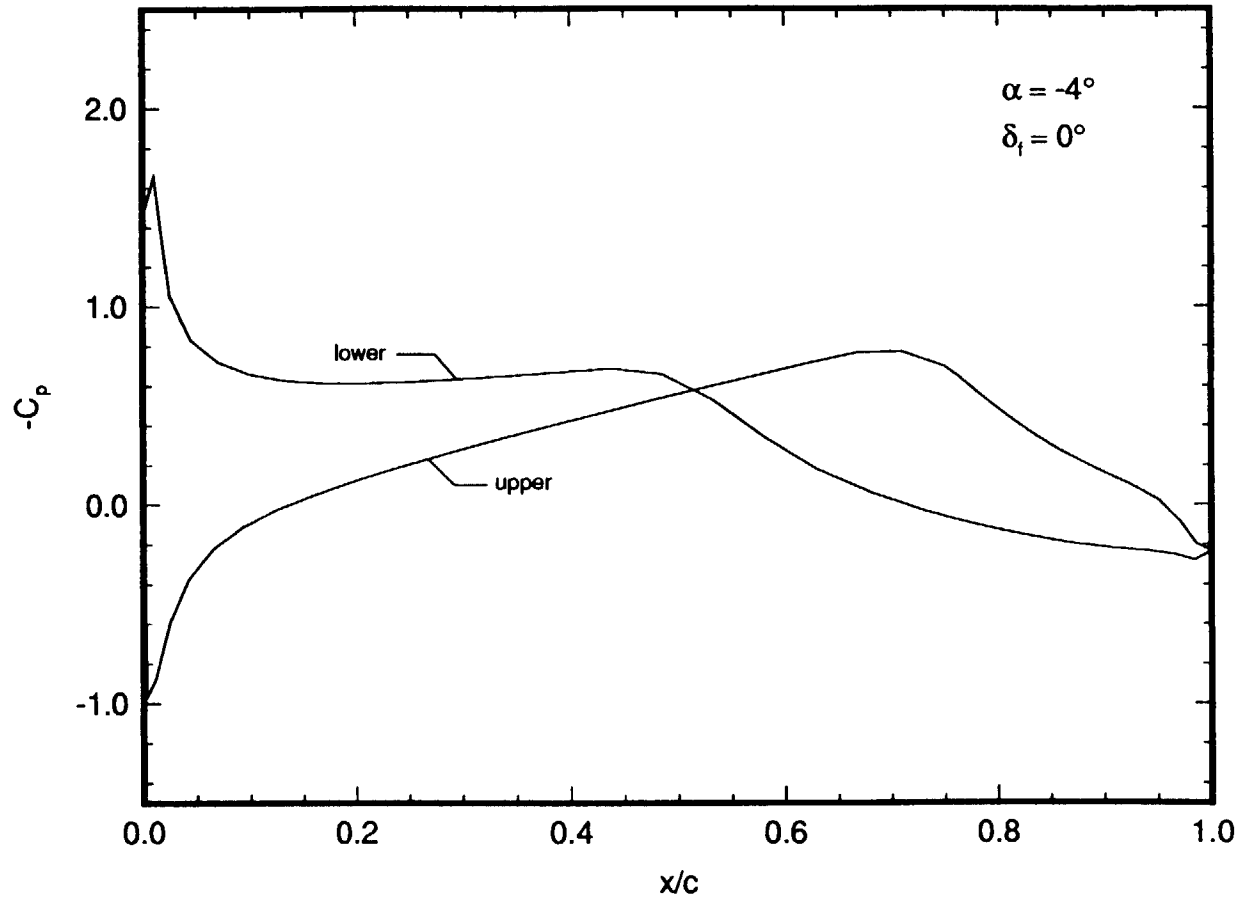


Figure 15. NLF(2)-0415 Pressure Distribution for $\alpha = -4^\circ$ and $\delta_f = 0^\circ$ in UWT.

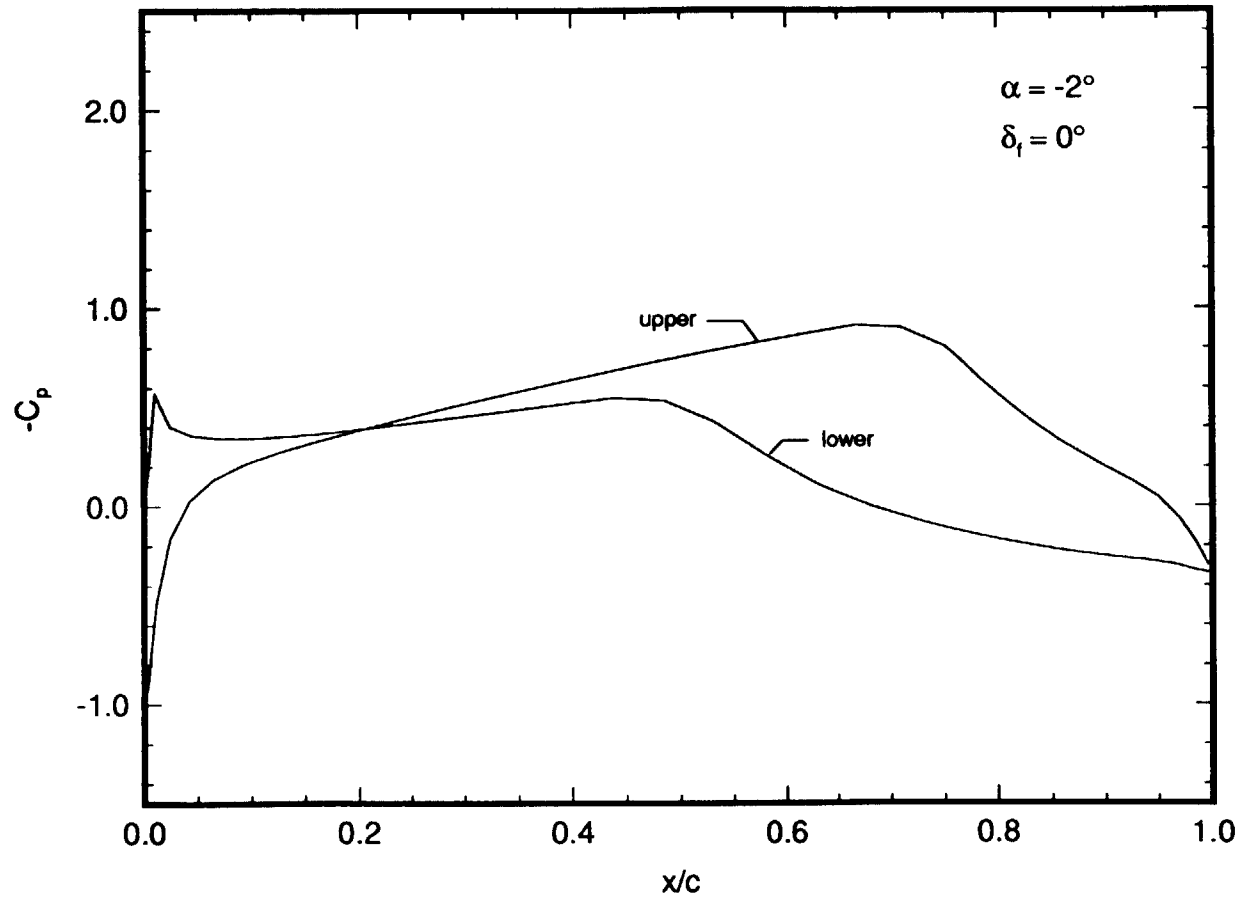


Figure 16. NLF(2)-0415 Pressure Distribution for $\alpha = -2^\circ$ and $\delta_f = 0^\circ$ in UWT.

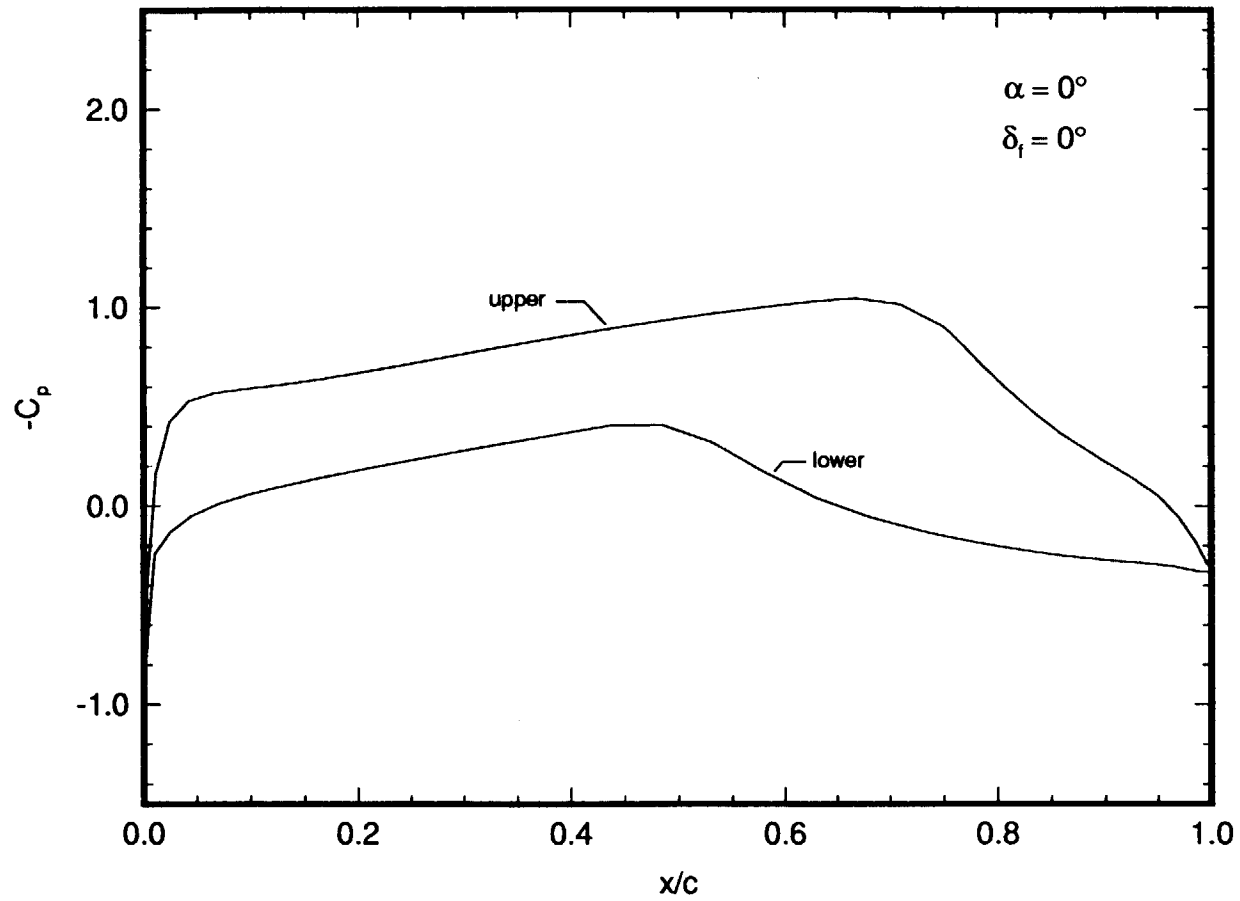


Figure 17. NLF(2)-0415 Pressure Distribution for $\alpha = 0^\circ$ and $\delta_f = 0^\circ$ in UWT.

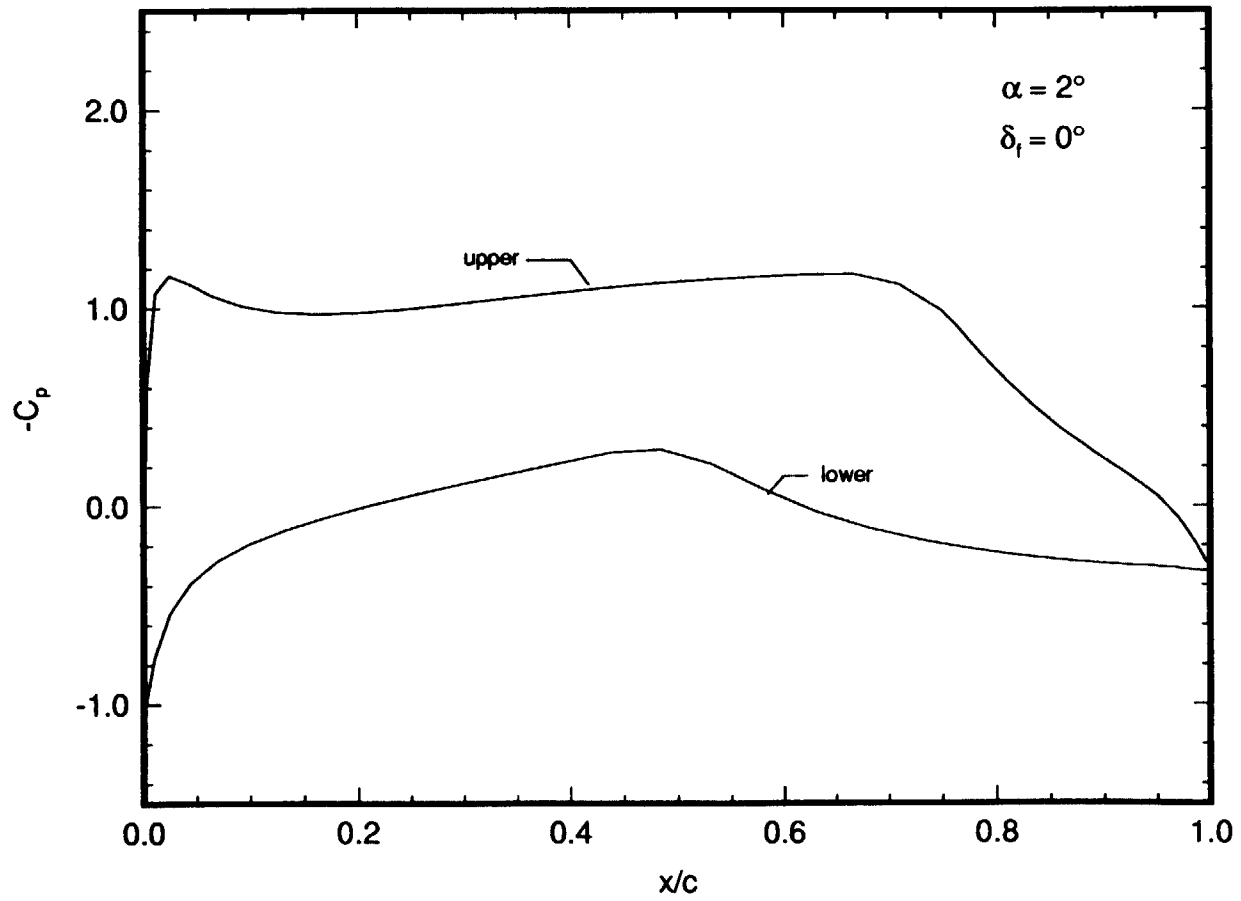


Figure 18. NLF(2)-0415 Pressure Distribution for $\alpha = 2^\circ$ and $\delta_t = 0^\circ$ in UWT.

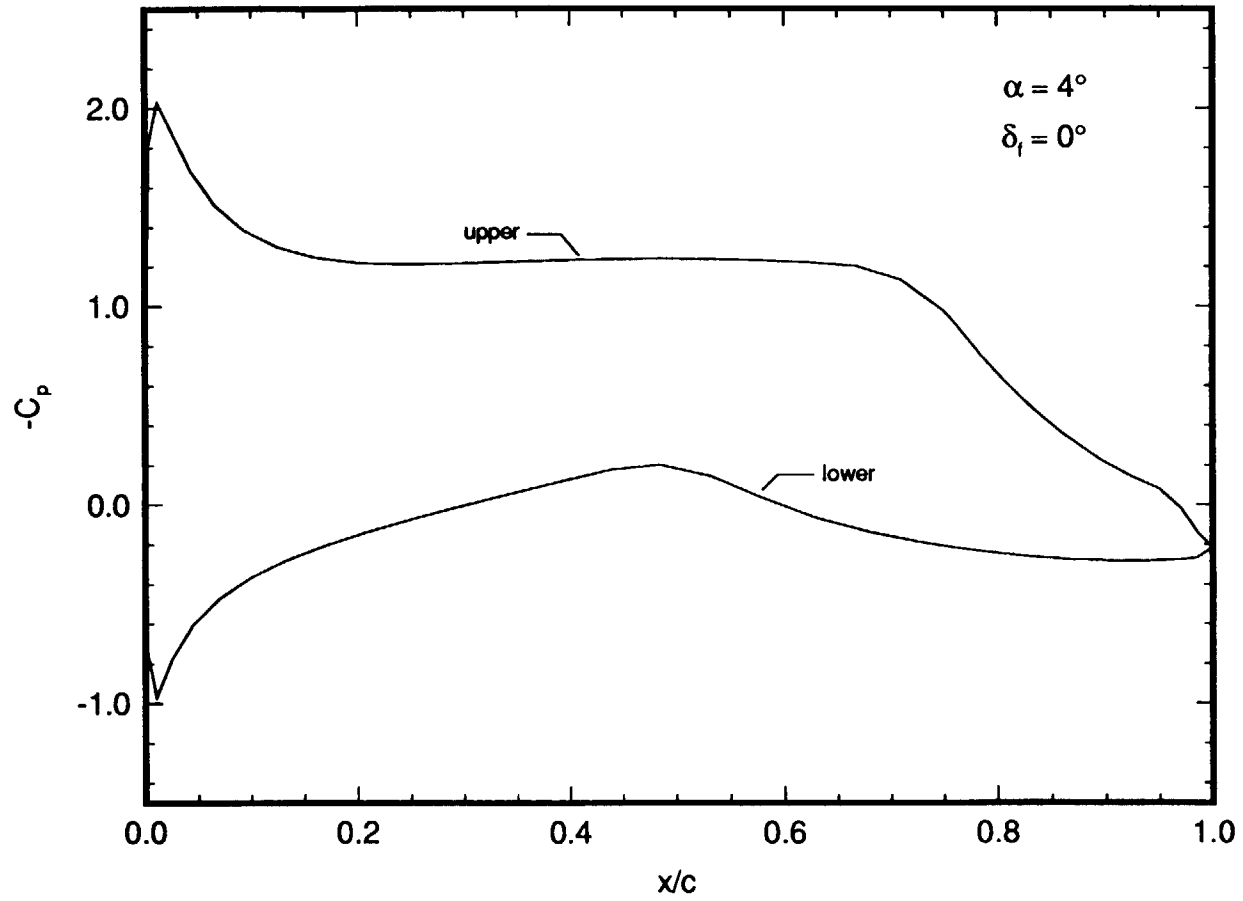


Figure 19. NLF(2)-0415 Pressure Distribution for $\alpha = 4^\circ$ and $\delta_f = 0^\circ$ in UWT.

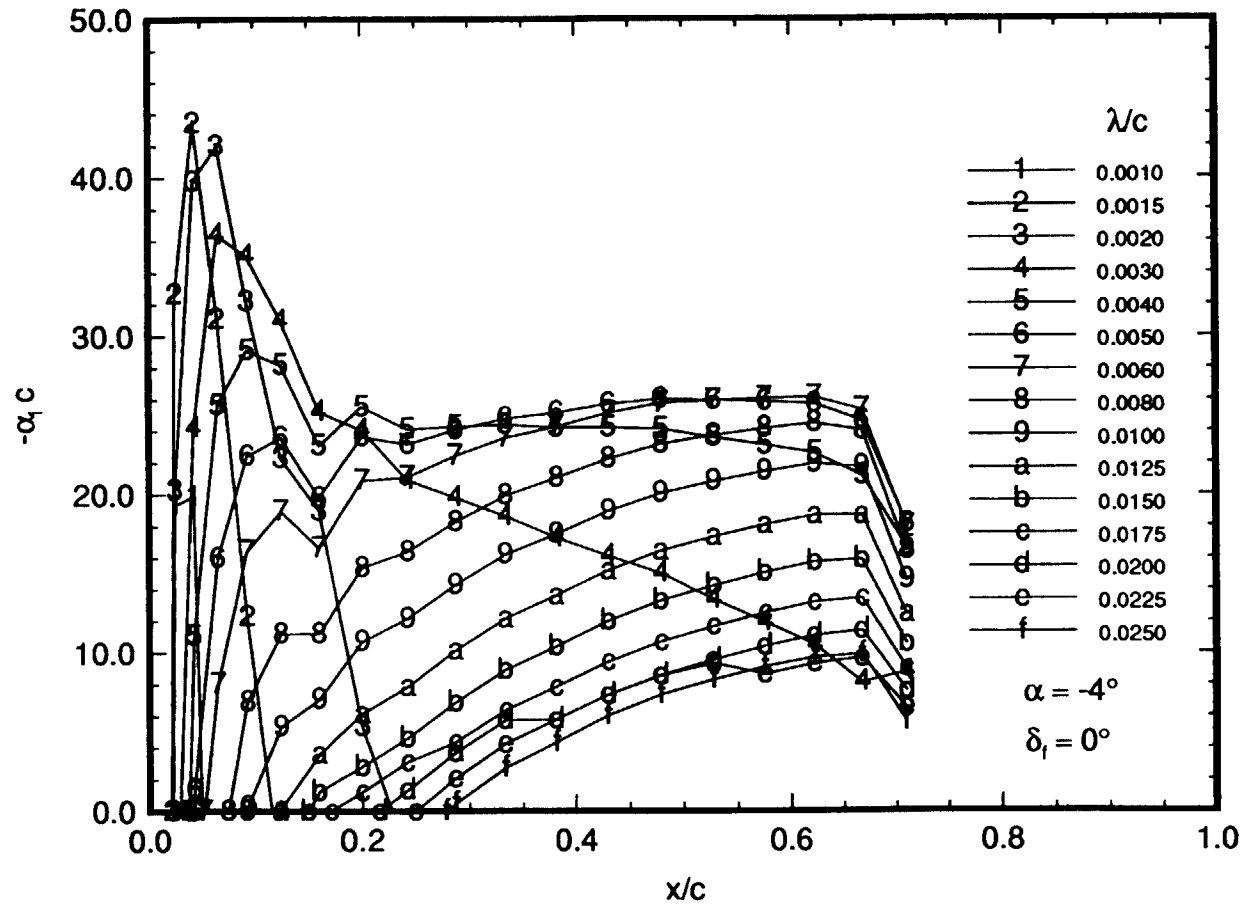


Figure 20. Local Spatial Growth Rates for Stationary Crossflow Vortices at $\alpha = -4^\circ$ and $\delta_1 = 0^\circ$ in UWT, $R_c = 3.81 \times 10^6$.

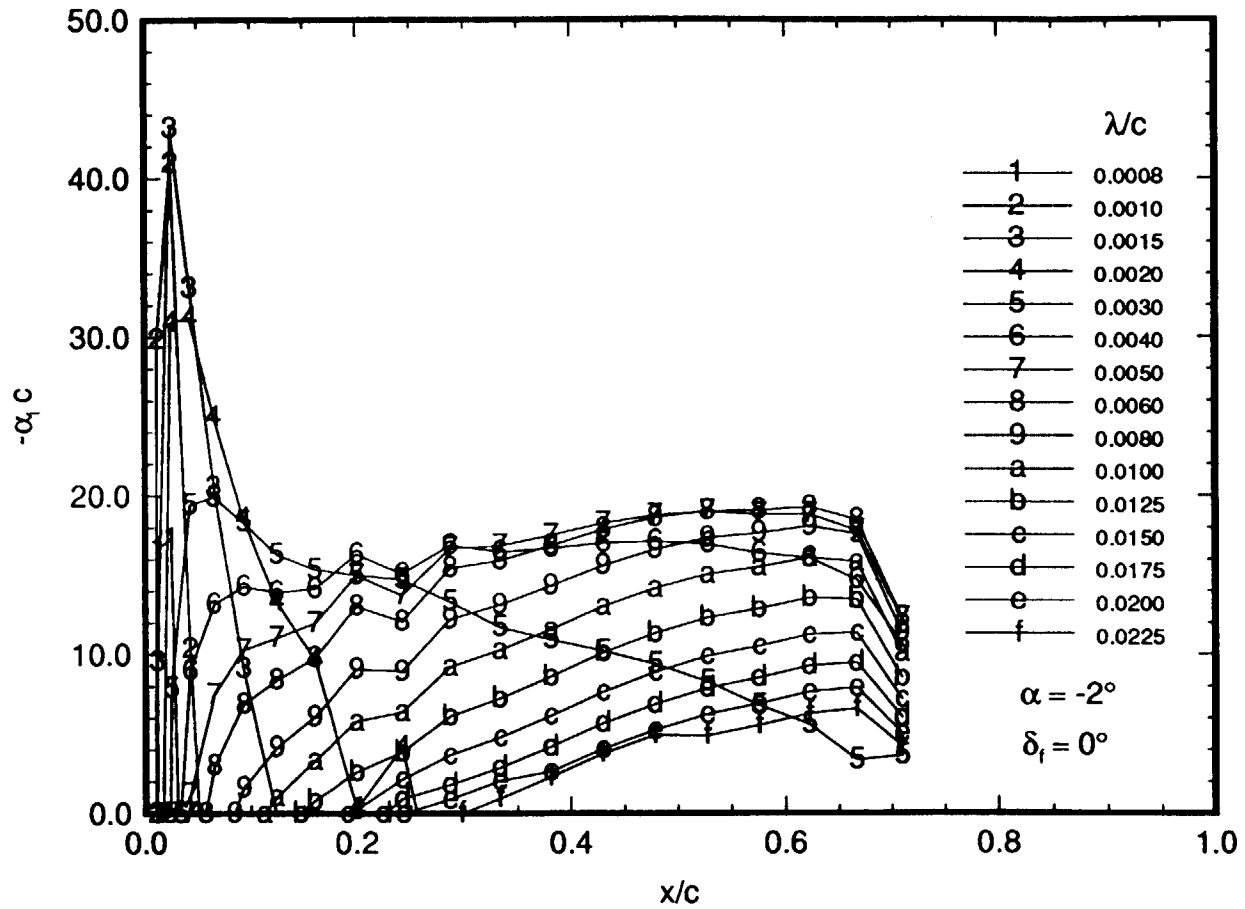


Figure 21. Local Spatial Growth Rates for Stationary Crossflow Vortices at $\alpha = -2^\circ$ and $\delta_f = 0^\circ$ in UWT, $R_c = 3.81 \times 10^6$.

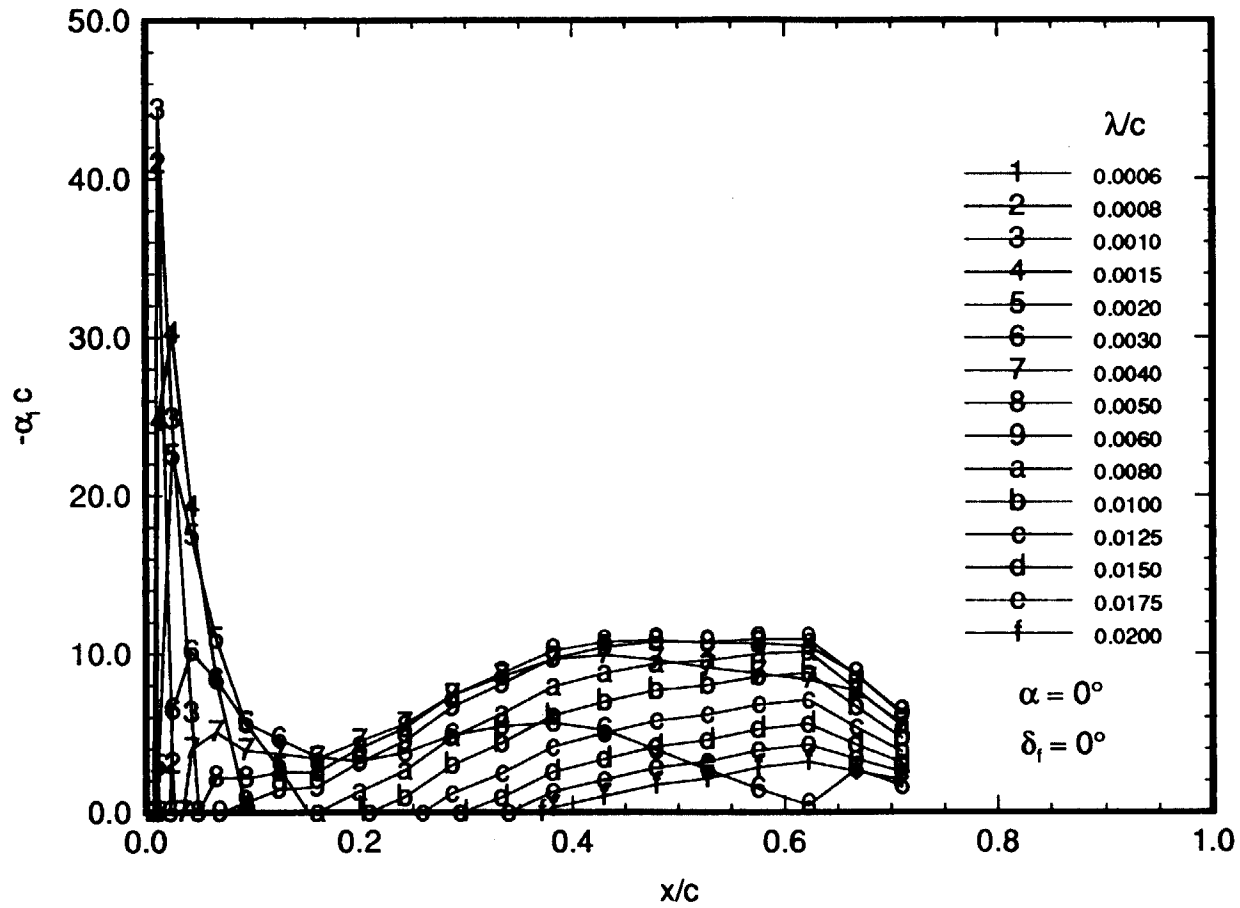


Figure 22. Local Spatial Growth Rates for Stationary Crossflow Vortices at $\alpha = 0^\circ$ and $\delta_f = 0^\circ$ in UWT, $R_c = 3.81 \times 10^6$.

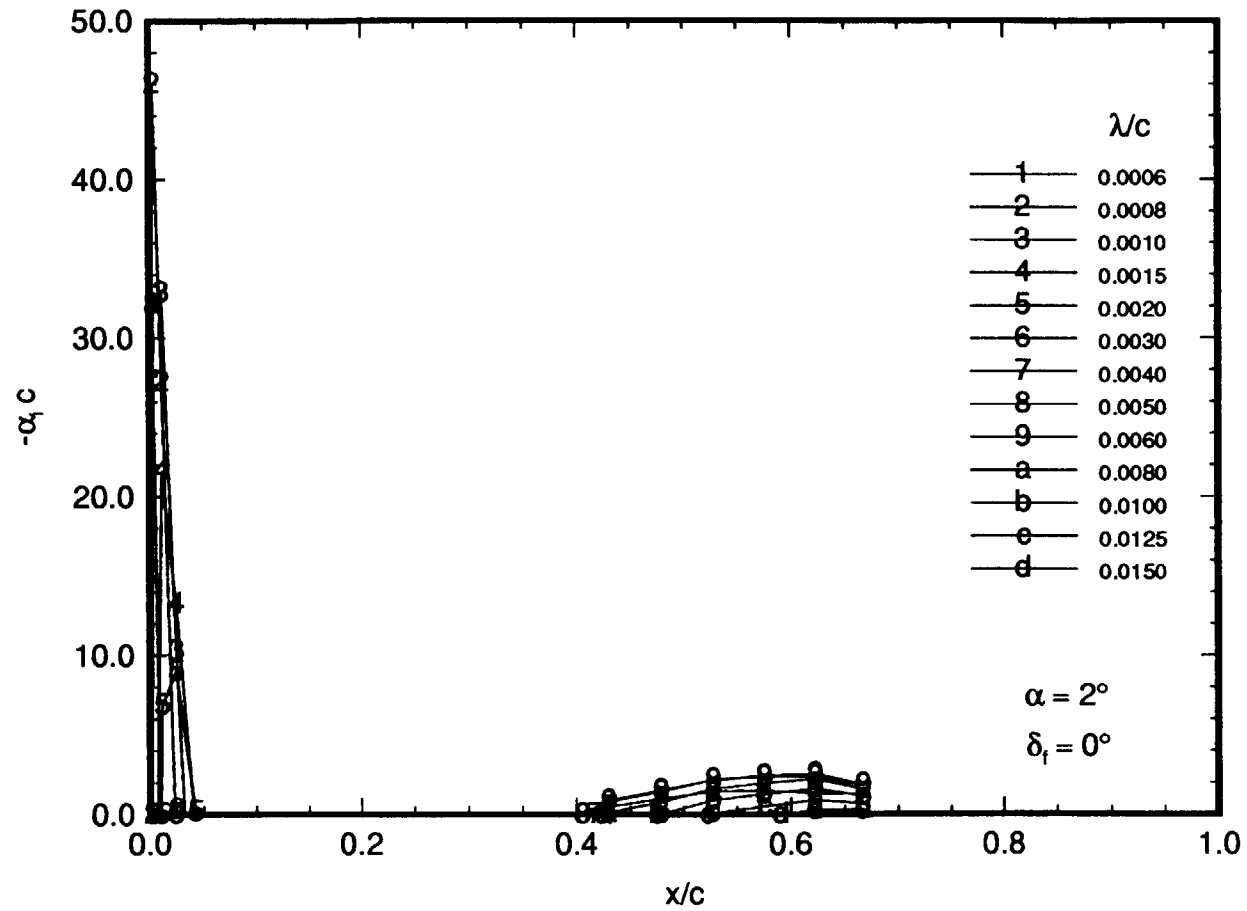


Figure 23. Local Spatial Growth Rates for Stationary Crossflow Vortices at $\alpha = 2^\circ$ and $\delta_f = 0^\circ$ in UWT, $R_c = 3.81 \times 10^6$.

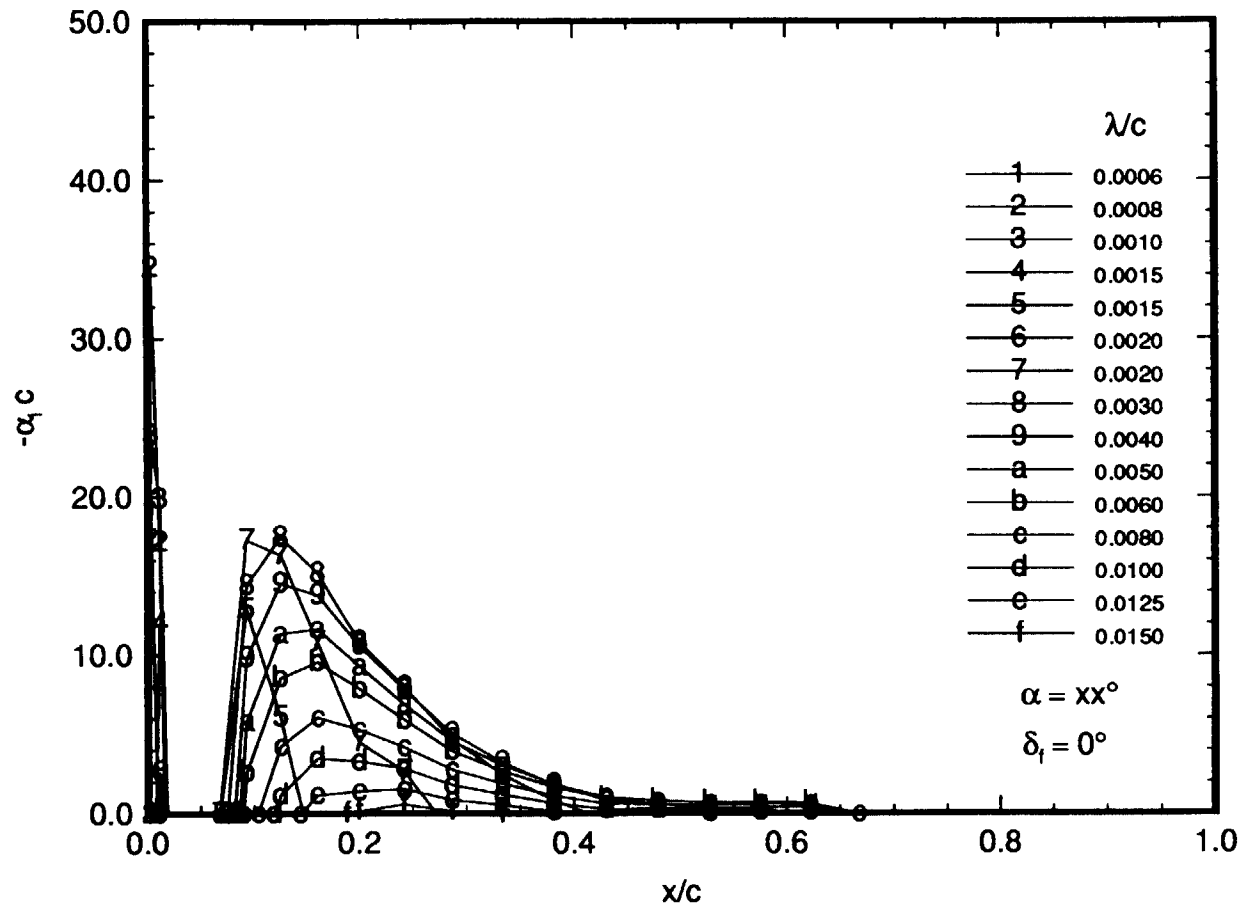


Figure 24. Local Spatial Growth Rates for Stationary Crossflow Vortices at $\alpha = 4^\circ$ and $\delta_f = 0^\circ$ in UWT, $R_c = 3.81 \times 10^6$.

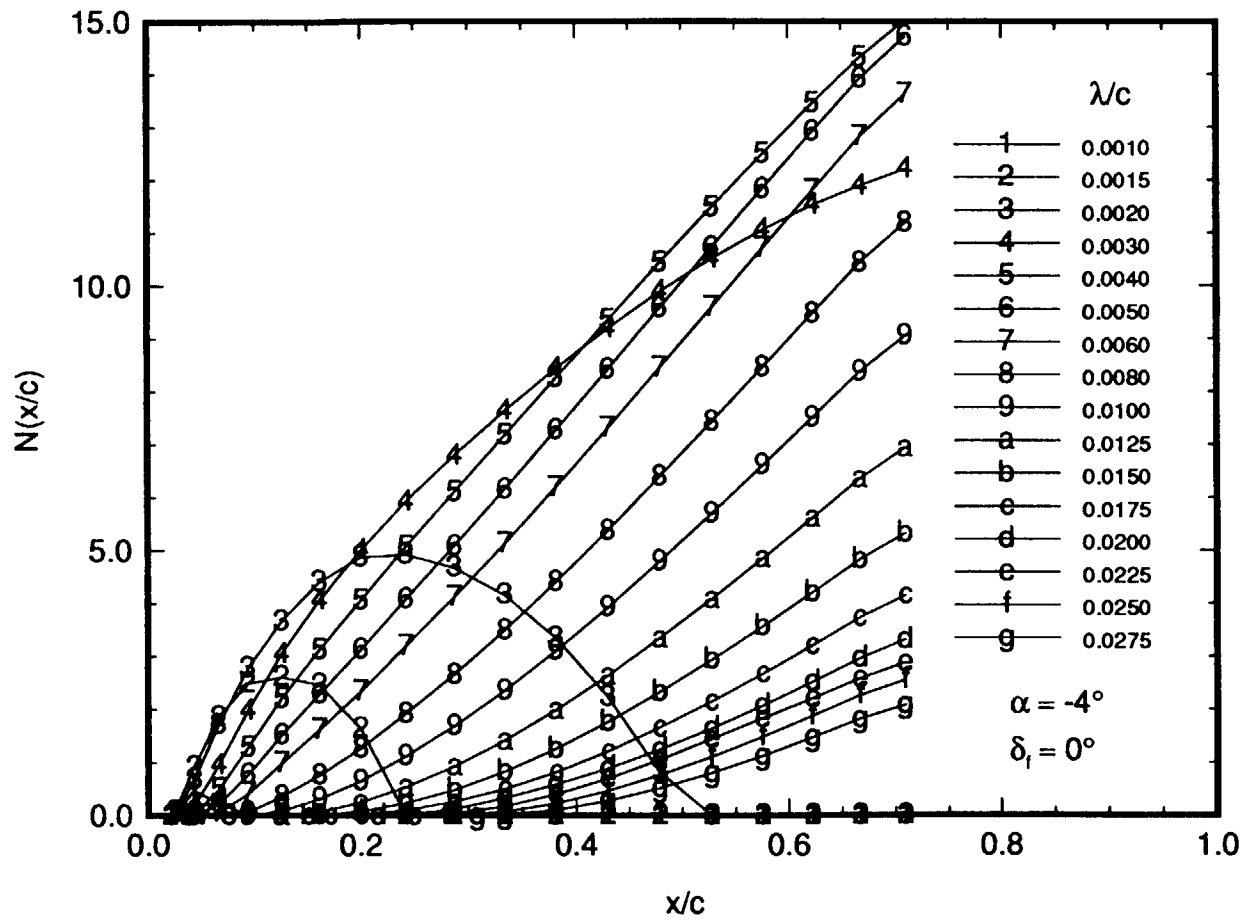


Figure 25. N-factors for Stationary Crossflow Vortices at $\alpha = -4^\circ$ and $\delta_f = 0^\circ$ in UWT, $R_c = 3.81 \times 10^6$.

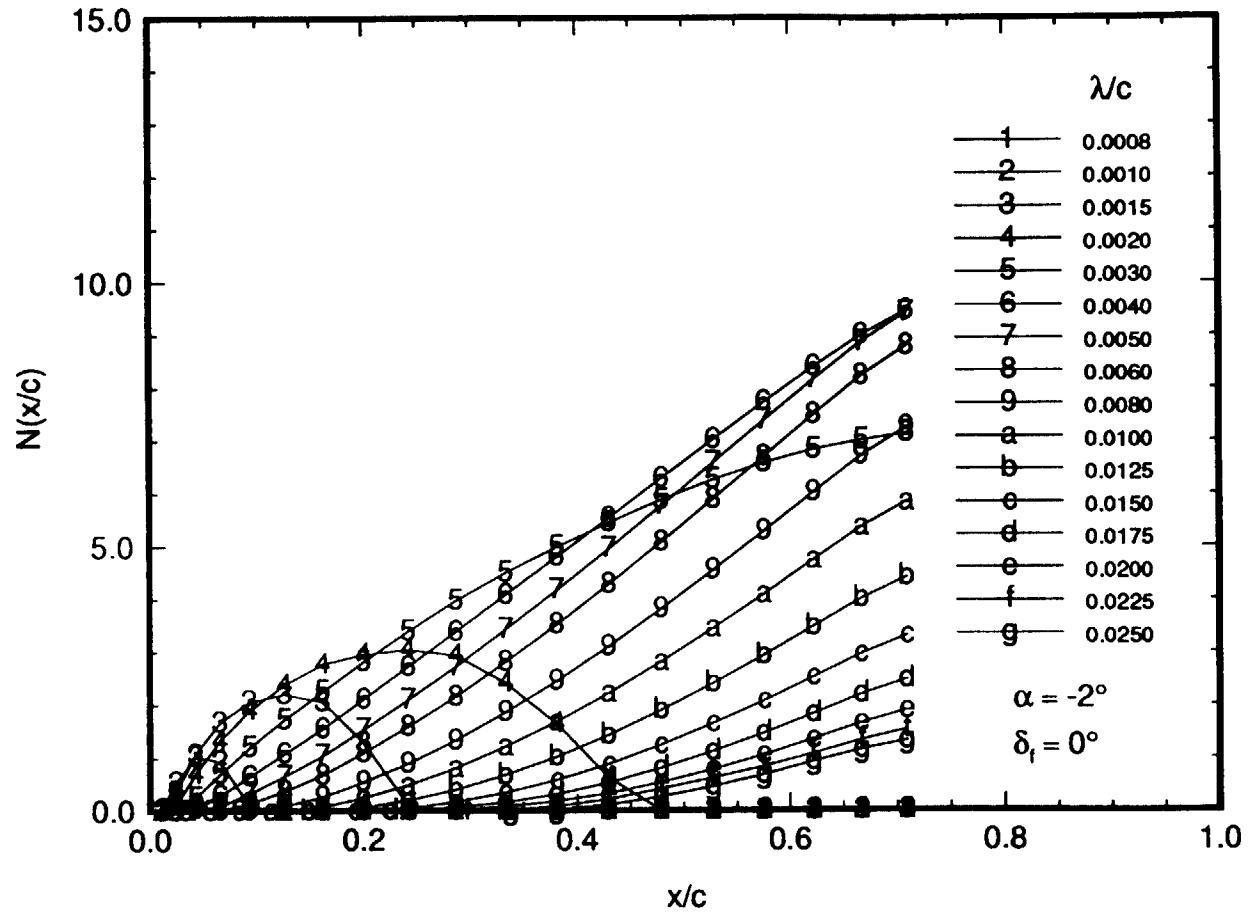


Figure 26. N-factors for Stationary Crossflow Vortices at $\alpha = -2^\circ$ and $\delta_f = 0^\circ$ in UWT, $R_c = 3.81 \times 10^6$.

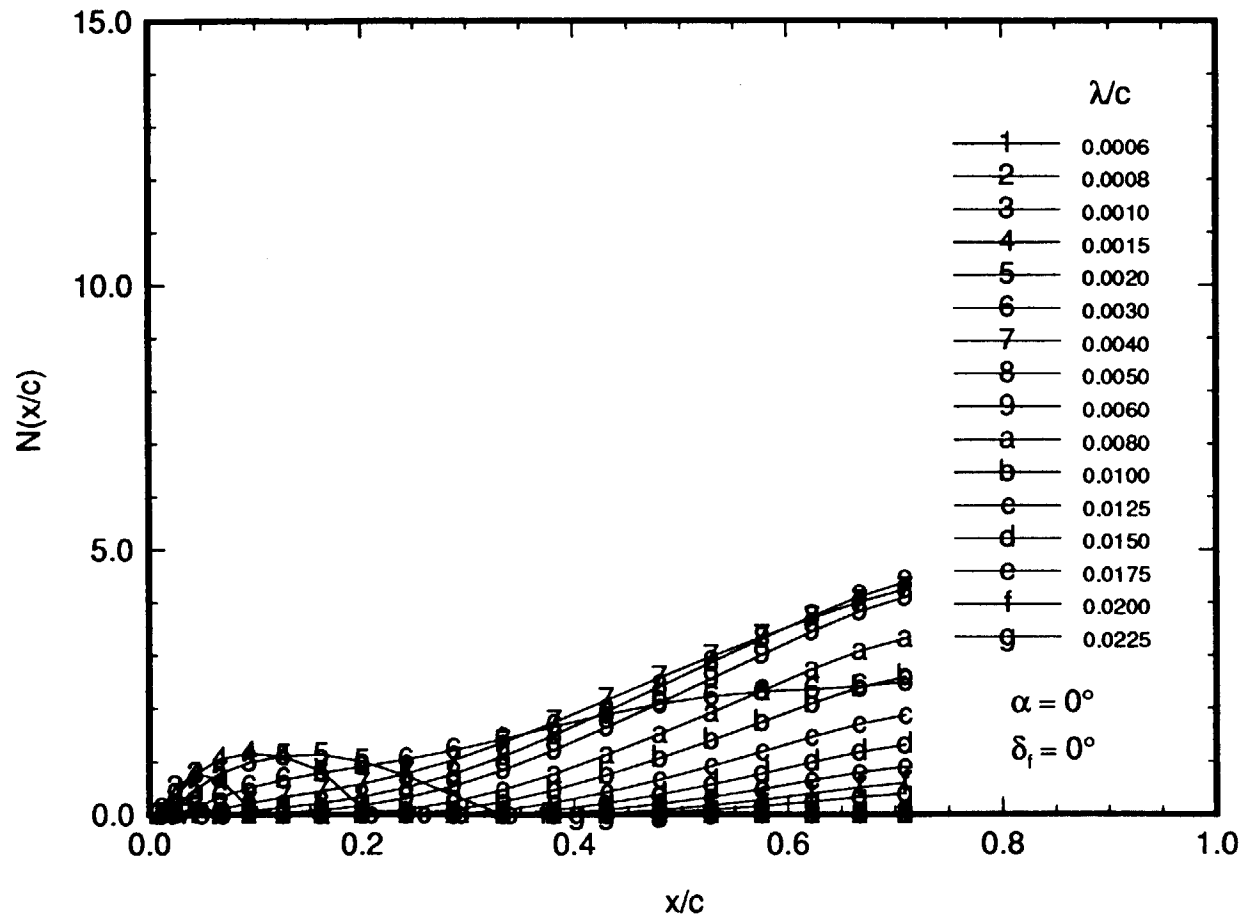


Figure 27. N-factors for Stationary Crossflow Vortices at $\alpha = 0^\circ$ and $\delta_f = 0^\circ$ in UWT, $R_c = 3.81 \times 10^6$.

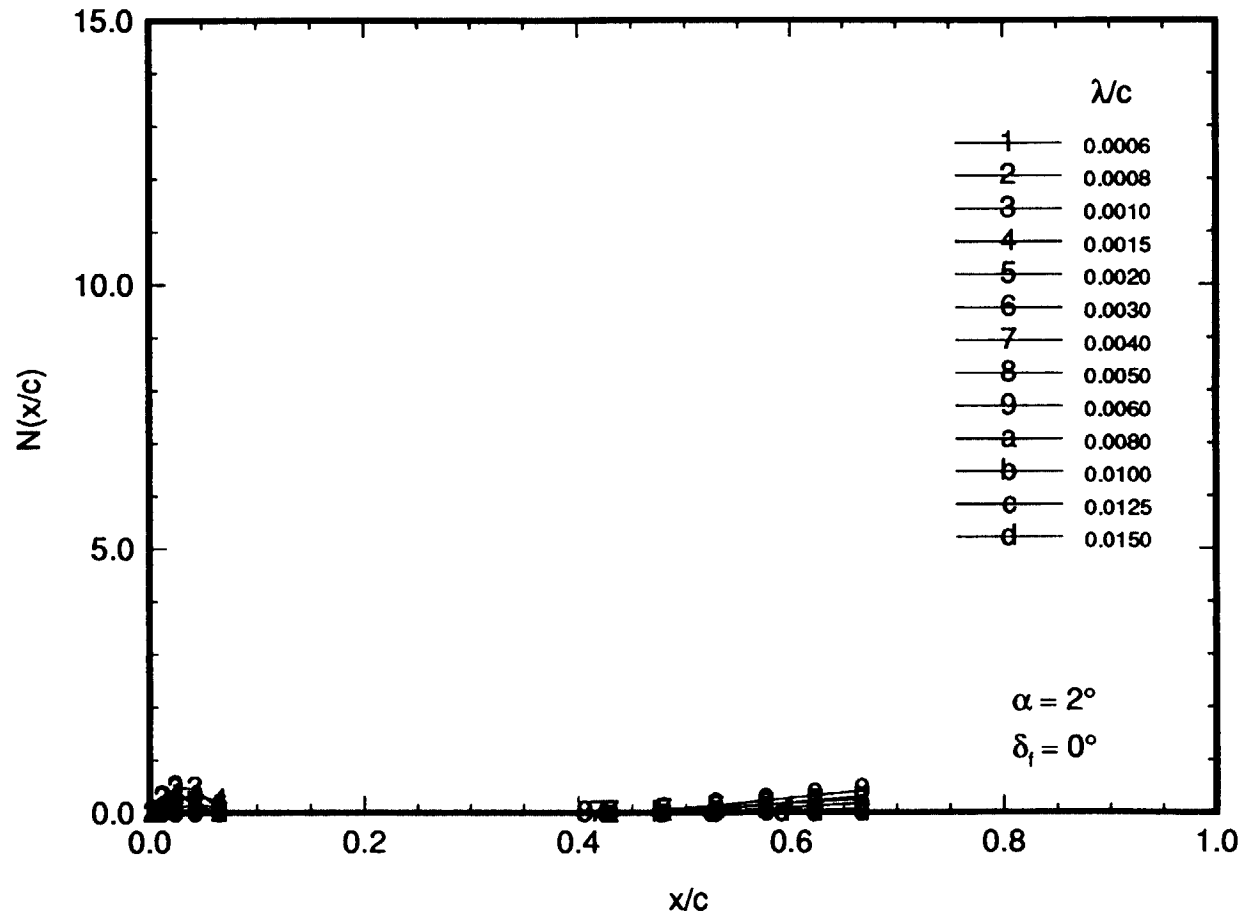


Figure 28. N-factors for Stationary Crossflow Vortices at $\alpha = 2^\circ$ and $\delta_f = 0^\circ$ in UWT, $R_c = 3.81 \times 10^6$.

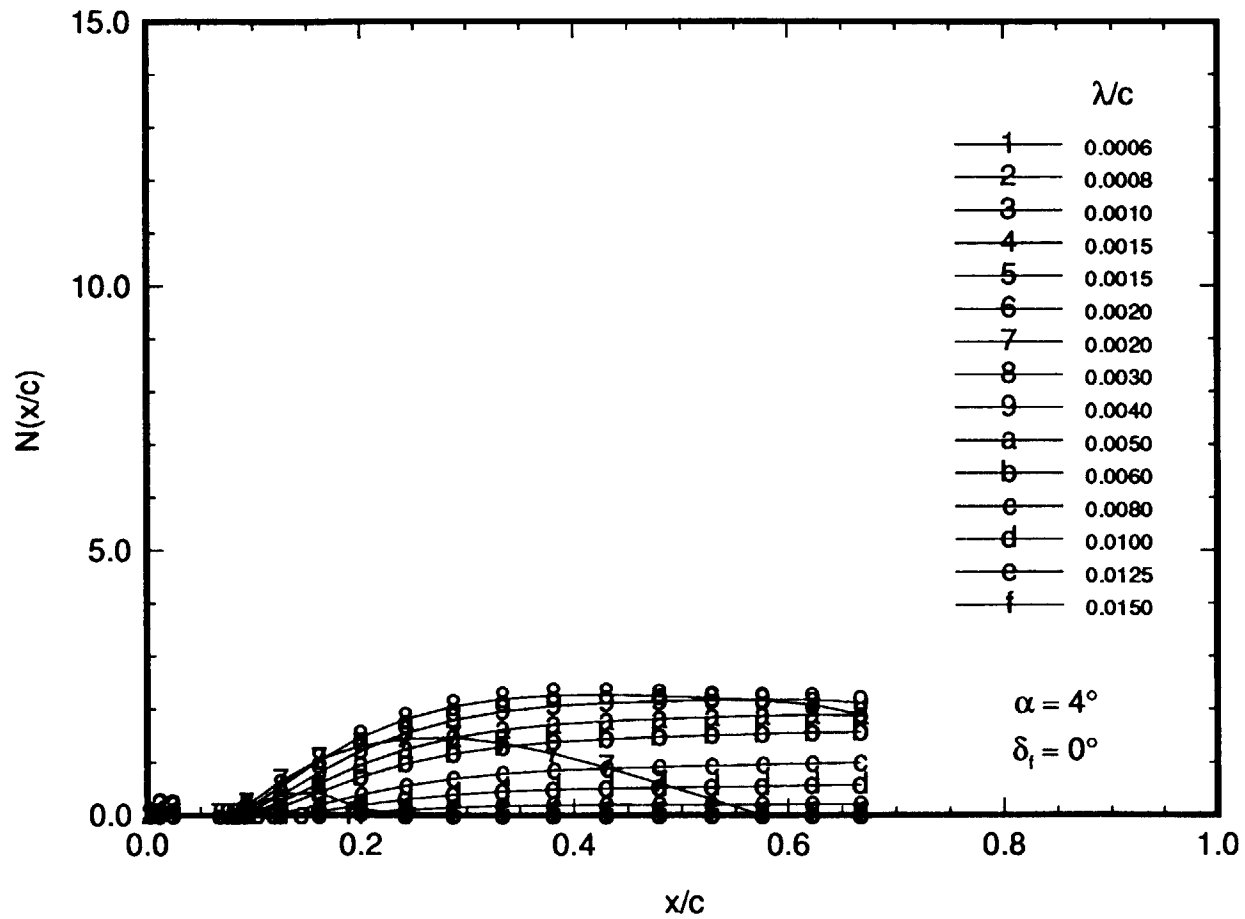


Figure 29. N-factors for Stationary Crossflow Vortices at $\alpha = 4^\circ$ and $\delta_f = 0^\circ$ in UWT, $R_c = 3.81 \times 10^6$.

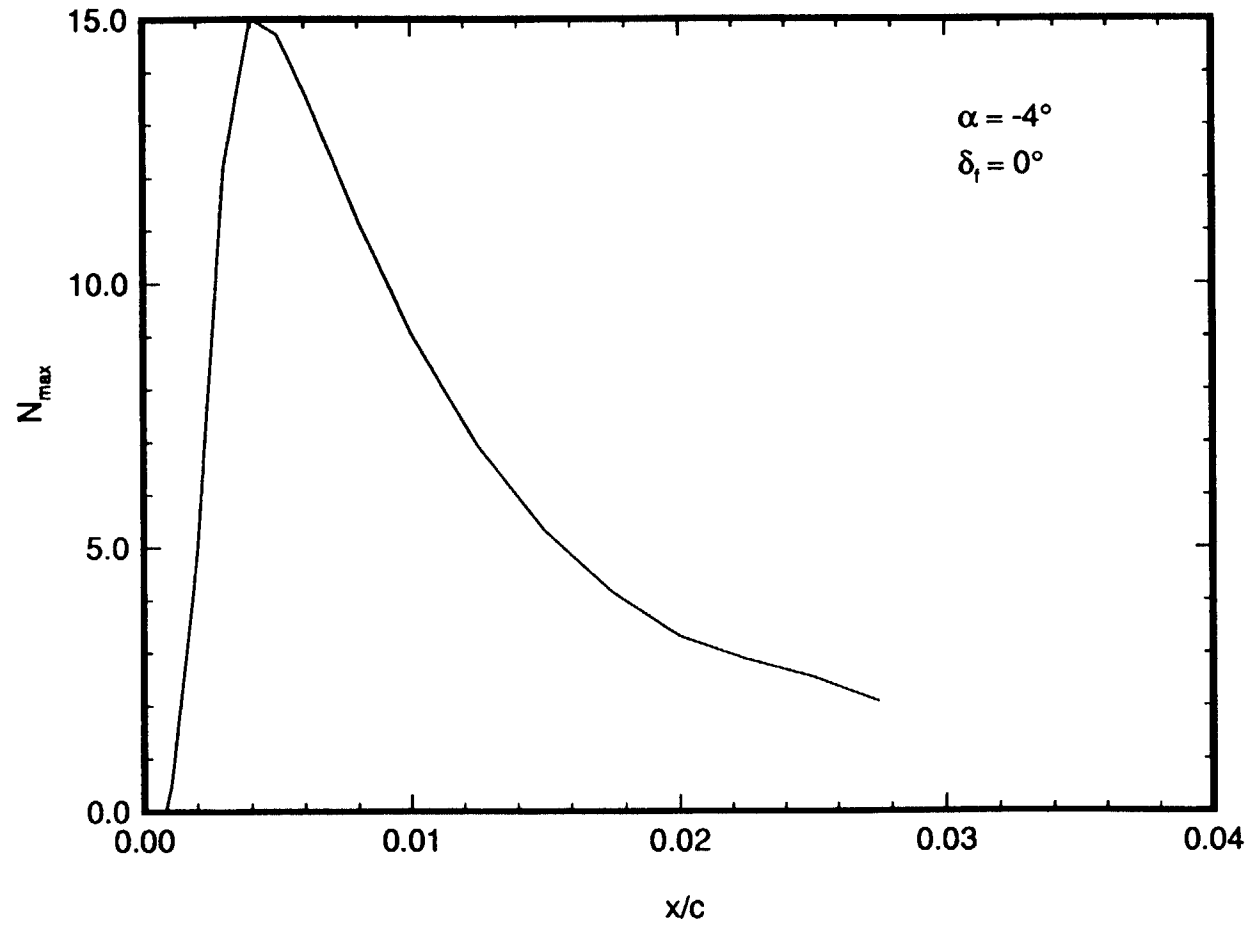


Figure 30. Maximum N-factors for Stationary Crossflow Vortices at $\alpha = -4^\circ$ and $\delta_f = 0^\circ$ in UWT, $R_c = 3.81 \times 10^6$.

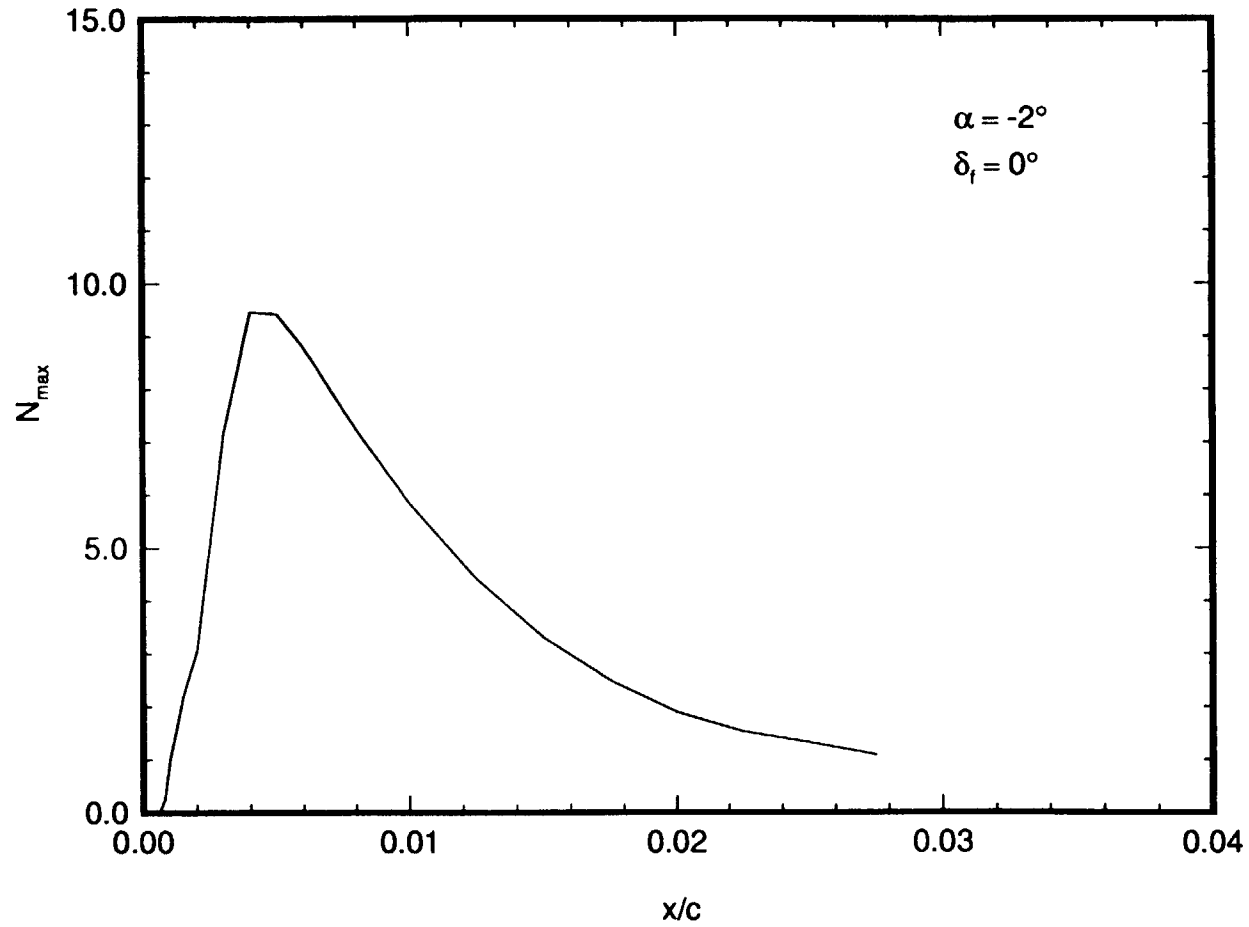


Figure 31. Maximum N-factors for Stationary Crossflow Vortices at $\alpha = -2^\circ$ and $\delta_f = 0^\circ$ in UWT, $R_c = 3.81 \times 10^6$.

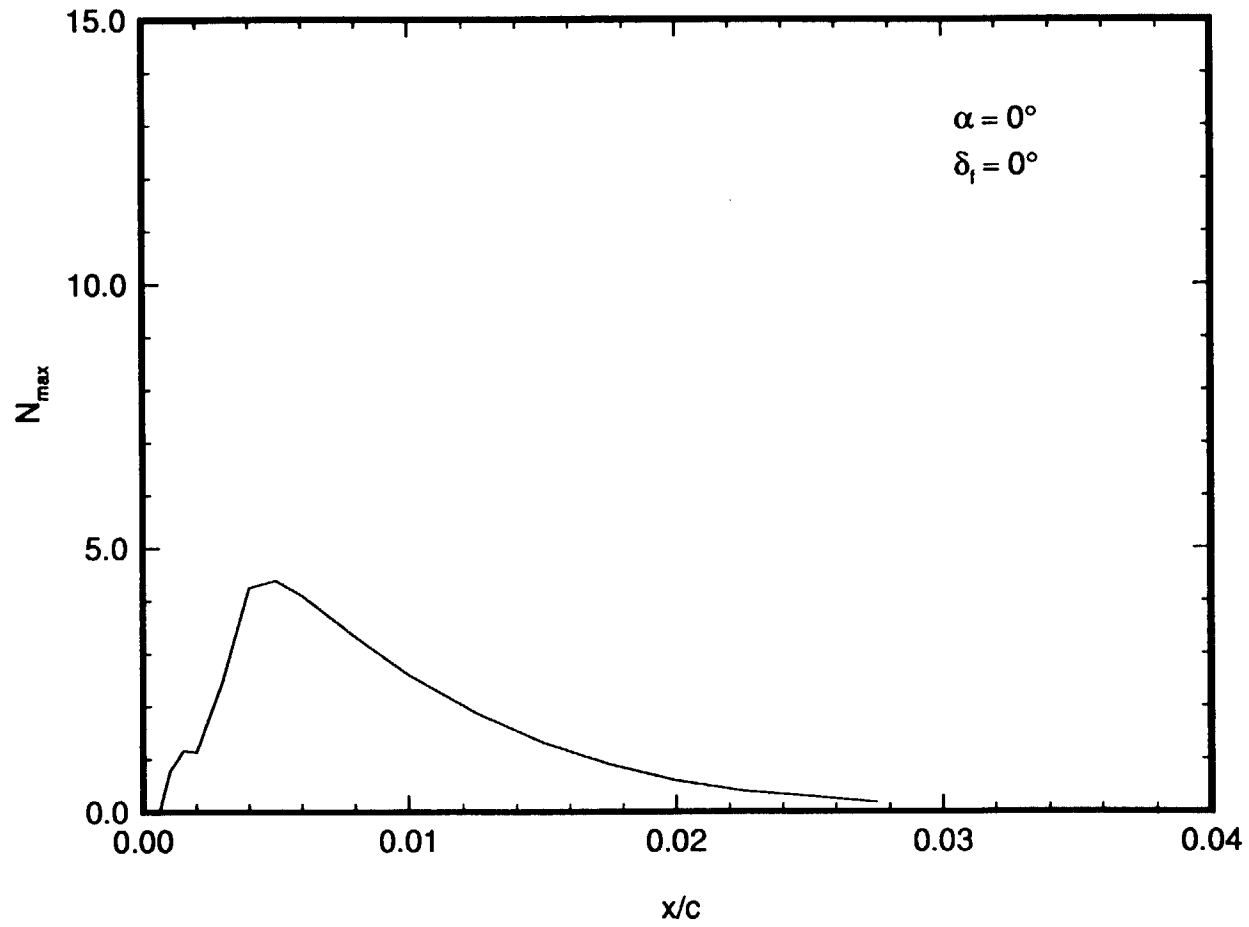


Figure 32. Maximum N-factors for Stationary Crossflow Vortices at $\alpha = 0^\circ$ and $\delta_f = 0^\circ$ in UWT, $R_c = 3.81 \times 10^6$.

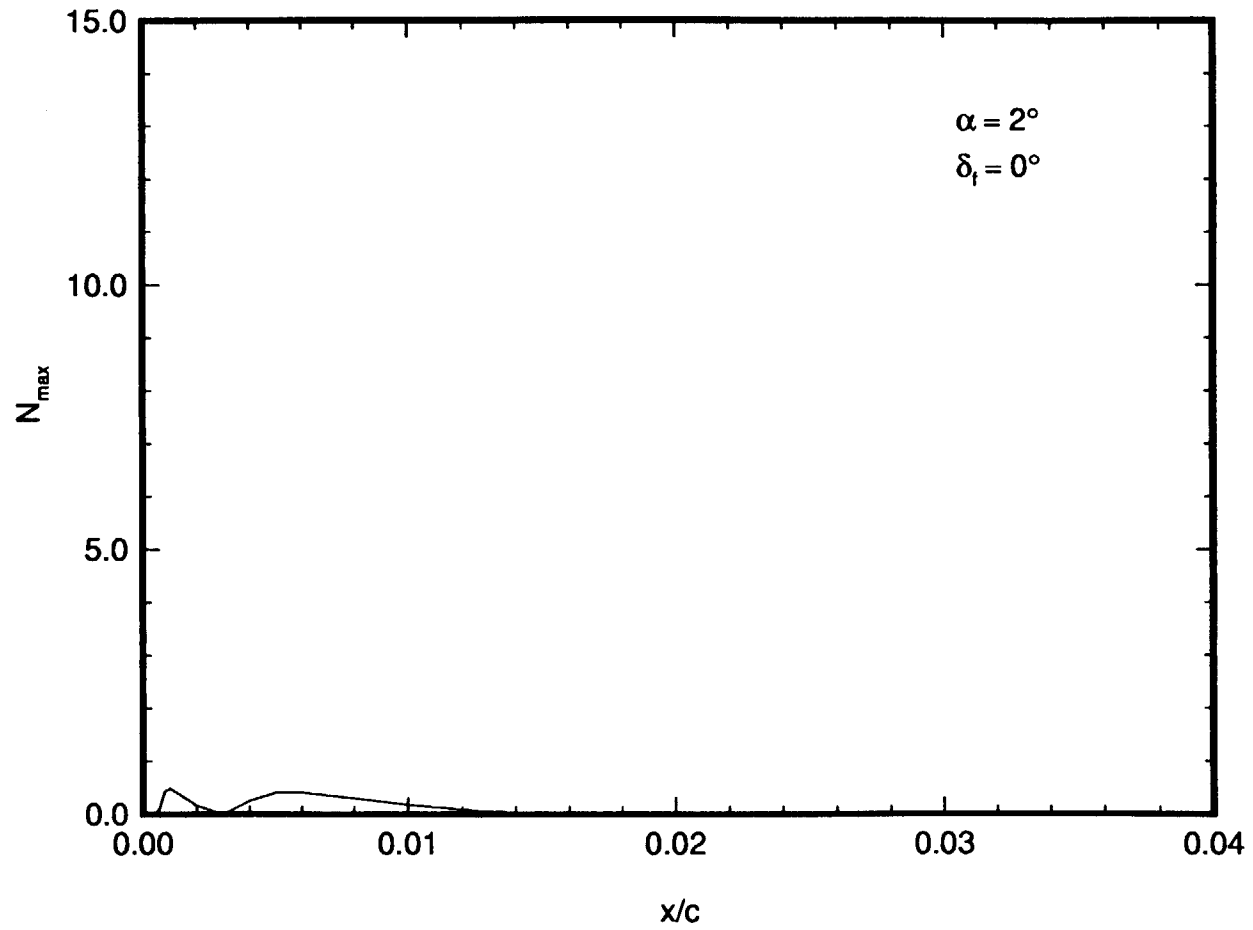


Figure 33. Maximum N-factors for Stationary Crossflow Vortices at $\alpha = 2^\circ$ and $\delta_f = 0^\circ$ in UWT, $R_c = 3.81 \times 10^6$.

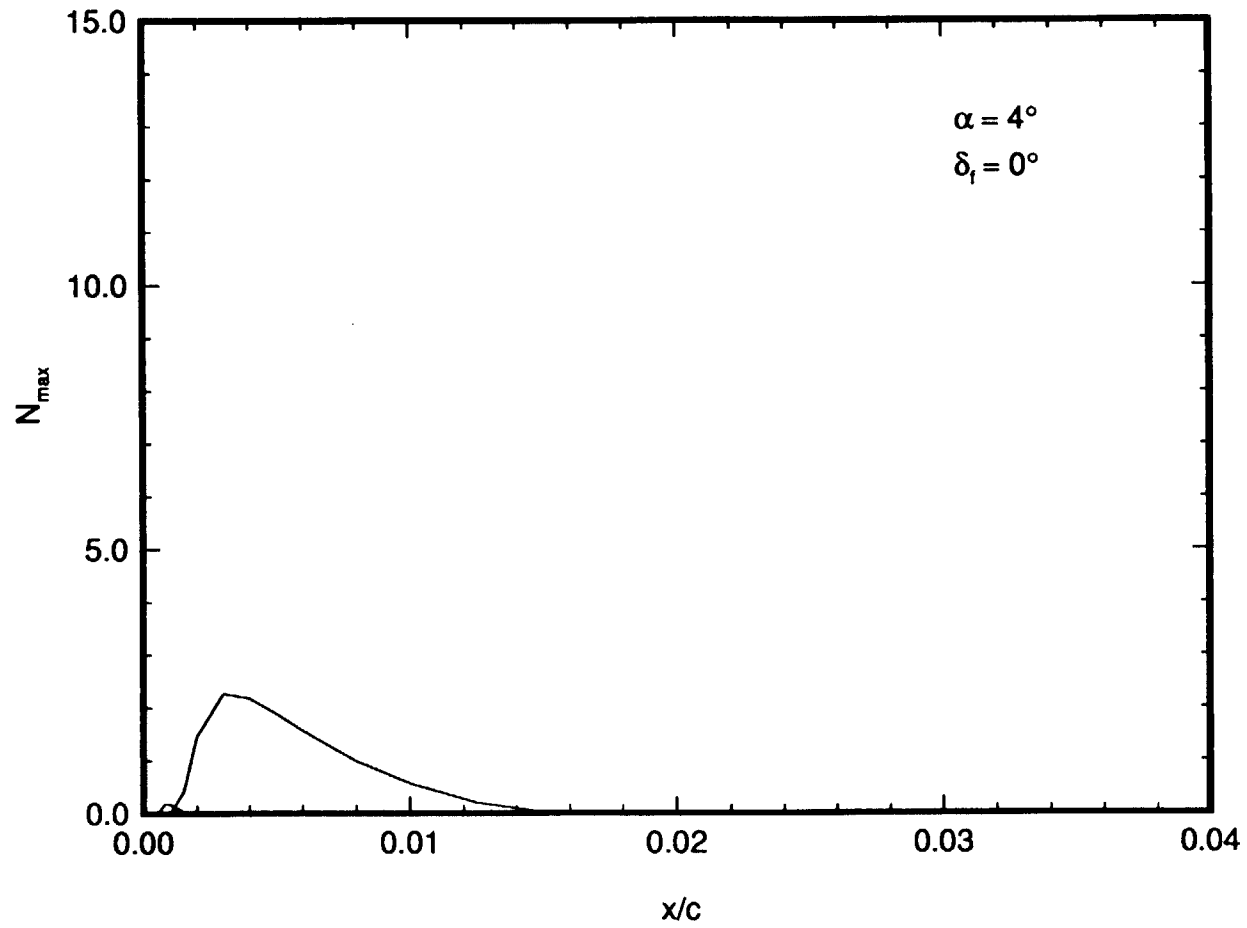


Figure 34. Maximum N-factors for Stationary Crossflow Vortices at $\alpha = 4^\circ$ and $\delta_f = 0^\circ$ in UWT, $R_c = 3.81 \times 10^6$.

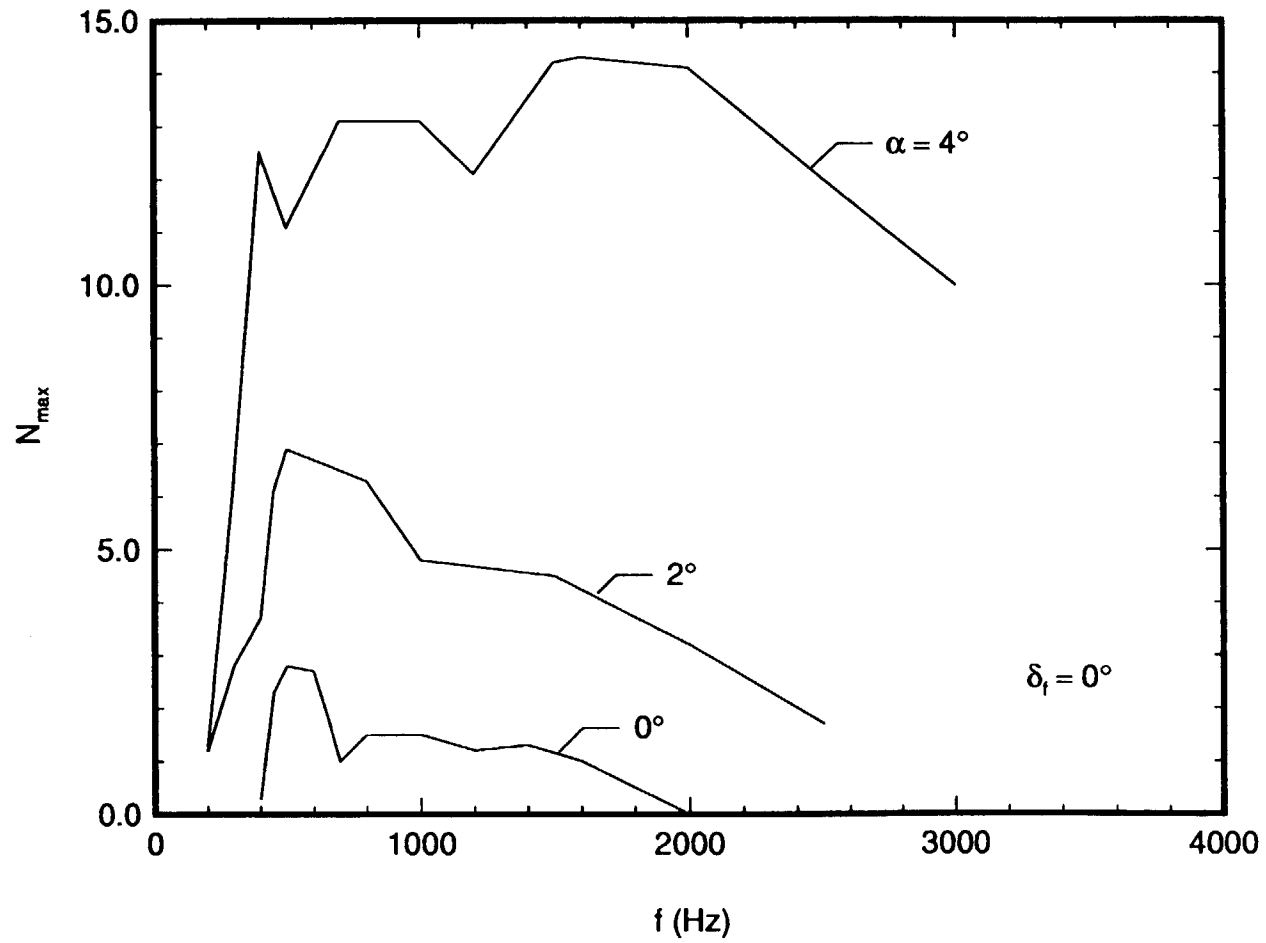


Figure 35. Maximum N-factors for Tollmien-Schlichting Waves for $\alpha = 0, 2,$ and 4° and $\delta_f = 0^\circ$ in UWT, $R_c = 3.81 \times 10^6$.

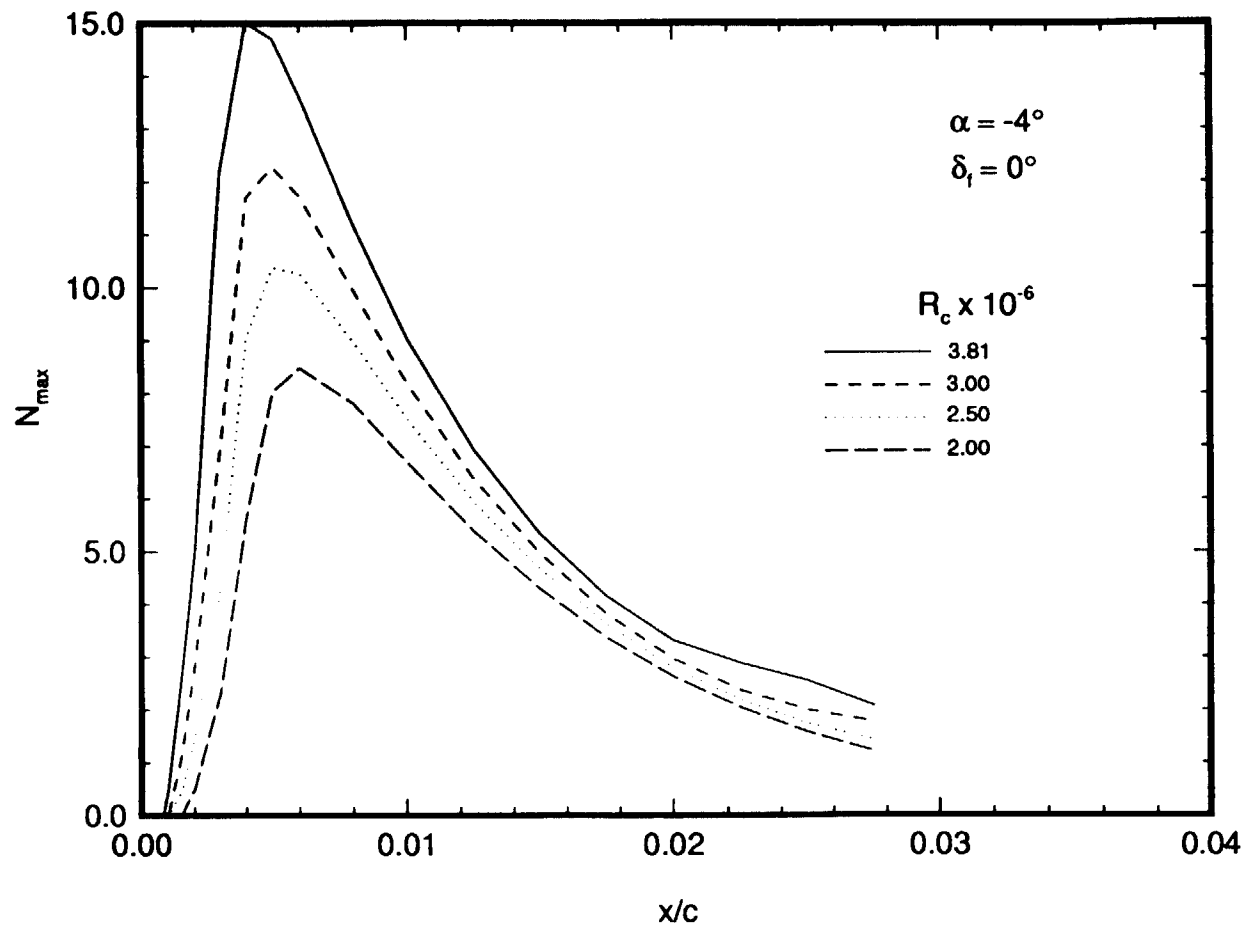


Figure 36. Maximum N-factors for Stationary Crossflow Vortices at $\alpha = -4^\circ$ and $\delta_f = 0^\circ$ in UWT for a Range of Reynolds Numbers.

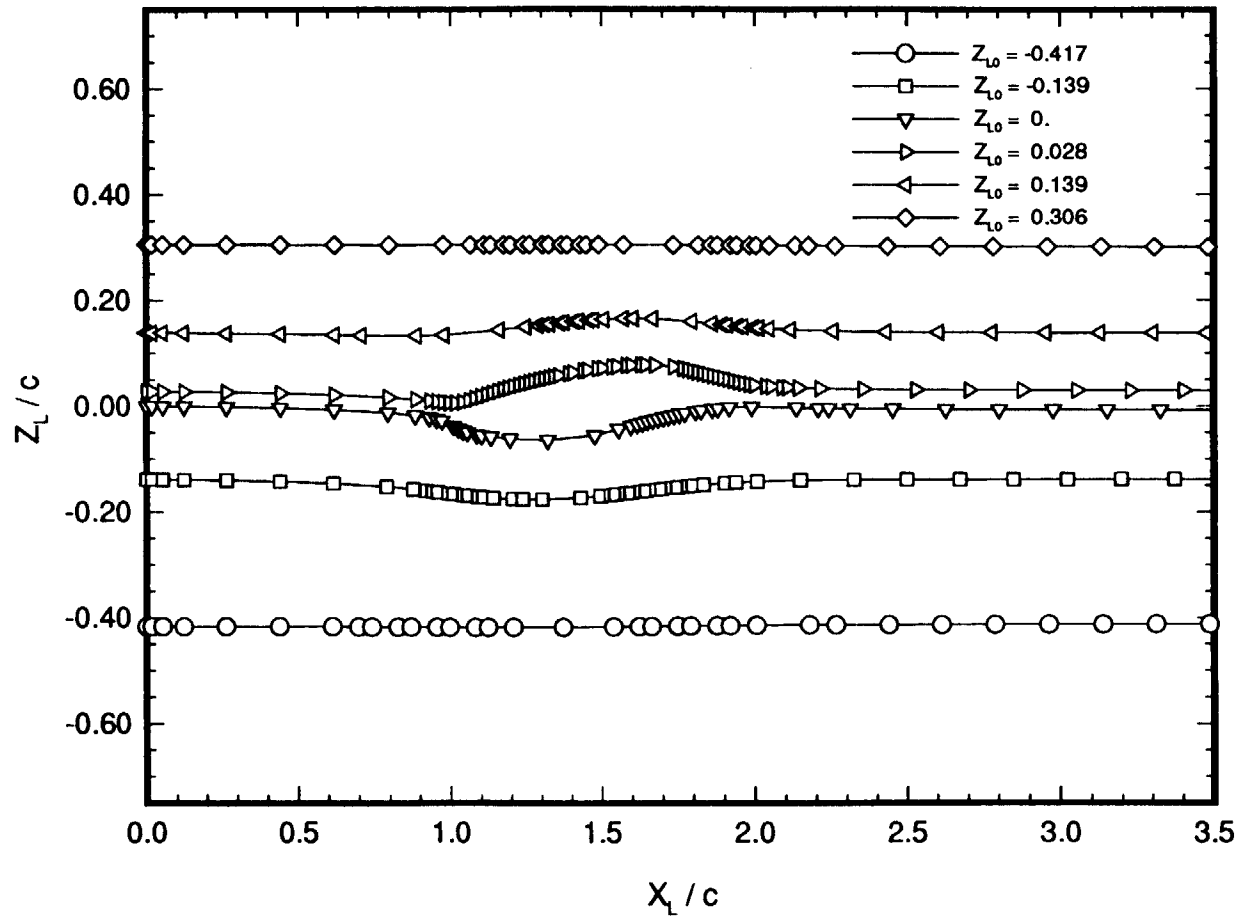


Figure 37. Streamline Traces of Wind-Tunnel End Liner on X_L-Z_L Plane.

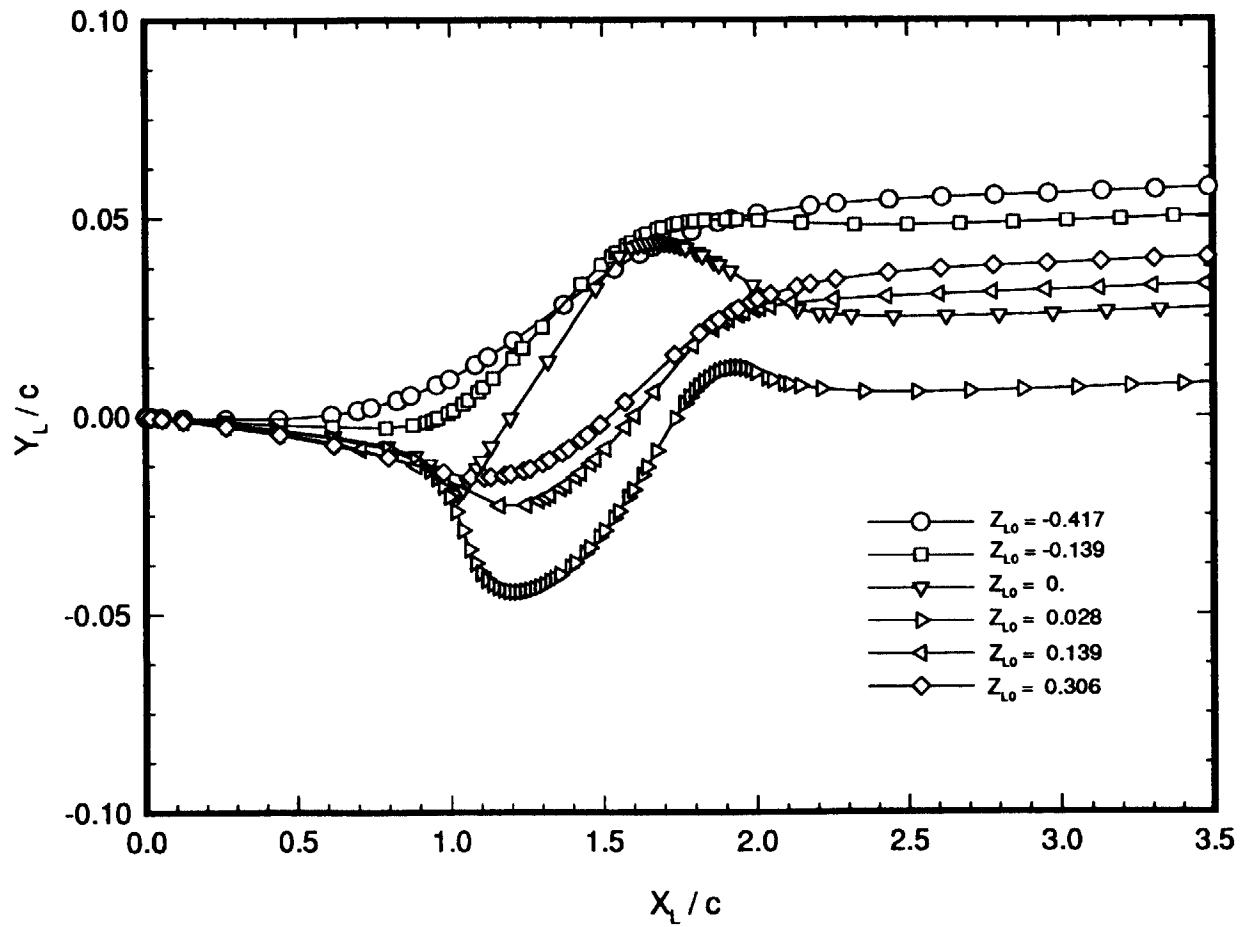


Figure 38. Lateral Deflections of End-Liner Surface at Various Distances from Wing-Chord Plane.

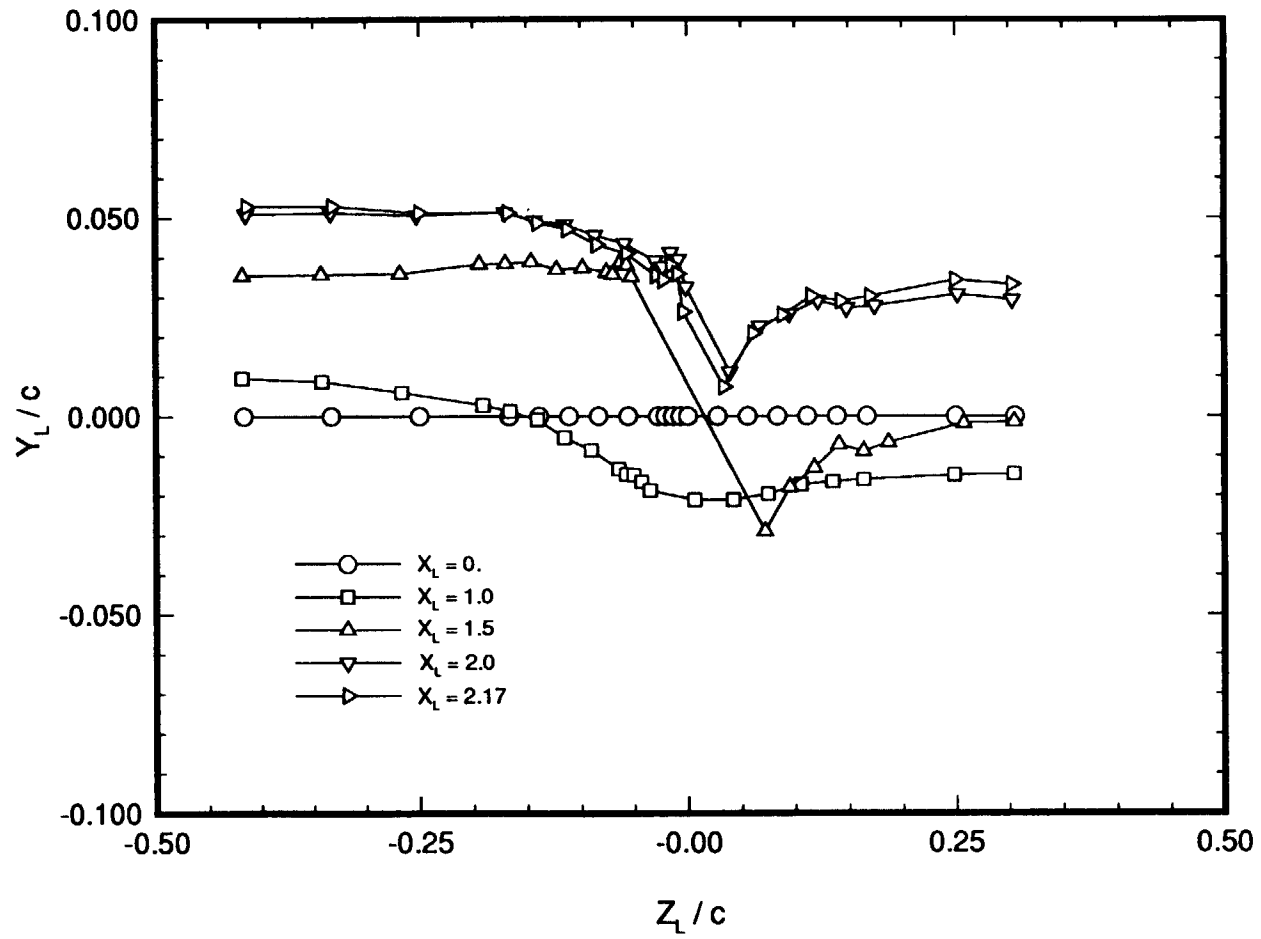


Figure 39. End-Liner Contours in the Y_L - Z_L Plane at Various Longitudinal Positions.

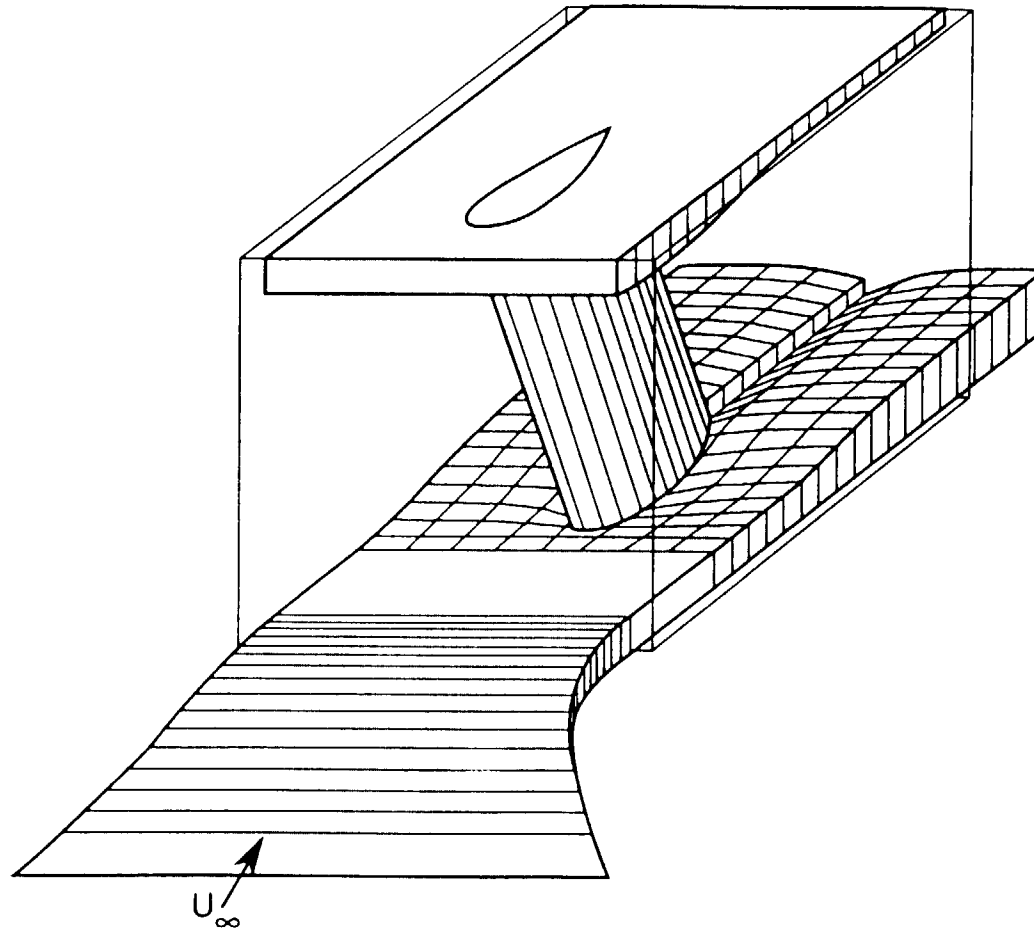


Figure 40. Diagram of Wind-Tunnel Test Section with Swept-Wing Model and End Liners Installed.

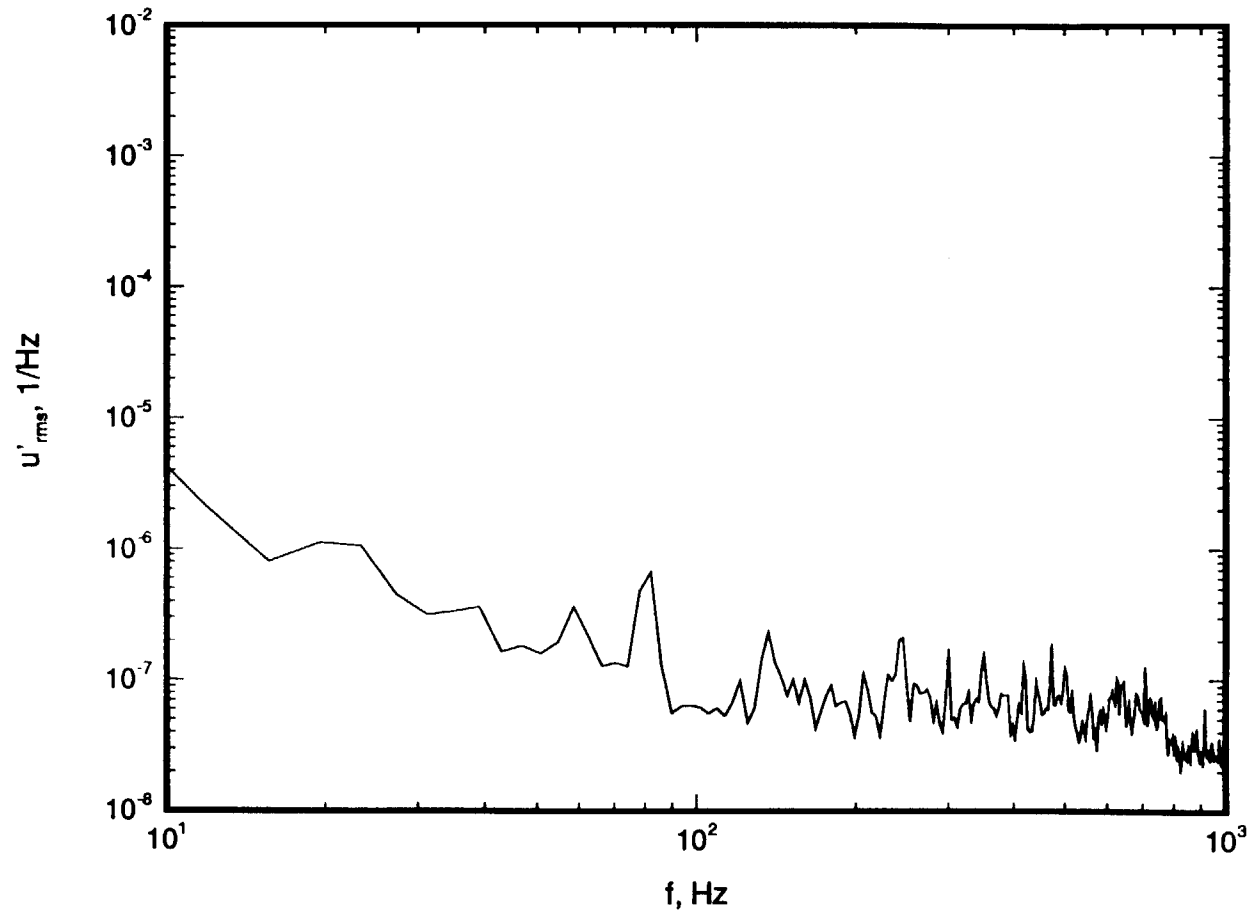


Figure 41. Freestream Velocity Spectrum for $R_c = 3.27 \times 10^6$.

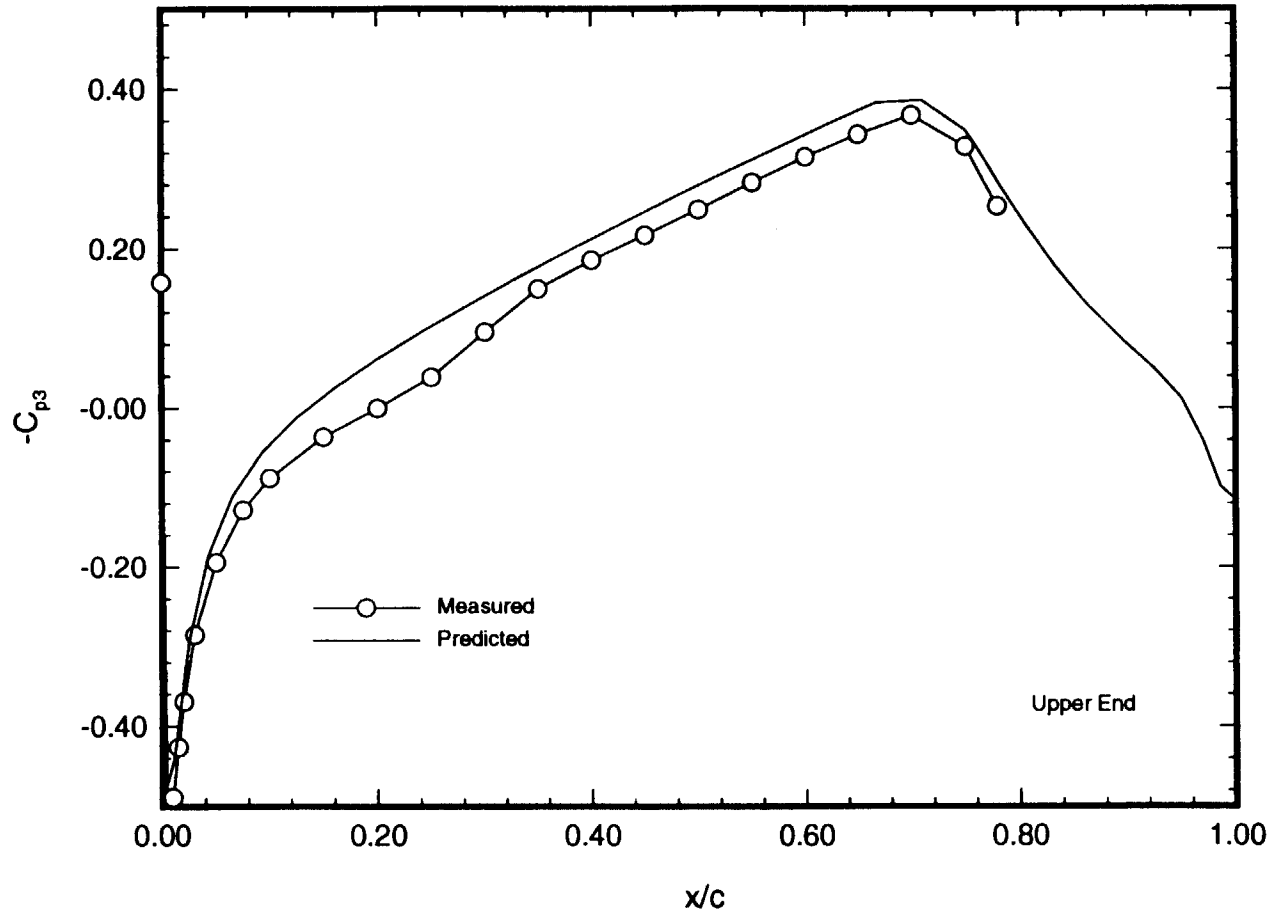


Figure 42. Comparison of Measured and Predicted Model Pressure Coefficients at the Upper End of the Model, $\alpha = -4^\circ$.

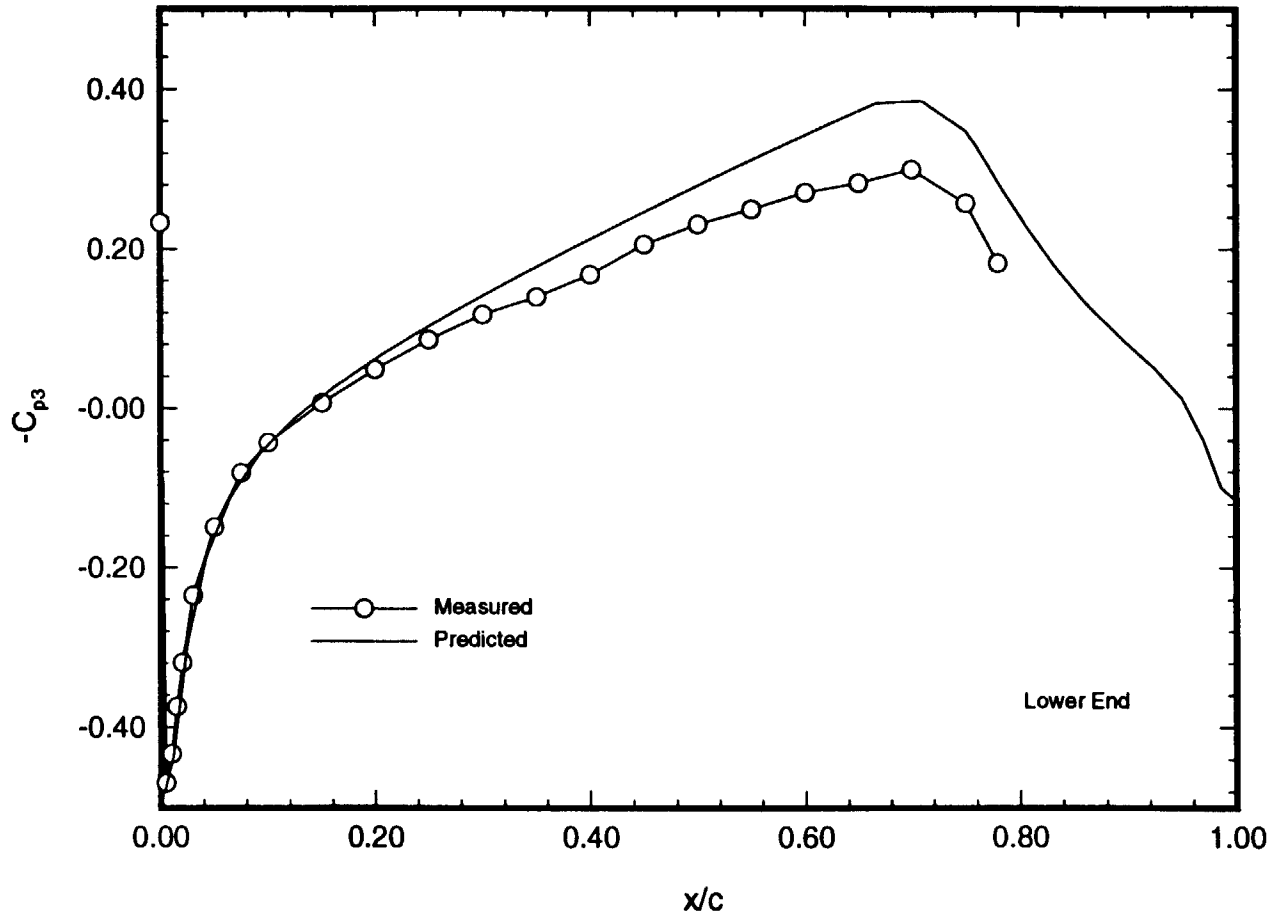


Figure 43. Comparison of Measured and Predicted Model Pressure Coefficients at the Lower End of the Model, $\alpha = -4^\circ$.

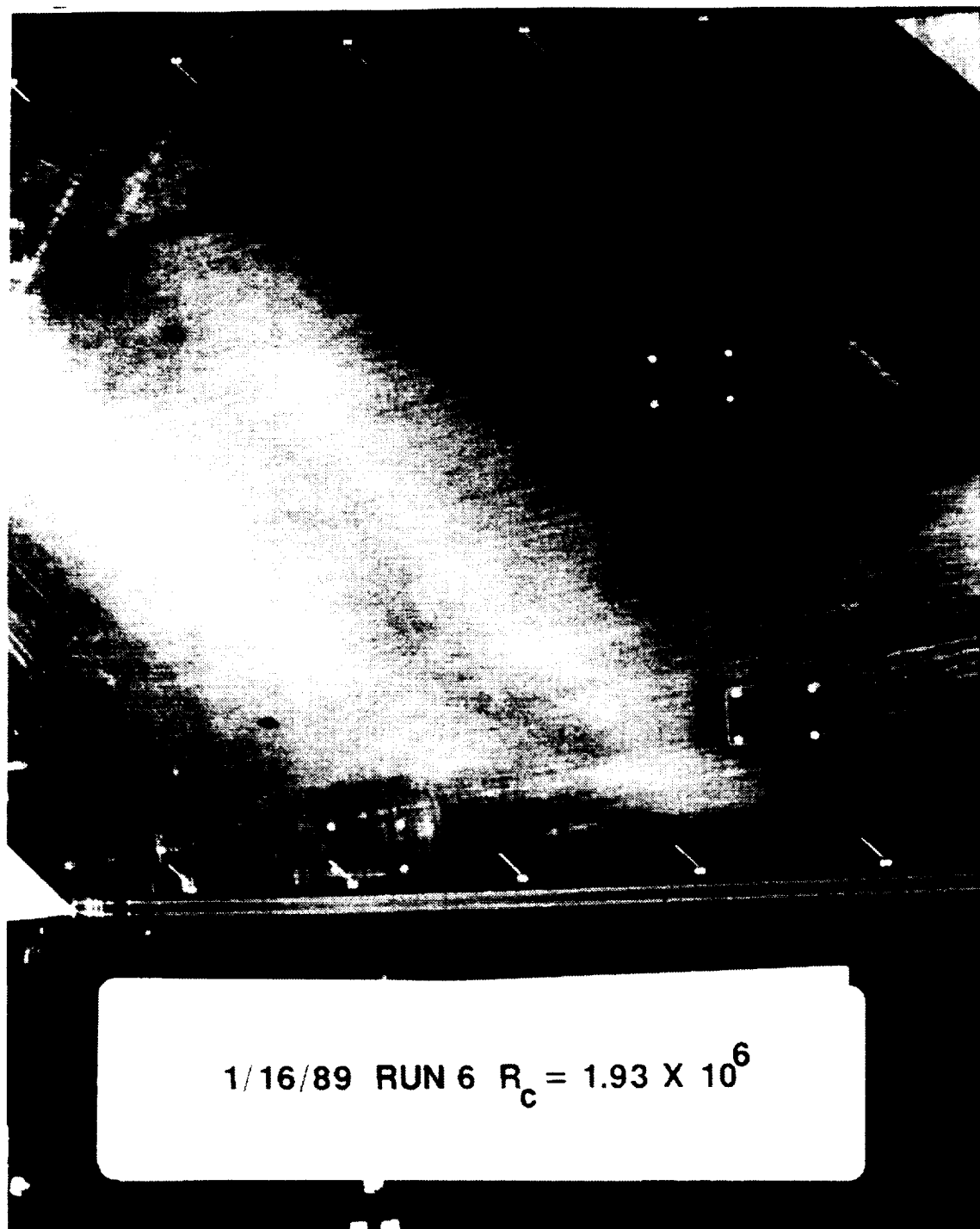


Figure 44. Naphthalene Flow Visualization, $\alpha = -4^\circ$, $R_c = 1.93 \times 10^6$.

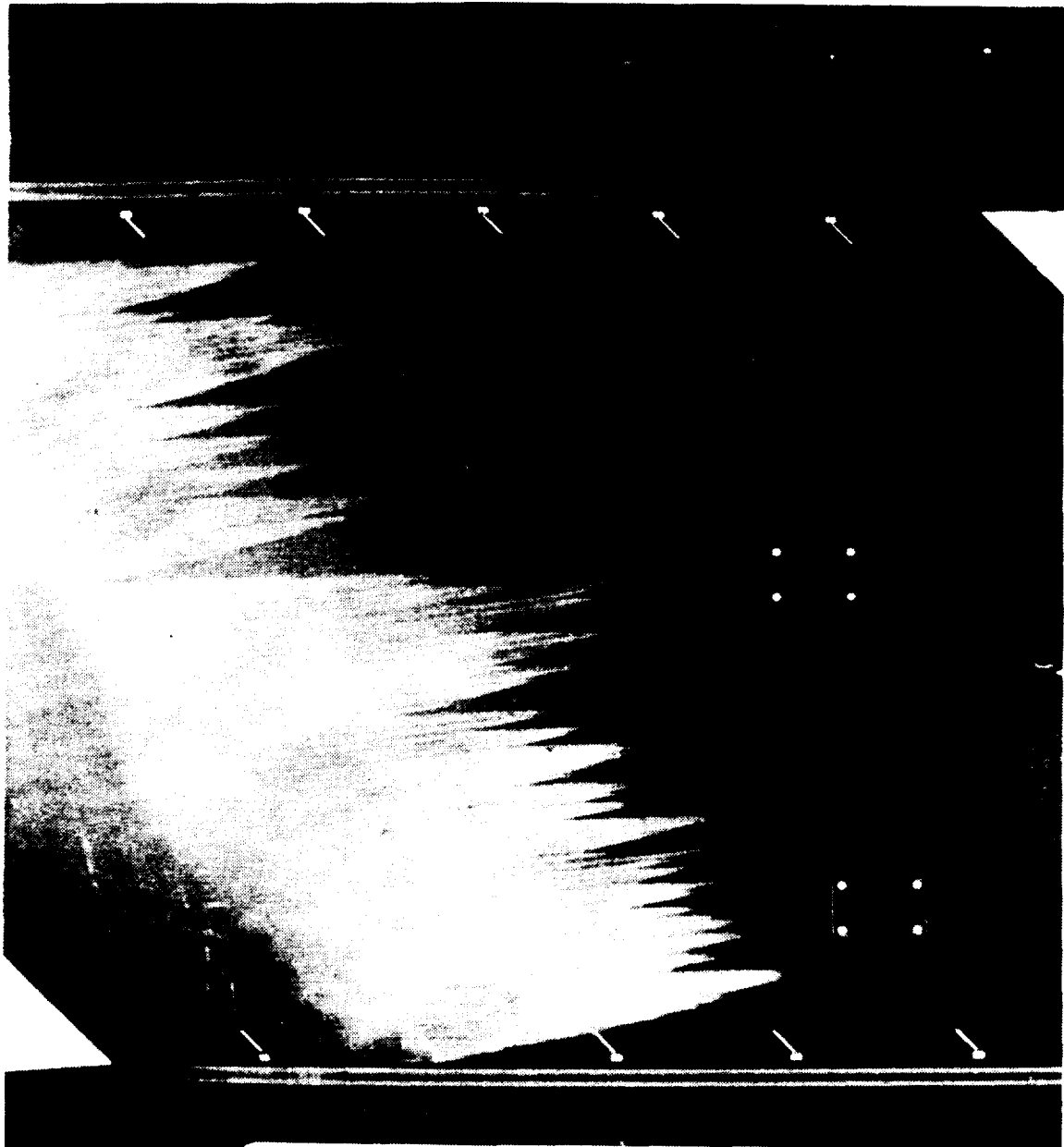


Figure 45. Naphthalene Flow Visualization, $\alpha = -4^\circ$, $R_c = 2.19 \times 10^6$.



1/16/89 RUN 11 $R_c = 2.40 \times 10^6$

Figure 46. Naphthalene Flow Visualization, $\alpha = -4^\circ$, $R_c = 2.40 \times 10^6$.



1/16/89 RUN 8 $R_c = 2.73 \times 10^6$

Figure 47. Naphthalene Flow Visualization, $\alpha = -4^\circ$, $R_c = 2.73 \times 10^6$.



Figure 48. Naphthalene Flow Visualization, $\alpha = -4^\circ$, $R_c = 3.27 \times 10^6$.



2/23/89

Figure 49. Naphthalene Flow Visualization
Showing Vortex Tracks in the Turbulent Regions.

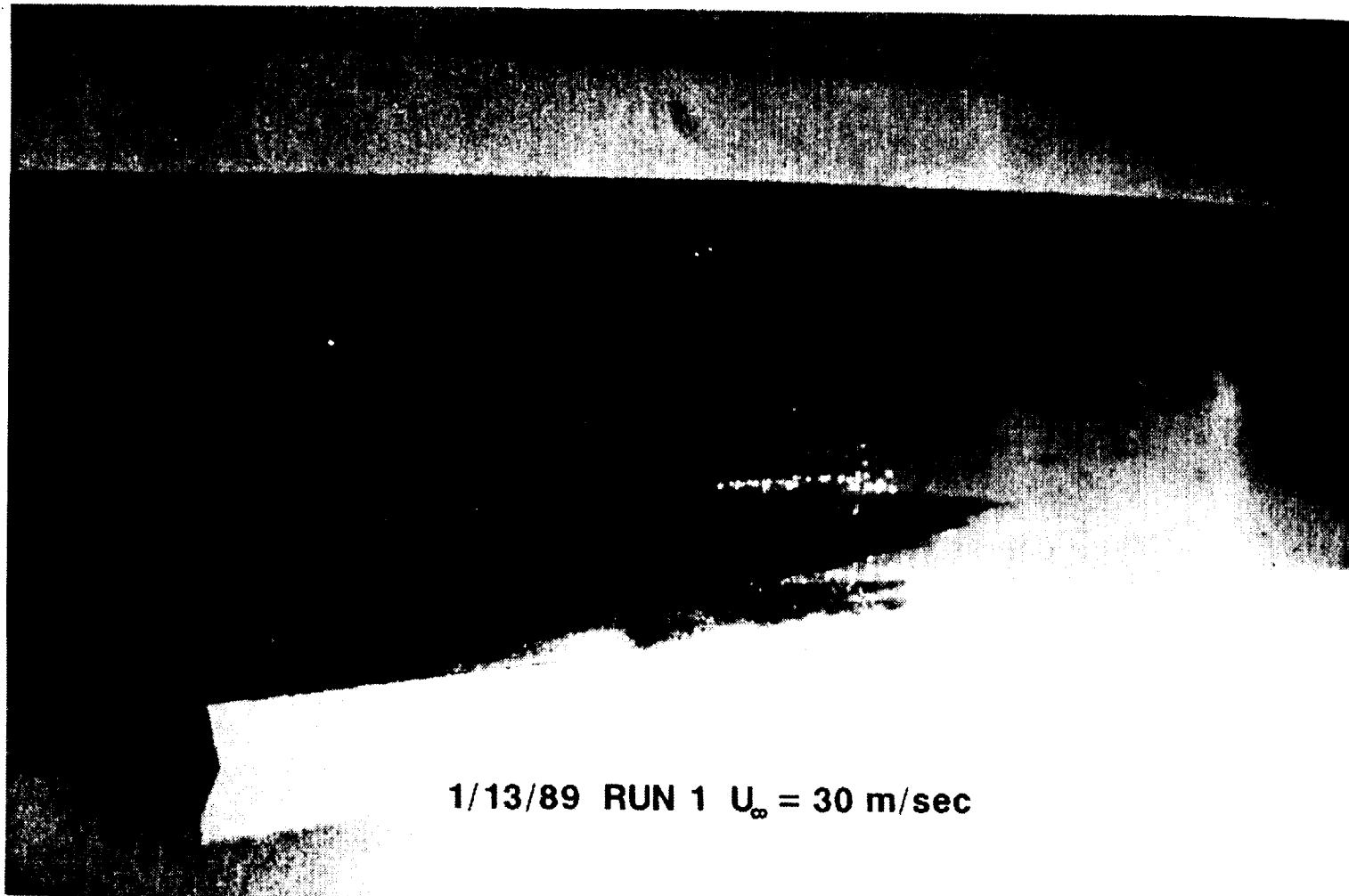


Figure 50. Liquid-crystal Flow Visualization.

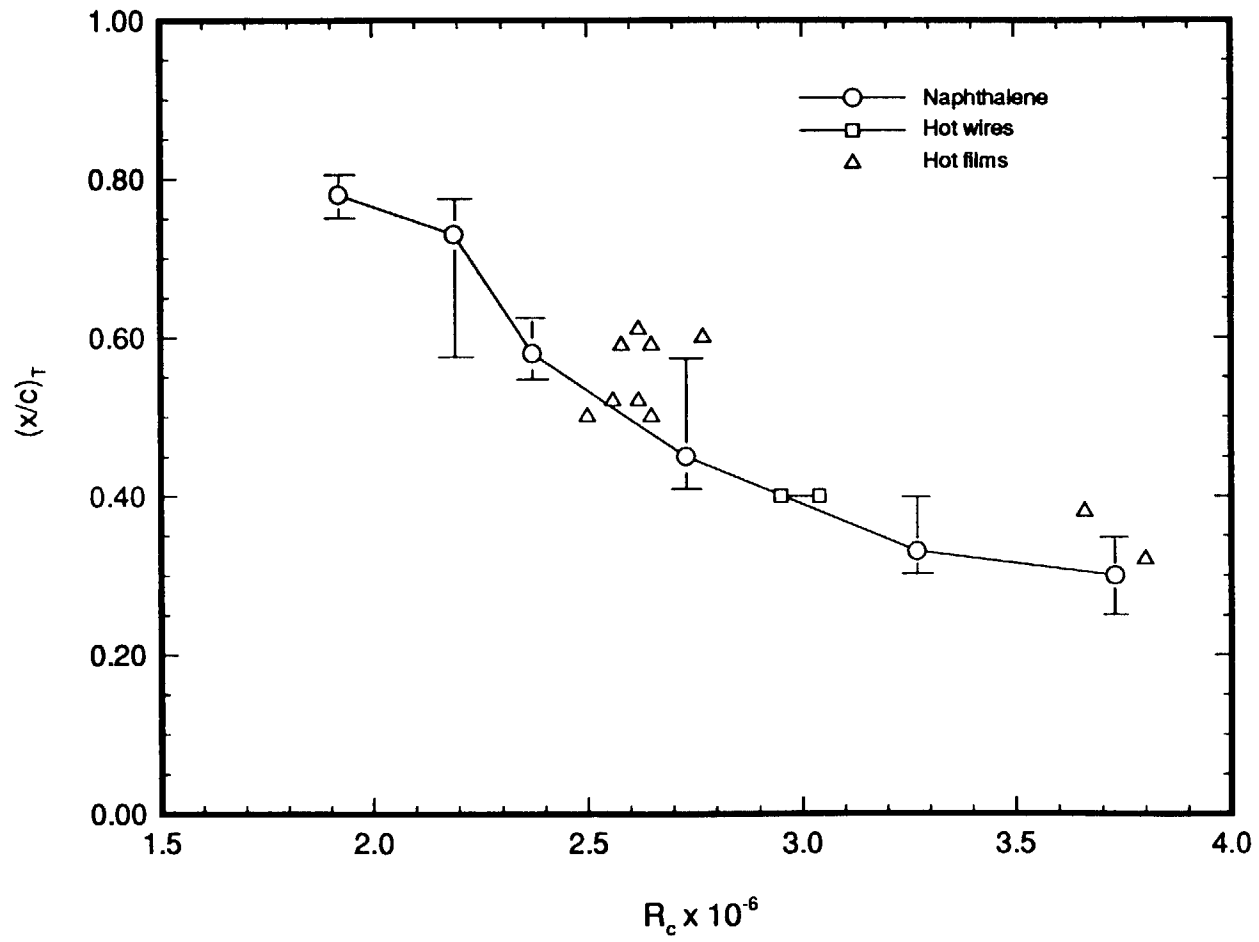


Figure 51. Transition Location Versus Reynolds Number.

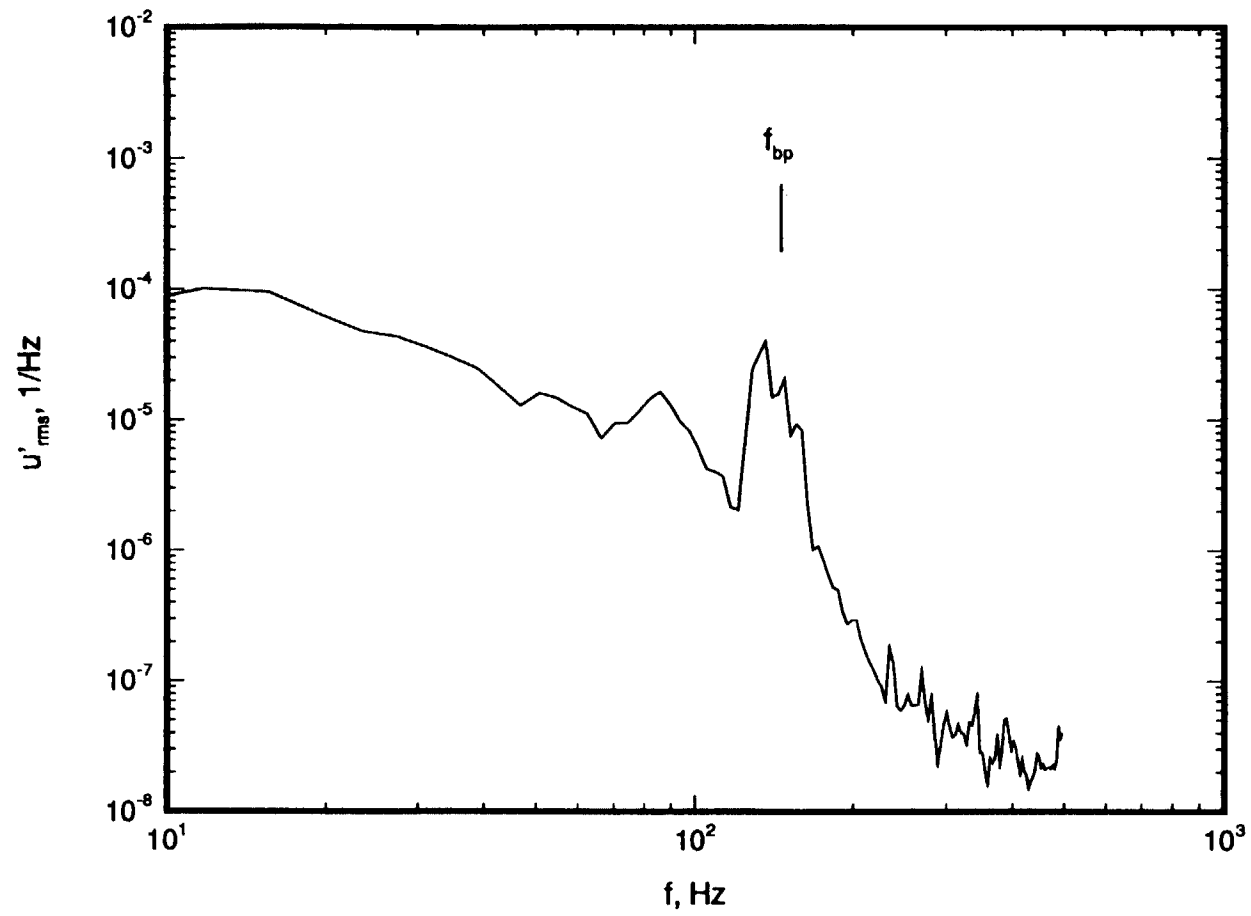


Figure 52. Boundary-Layer Velocity Spectrum, $\alpha = -4^\circ$, $R_c = 2.62 \times 10^6$.

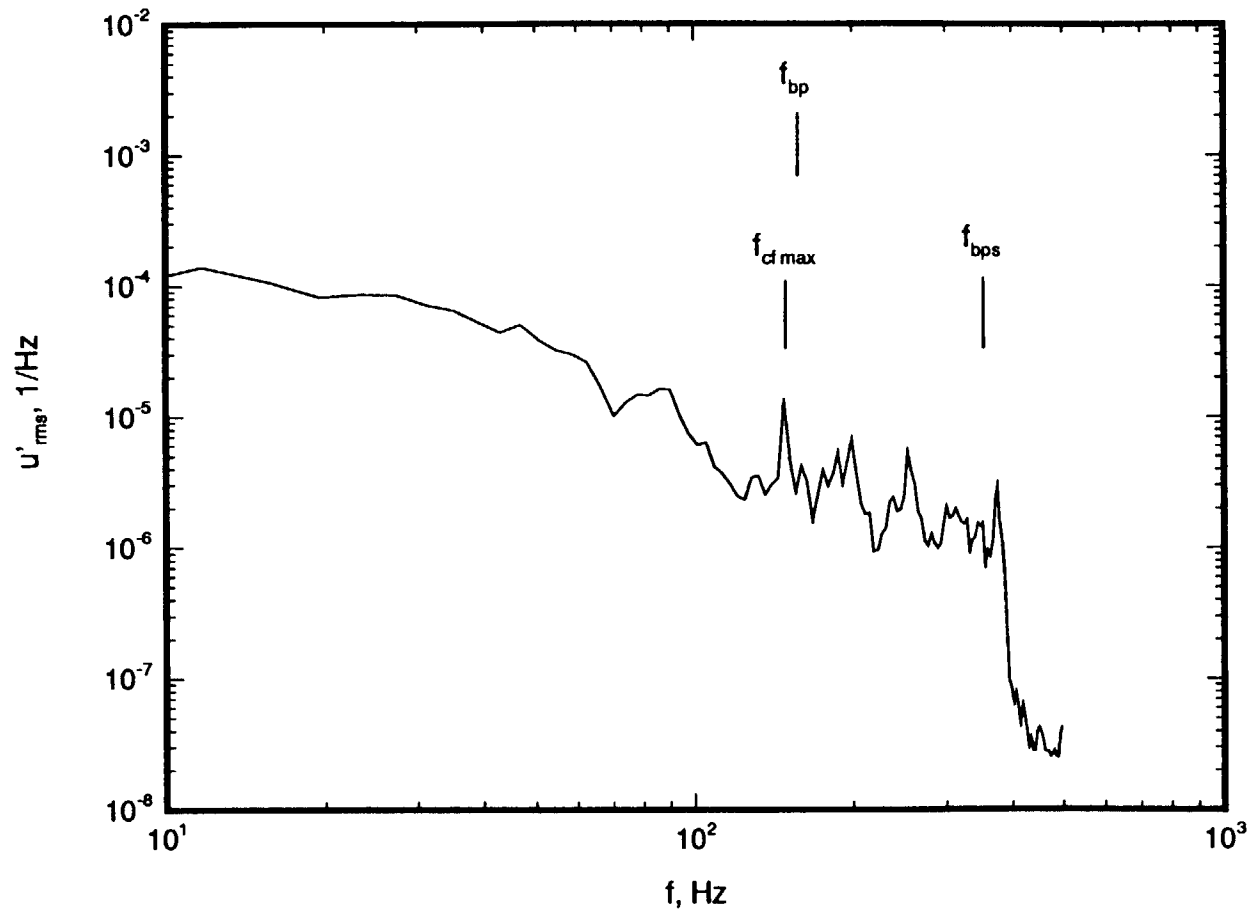


Figure 53. Boundary-Layer Velocity Spectrum, $\alpha = -4^\circ$, $R_c = 2.82 \times 10^6$.

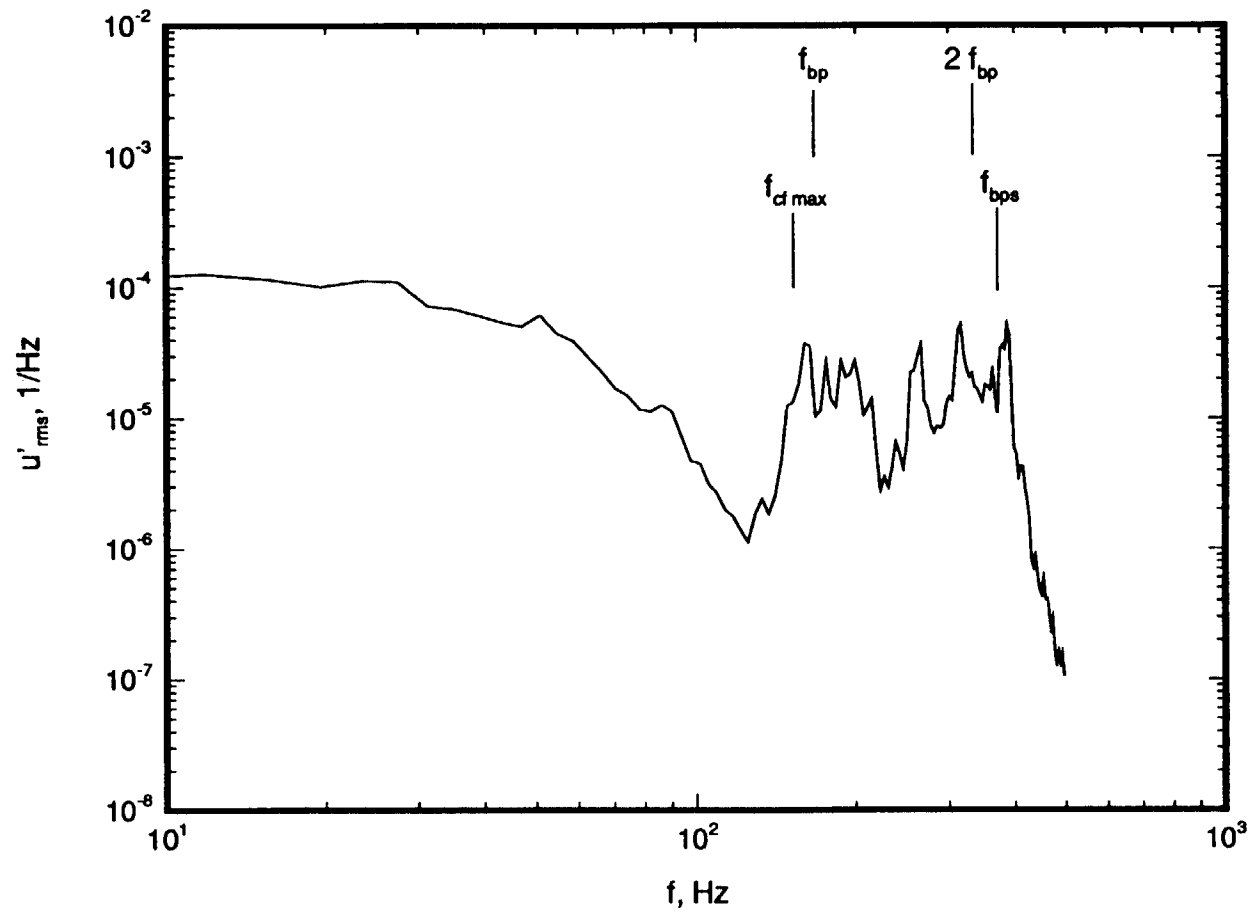


Figure 54. Boundary-Layer Velocity Spectrum, $\alpha = -4^\circ$, $R_c = 2.92 \times 10^6$.

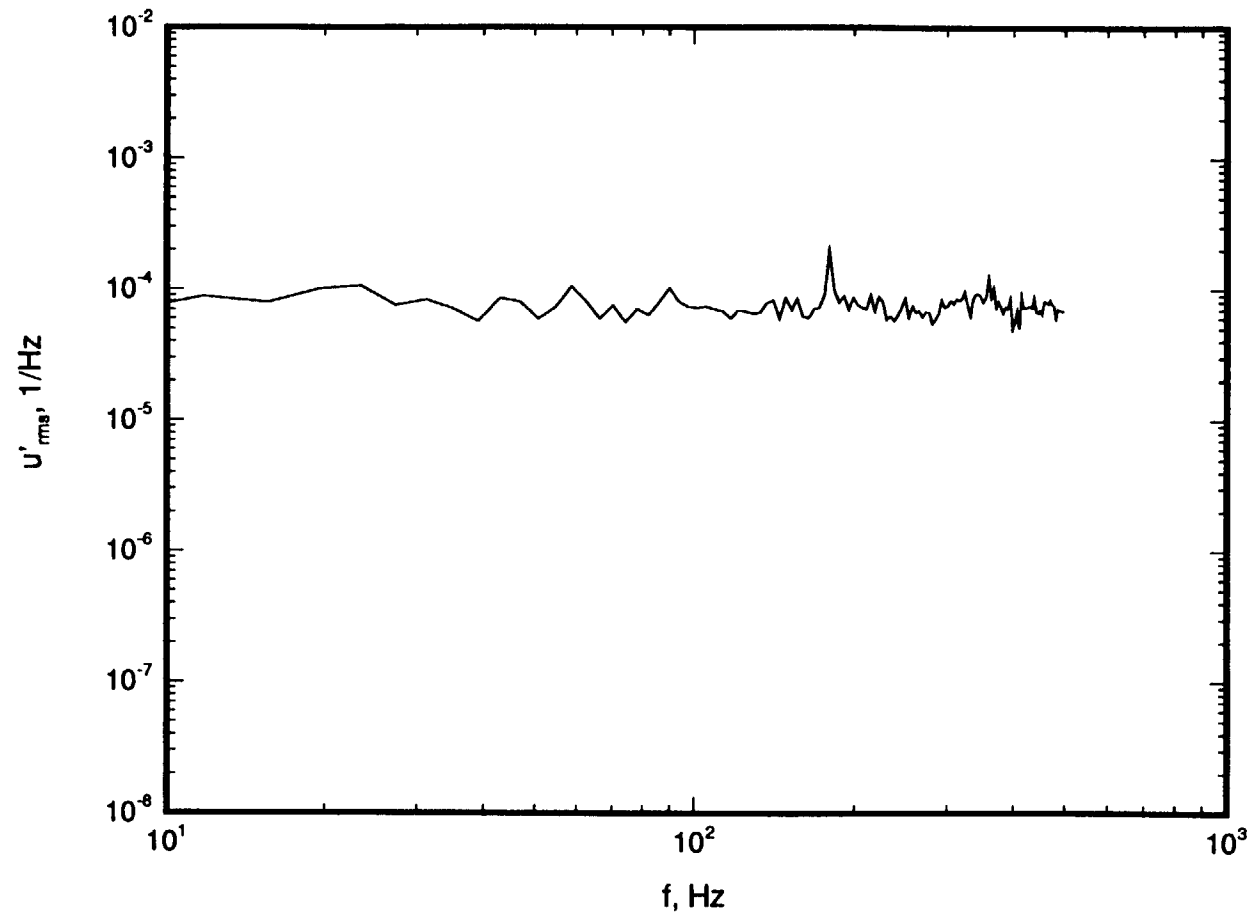


Figure 55. Boundary-Layer Velocity Spectrum, $\alpha = -4^\circ$, $R_c = 3.28 \times 10^6$.

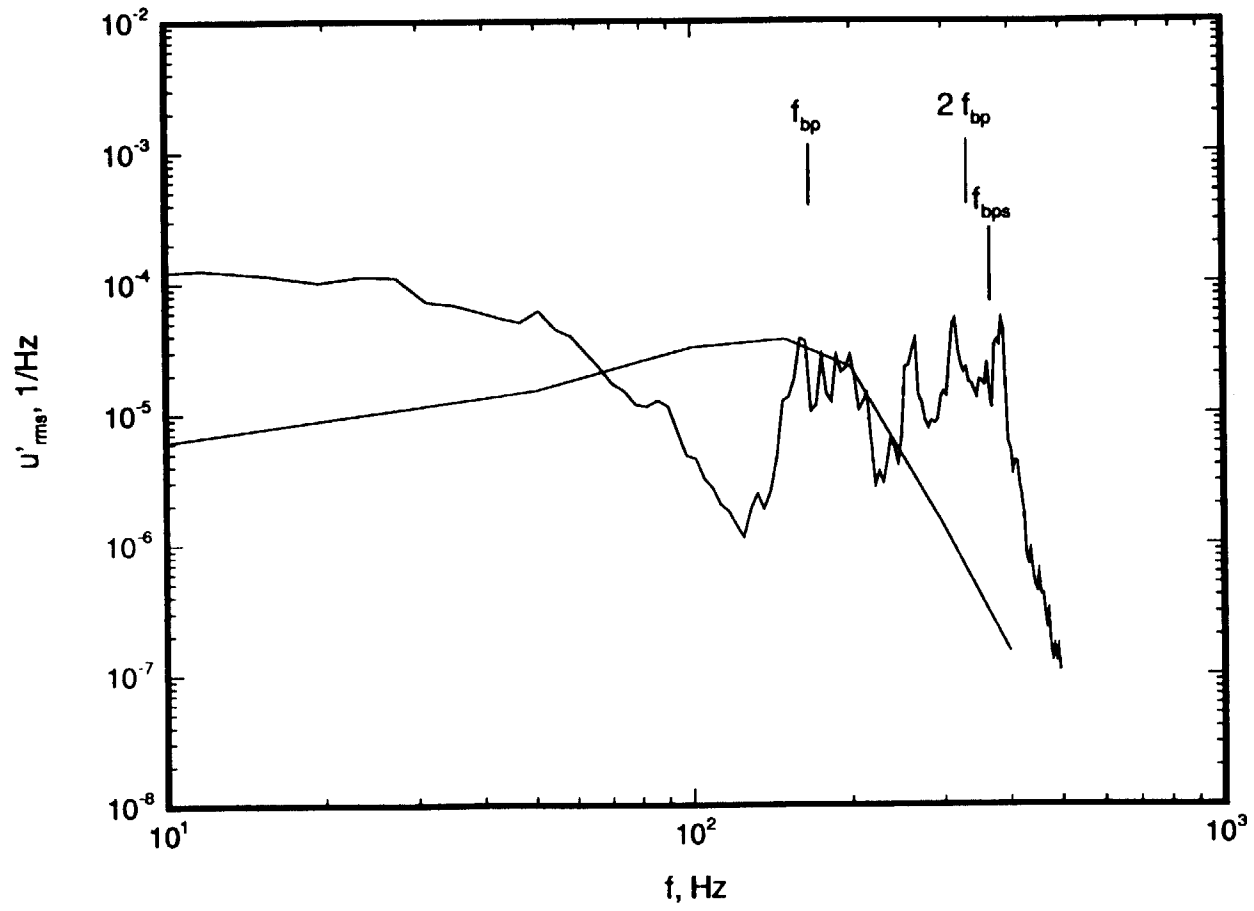


Figure 56. Comparison of Measured and Predicted Boundary-Layer Velocity Spectra, $\alpha = -4^\circ$, $R_c = 2.92 \times 10^6$.

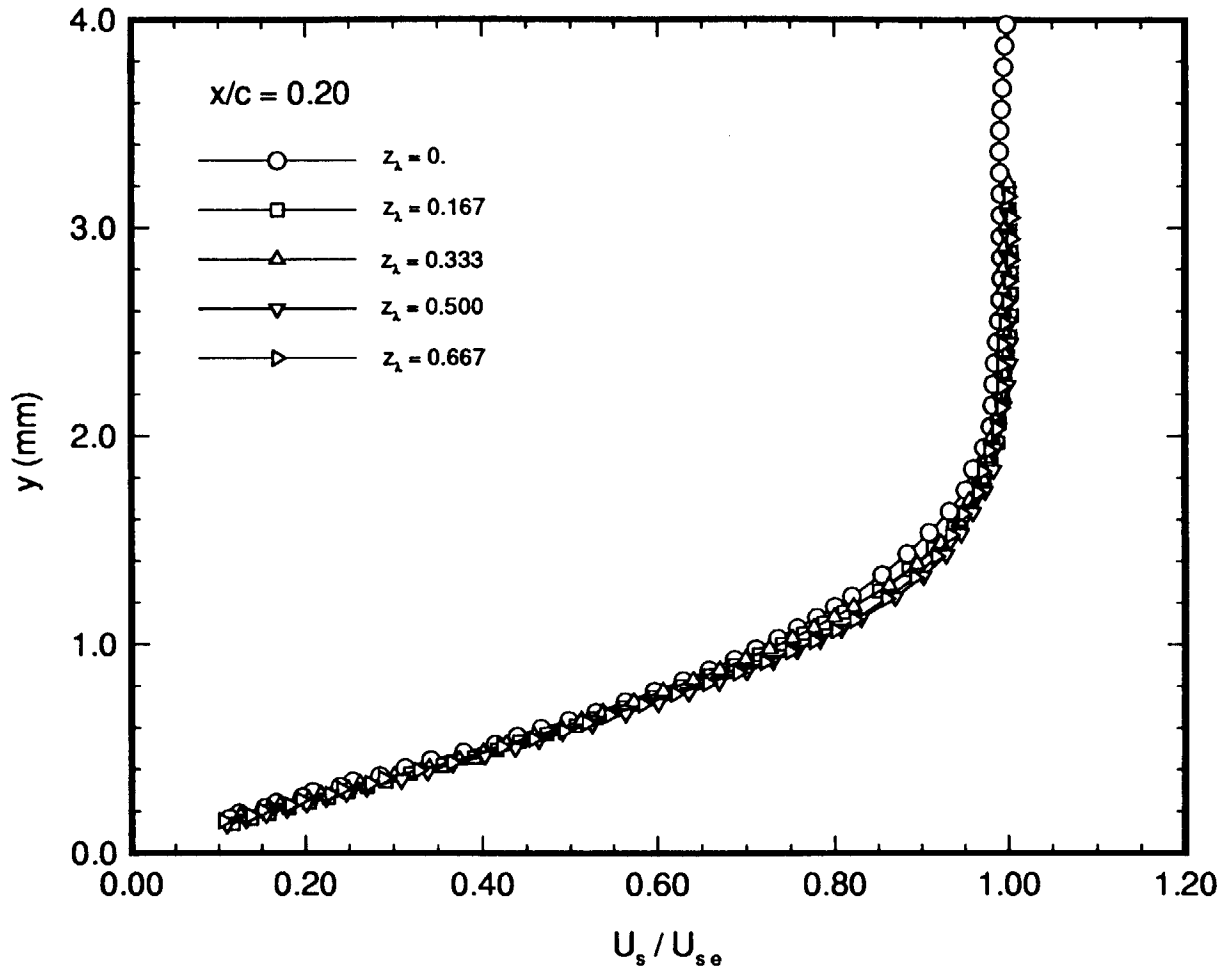


Figure 57. Streamwise-Velocity Profiles at $x/c = 0.20$, $\alpha = -4^\circ$, $R_c = 2.37 \times 10^6$.

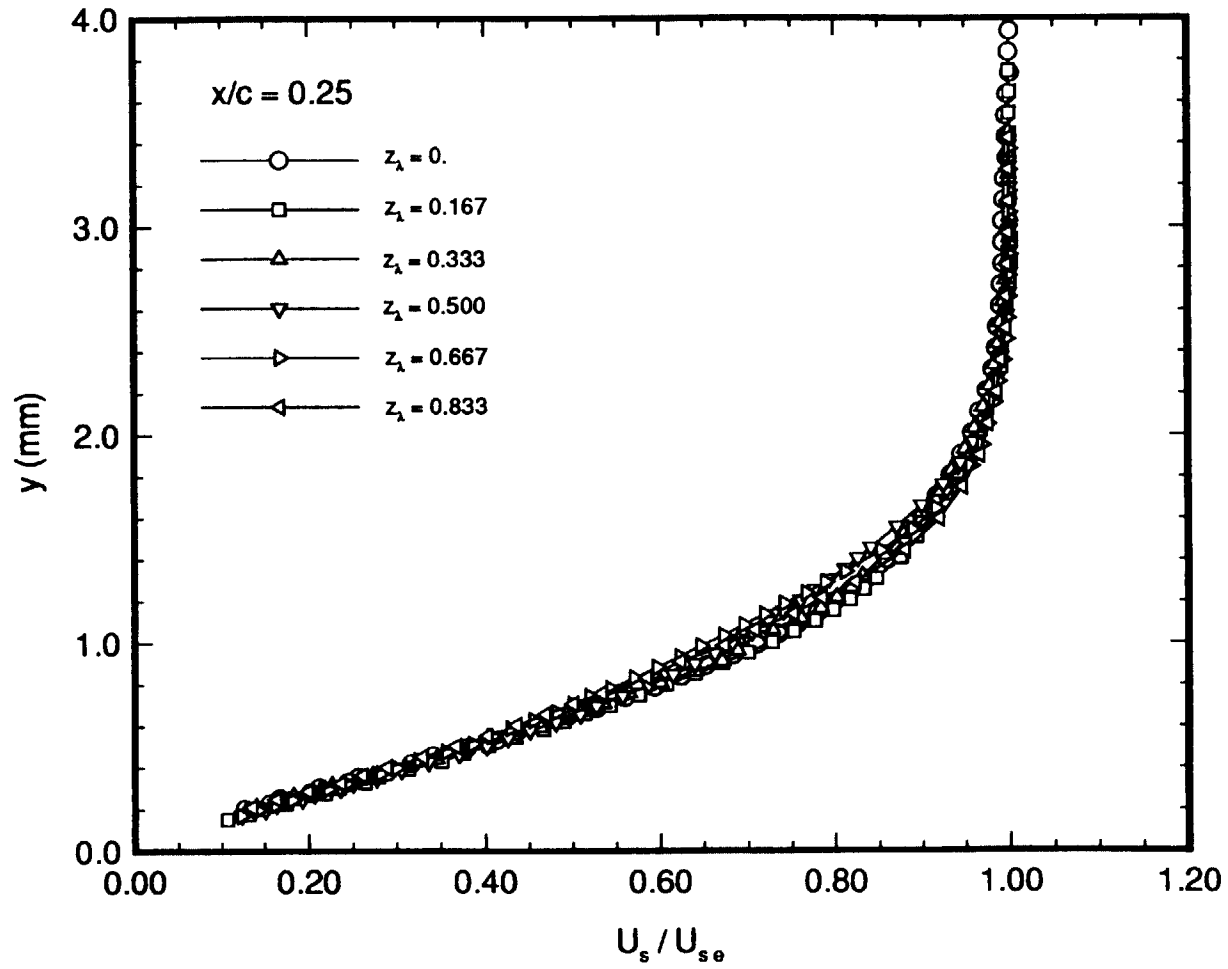


Figure 58. Streamwise-Velocity Profiles at $x/c = 0.25$, $\alpha = -4^\circ$, $R_c = 2.37 \times 10^6$.

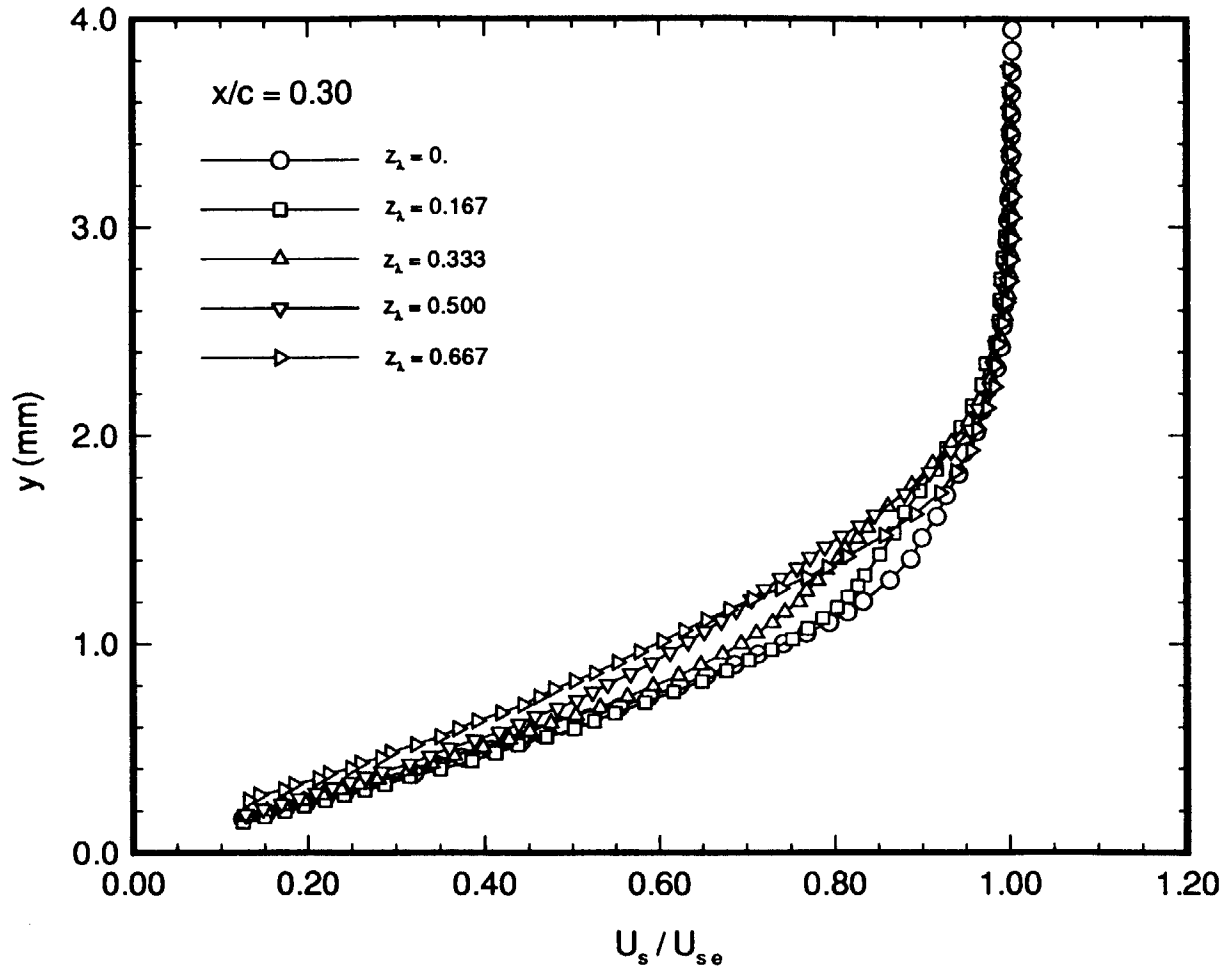


Figure 59. Streamwise-Velocity Profiles at $x/c = 0.30$, $\alpha = -4^\circ$, $R_c = 2.37 \times 10^6$.

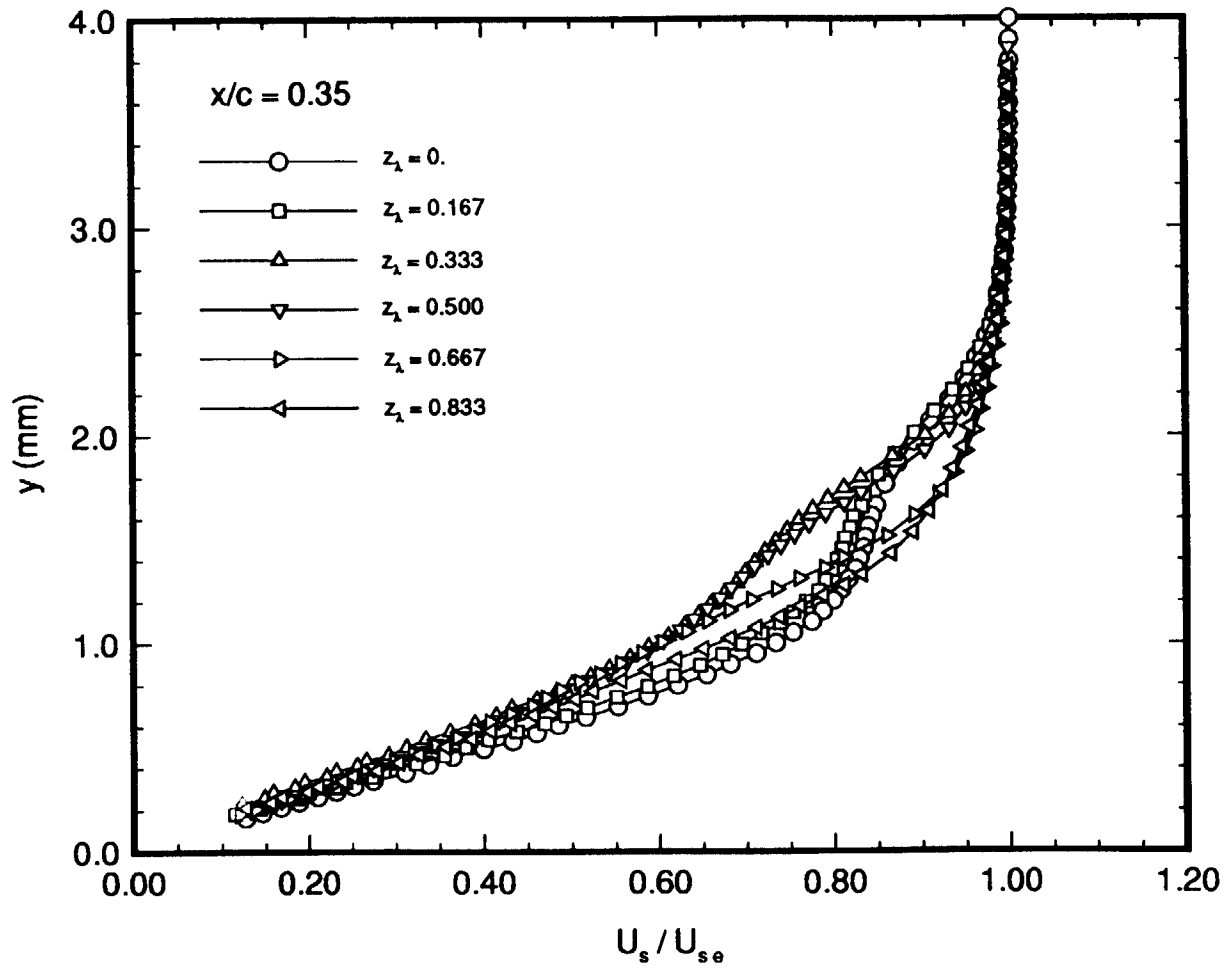


Figure 60. Streamwise-Velocity Profiles at $x/c = 0.35$, $\alpha = -4^\circ$, $R_c = 2.37 \times 10^6$.

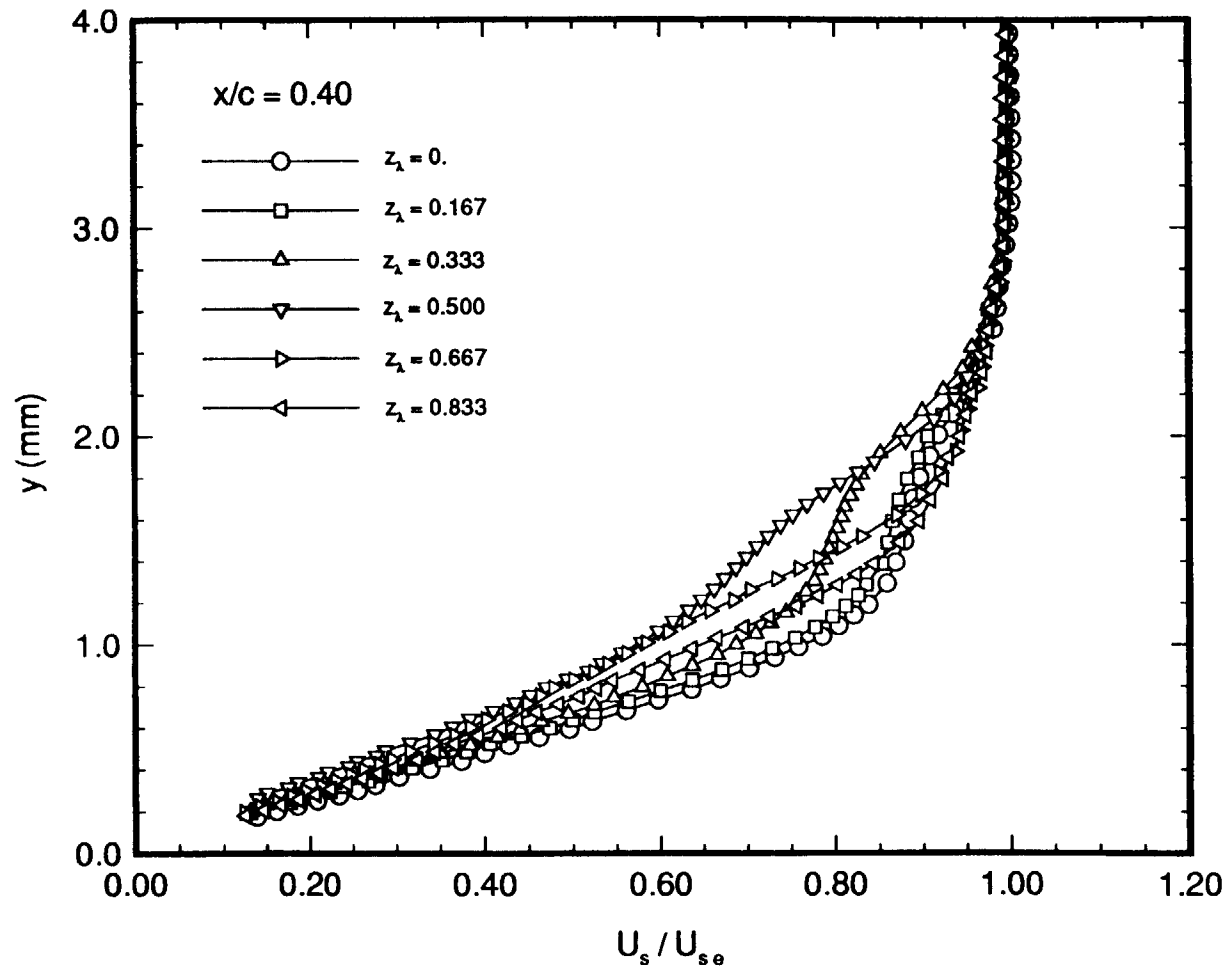


Figure 61. Streamwise-Velocity Profiles at $x/c = 0.40$, $\alpha = -4^\circ$, $R_c = 2.37 \times 10^6$.

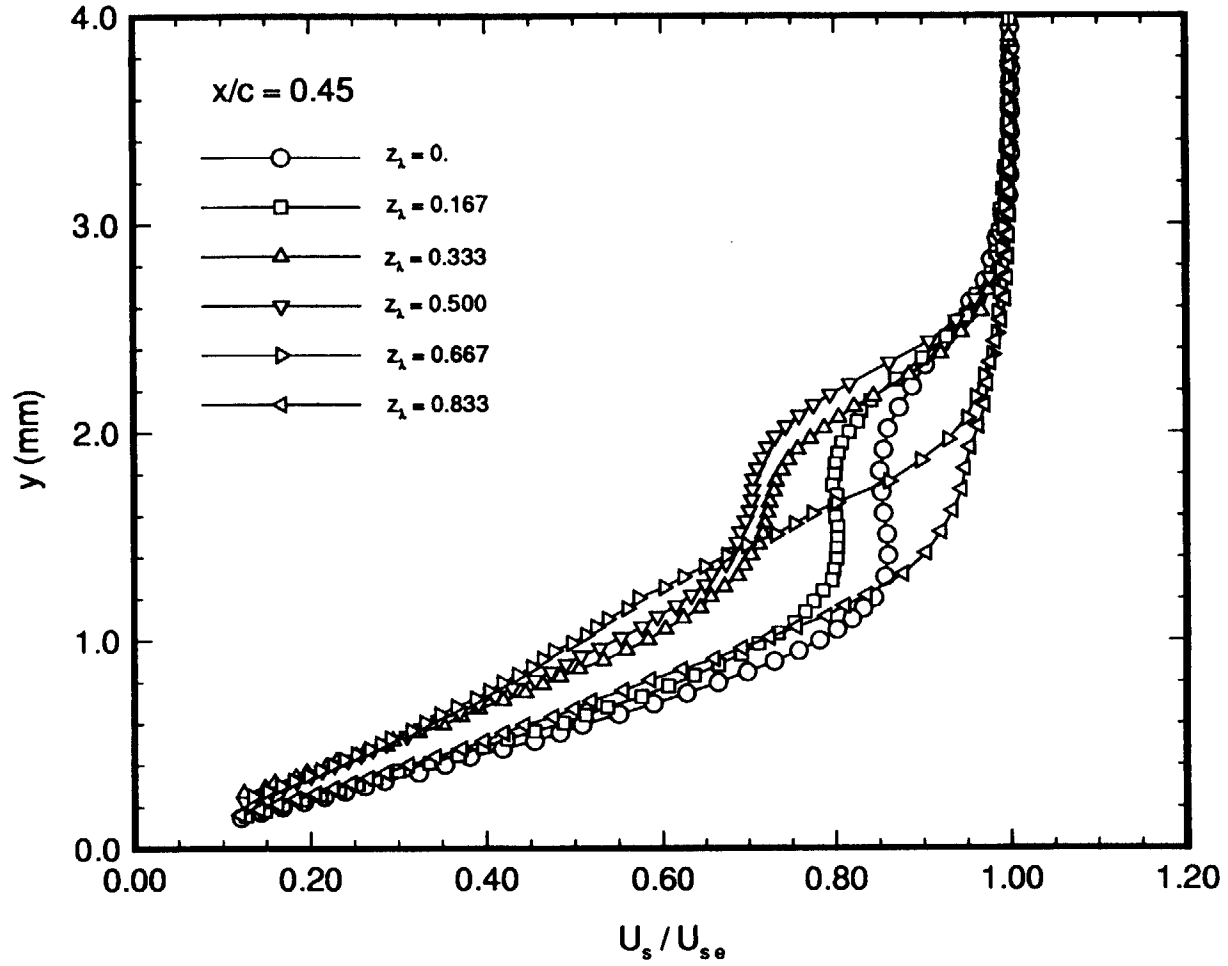


Figure 62. Streamwise-Velocity Profiles at $x/c = 0.45$, $\alpha = -4^\circ$, $R_c = 2.37 \times 10^6$.

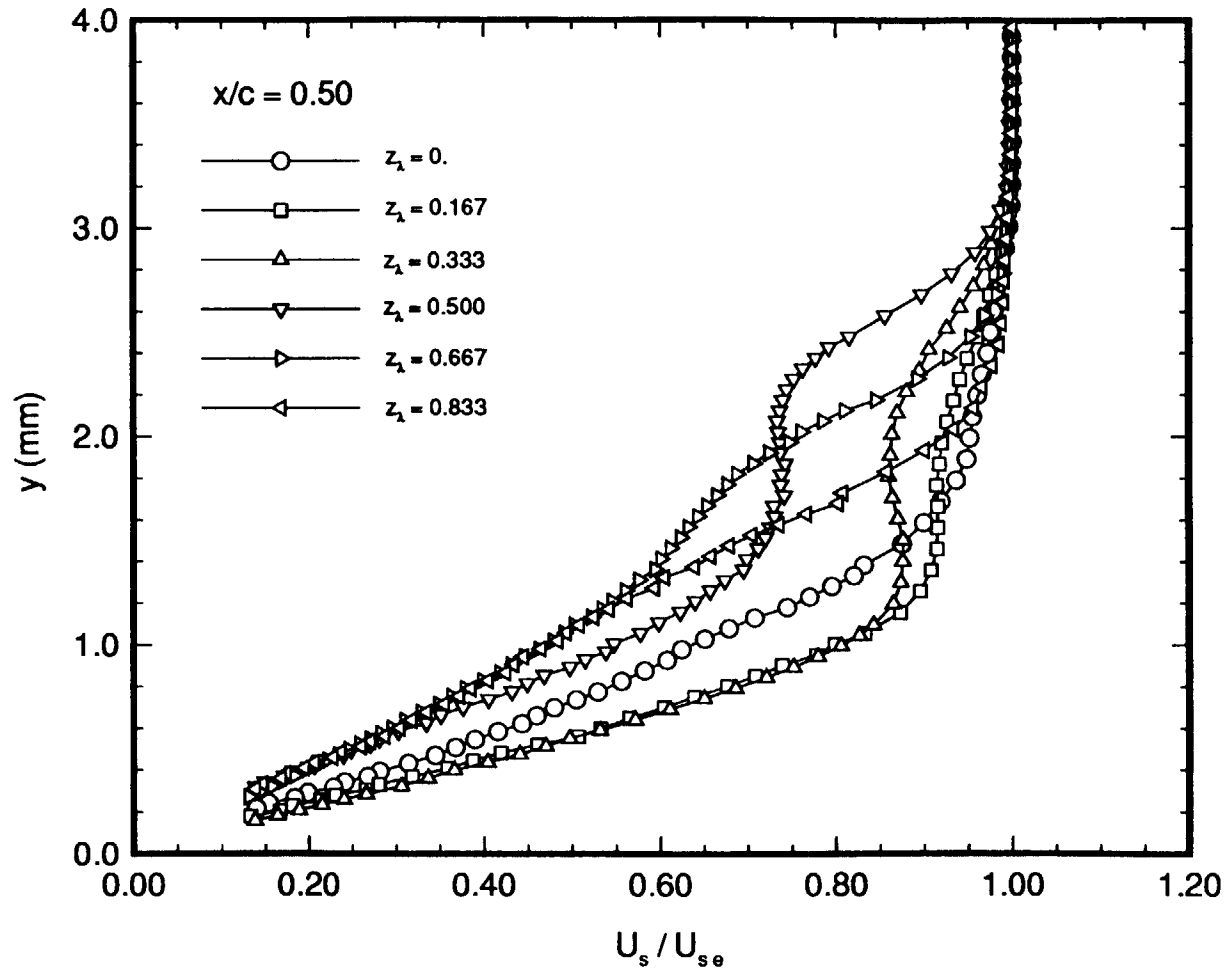


Figure 63. Streamwise-Velocity Profiles at $x/c = 0.50$, $\alpha = -4^\circ$, $R_c = 2.37 \times 10^6$.

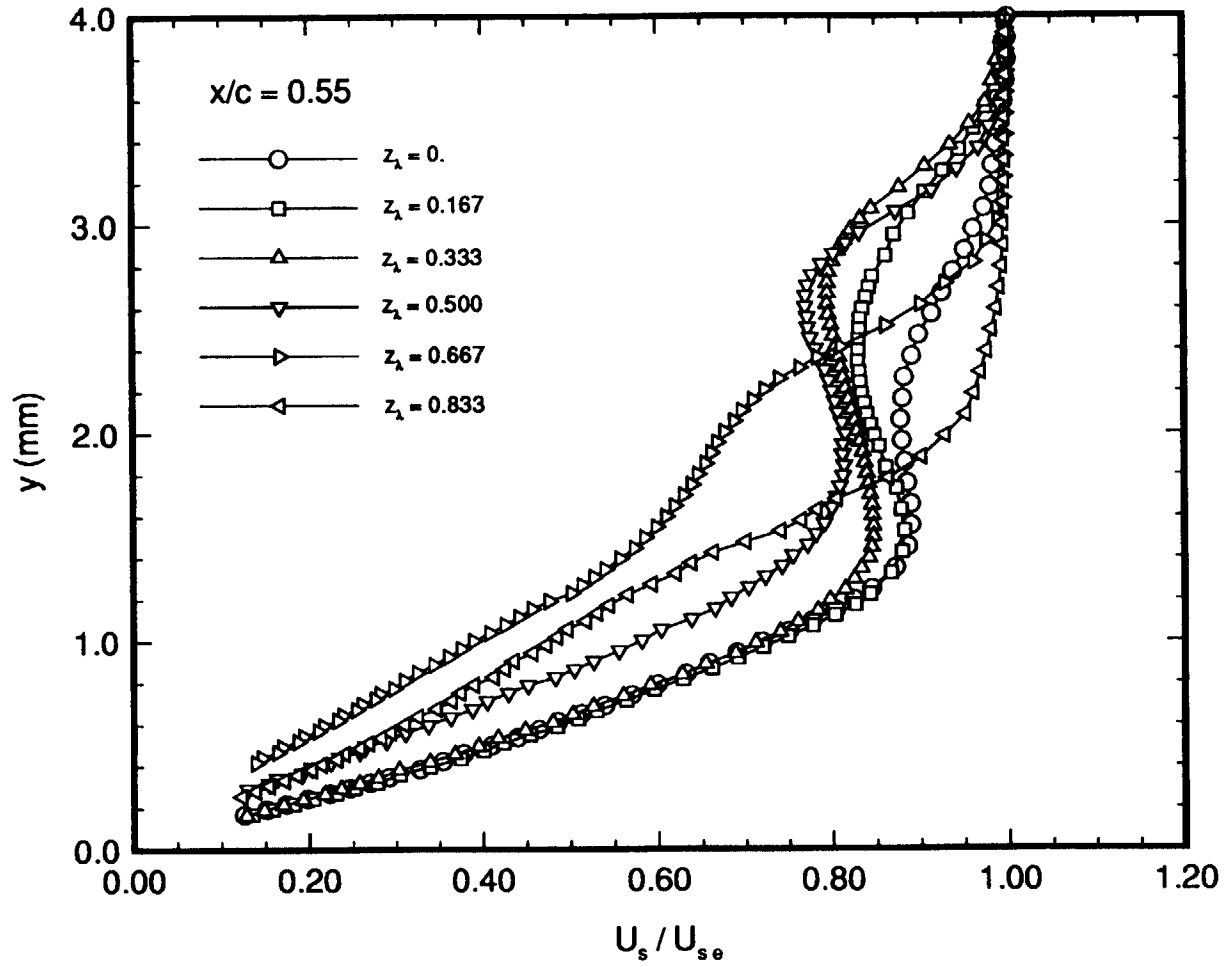


Figure 64. Streamwise-Velocity Profiles at $x/c = 0.55$, $\alpha = -4^\circ$, $R_c = 2.37 \times 10^6$.

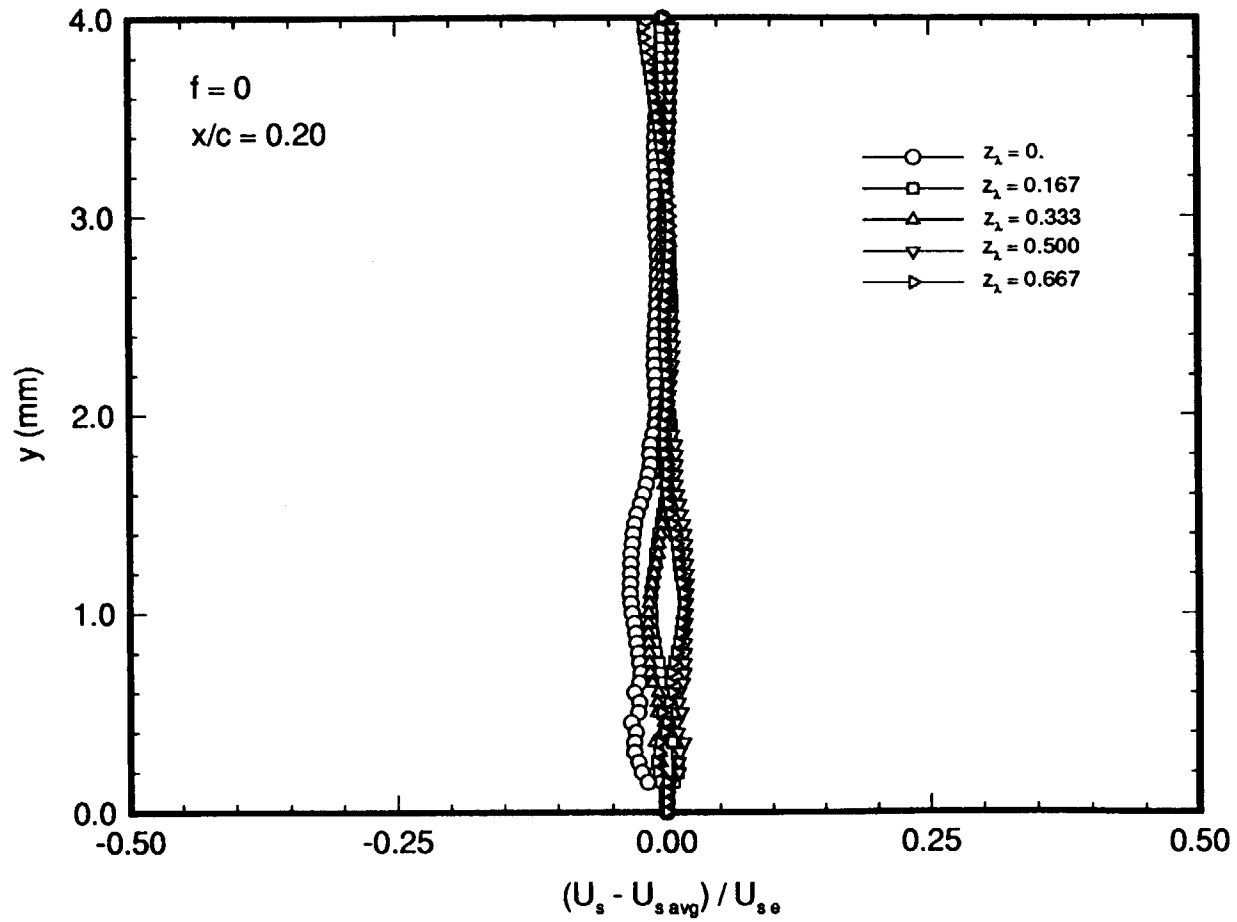


Figure 65. Stationary Crossflow-Disturbance Velocity Profiles at $x/c = 0.20$, $\alpha = -4^\circ$, $R_c = 2.37 \times 10^6$ Obtained From $U_s - U_{s,avg}$.

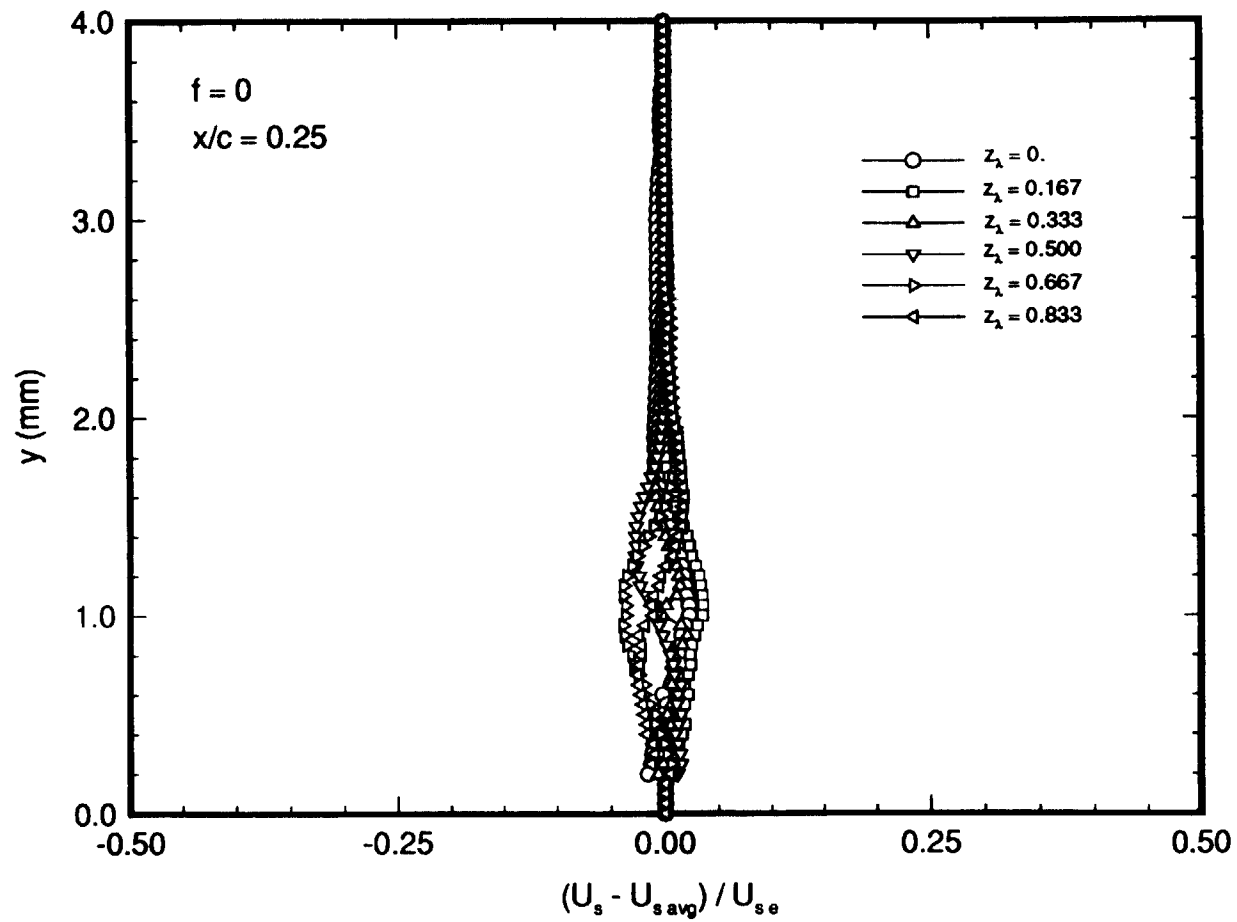


Figure 66. Stationary Crossflow-Disturbance Velocity Profiles at $x/c = 0.25$, $\alpha = -4^\circ$, $R_c = 2.37 \times 10^6$ Obtained From $U_s - U_{s\text{ avg}}$.

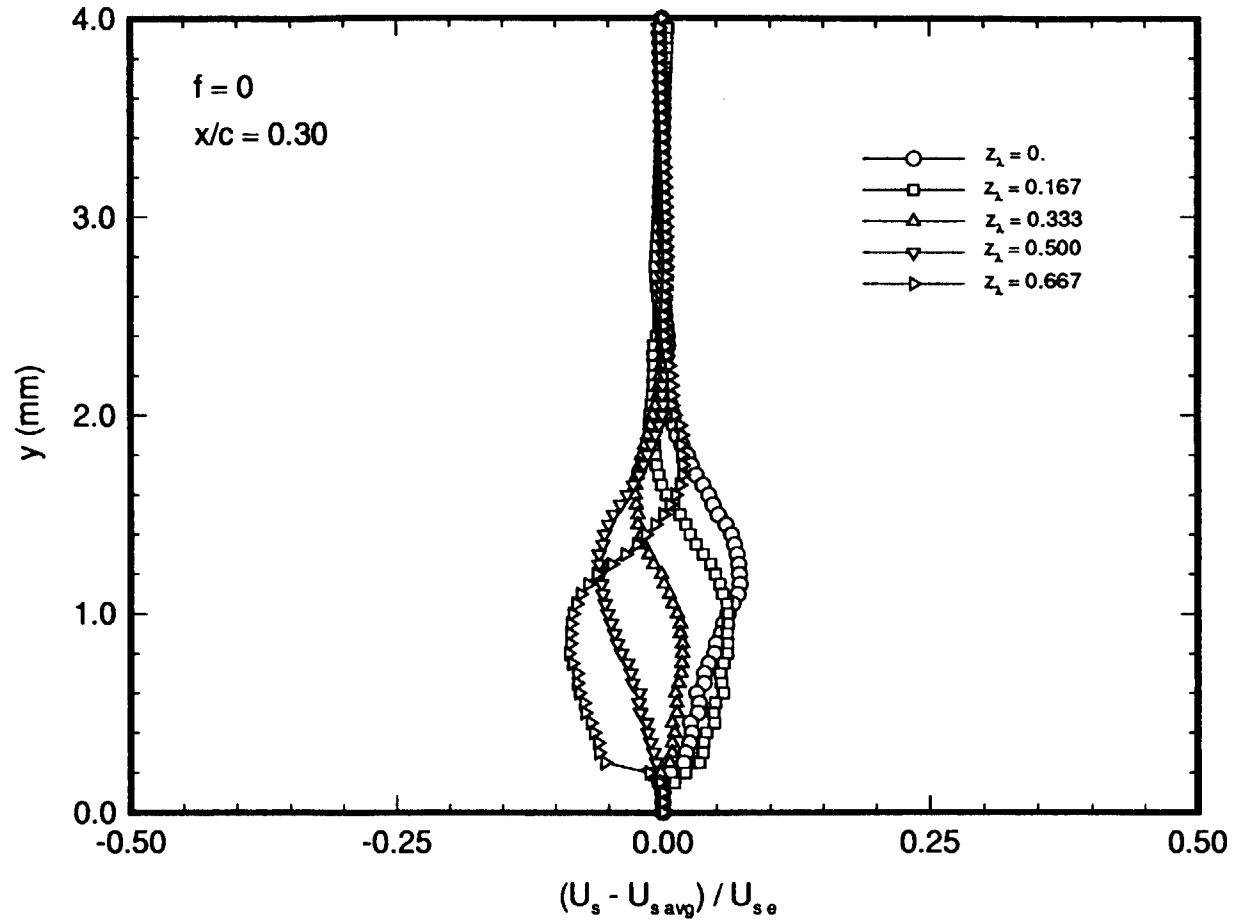


Figure 67. Stationary Crossflow-Disturbance Velocity Profiles at $x/c = 0.30$, $\alpha = -4^\circ$, $R_c = 2.37 \times 10^6$ Obtained From $U_s - U_{s\text{avg}}$.

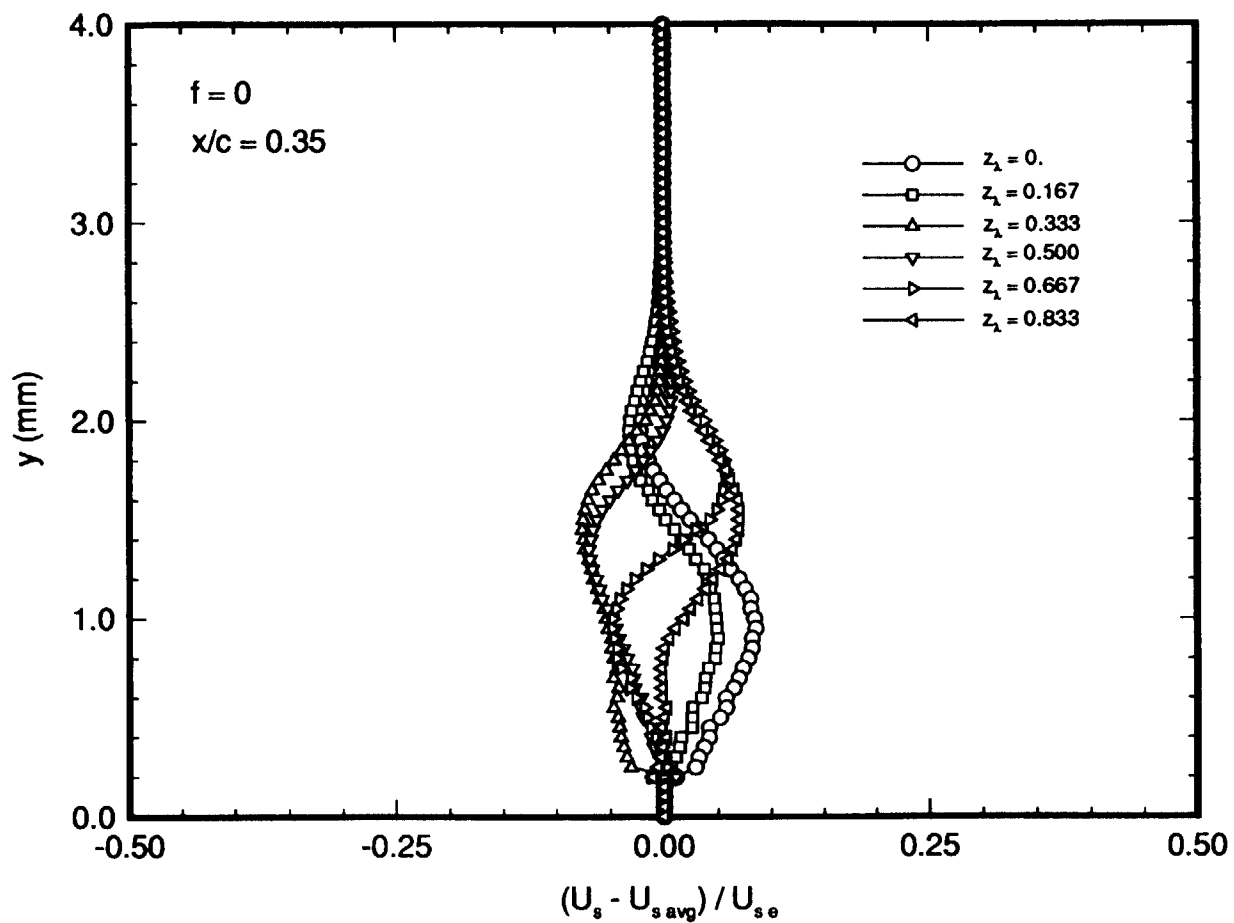


Figure 68. Stationary Crossflow-Disturbance Velocity Profiles at $x/c = 0.35$, $\alpha = -4^\circ$, $R_c = 2.37 \times 10^6$ Obtained From $U_s - U_{s,avg}$.

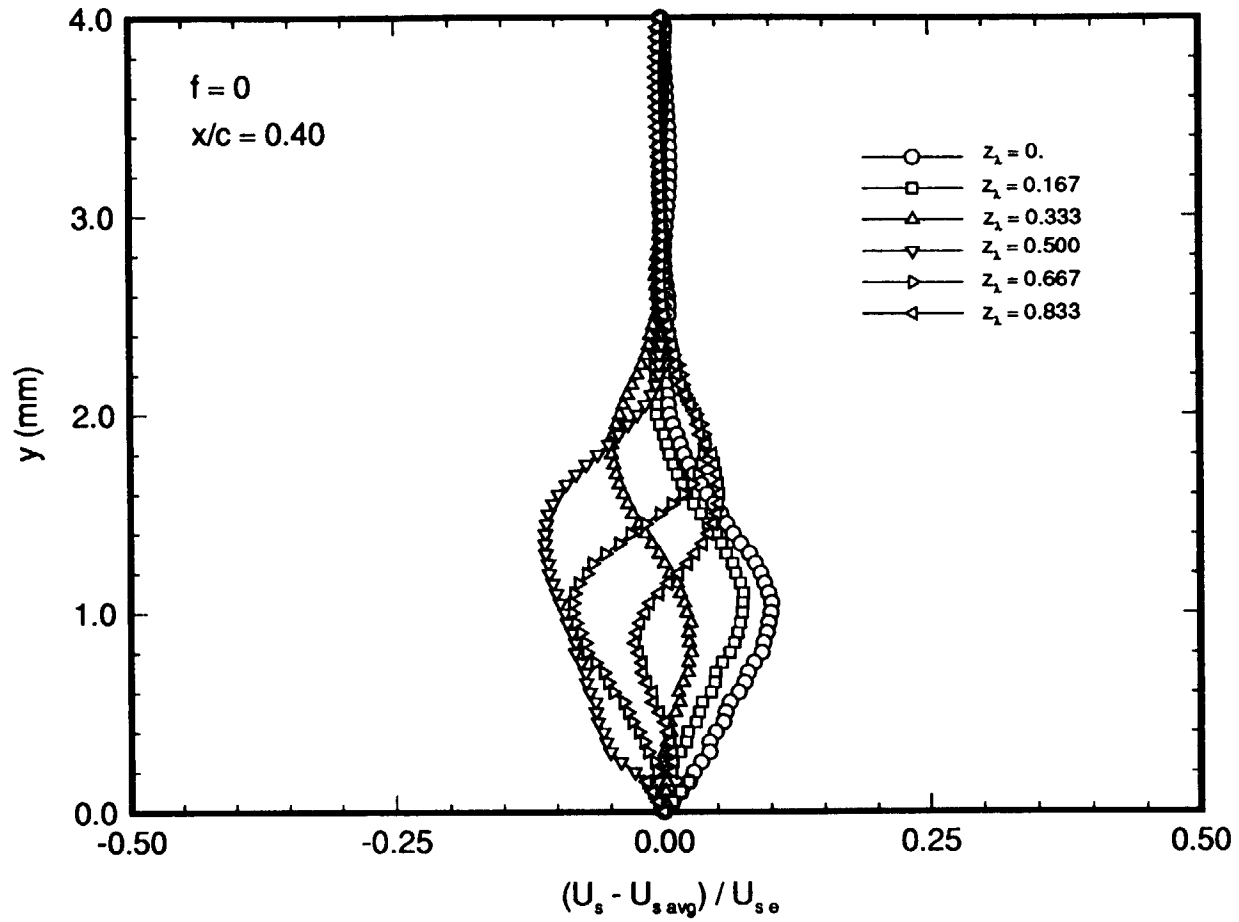


Figure 69. Stationary Crossflow-Disturbance Velocity Profiles at $x/c = 0.40$, $\alpha = -4^\circ$, $R_c = 2.37 \times 10^6$ Obtained From $U_s - U_{s,avg}$.

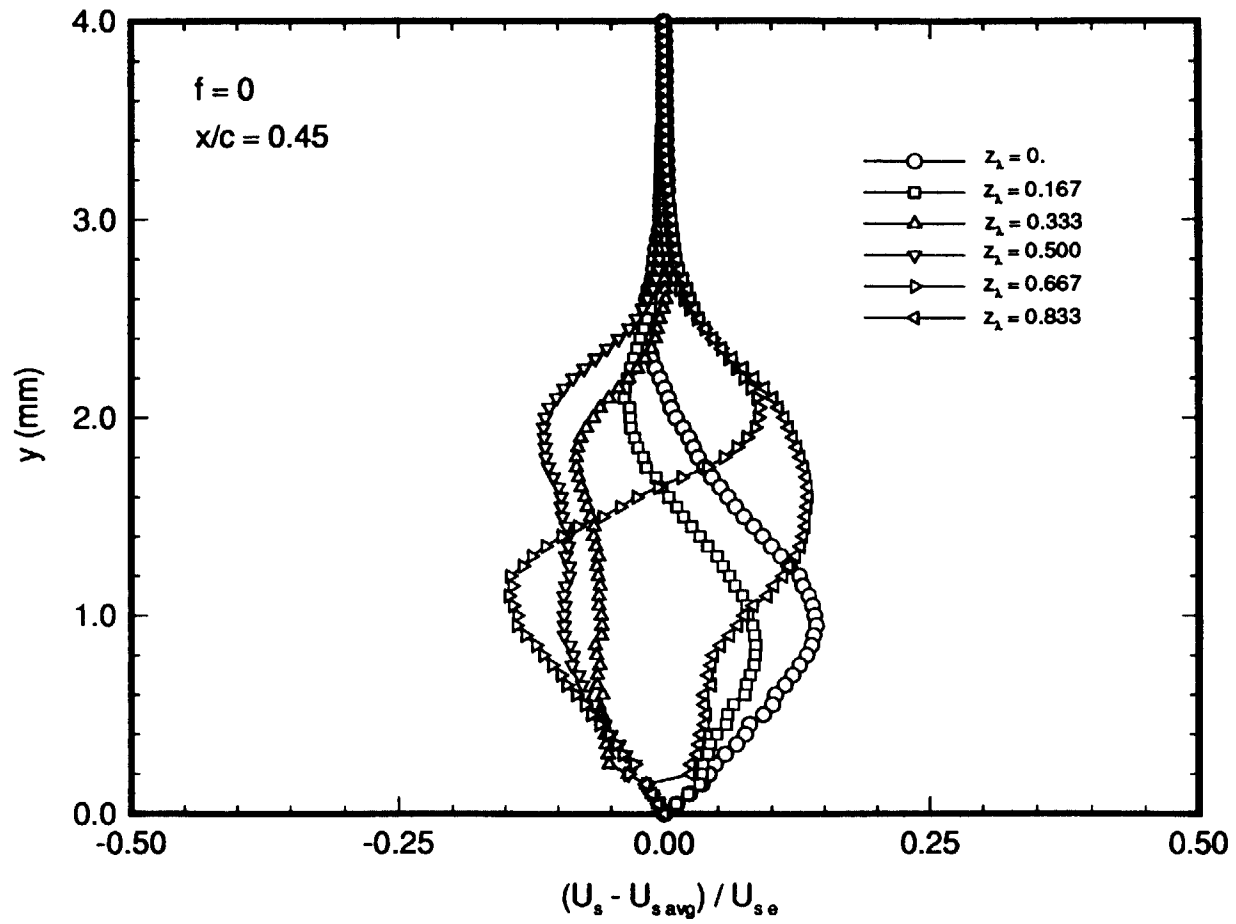


Figure 70. Stationary Crossflow-Disturbance Velocity Profiles at $x/c = 0.45$, $\alpha = -4^\circ$, $R_c = 2.37 \times 10^6$ Obtained From $U_s - U_{s,avg}$.

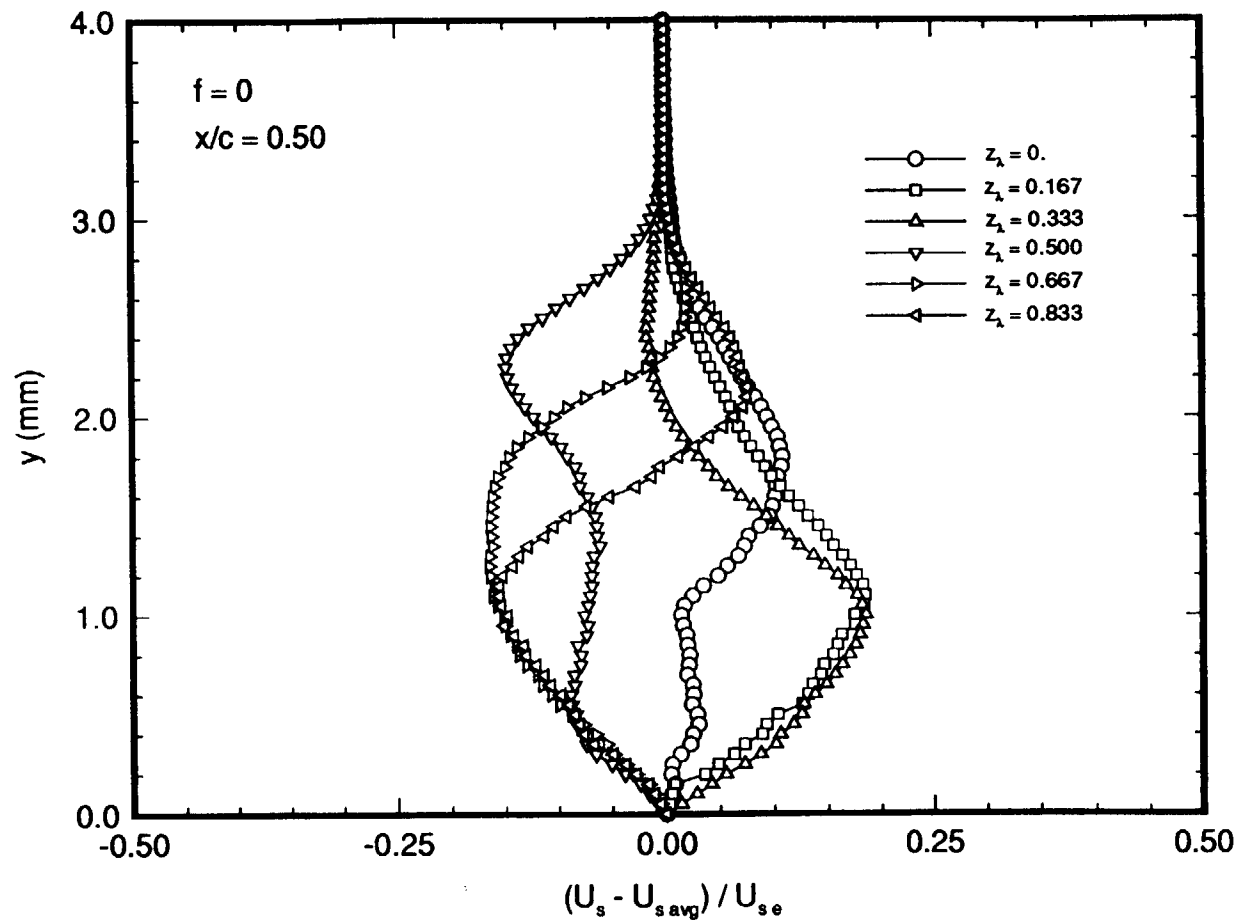


Figure 71. Stationary Crossflow-Disturbance Velocity Profiles at $x/c = 0.50$, $\alpha = -4^\circ$, $R_c = 2.37 \times 10^6$ Obtained From $U_s - U_{s\text{avg}}$.

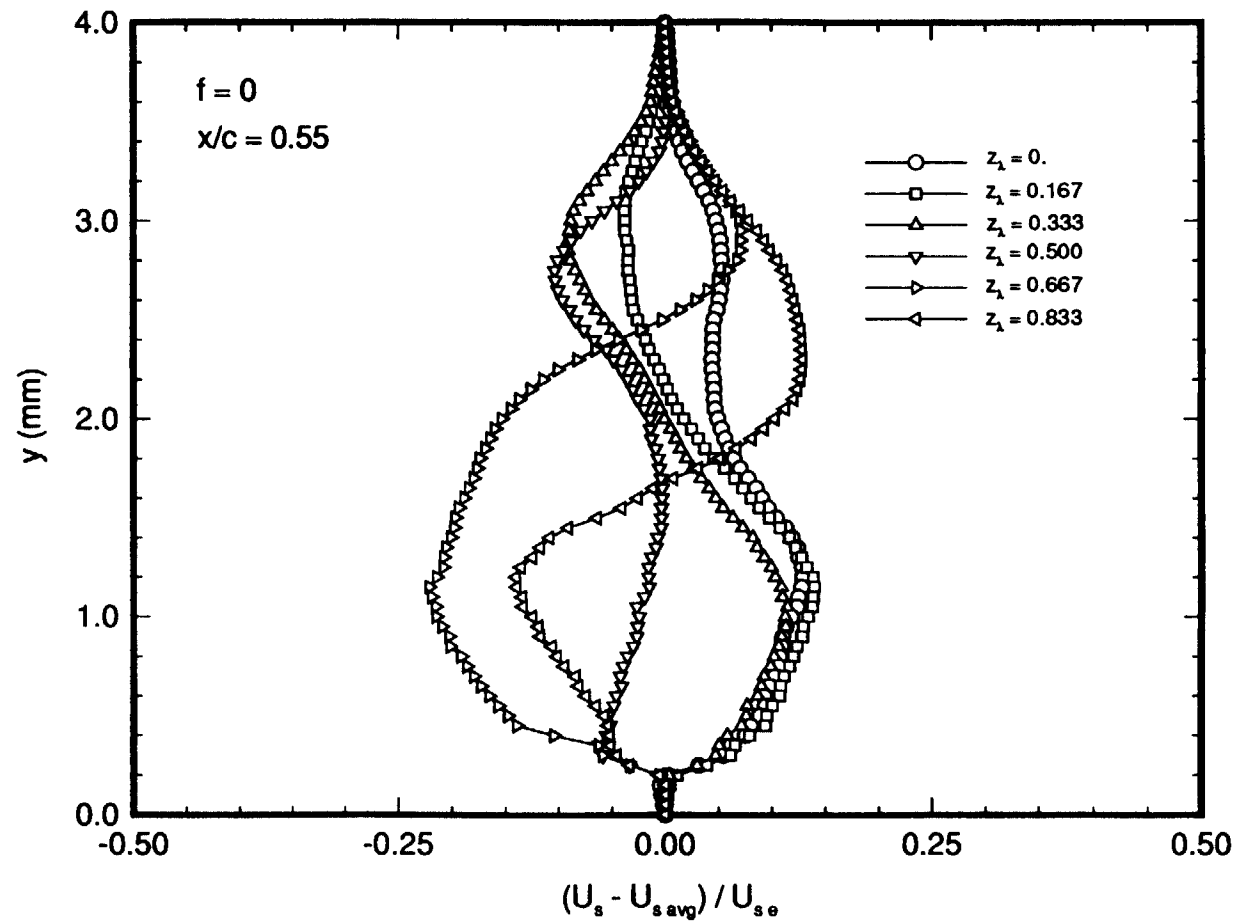


Figure 72. Stationary Crossflow-Disturbance Velocity Profiles at $x/c = 0.55$, $\alpha = -4^\circ$, $R_c = 2.37 \times 10^6$ Obtained From $U_s - U_{s\text{ avg}}$.

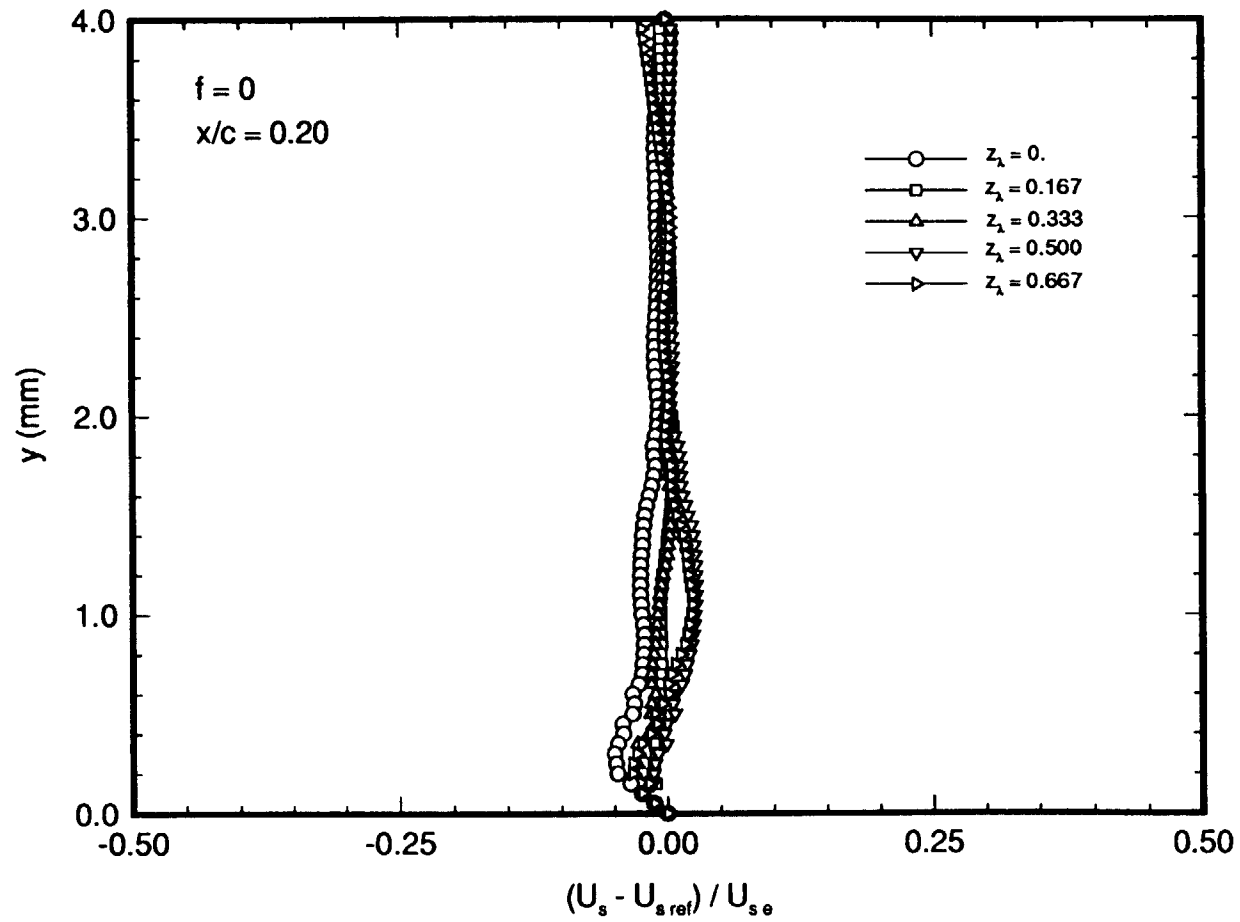


Figure 73. Stationary Crossflow-Disturbance Velocity Profiles at $x/c = 0.20$, $\alpha = -4^\circ$, $R_c = 2.37 \times 10^6$ Obtained From $U_s - U_{s,ref}$.

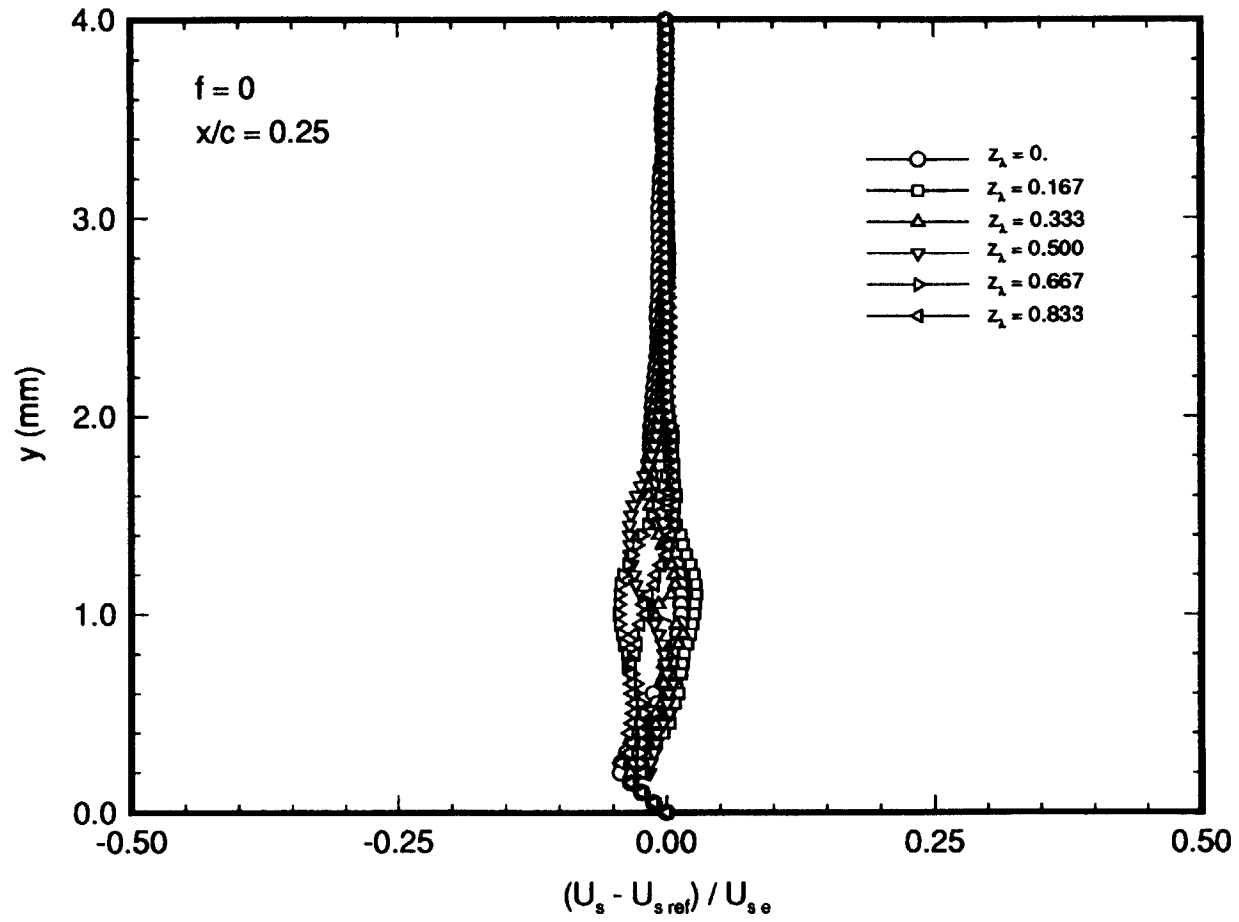


Figure 74. Stationary Crossflow-Disturbance Velocity Profiles at $x/c = 0.25$, $\alpha = -4^\circ$, $R_c = 2.37 \times 10^6$ Obtained From $U_s - U_{s\text{ref}}$.

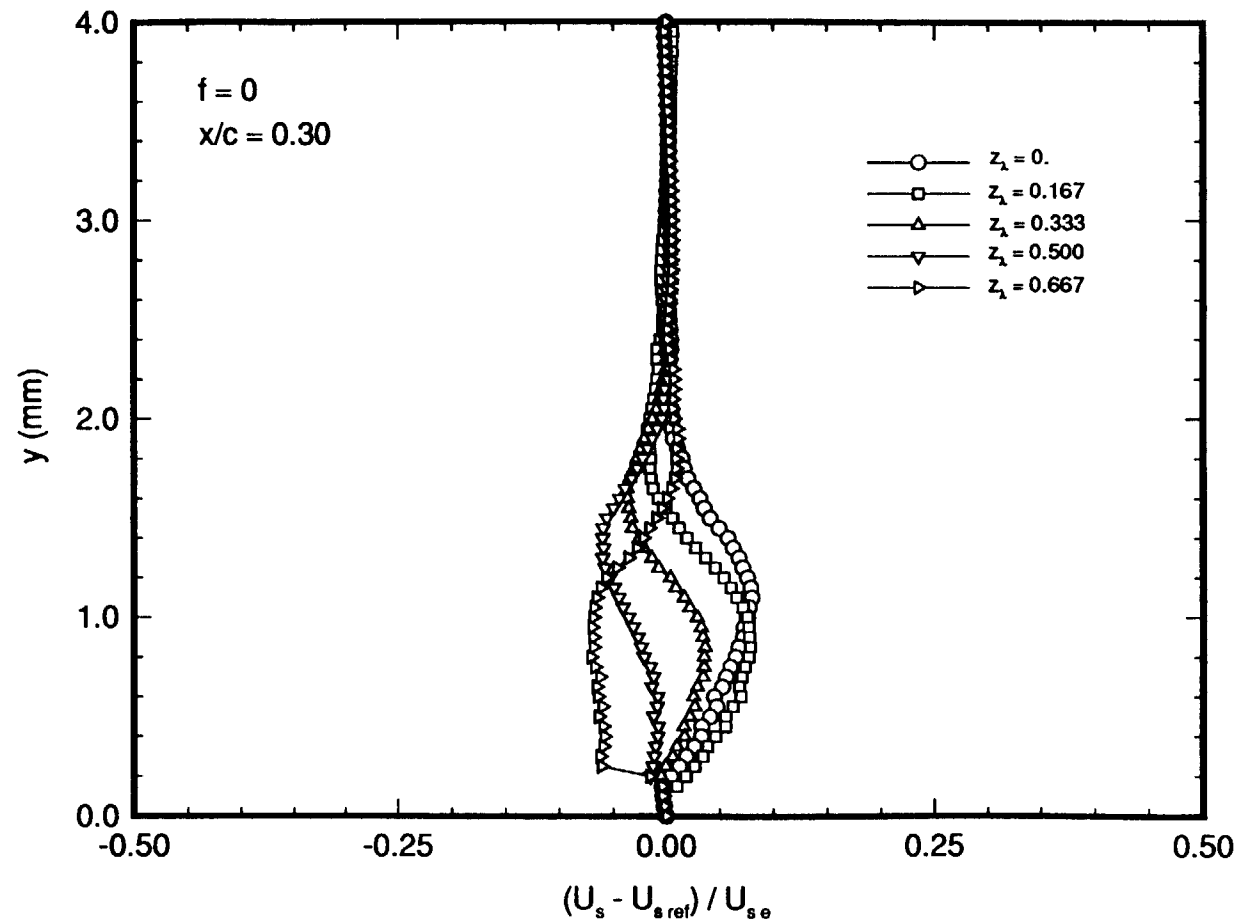


Figure 75. Stationary Crossflow-Disturbance Velocity Profiles at $x/c = 0.30$, $\alpha = -4^\circ$, $R_c = 2.37 \times 10^6$ Obtained From $U_s - U_{s,ref}$.

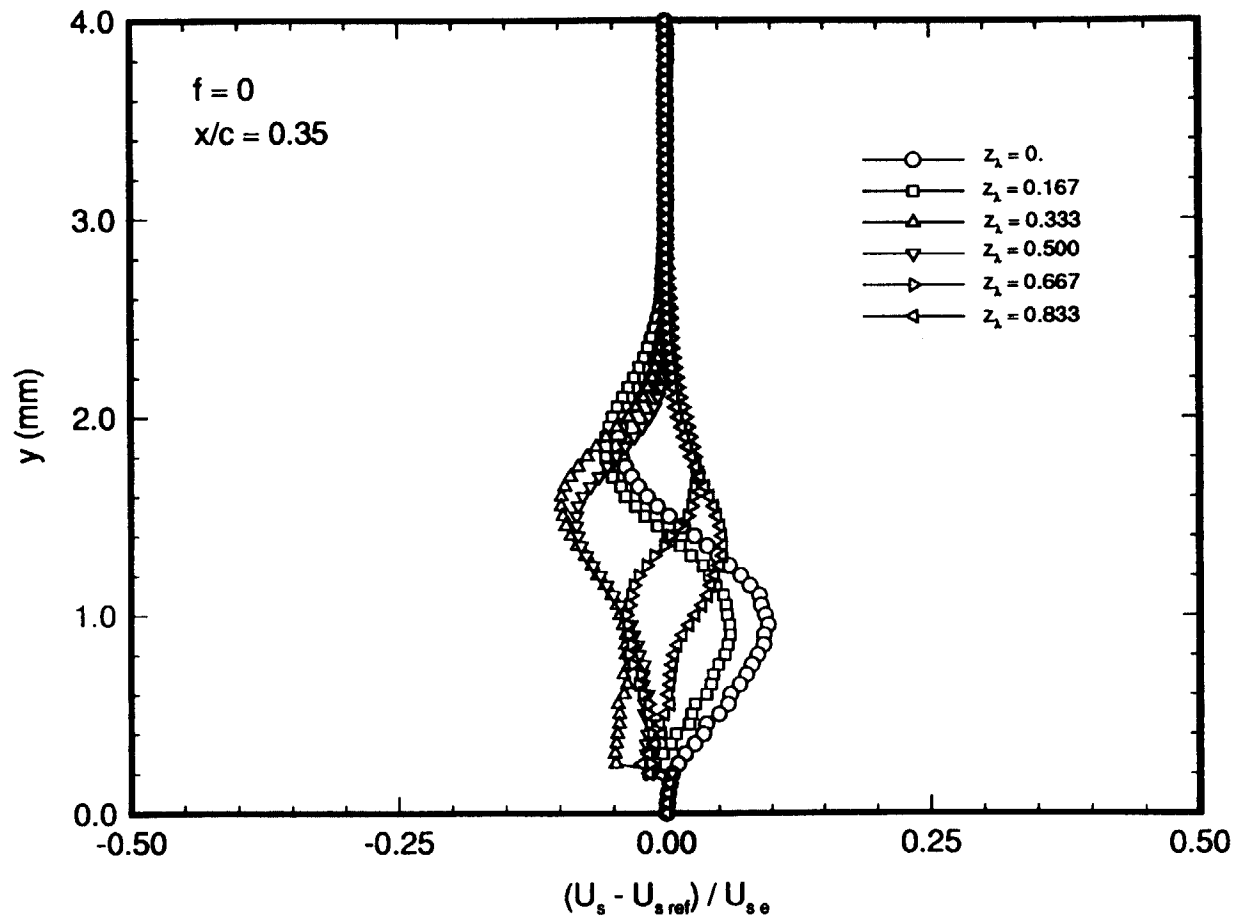


Figure 76. Stationary Crossflow-Disturbance Velocity Profiles at $x/c = 0.35$, $\alpha = -4^\circ$, $R_c = 2.37 \times 10^6$ Obtained From $U_s - U_{s,ref}$.

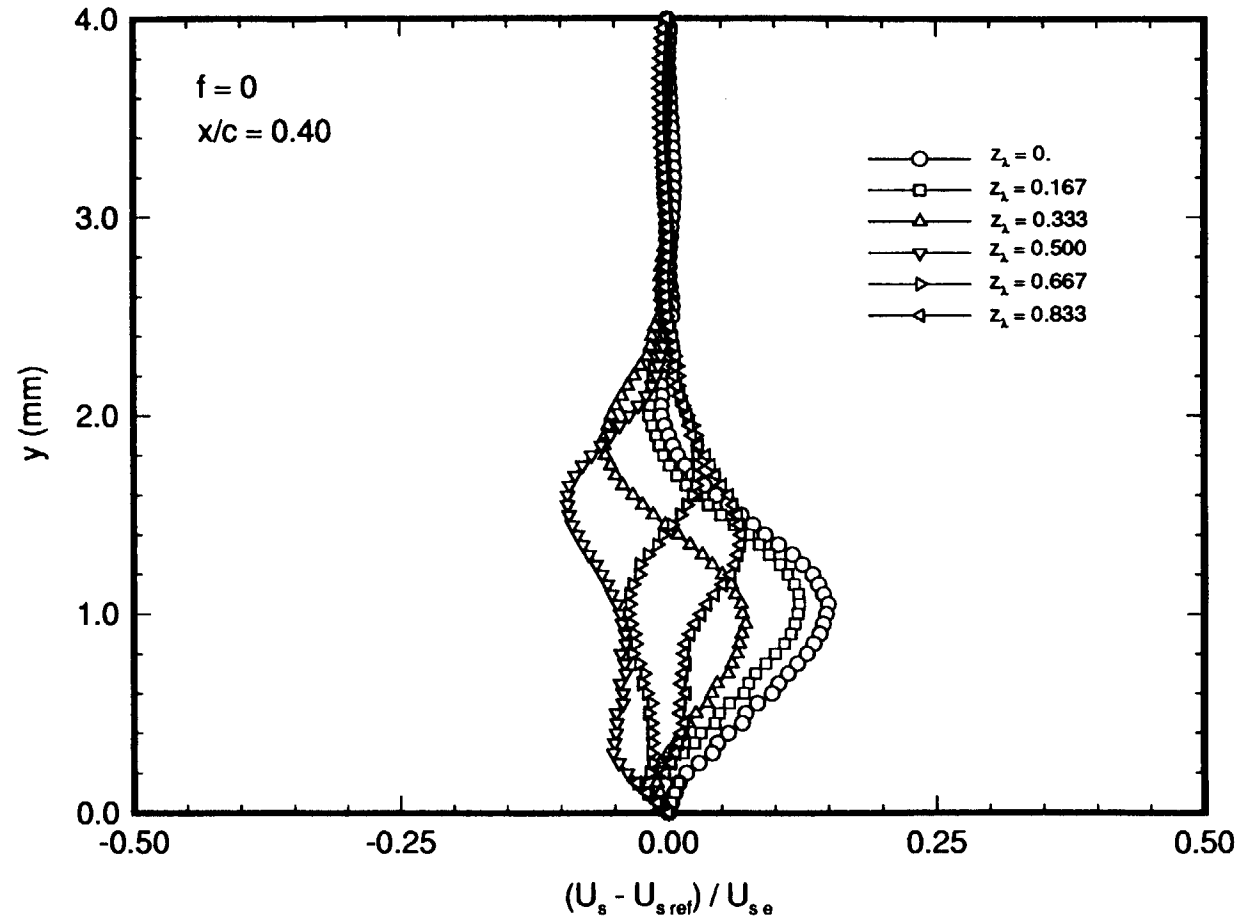


Figure 77. Stationary Crossflow-Disturbance Velocity Profiles at $x/c = 0.40$, $\alpha = -4^\circ$, $R_c = 2.37 \times 10^6$ Obtained From $U_s - U_{s\text{ref}}$.

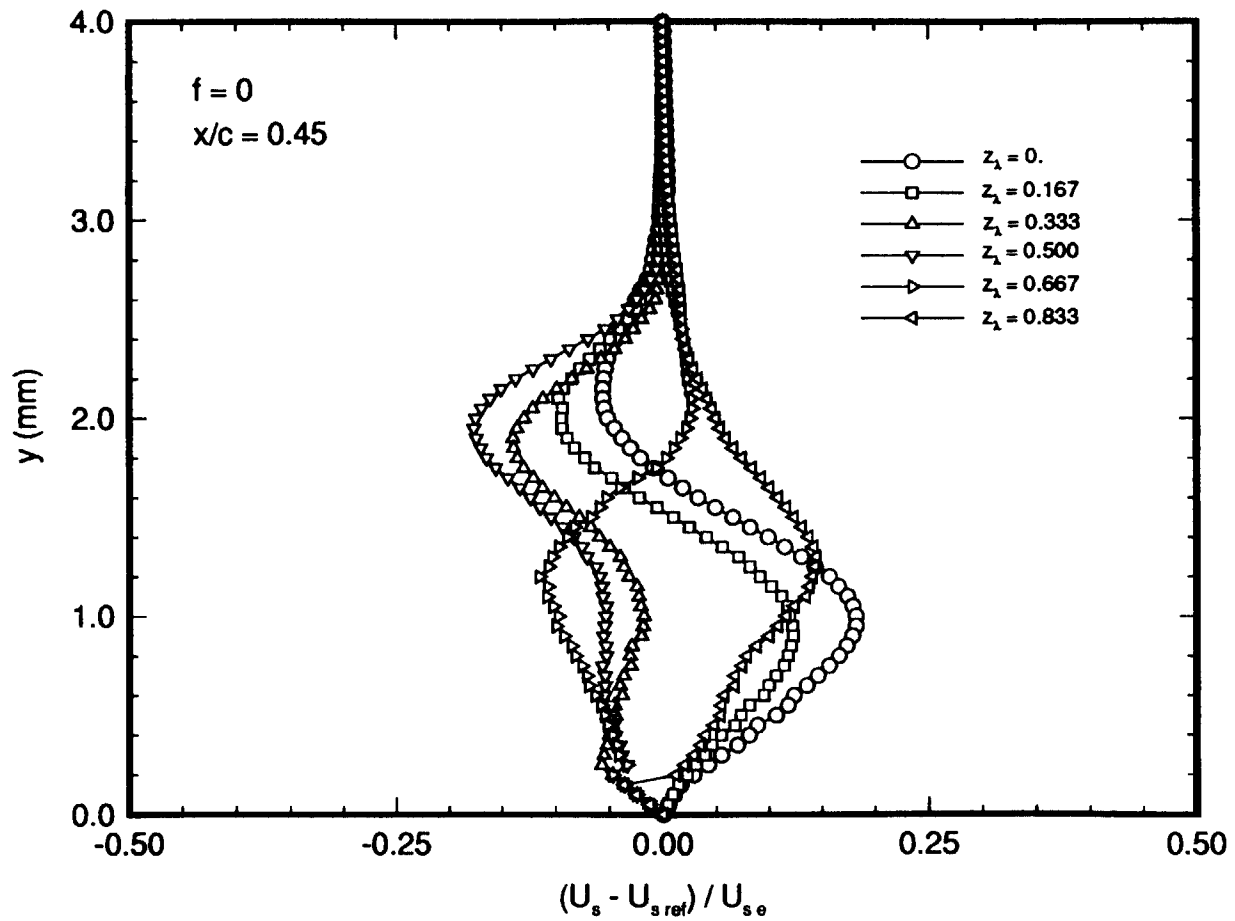


Figure 78. Stationary Crossflow-Disturbance Velocity Profiles at $x/c = 0.45$, $\alpha = -4^\circ$, $R_c = 2.37 \times 10^6$ Obtained From $U_s - U_{s,ref}$.

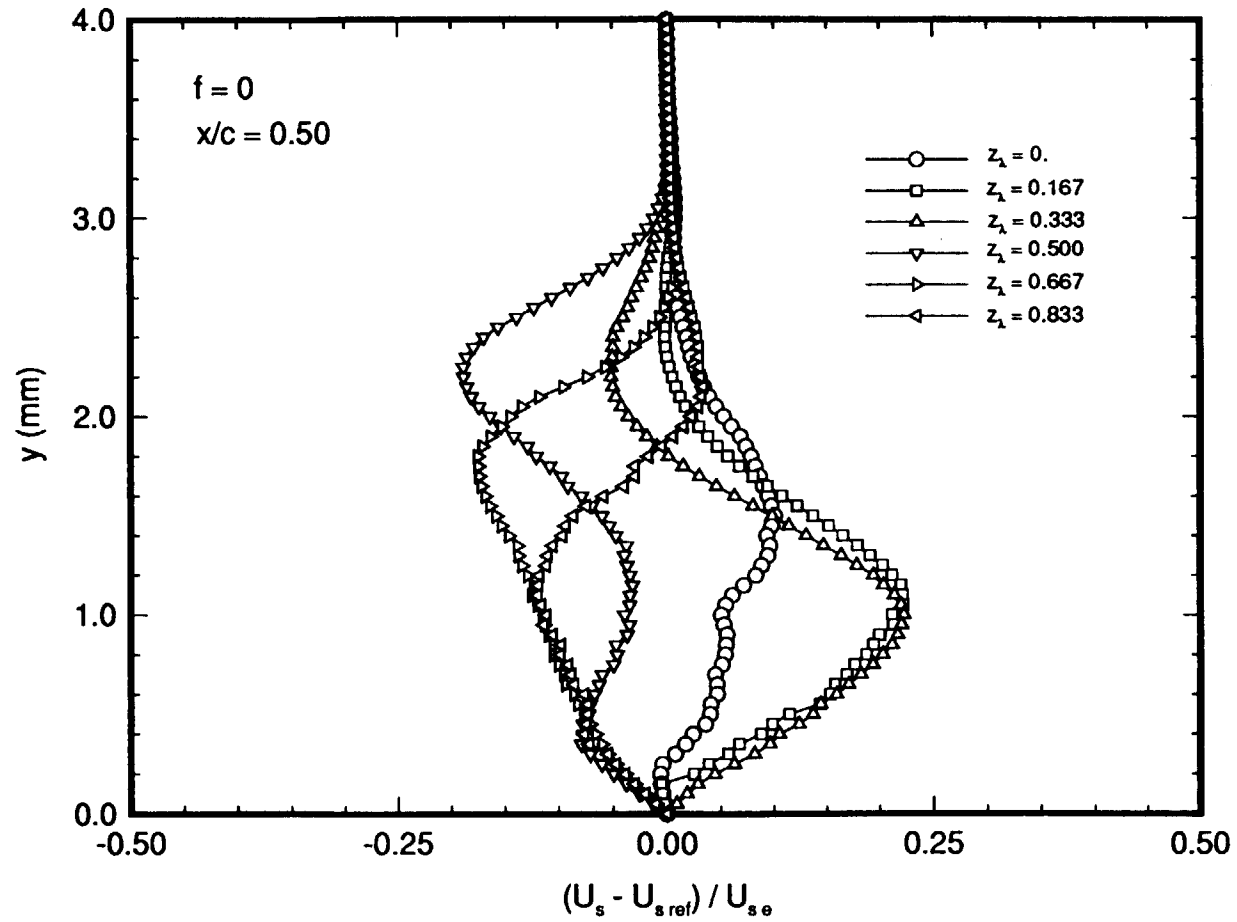


Figure 79. Stationary Crossflow-Disturbance Velocity Profiles at $x/c = 0.50$, $\alpha = -4^\circ$, $R_c = 2.37 \times 10^6$ Obtained From $U_s - U_{s,ref}$.

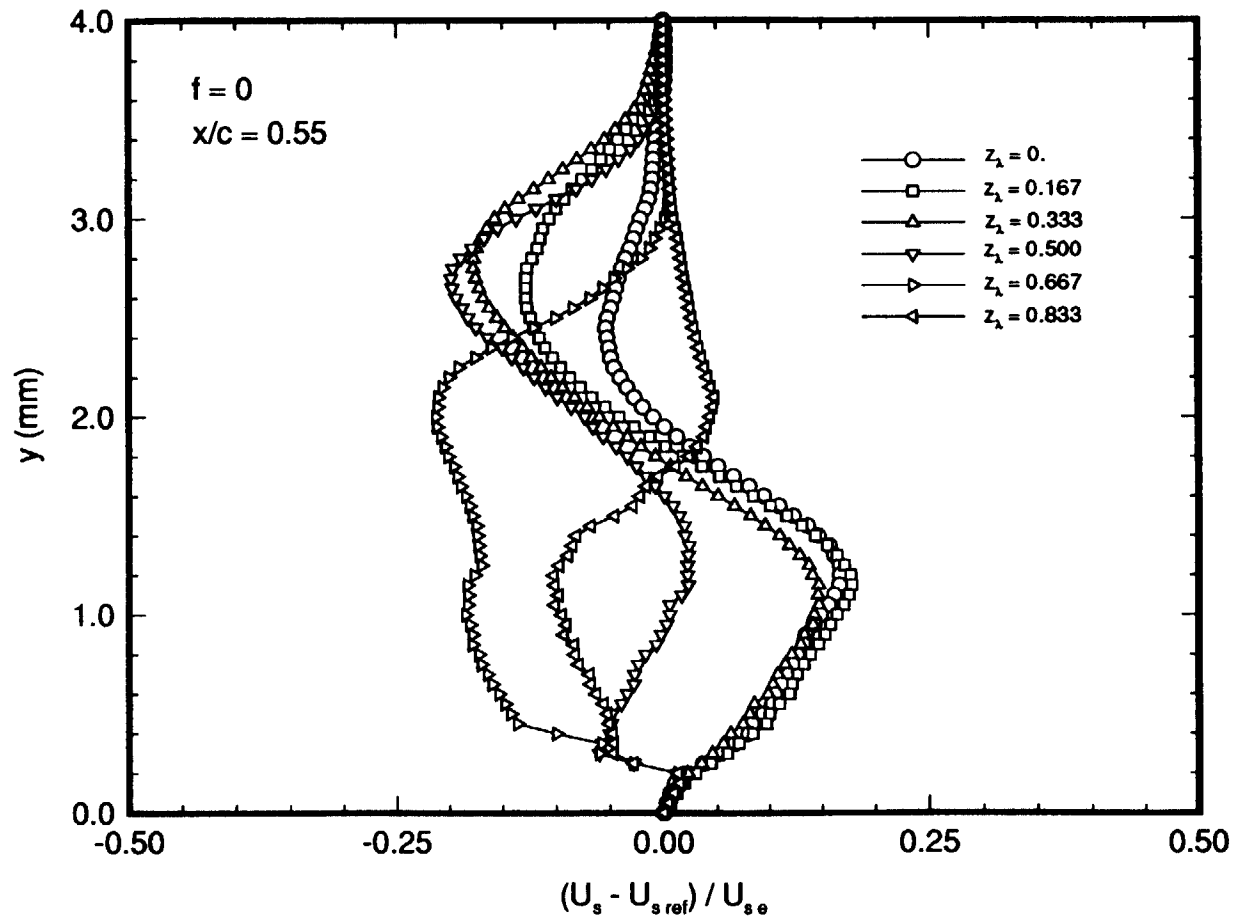


Figure 80. Stationary Crossflow-Disturbance Velocity Profiles at $x/c = 0.55$, $\alpha = -4^\circ$, $R_c = 2.37 \times 10^6$ Obtained From $U_s - U_{s\text{ref}}$.

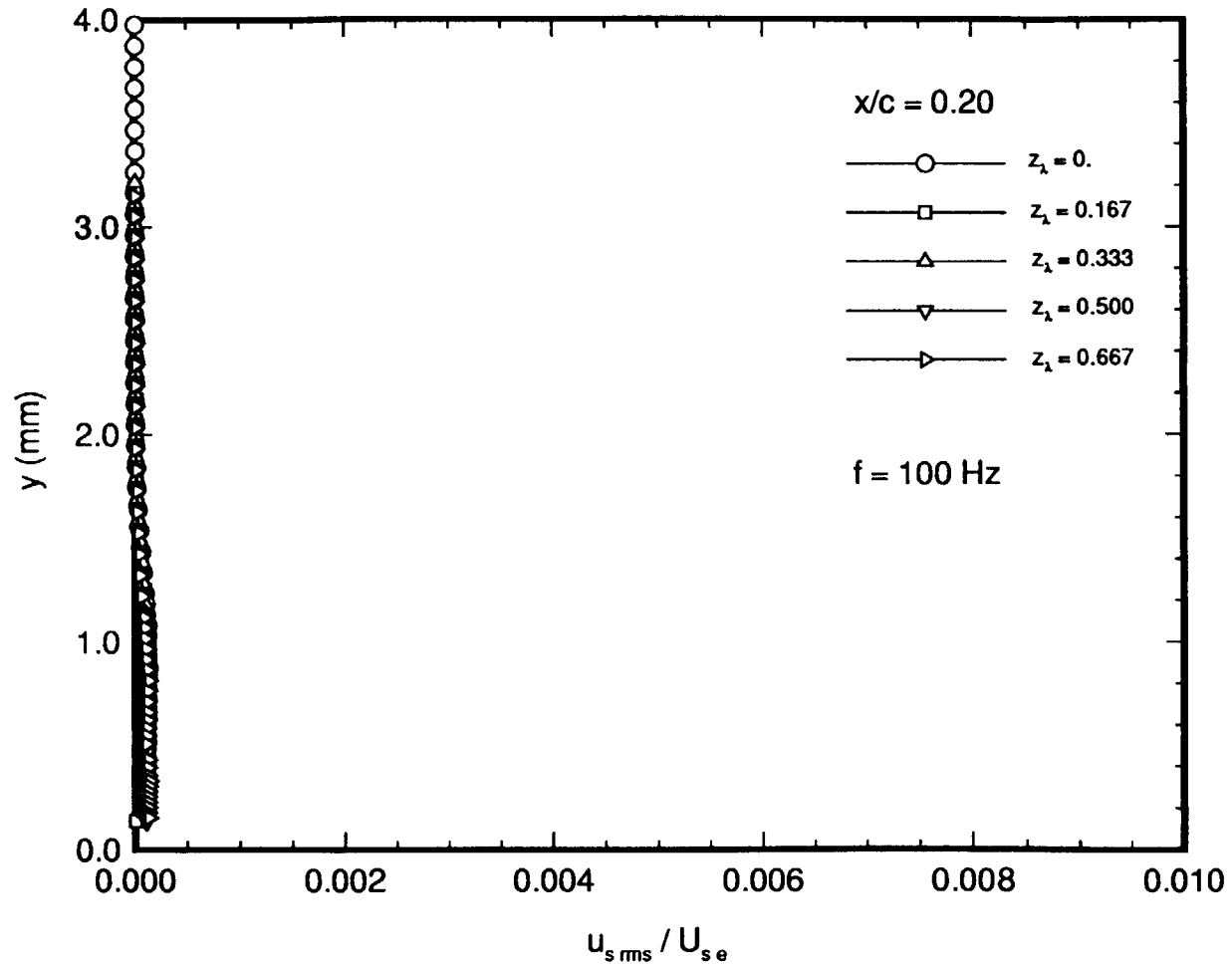


Figure 81. Travelling Wave Disturbance Velocity Profiles for $f = 100 \text{ Hz}$ at $x/c = 0.20$, $\alpha = -4^\circ$, $R_c = 2.37 \times 10^6$.

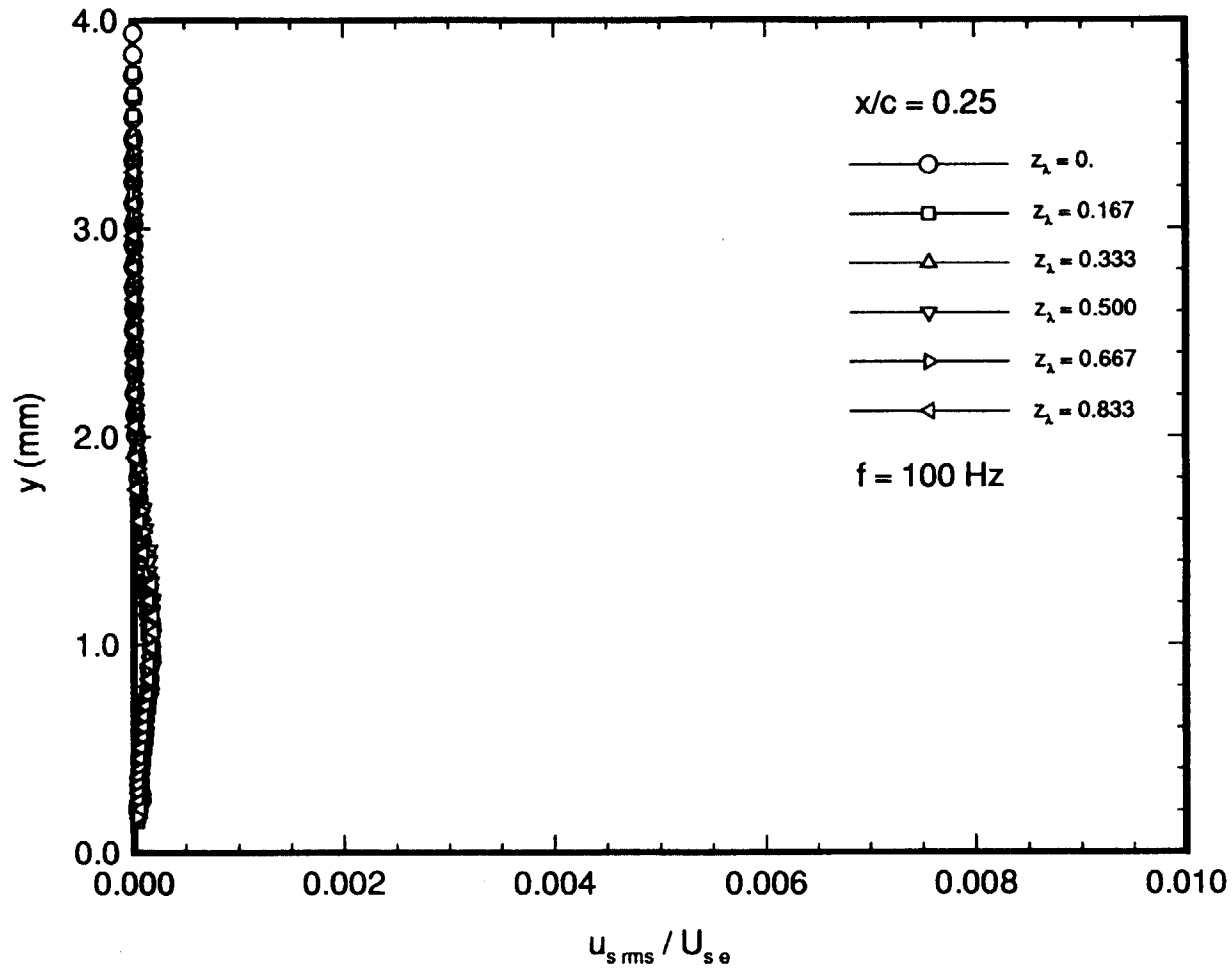


Figure 82. Travelling Wave Disturbance Velocity Profiles for $f = 100 \text{ Hz}$ at $x/c = 0.25$, $\alpha = -4^\circ$, $R_c = 2.37 \times 10^6$.

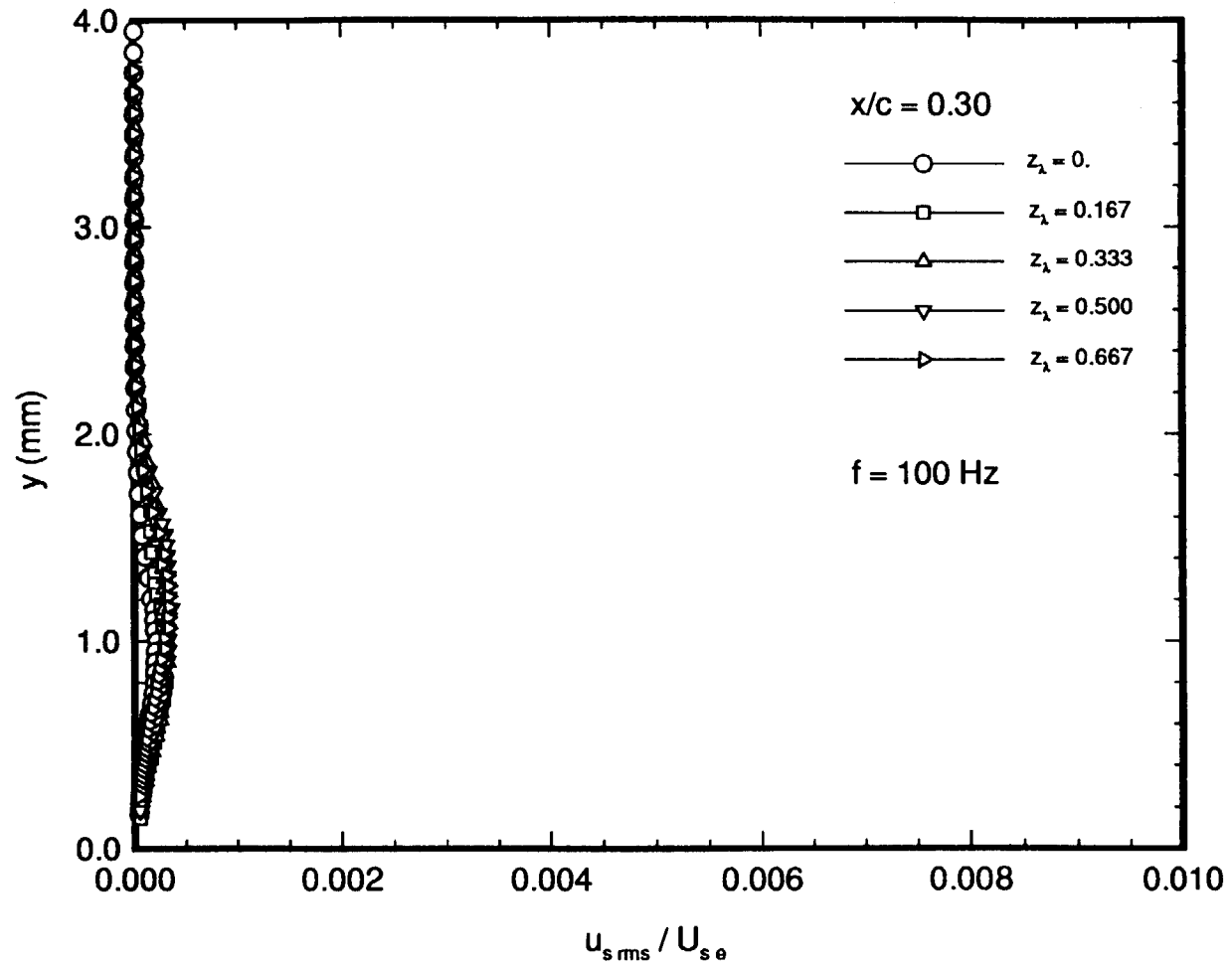


Figure 83. Travelling Wave Disturbance Velocity Profiles for $f = 100 \text{ Hz}$ at $x/c = 0.30$, $\alpha = -4^\circ$, $R_c = 2.37 \times 10^6$.

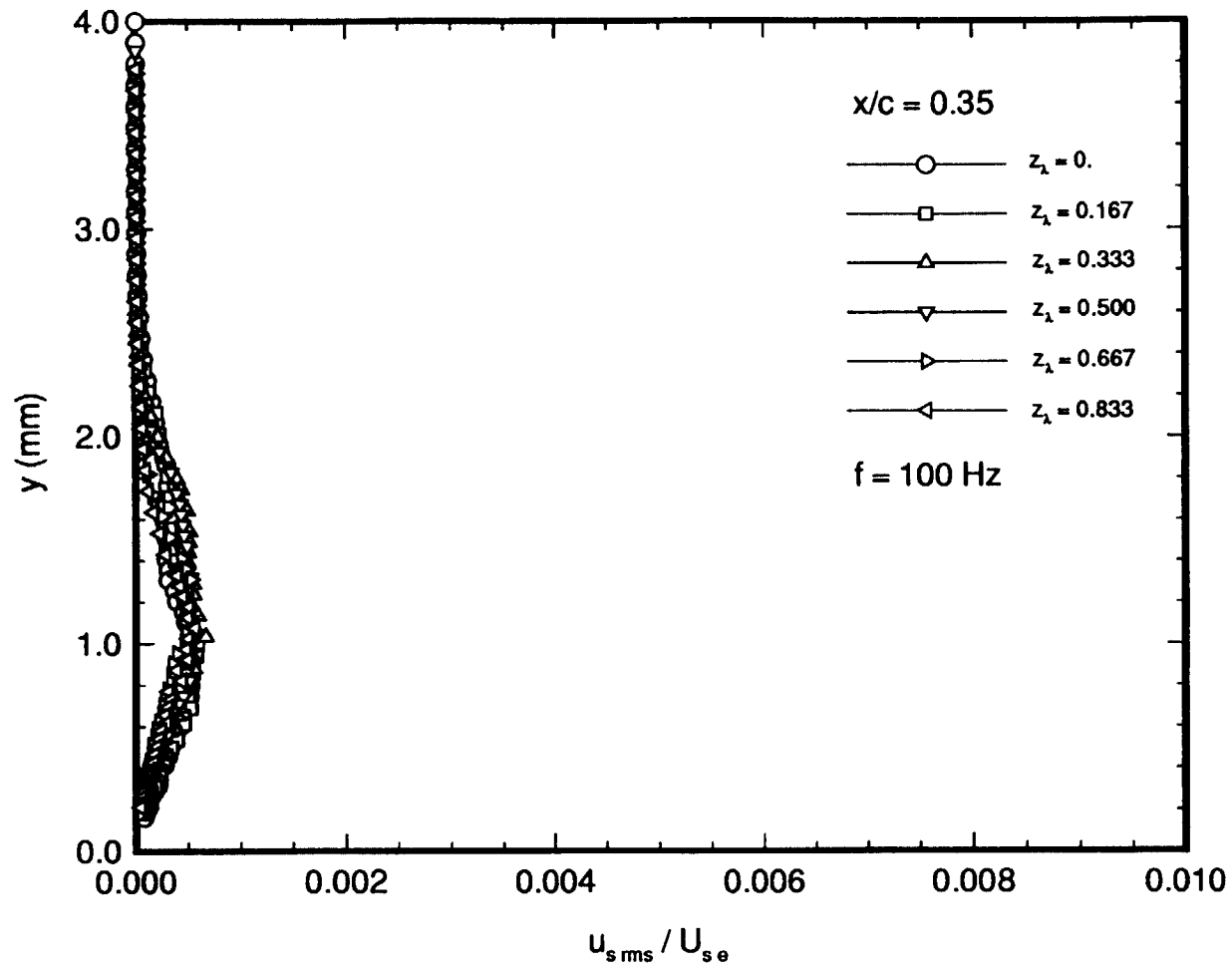


Figure 84. Travelling Wave Disturbance Velocity Profiles for $f = 100$ Hz at $x/c = 0.35$, $\alpha = -4^\circ$, $R_c = 2.37 \times 10^6$.

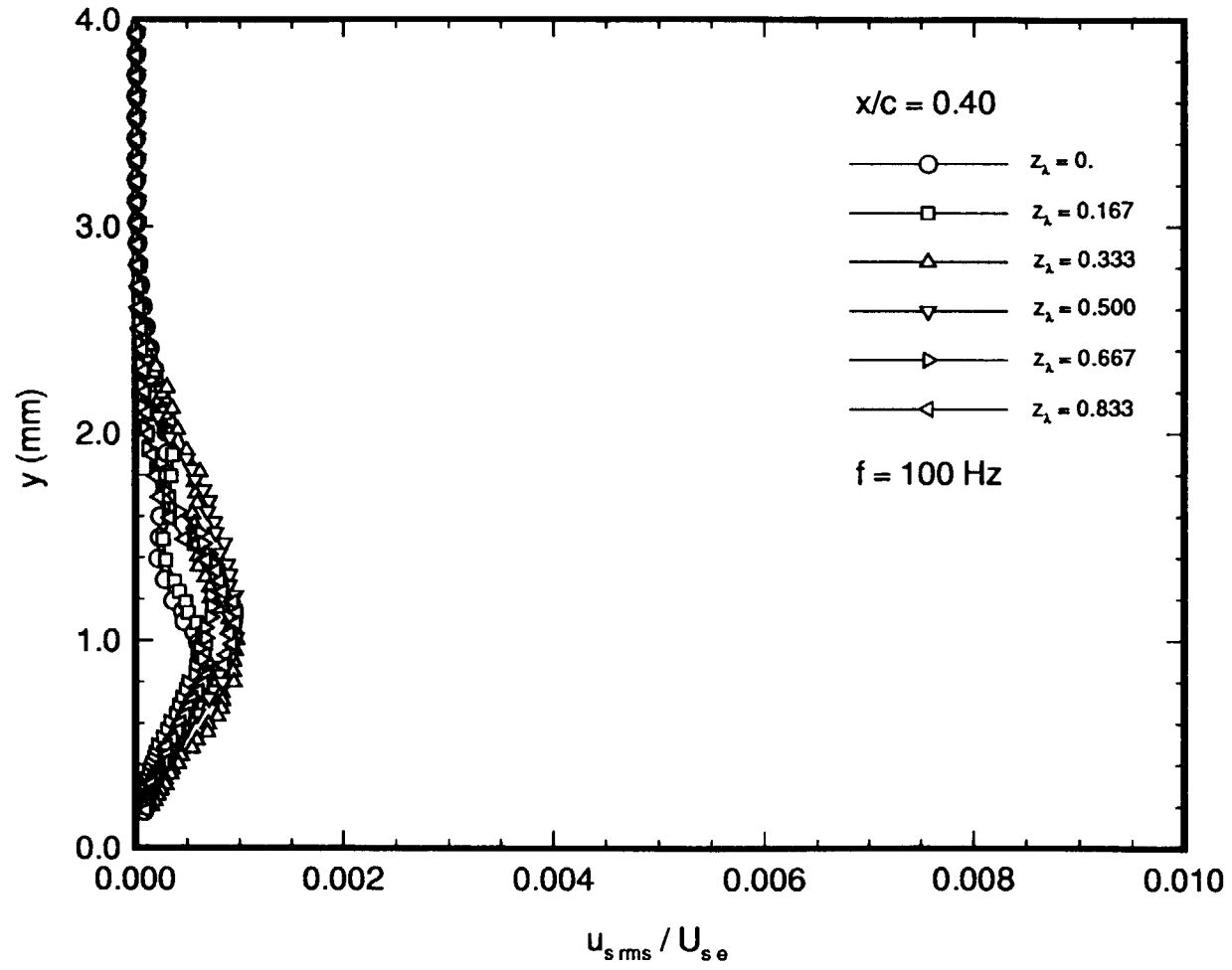


Figure 85. Travelling Wave Disturbance Velocity Profiles for $f = 100$ Hz at $x/c = 0.40$, $\alpha = -4^\circ$, $R_c = 2.37 \times 10^6$.

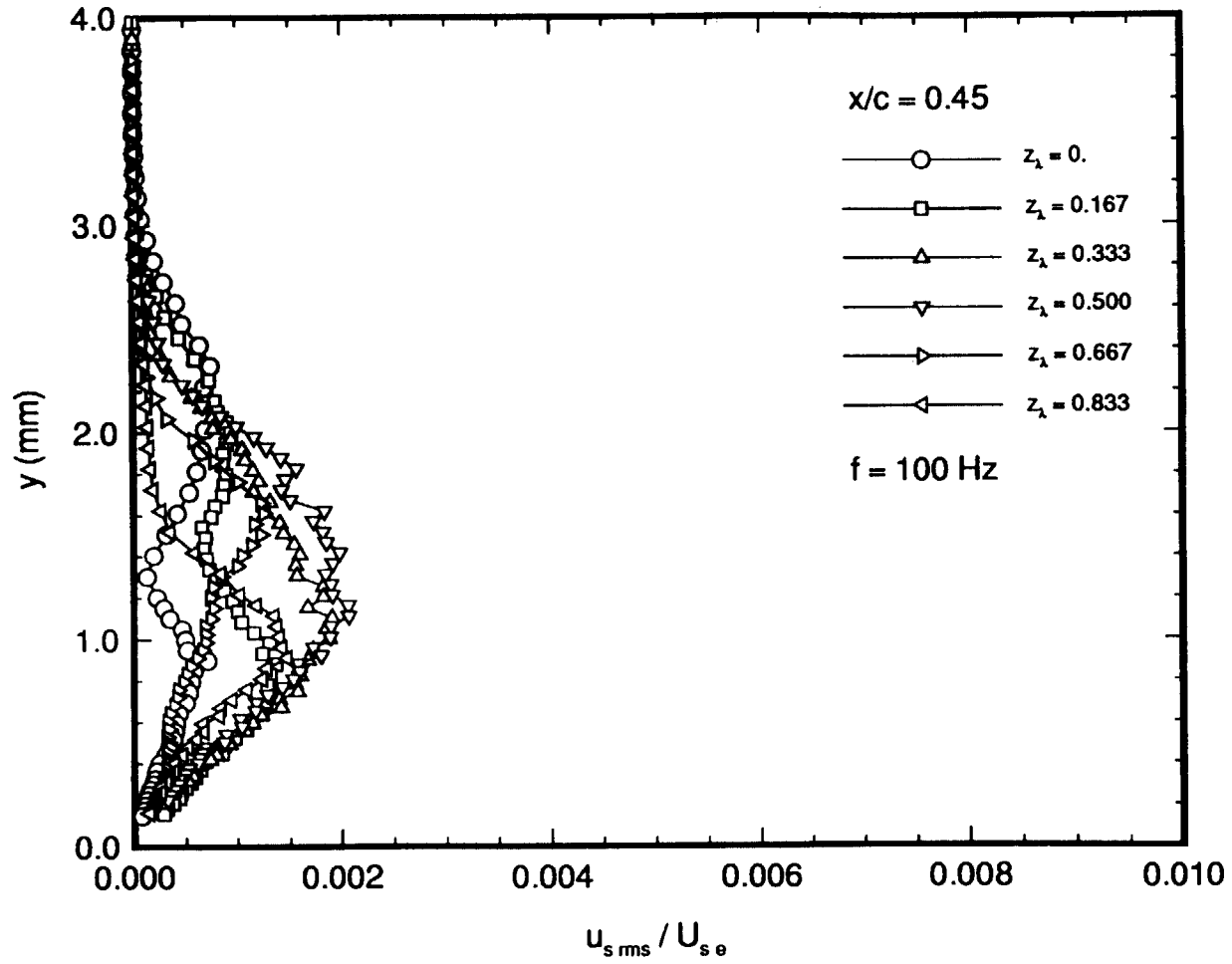


Figure 86. Travelling Wave Disturbance Velocity Profiles for $f = 100$ Hz at $x/c = 0.45$, $\alpha = -4^\circ$, $R_c = 2.37 \times 10^6$.

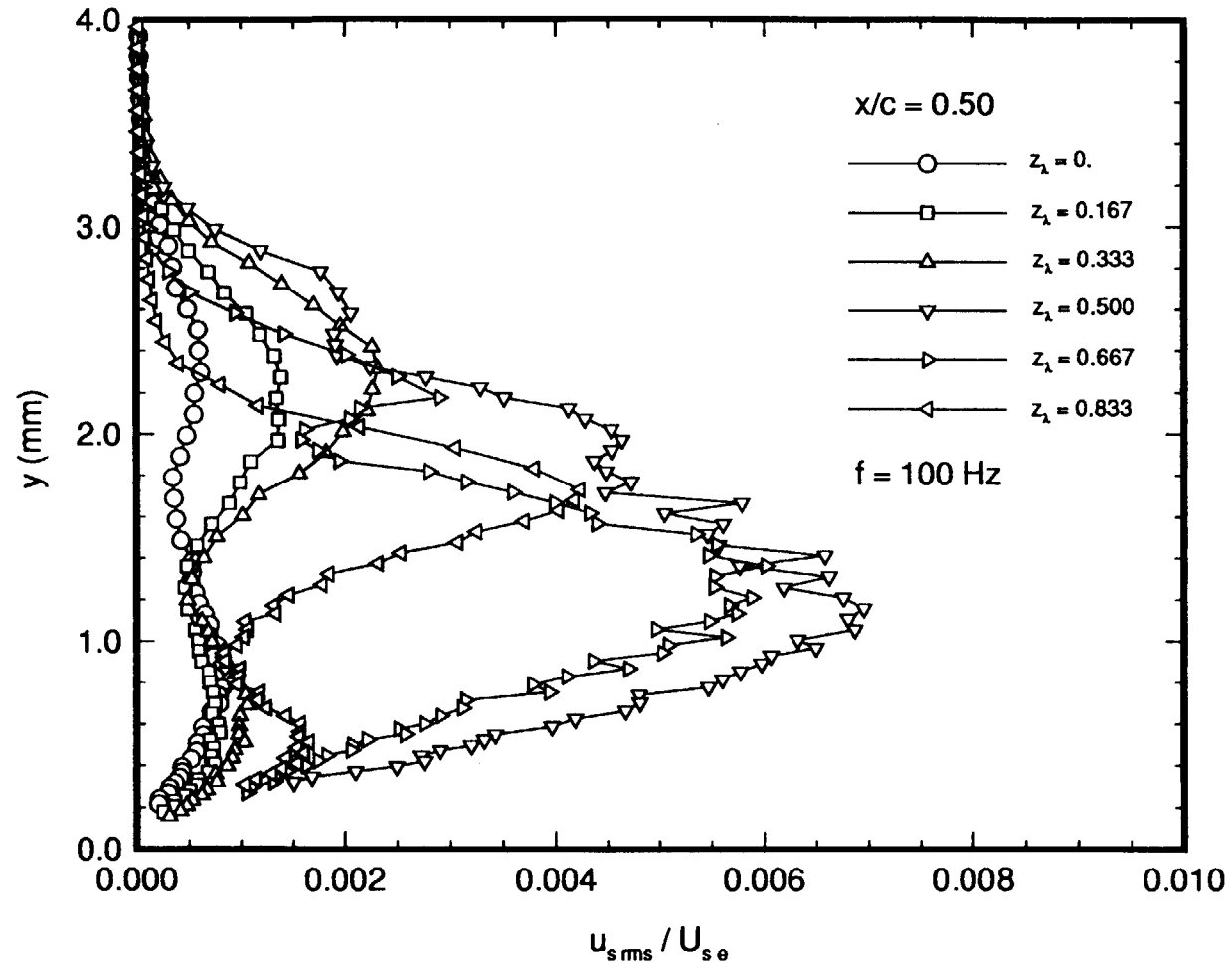


Figure 87. Travelling Wave Disturbance Velocity Profiles for $f = 100 \text{ Hz}$ at $x/c = 0.50$, $\alpha = -4^\circ$, $R_c = 2.37 \times 10^6$.

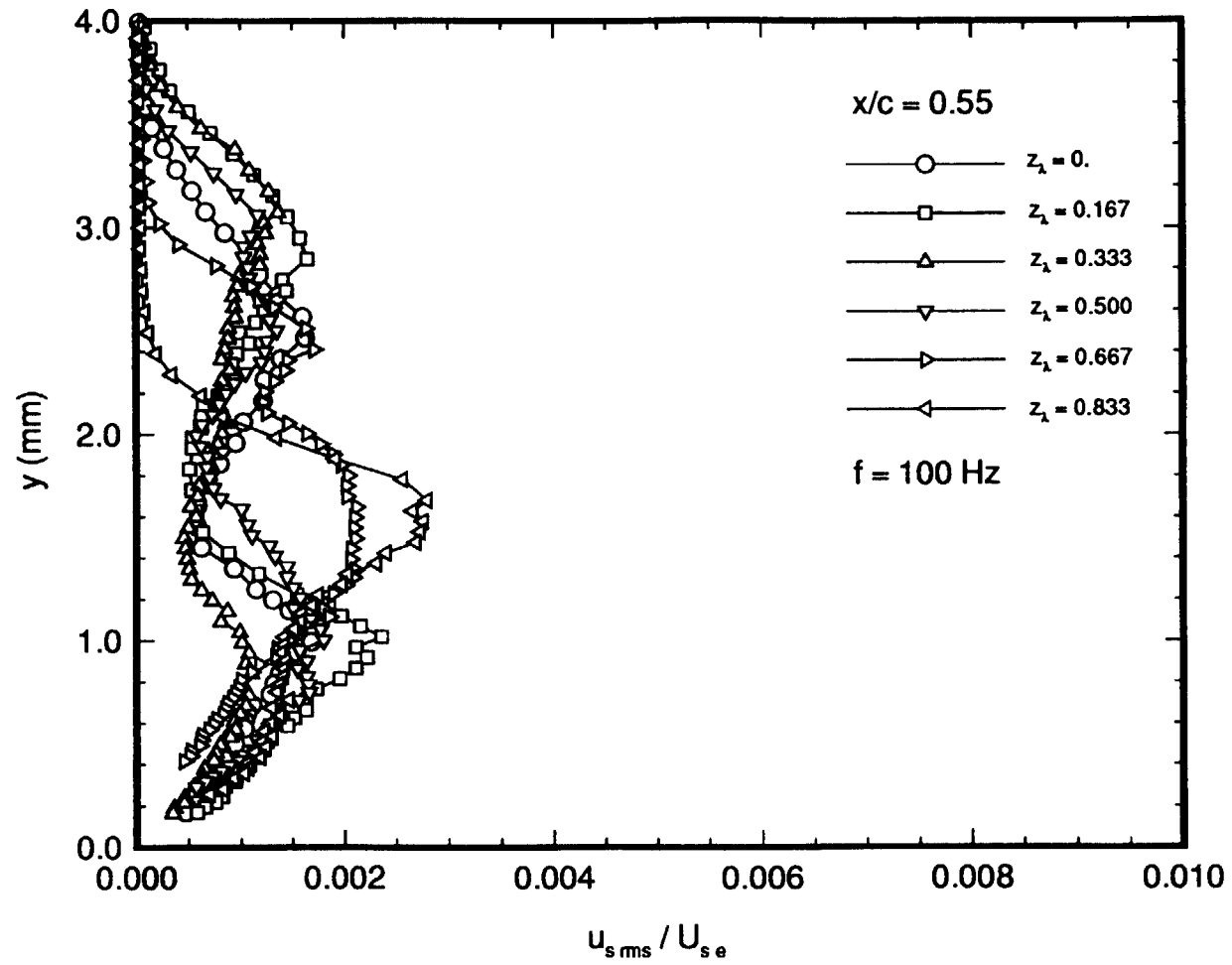


Figure 88. Travelling Wave Disturbance Velocity Profiles for $f = 100 \text{ Hz}$ at $x/c = 0.55$, $\alpha = -4^\circ$, $R_c = 2.37 \times 10^6$.

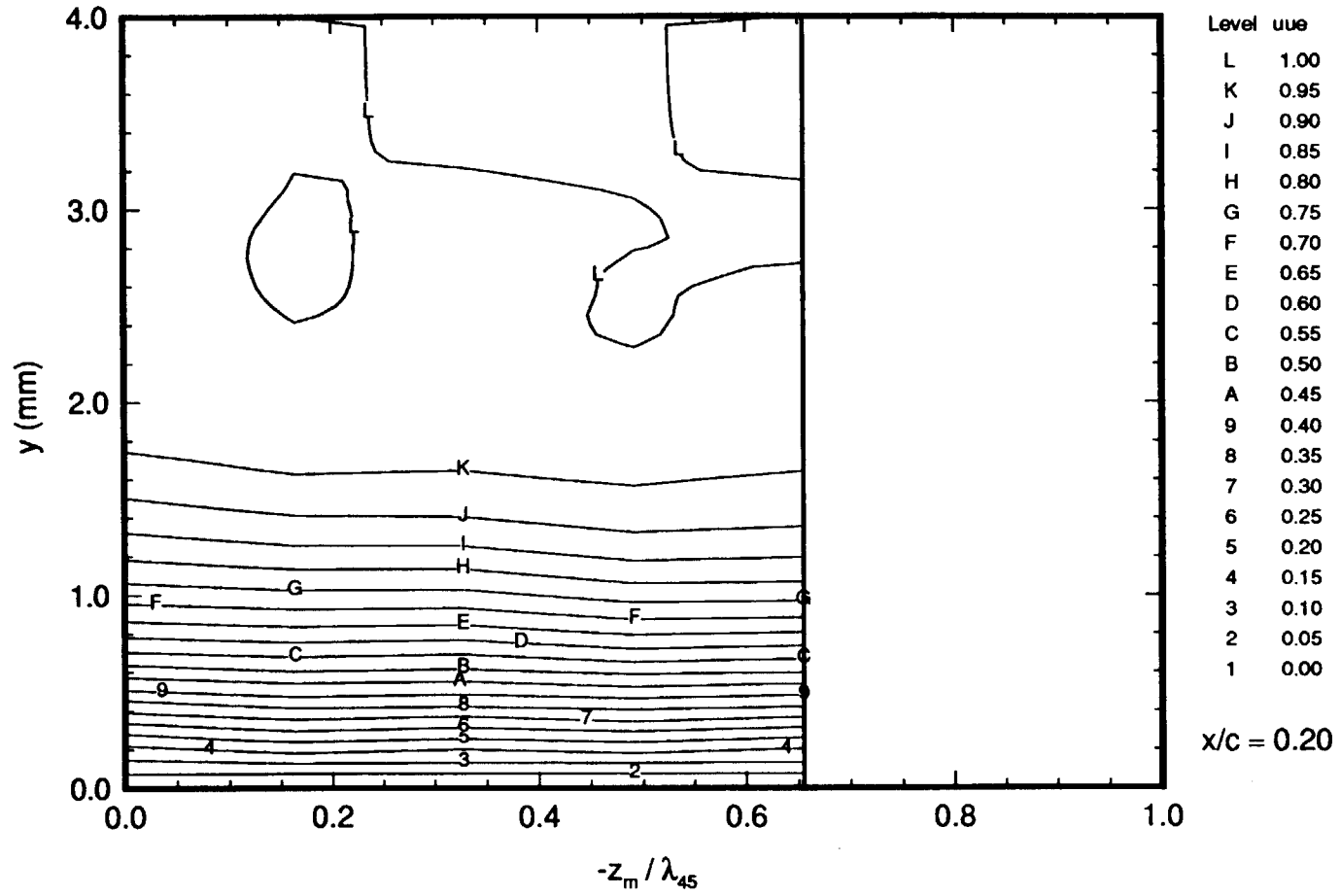


Figure 89. Mean Streamwise-Velocity Contours at $x/c = 0.20$, $\alpha = -4^\circ$, $R_c = 2.37 \times 10^6$.

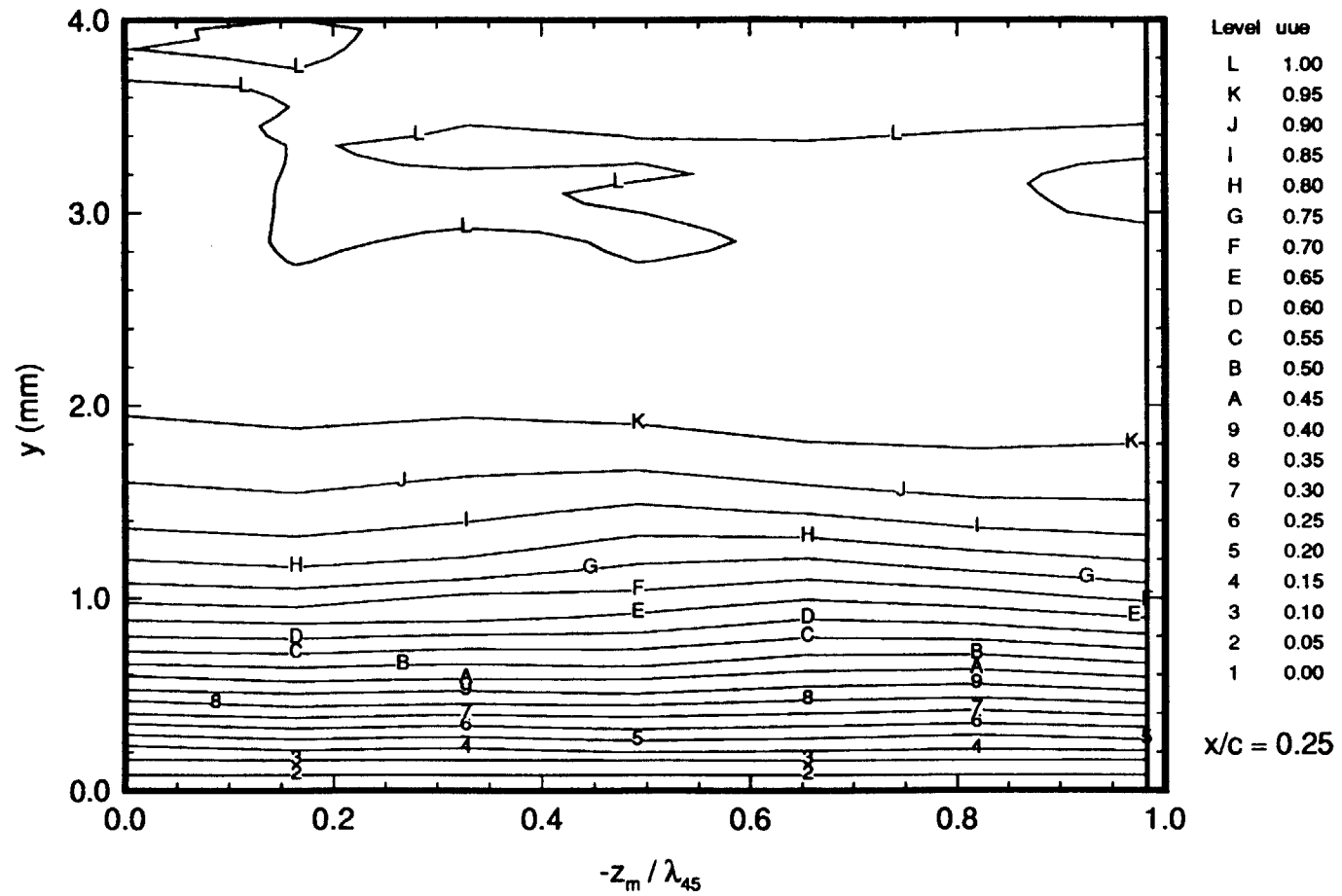


Figure 90. Mean Streamwise-Velocity Contours at $x/c = 0.25$, $\alpha = -4^\circ$, $R_c = 2.37 \times 10^6$.

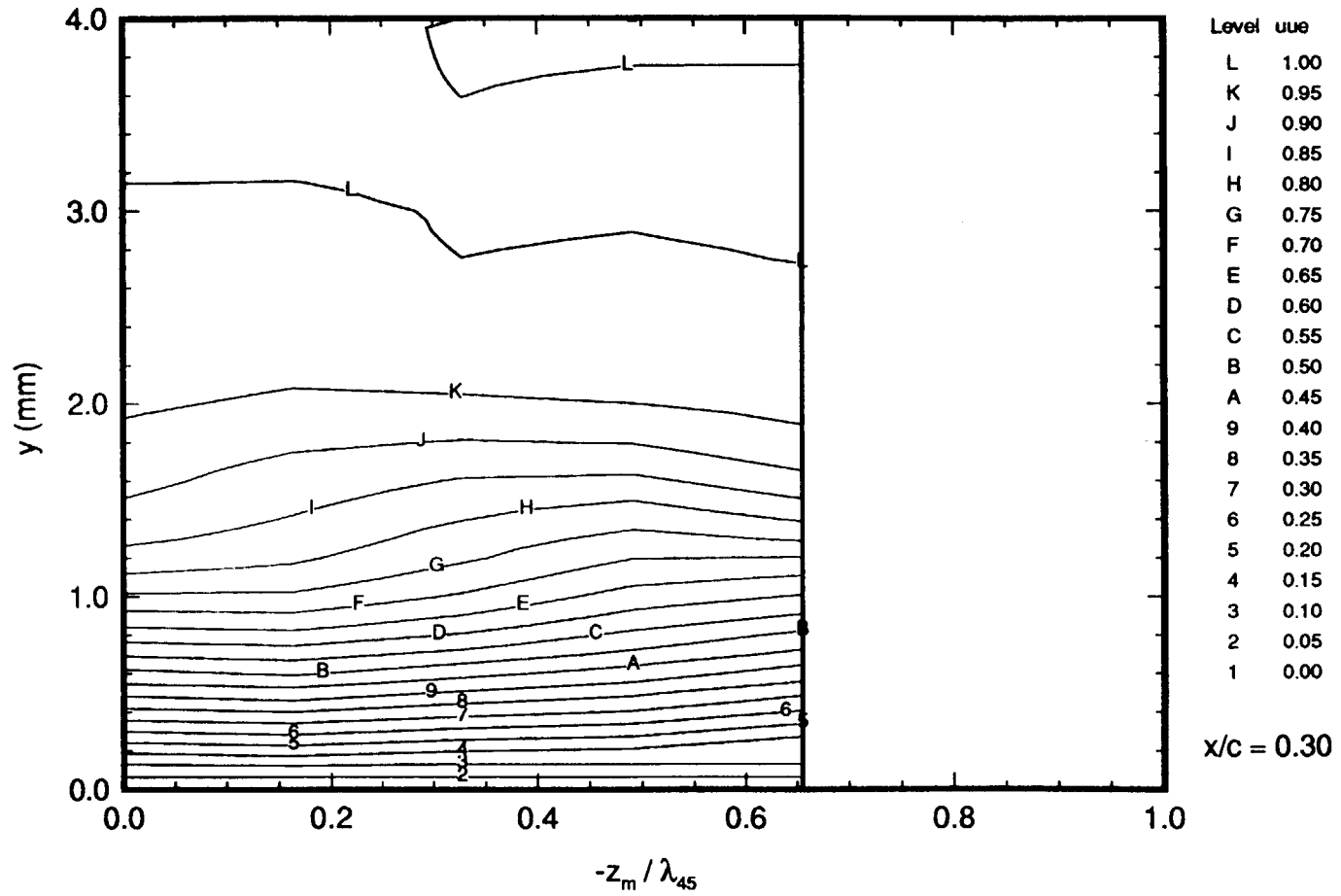


Figure 91. Mean Streamwise-Velocity Contours at $x/c = 0.30$, $\alpha = -4^\circ$, $R_c = 2.37 \times 10^6$.

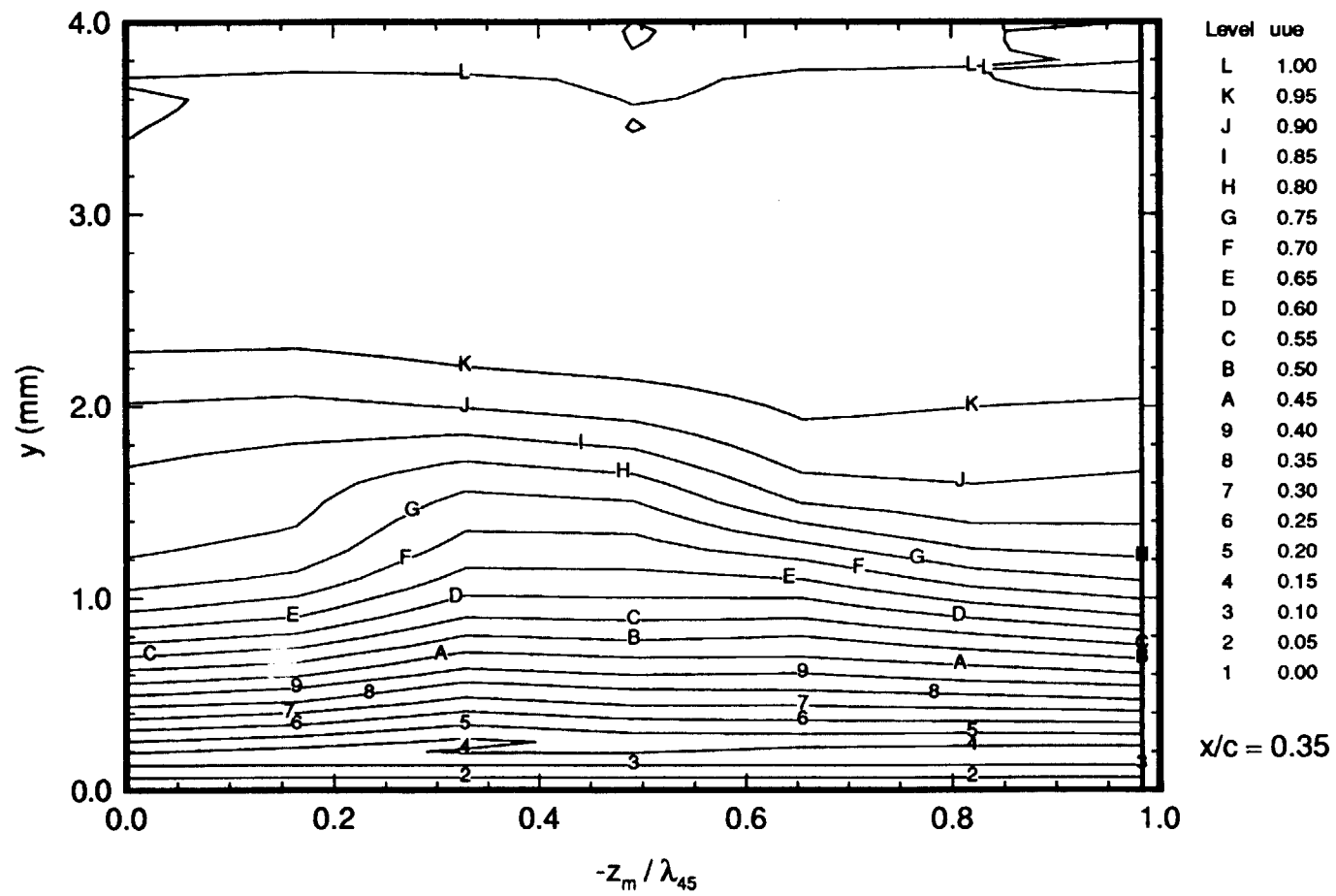


Figure 92. Mean Streamwise-Velocity Contours at $x/c = 0.35$, $\alpha = -4^\circ$, $R_c = 2.37 \times 10^6$.

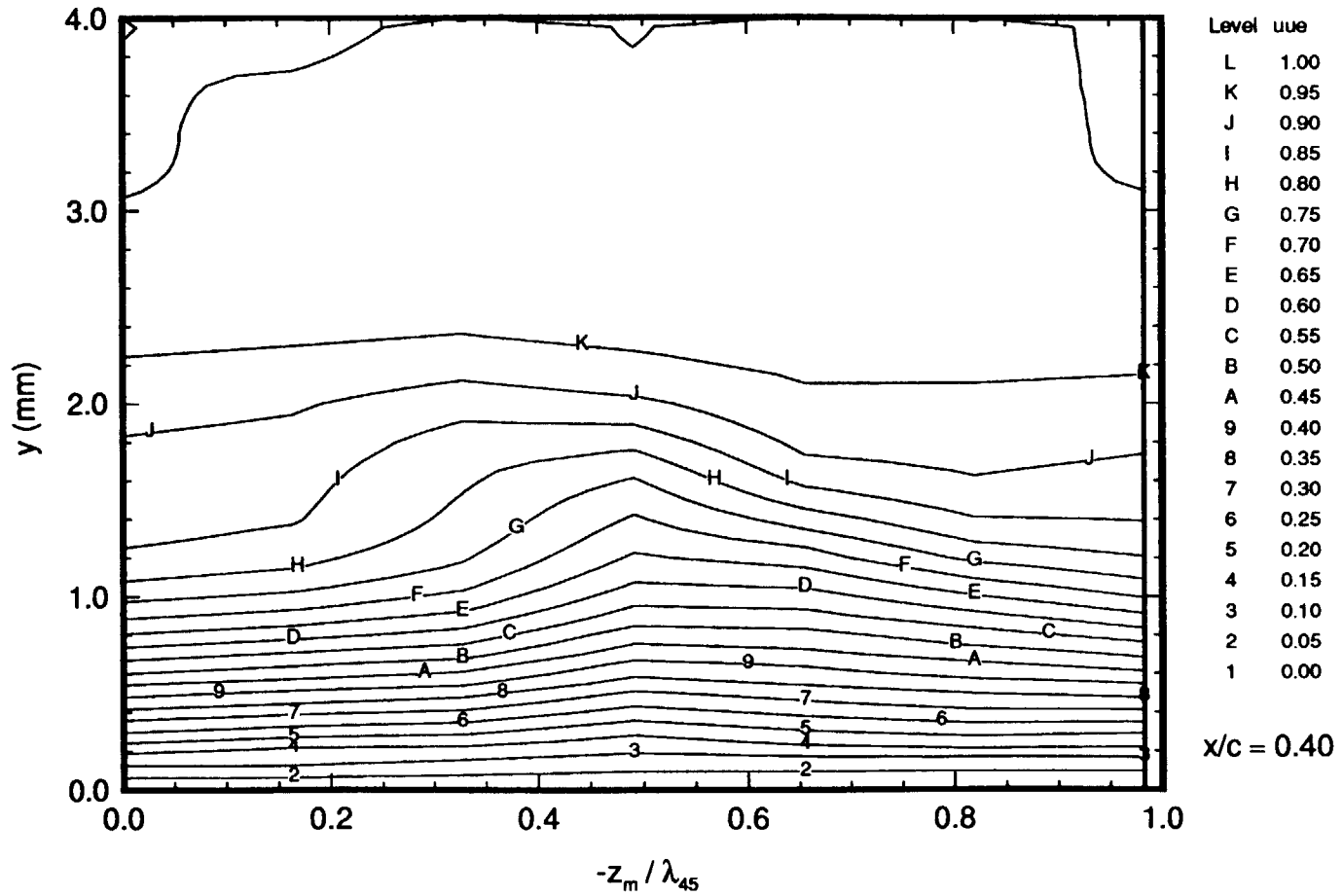


Figure 93. Mean Streamwise-Velocity Contours at $x/c = 0.40$, $\alpha = -4^\circ$, $R_c = 2.37 \times 10^6$.

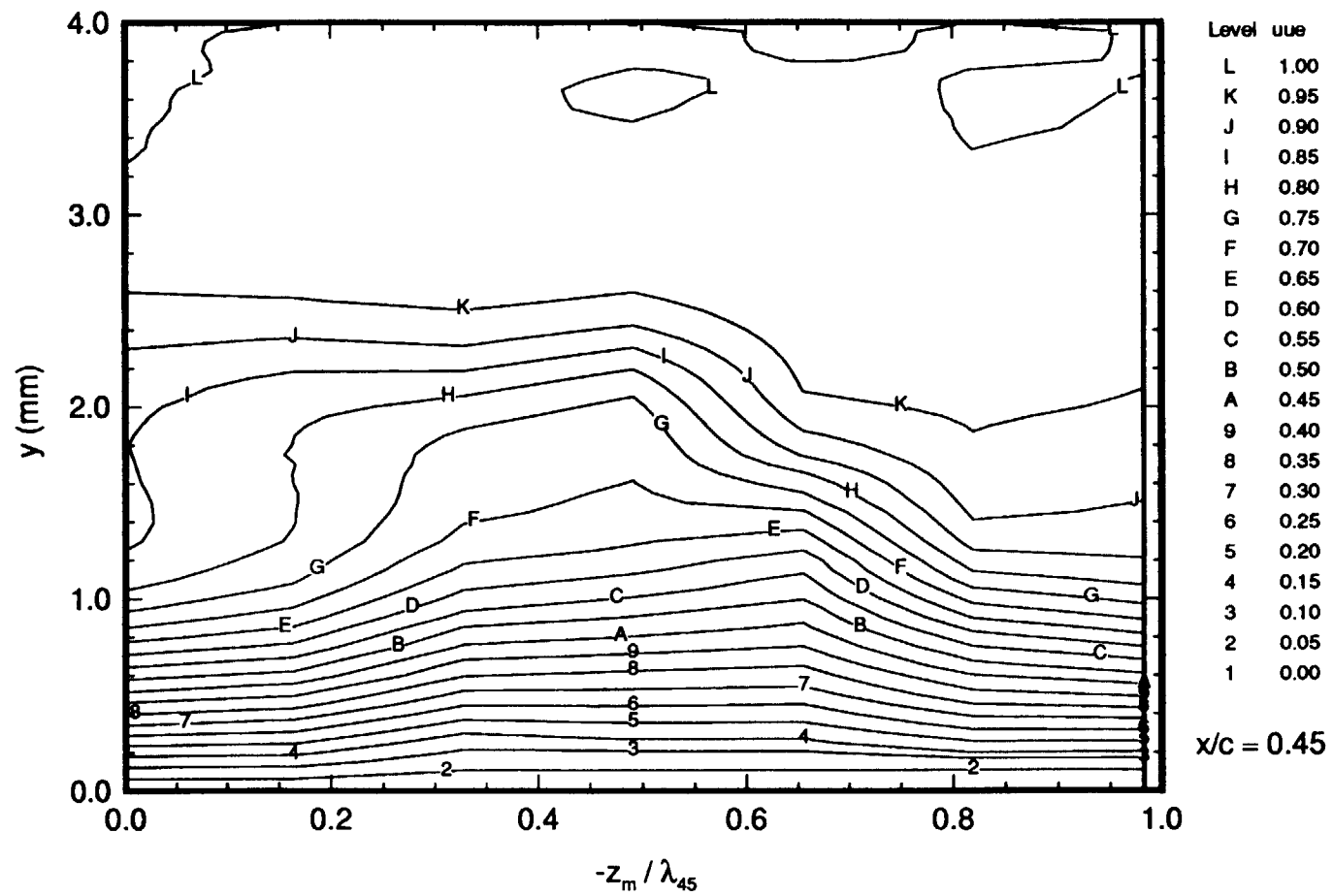


Figure 94. Mean Streamwise-Velocity Contours at $x/c = 0.45$, $\alpha = -4^\circ$, $R_c = 2.37 \times 10^6$.

0-3

179

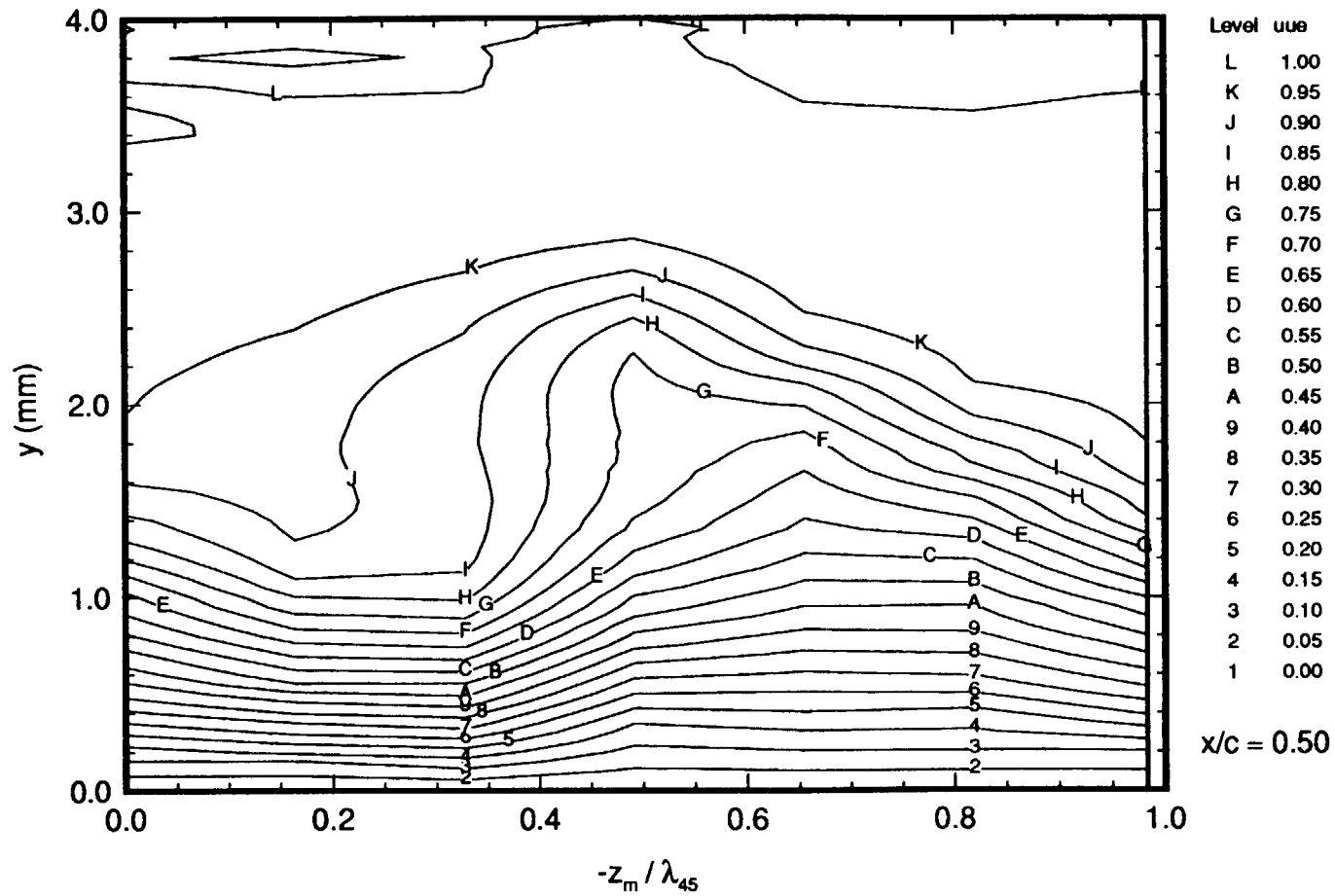


Figure 95. Mean Streamwise-Velocity Contours at $x/c = 0.50$, $\alpha = -4^\circ$, $R_c = 2.37 \times 10^6$.

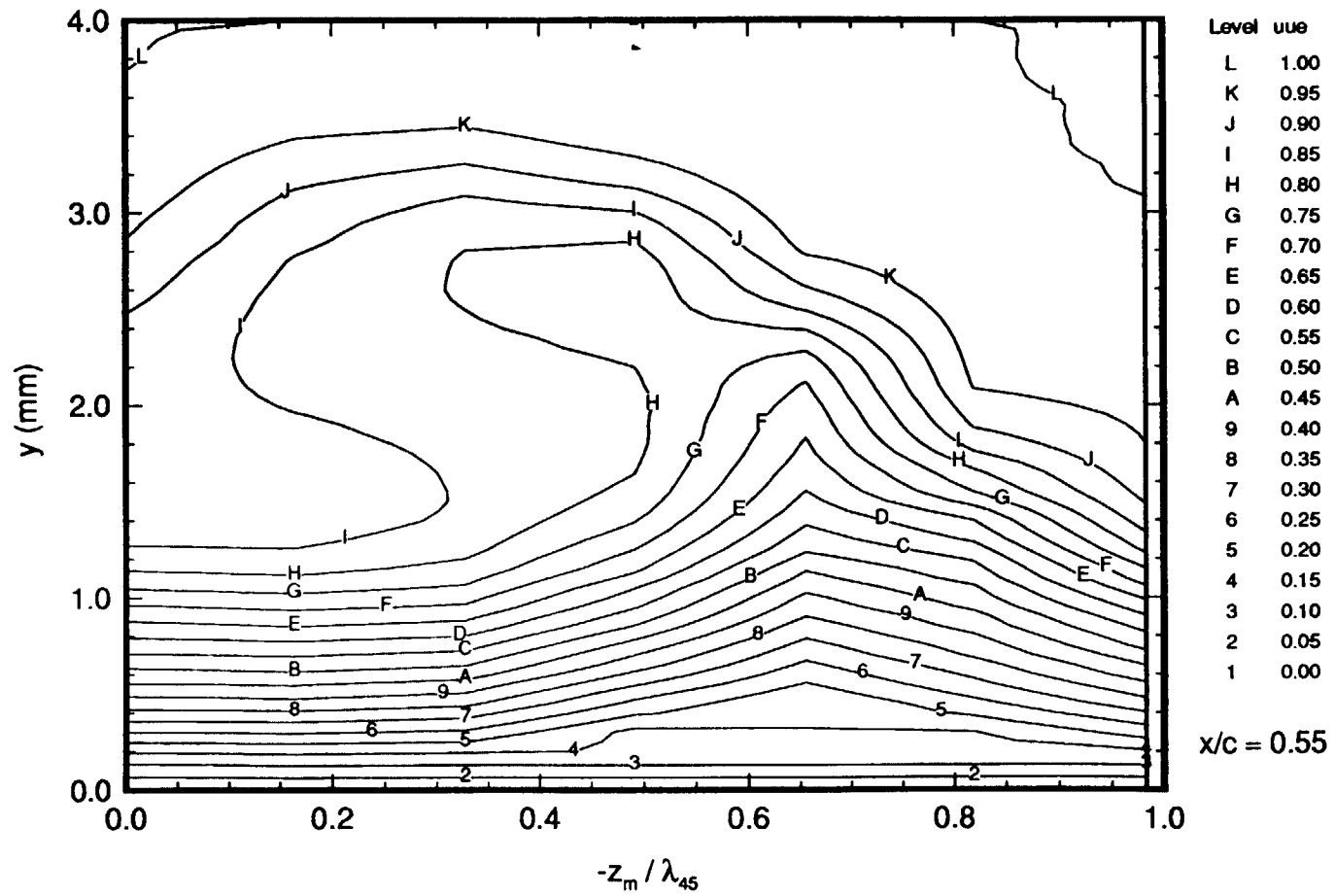


Figure 96. Mean Streamwise-Velocity Contours at $x/c = 0.55$, $\alpha = -4^\circ$, $R_c = 2.37 \times 10^6$.

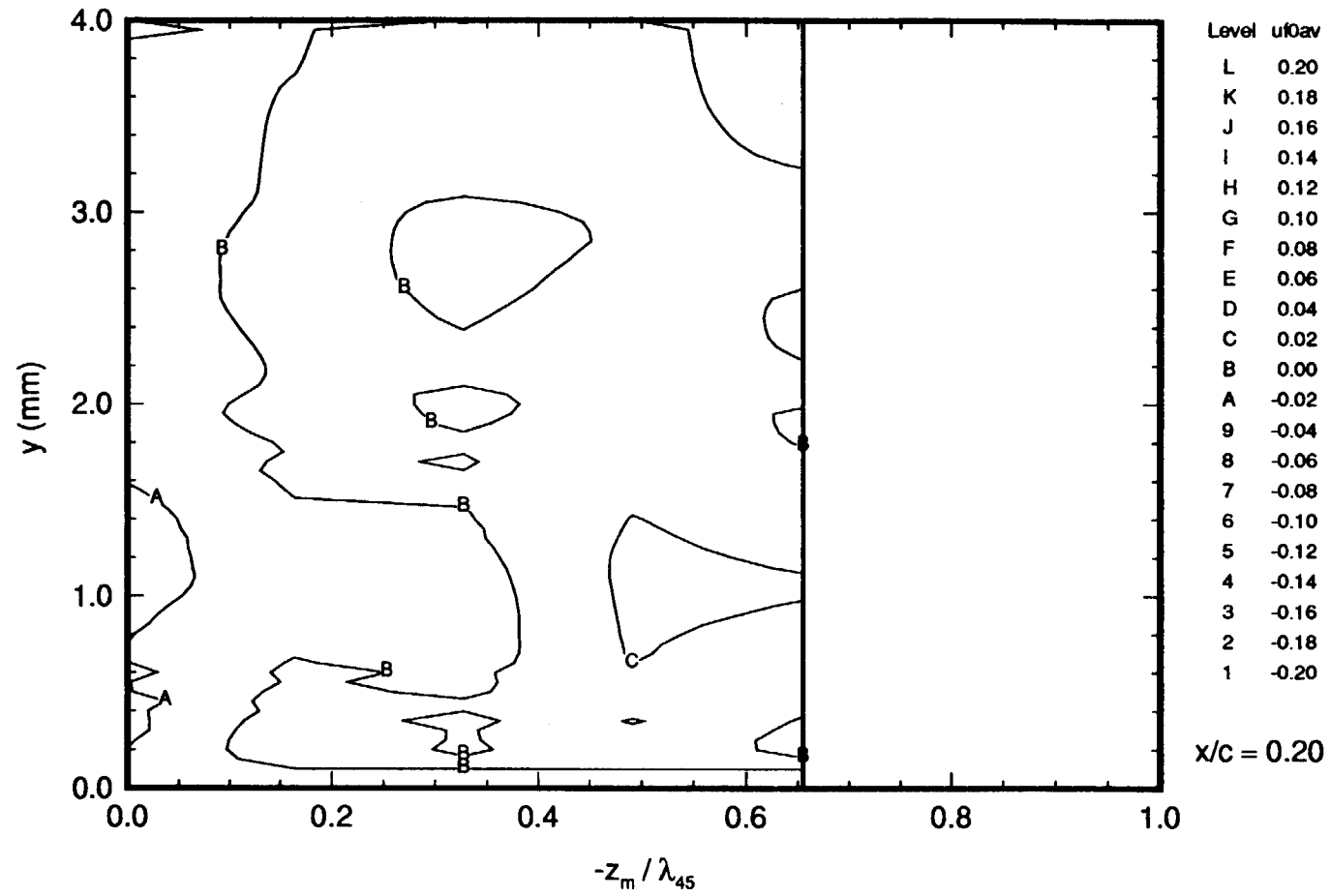


Figure 97. Stationary Crossflow-Vortex Velocity Contours Obtained From $U_s - U_{s\text{ avg}}$ at $x/c = 0.20$, $\alpha = -4^\circ$, $R_c = 2.37 \times 10^6$.

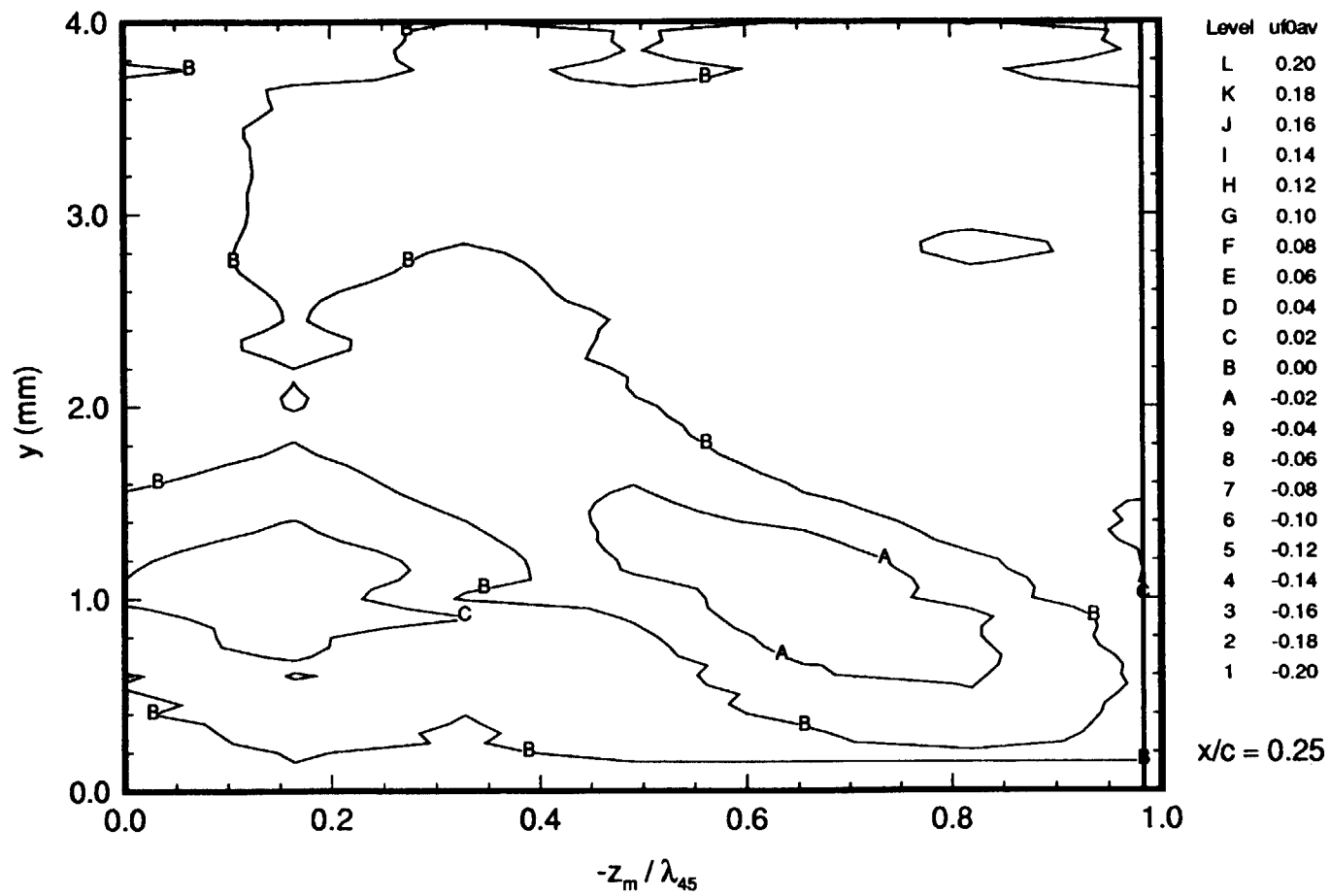


Figure 98. Stationary Crossflow-Vortex Velocity Contours Obtained From $U_s - U_{s\text{ avg}}$ at $x/c = 0.25$, $\alpha = -4^\circ$, $R_c = 2.37 \times 10^6$.

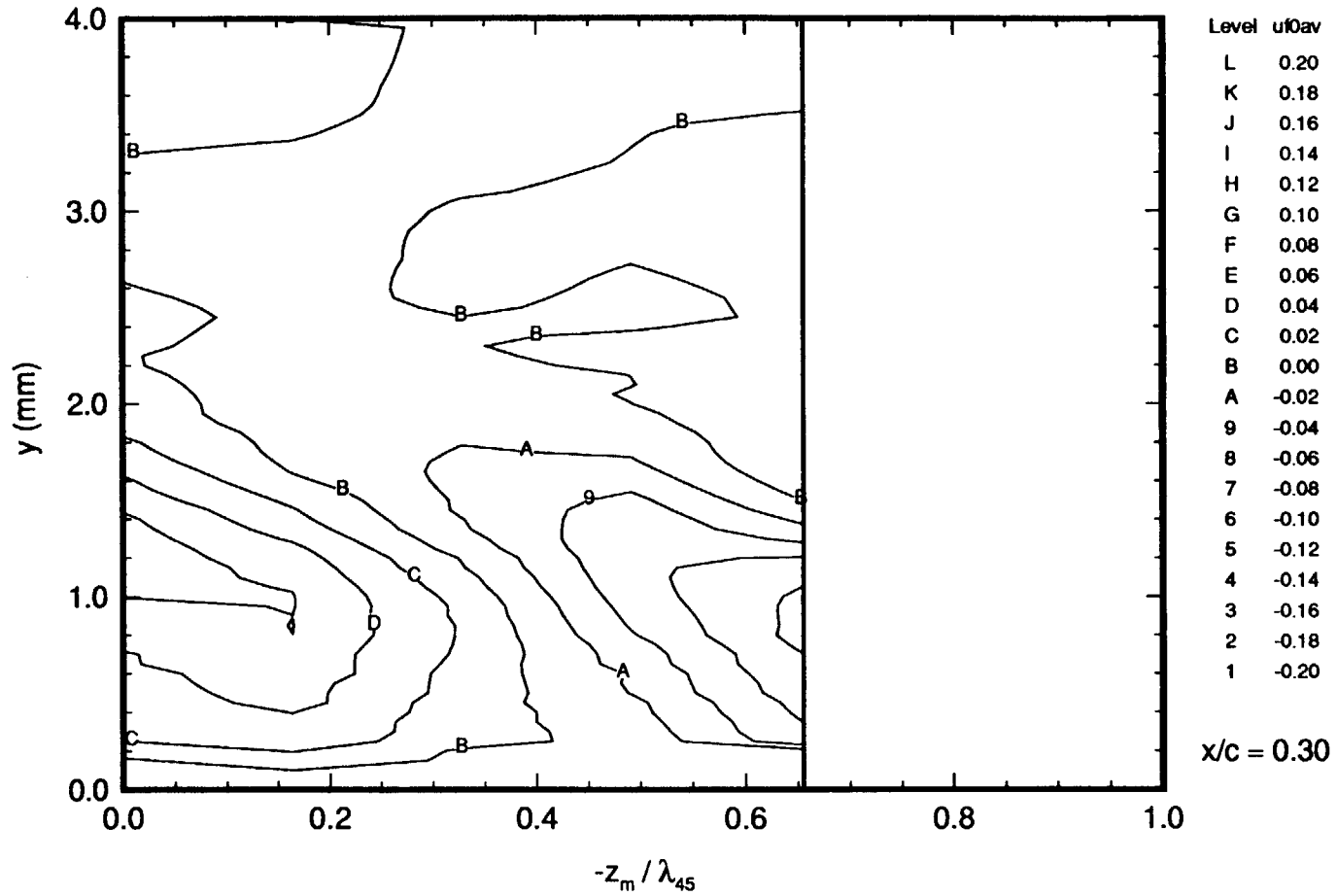


Figure 99. Stationary Crossflow-Vortex Velocity Contours Obtained From $U_s - U_{s \text{ avg}}$ at $x/c = 0.30$, $\alpha = -4^\circ$, $R_c = 2.37 \times 10^6$.

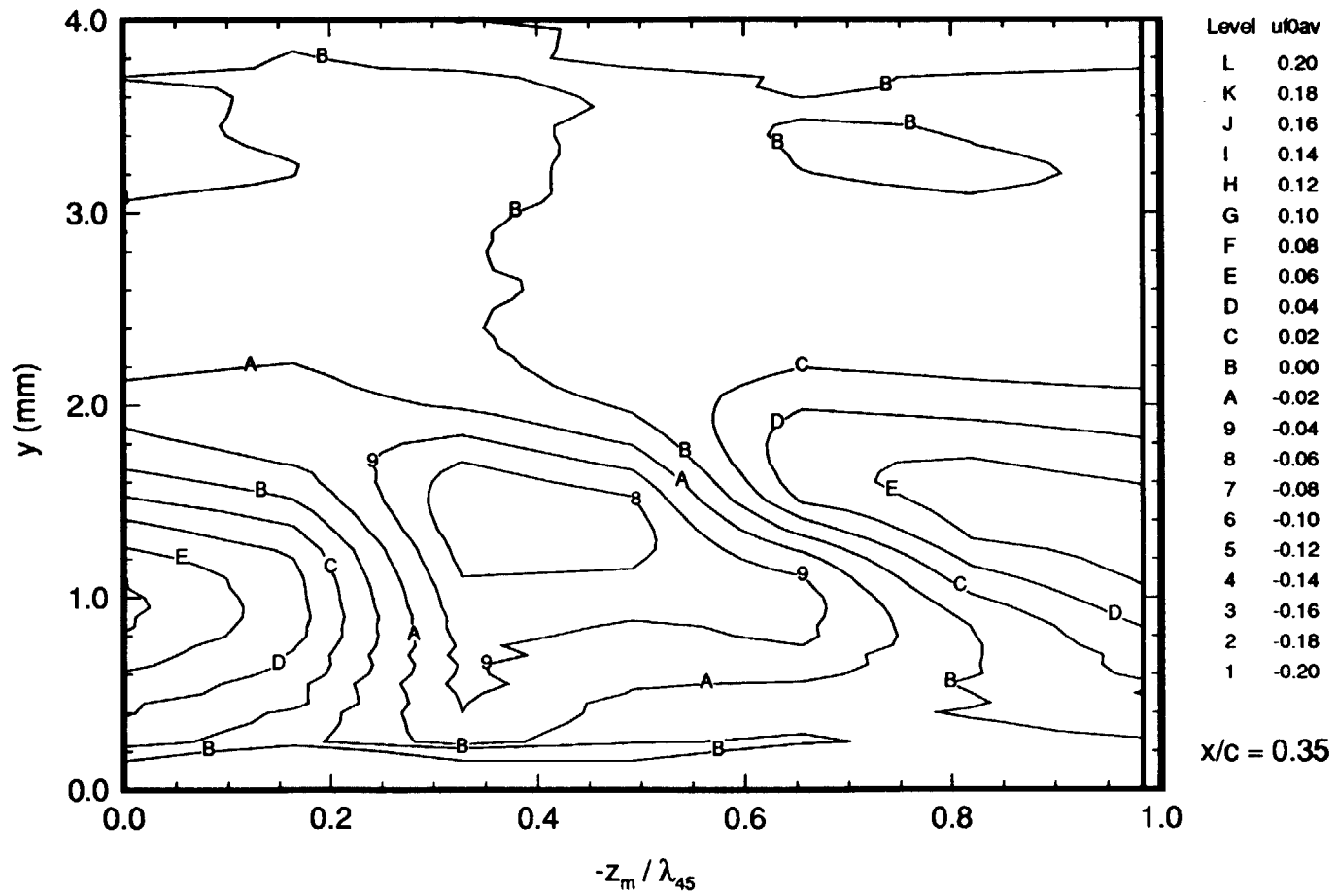


Figure 100. Stationary Crossflow-Vortex Velocity Contours
 Obtained From $U_s - U_{s\text{ avg}}$ at $x/c = 0.35$, $\alpha = -4^\circ$, $R_c = 2.37 \times 10^6$.

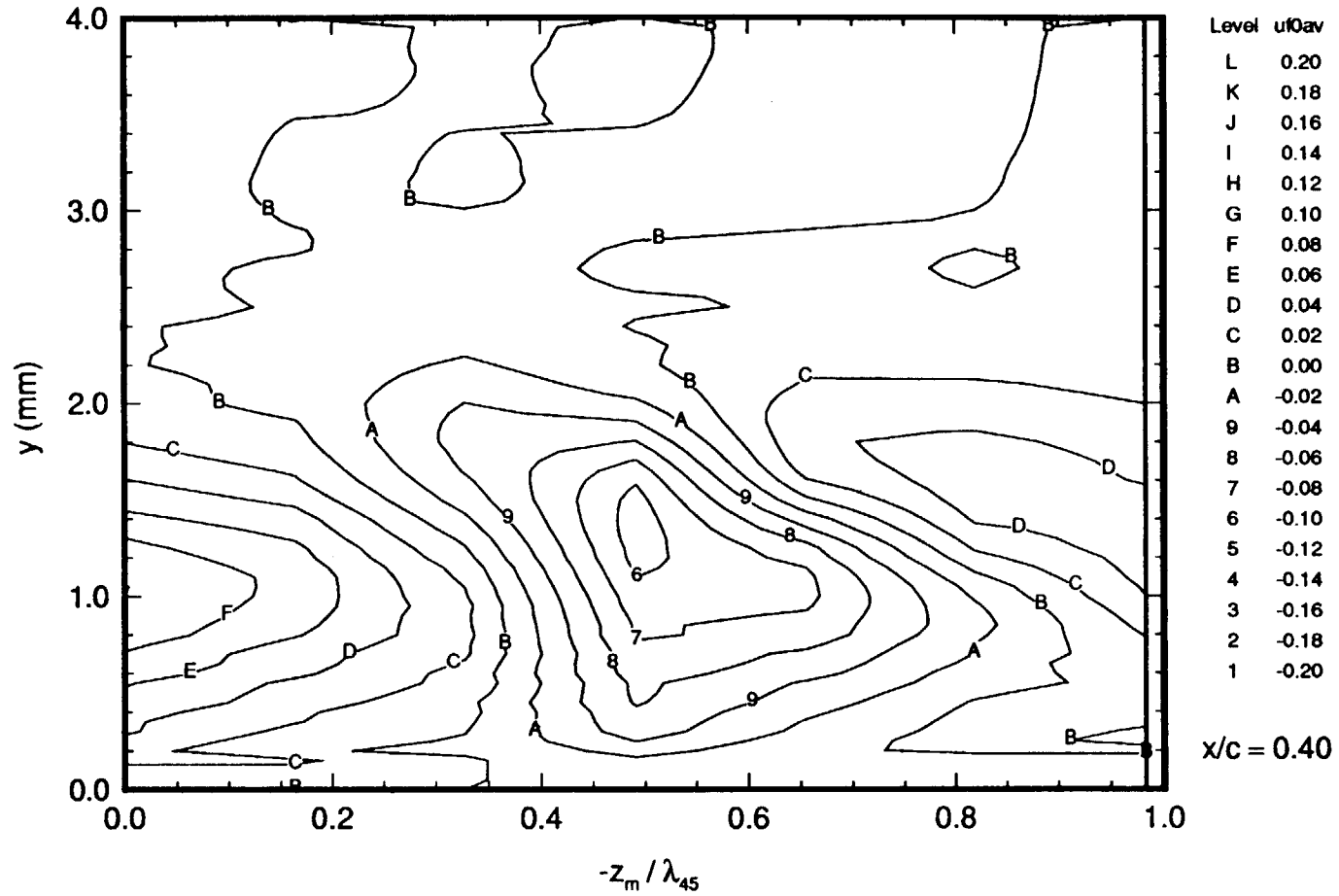


Figure 101. Stationary Crossflow-Vortex Velocity Contours
 Obtained From $U_s - U_{s\text{ avg}}$ at $x/c = 0.40$, $\alpha = -4^\circ$, $R_c = 2.37 \times 10^6$.

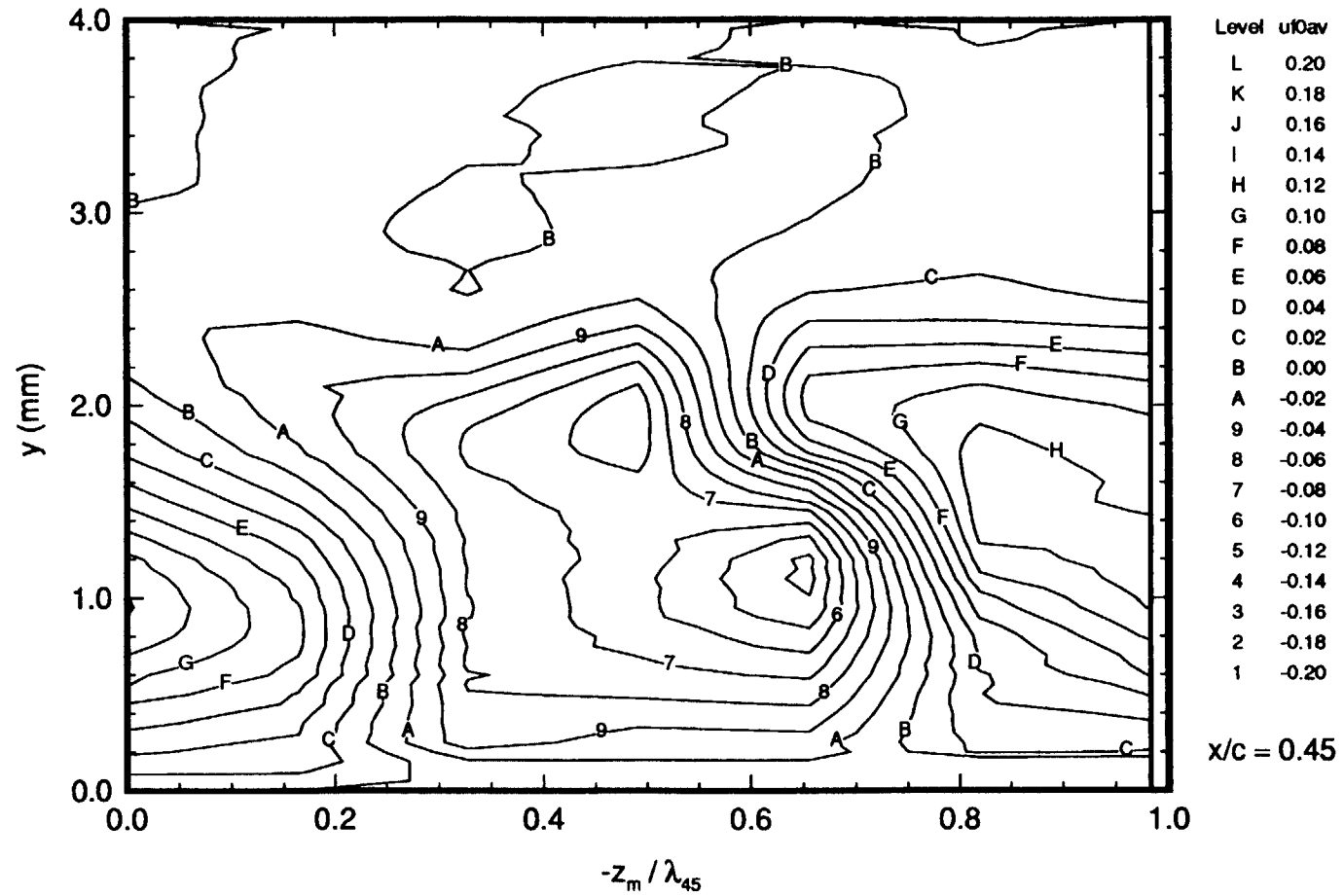


Figure 102. Stationary Crossflow-Vortex Velocity Contours
 Obtained From $U_s - U_{s\text{ avg}}$ at $x/c = 0.45$, $\alpha = -4^\circ$, $R_c = 2.37 \times 10^6$.

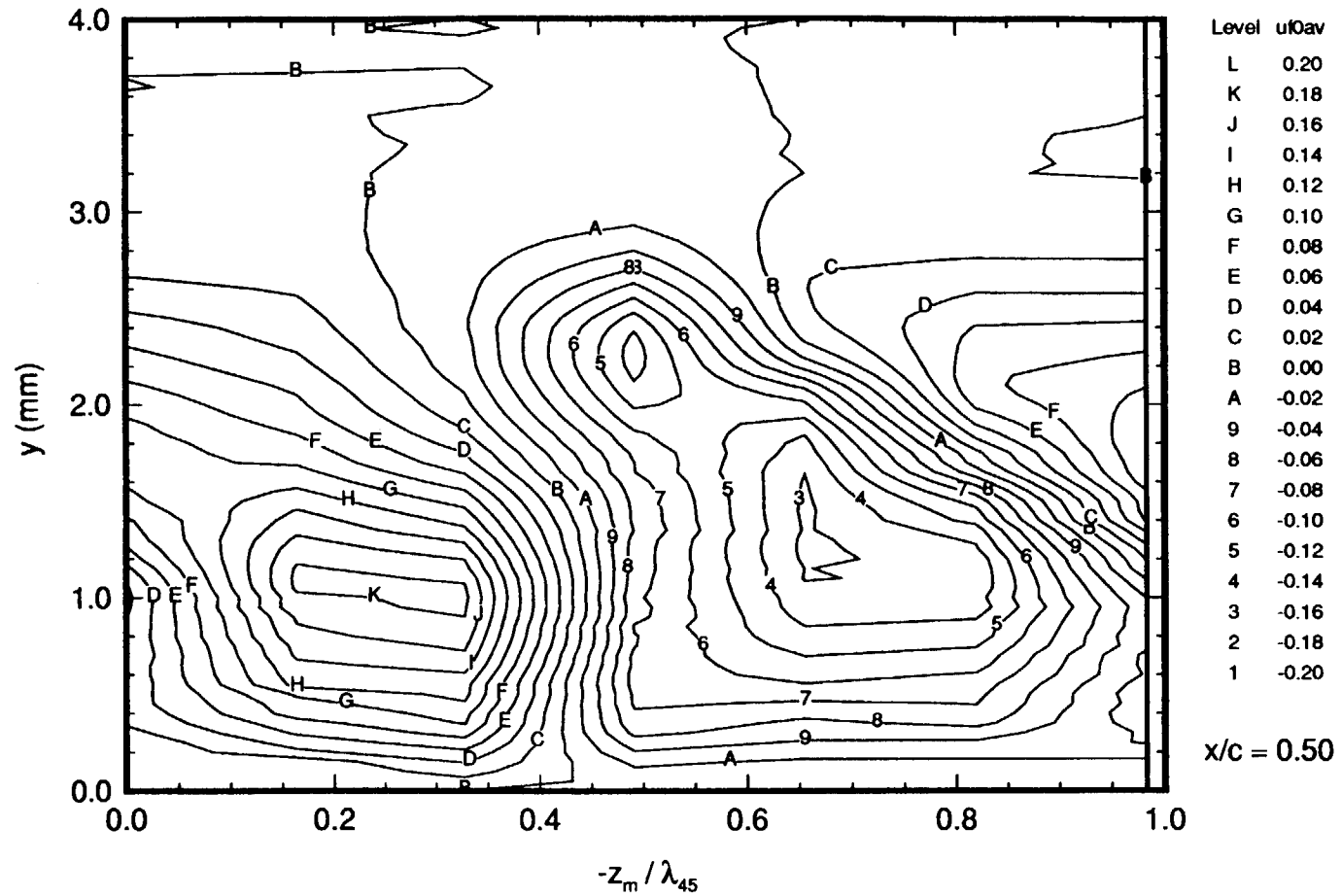


Figure 103. Stationary Crossflow-Vortex Velocity Contours
 Obtained From $U_s - U_{s\text{ avg}}$ at $x/c = 0.50$, $\alpha = -4^\circ$, $R_c = 2.37 \times 10^6$.

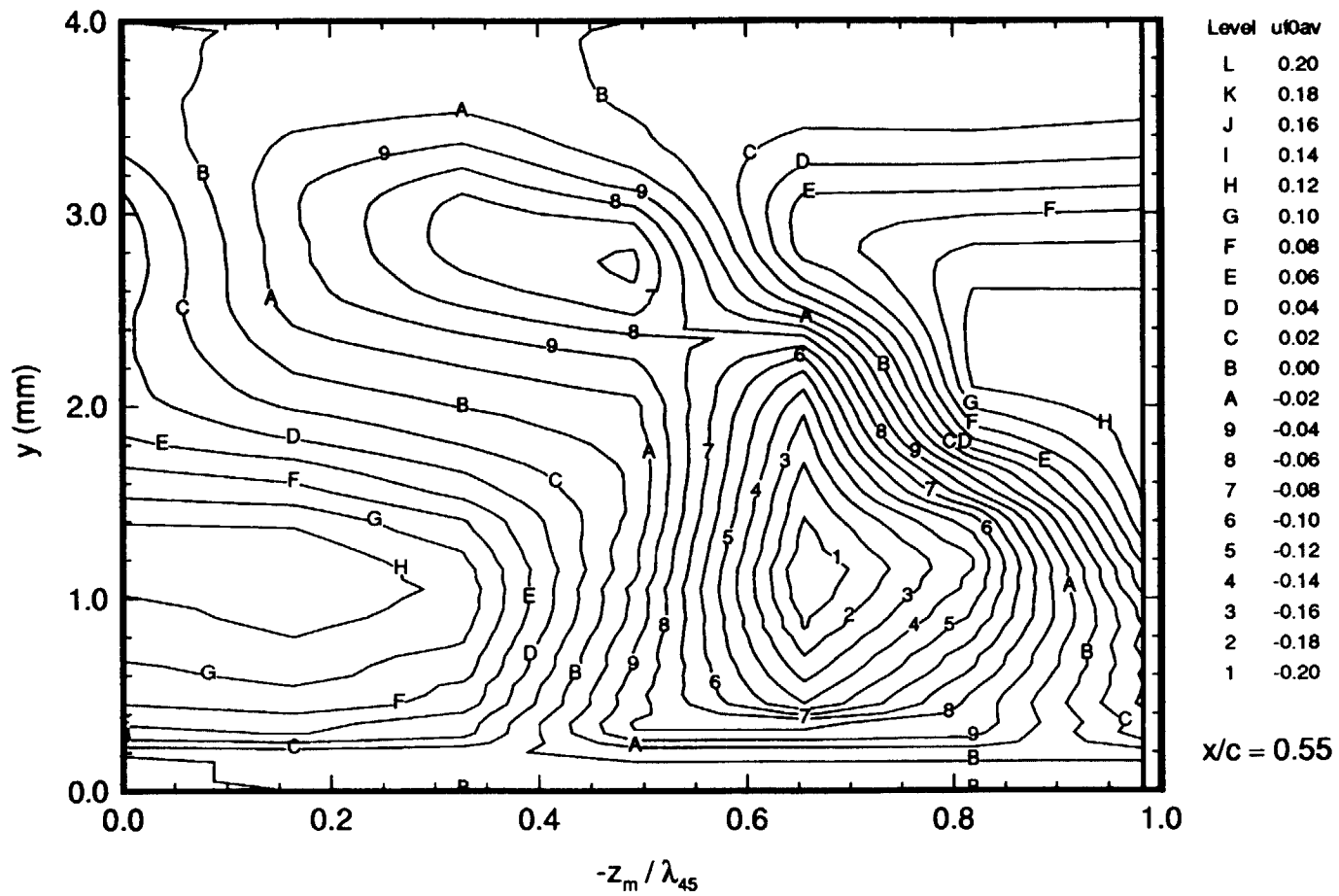


Figure 104. Stationary Crossflow-Vortex Velocity Contours
 Obtained From $U_s - U_{s\text{ avg}}$ at $x/c = 0.55$, $\alpha = -4^\circ$, $R_c = 2.37 \times 10^6$.

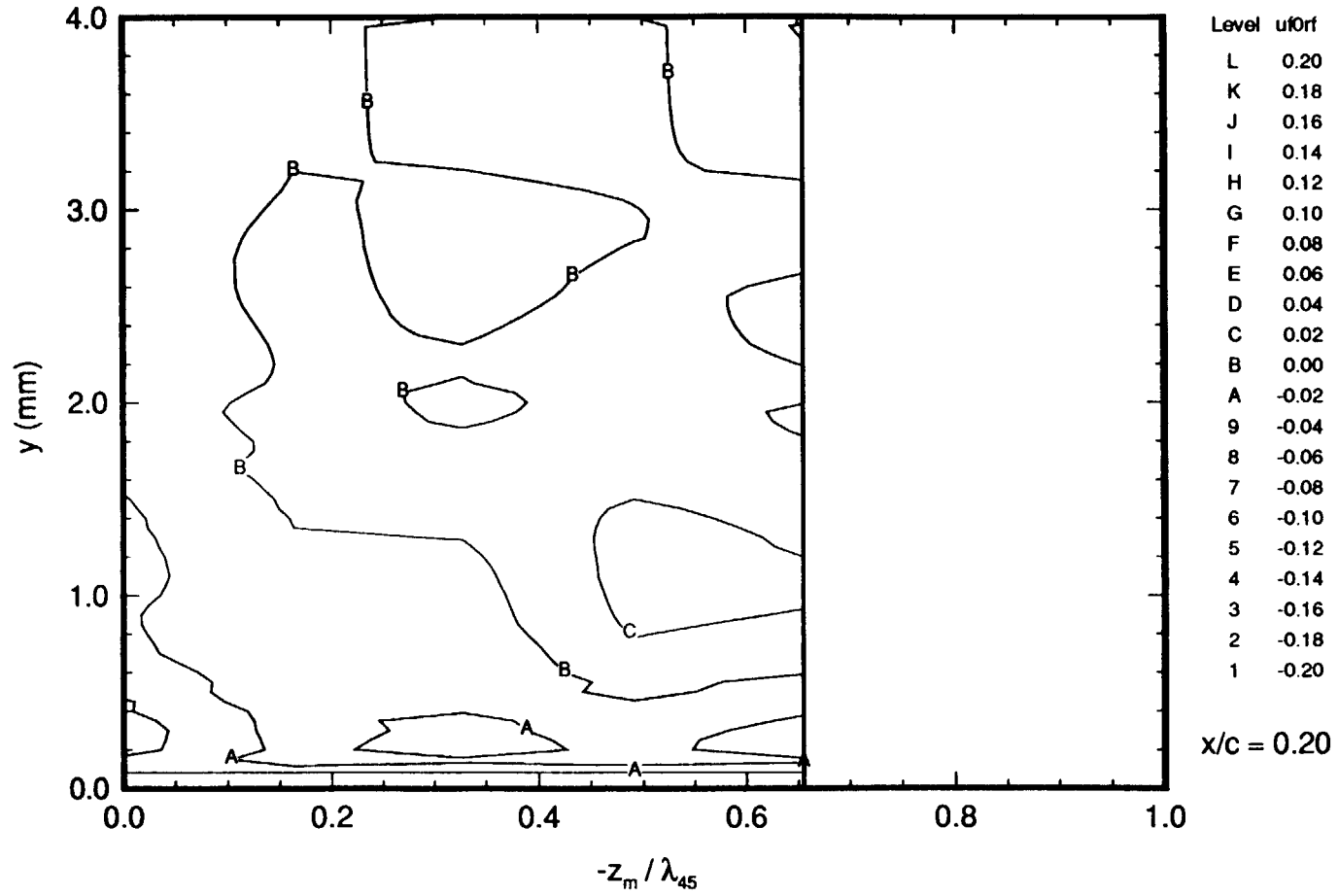


Figure 105. Stationary Crossflow-Vortex Velocity Contours
 Obtained From $U_s - U_{s\text{ref}}$ at $x/c = 0.20$, $\alpha = -4^\circ$, $R_c = 2.37 \times 10^6$.

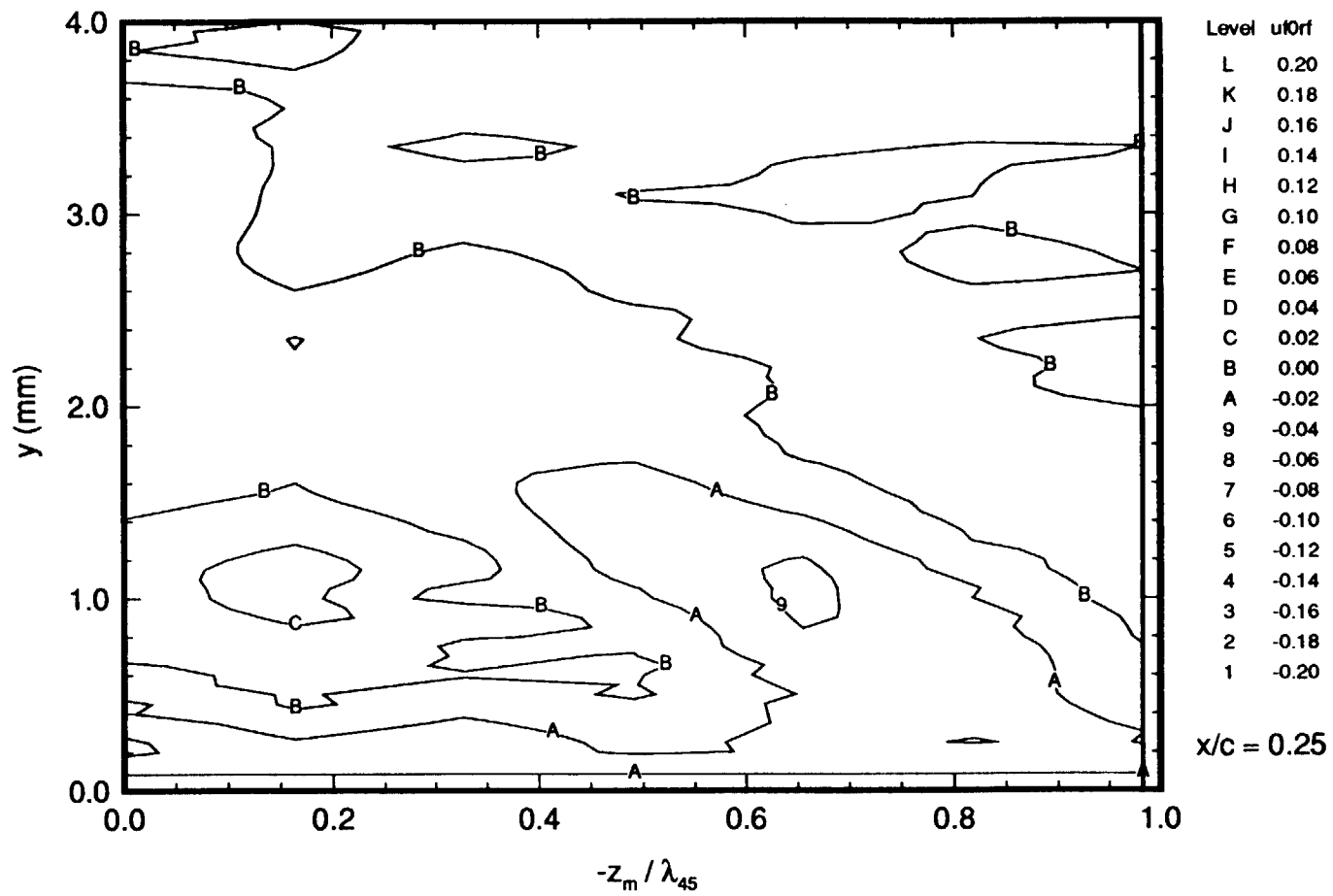


Figure 106. Stationary Crossflow-Vortex Velocity Contours
 Obtained From $U_s - U_{s\text{ref}}$ at $x/c = 0.25$, $\alpha = -4^\circ$, $R_c = 2.37 \times 10^6$.

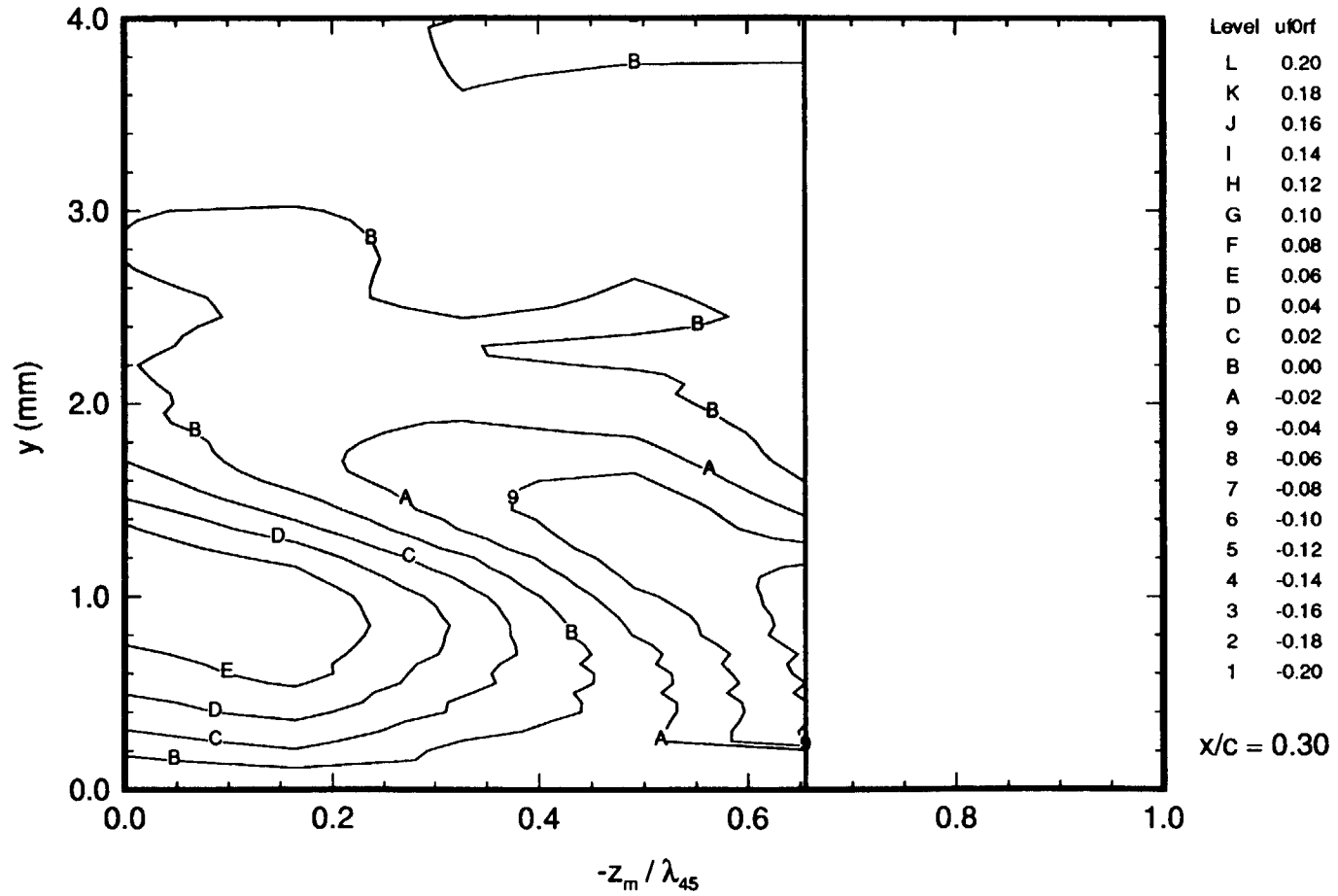


Figure 107. Stationary Crossflow-Vortex Velocity Contours
 Obtained From $U_s - U_{s\text{ref}}$ at $x/c = 0.30$, $\alpha = -4^\circ$, $R_c = 2.37 \times 10^6$.

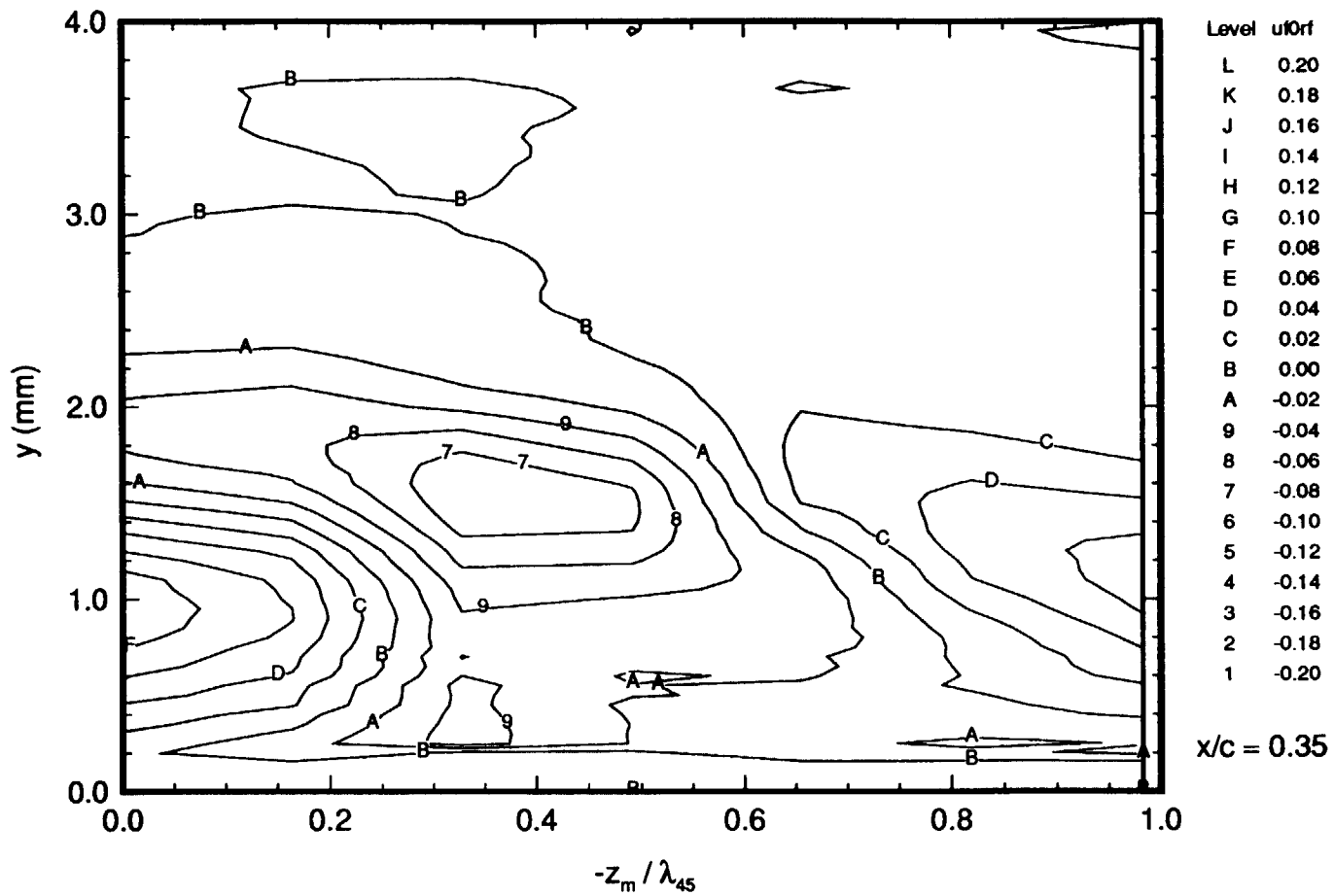


Figure 108. Stationary Crossflow-Vortex Velocity Contours
 Obtained From $U_s - U_{s ref}$ at $x/c = 0.35$, $\alpha = -4^\circ$, $Re_c = 2.37 \times 10^6$.

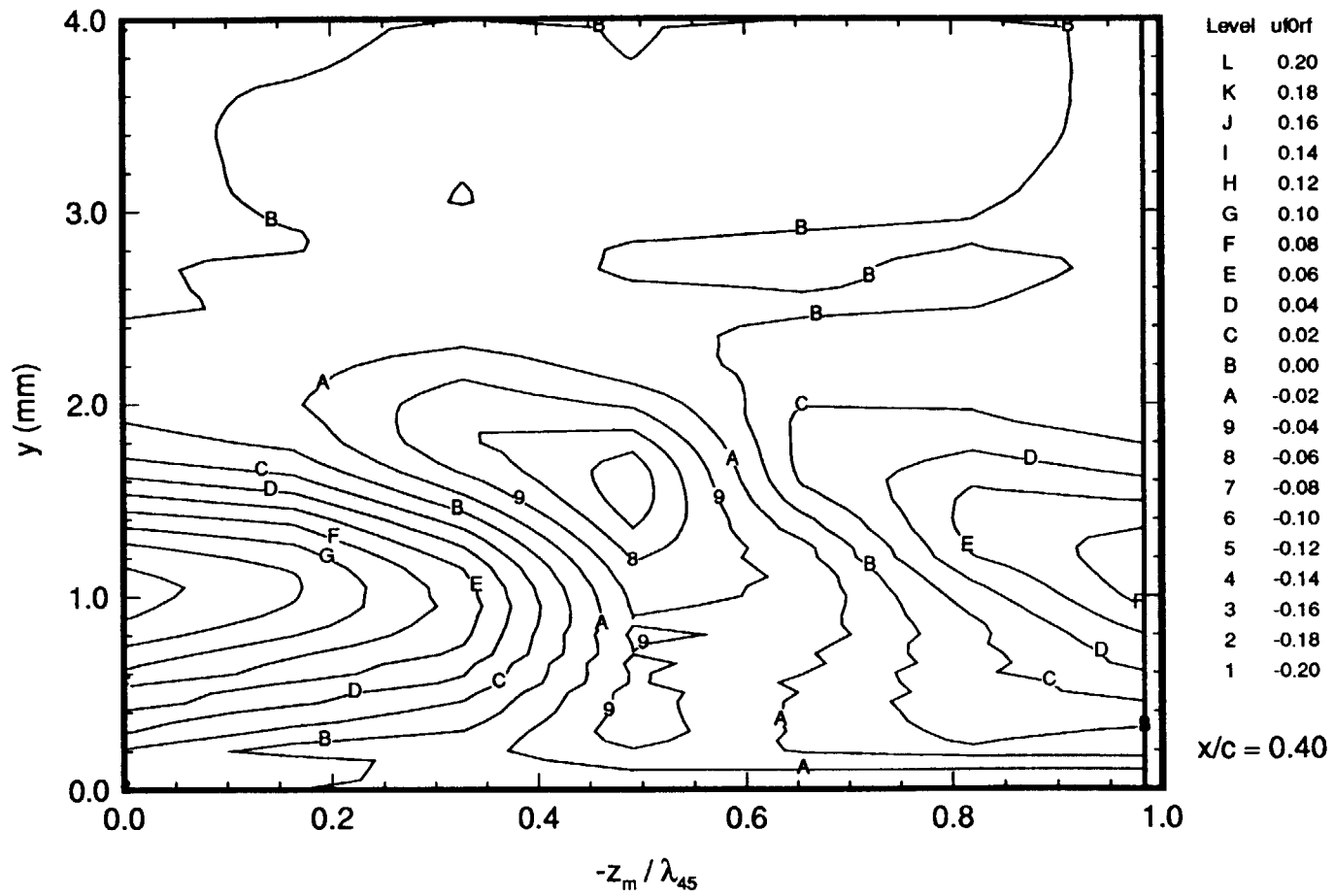


Figure 109. Stationary Crossflow-Vortex Velocity Contours
 Obtained From $U_s - U_{s \text{ ref}}$ at $x/c = 0.40$, $\alpha = -4^\circ$, $R_c = 2.37 \times 10^6$.

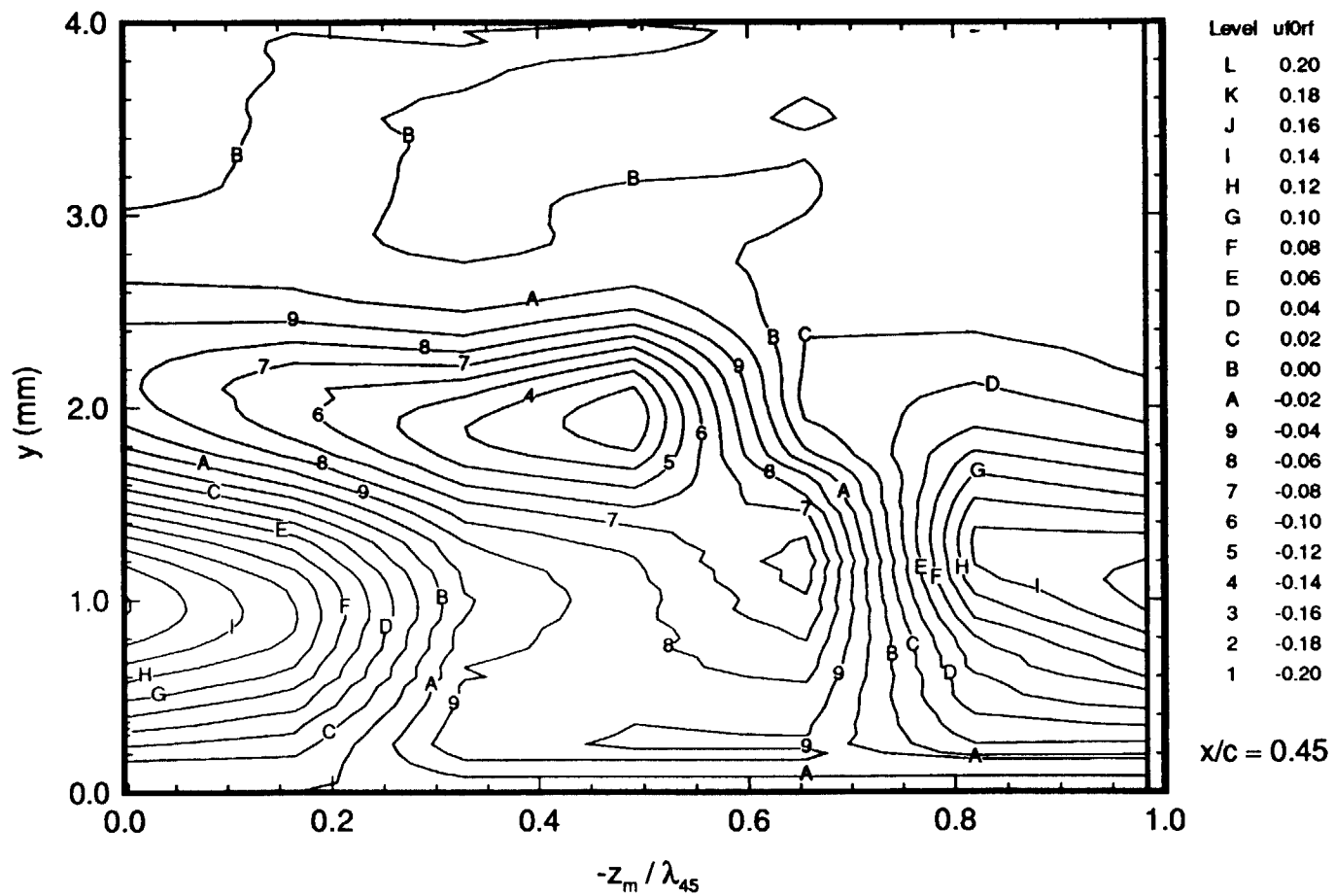


Figure 110. Stationary Crossflow-Vortex Velocity Contours
 Obtained From $U_s - U_{s\ ref}$ at $x/c = 0.45$, $\alpha = -4^\circ$, $R_c = 2.37 \times 10^6$.

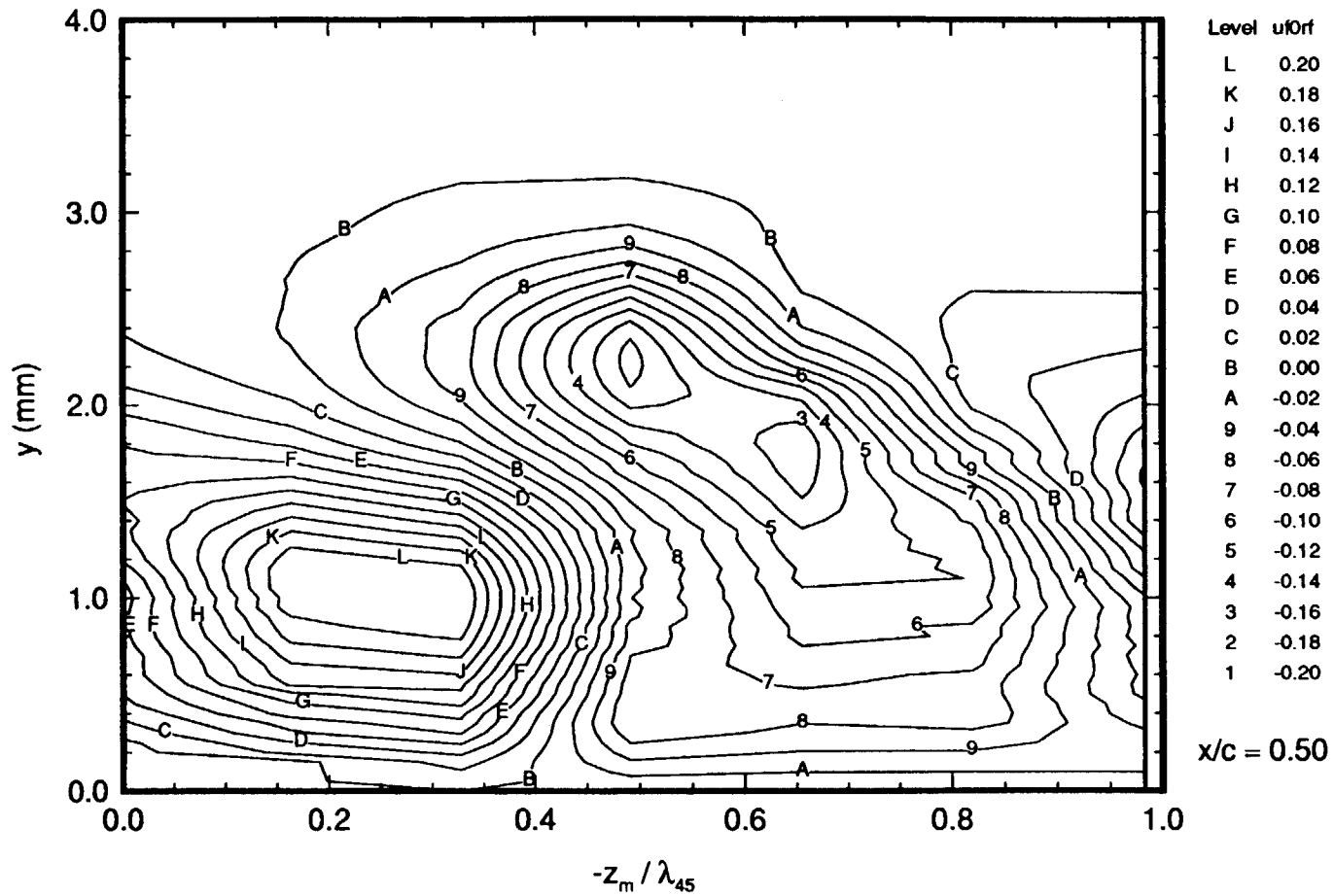


Figure 111. Stationary Crossflow-Vortex Velocity Contours
 Obtained From $U_s - U_{s\text{ref}}$ at $x/c = 0.50$, $\alpha = -4^\circ$, $R_c = 2.37 \times 10^6$.

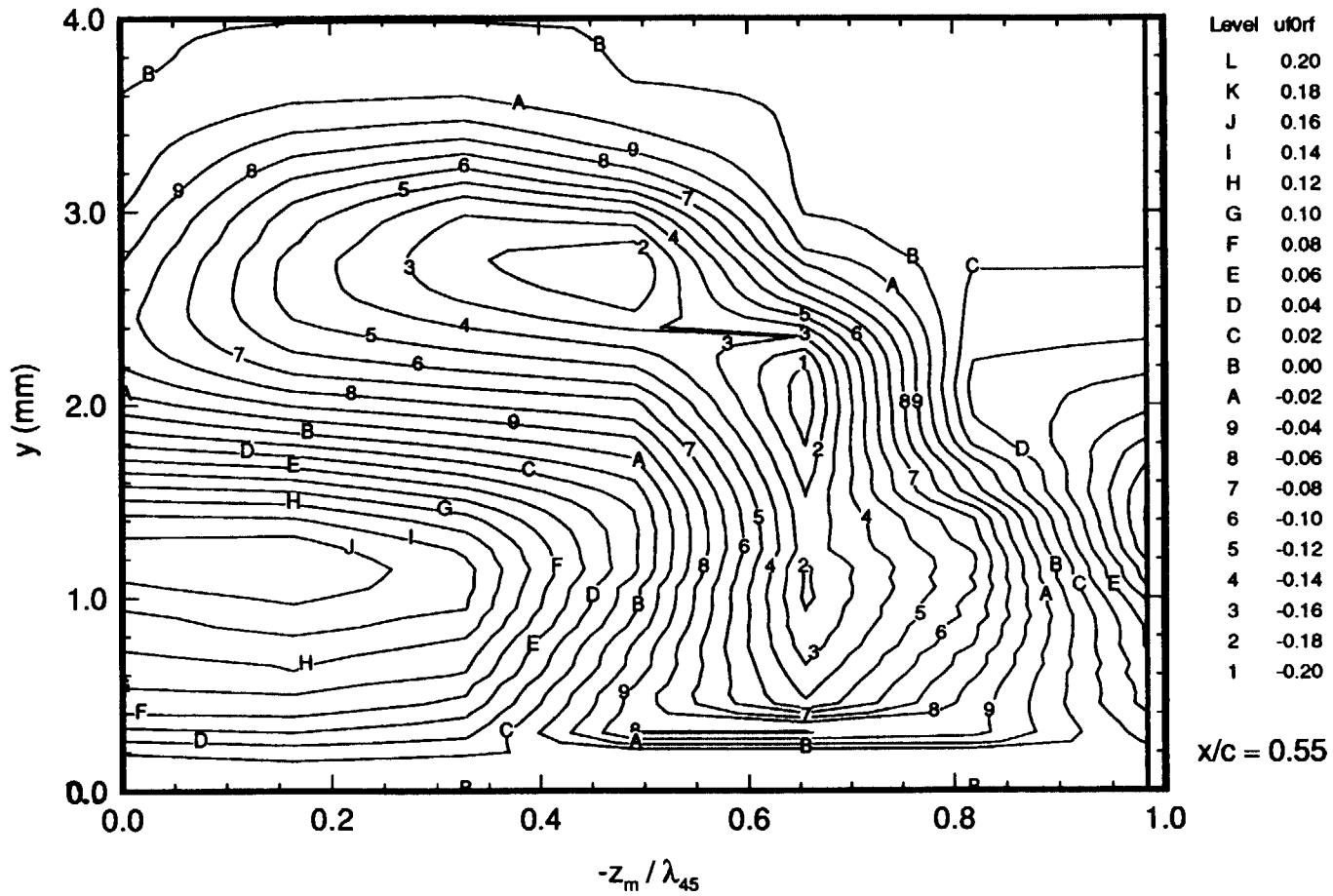


Figure 112. Stationary Crossflow-Vortex Velocity Contours
 Obtained From $U_s - U_{s\text{ref}}$ at $x/c = 0.55$, $\alpha = -4^\circ$, $R_c = 2.37 \times 10^6$.

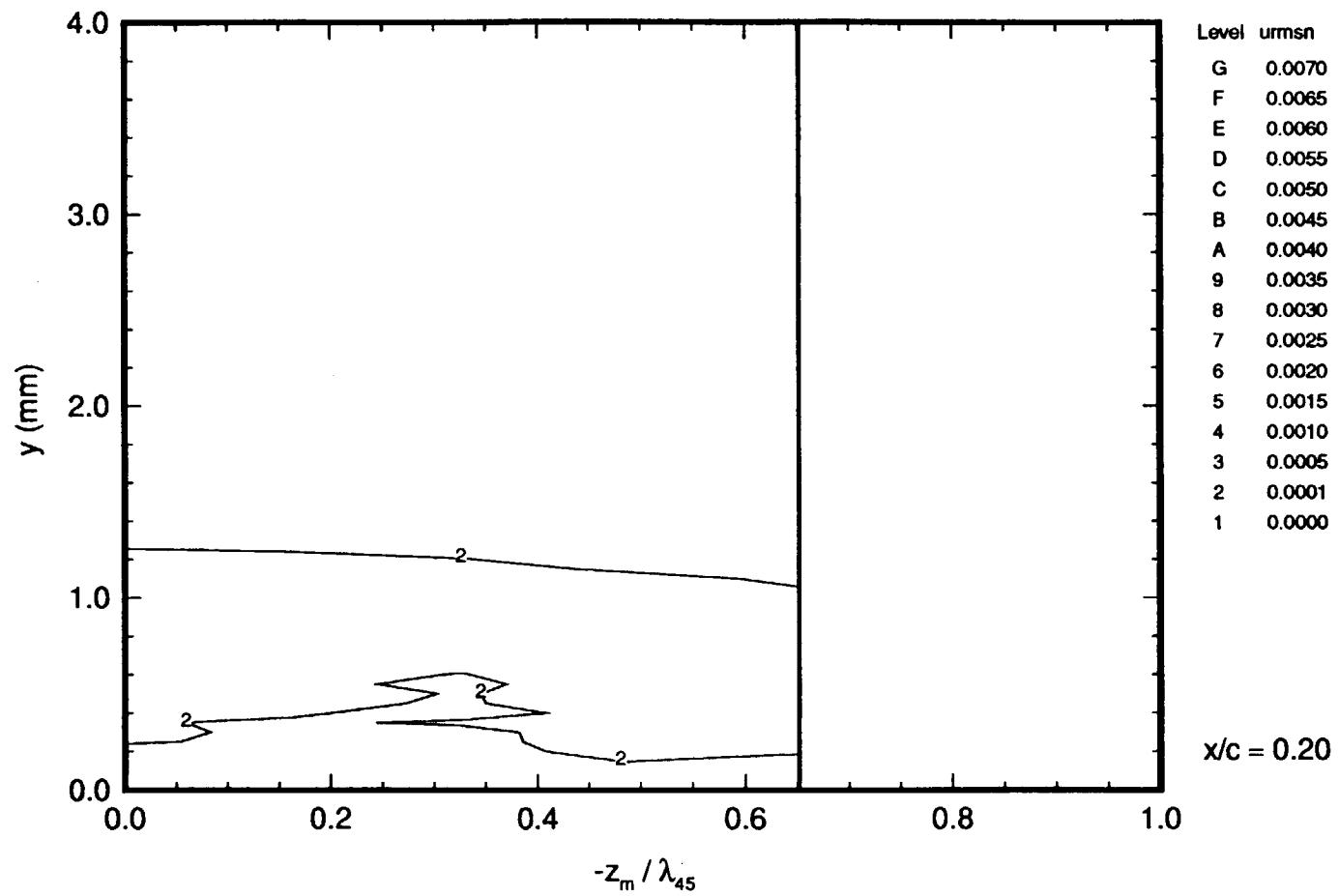


Figure 113. Travelling-Wave RMS-Velocity Contours for $f = 100$ Hz at $x/c = 0.20$, $\alpha = -4^\circ$, $R_c = 2.37 \times 10^6$.

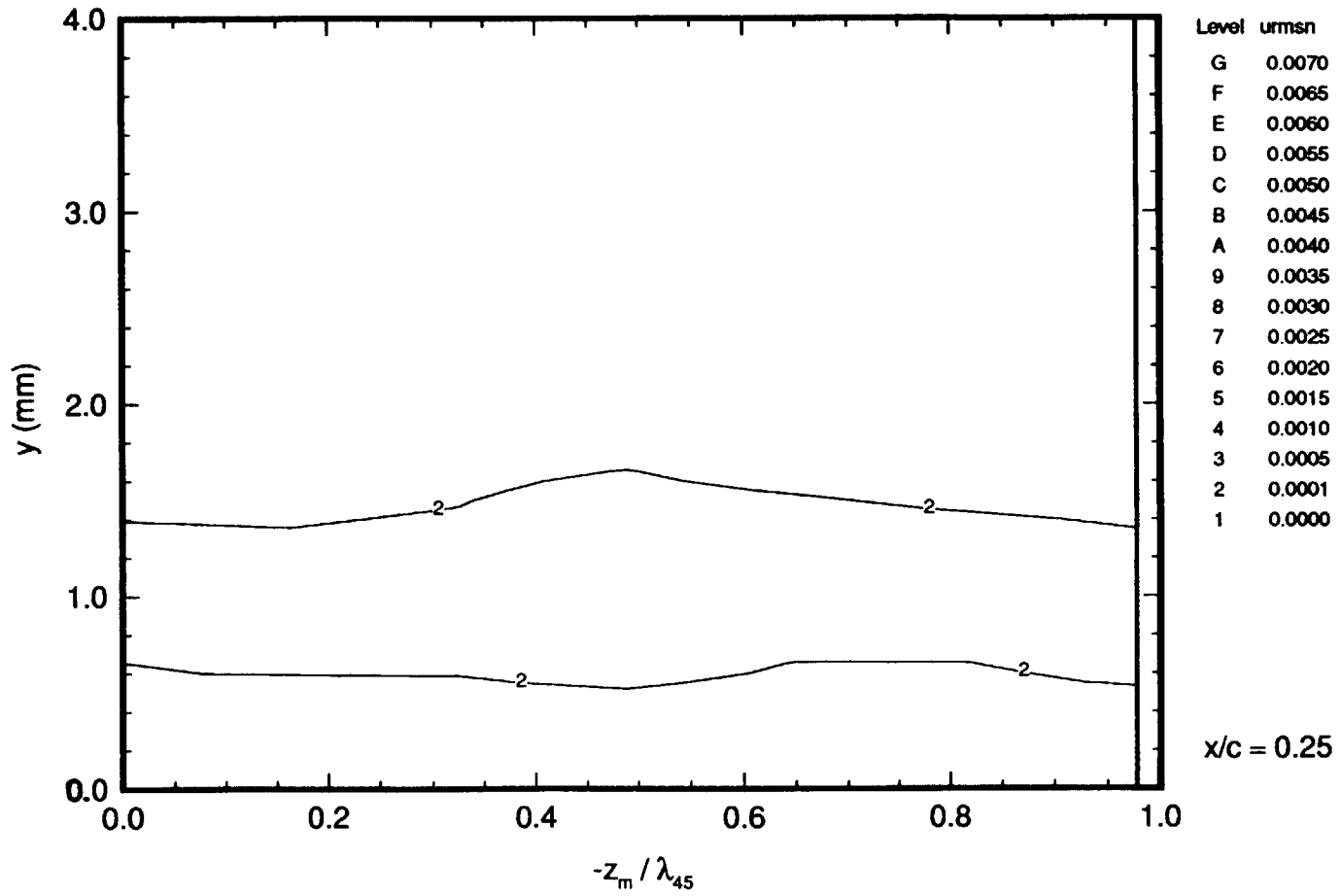


Figure 114. Travelling-Wave RMS-Velocity Contours for $f = 100$ Hz at $x/c = 0.25$, $\alpha = -4^\circ$, $R_c = 2.37 \times 10^6$.

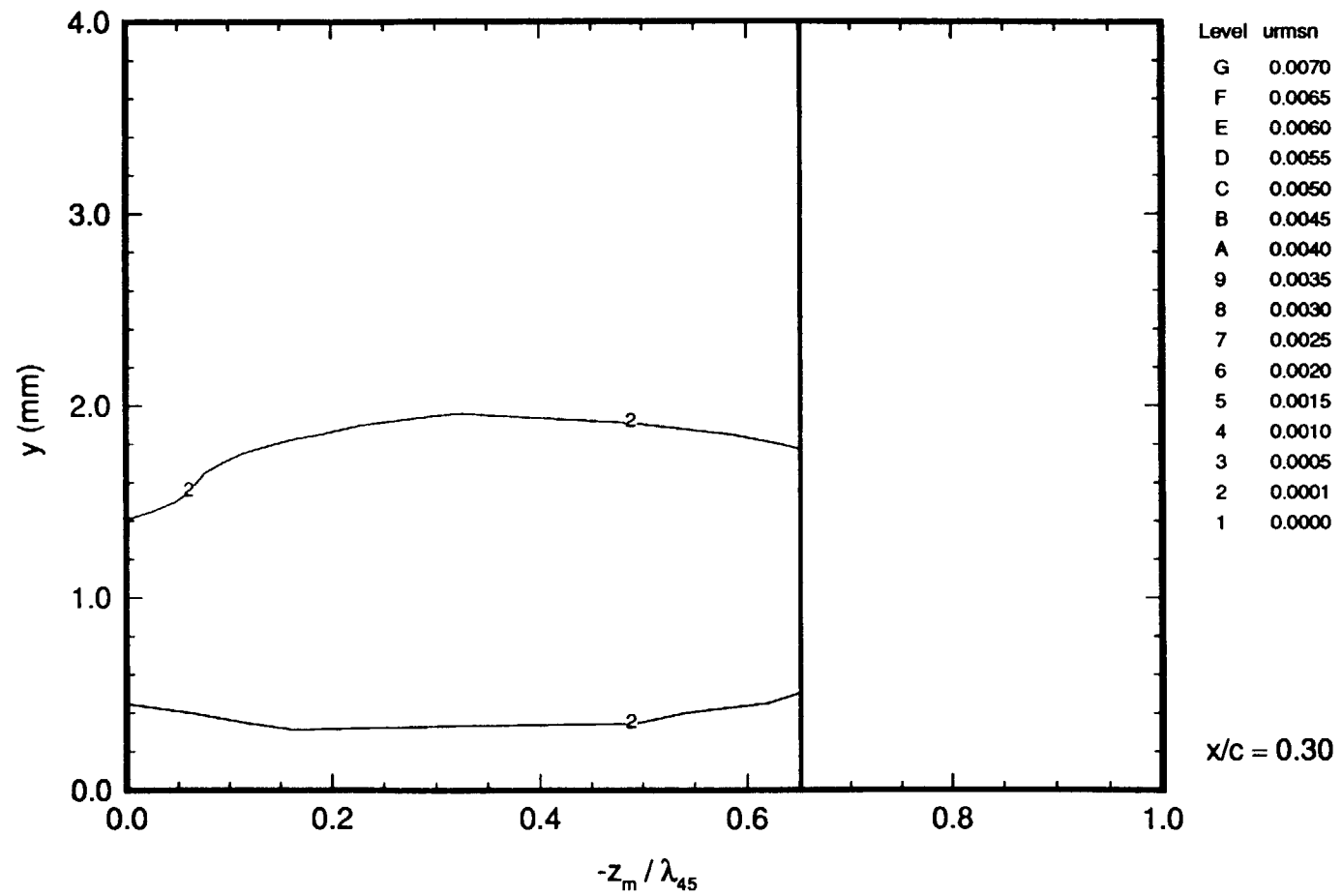


Figure 115. Travelling-Wave RMS-Velocity Contours for $f = 100$ Hz at $x/c = 0.30$, $\alpha = -4^\circ$, $R_c = 2.37 \times 10^6$.

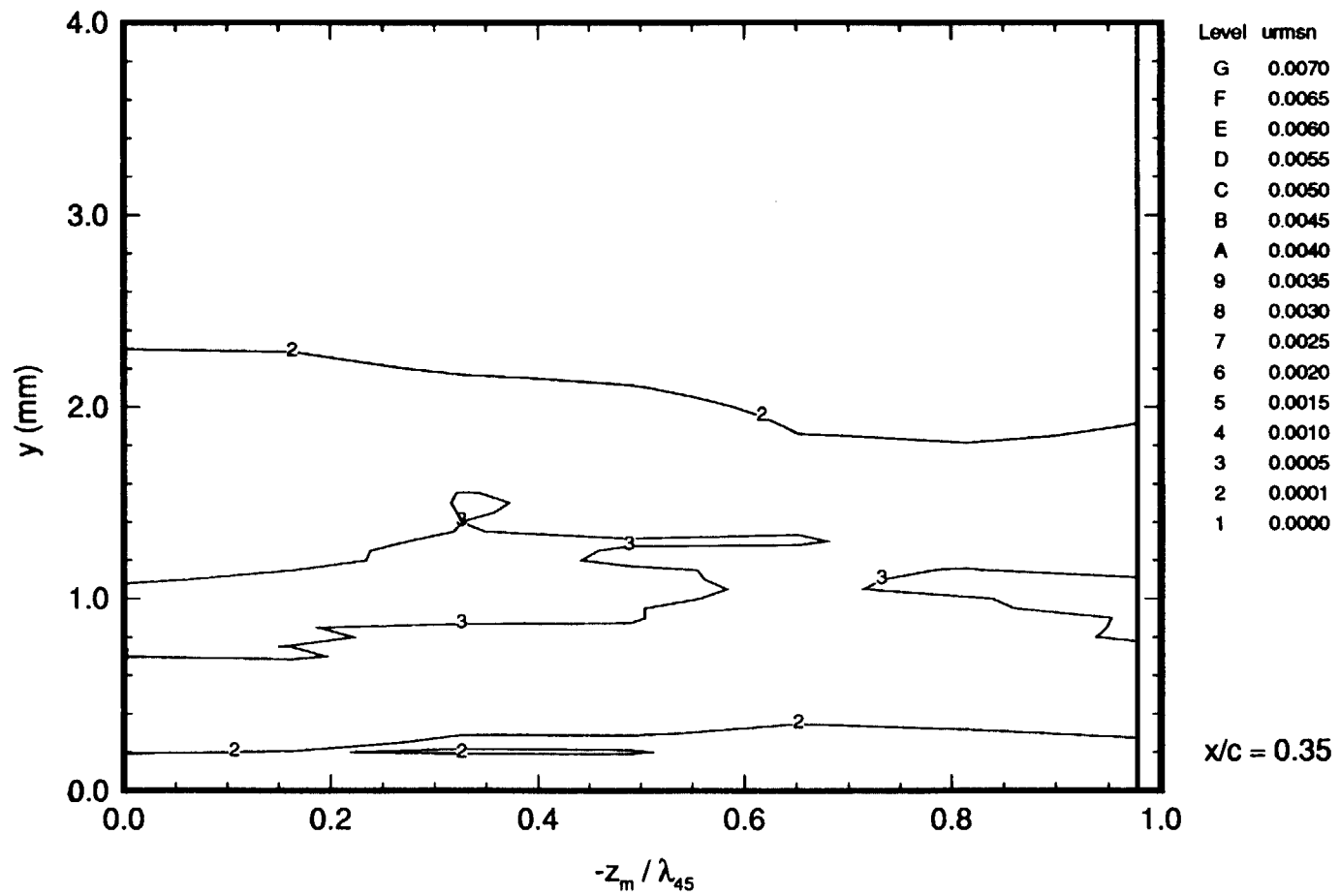


Figure 116. Travelling-Wave RMS-Velocity Contours for $f = 100$ Hz at $x/c = 0.35$, $\alpha = -4^\circ$, $R_c = 2.37 \times 10^6$.

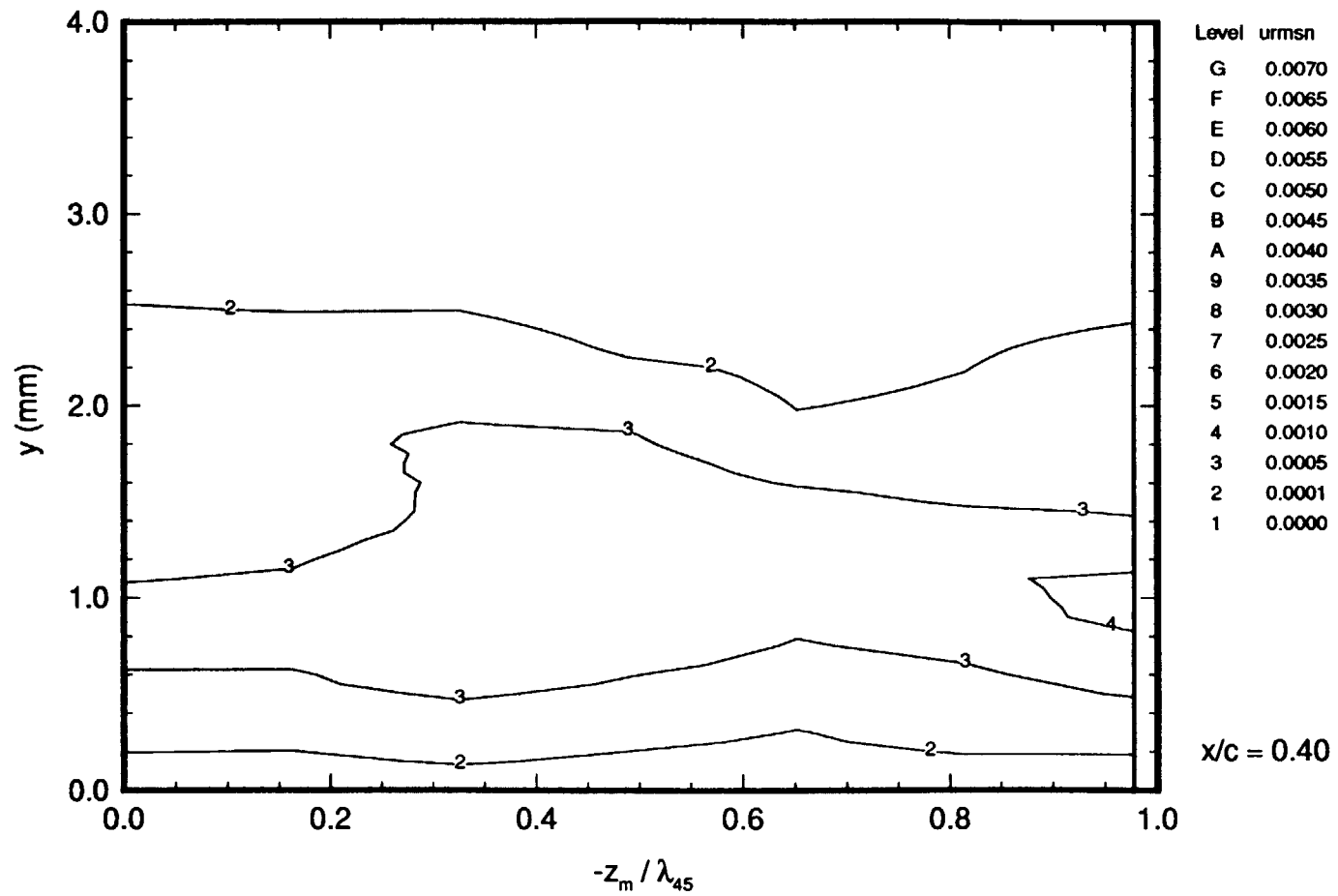


Figure 117. Travelling-Wave RMS-Velocity Contours for $f = 100$ Hz at $x/c = 0.40$, $\alpha = -4^\circ$, $R_c = 2.37 \times 10^6$.

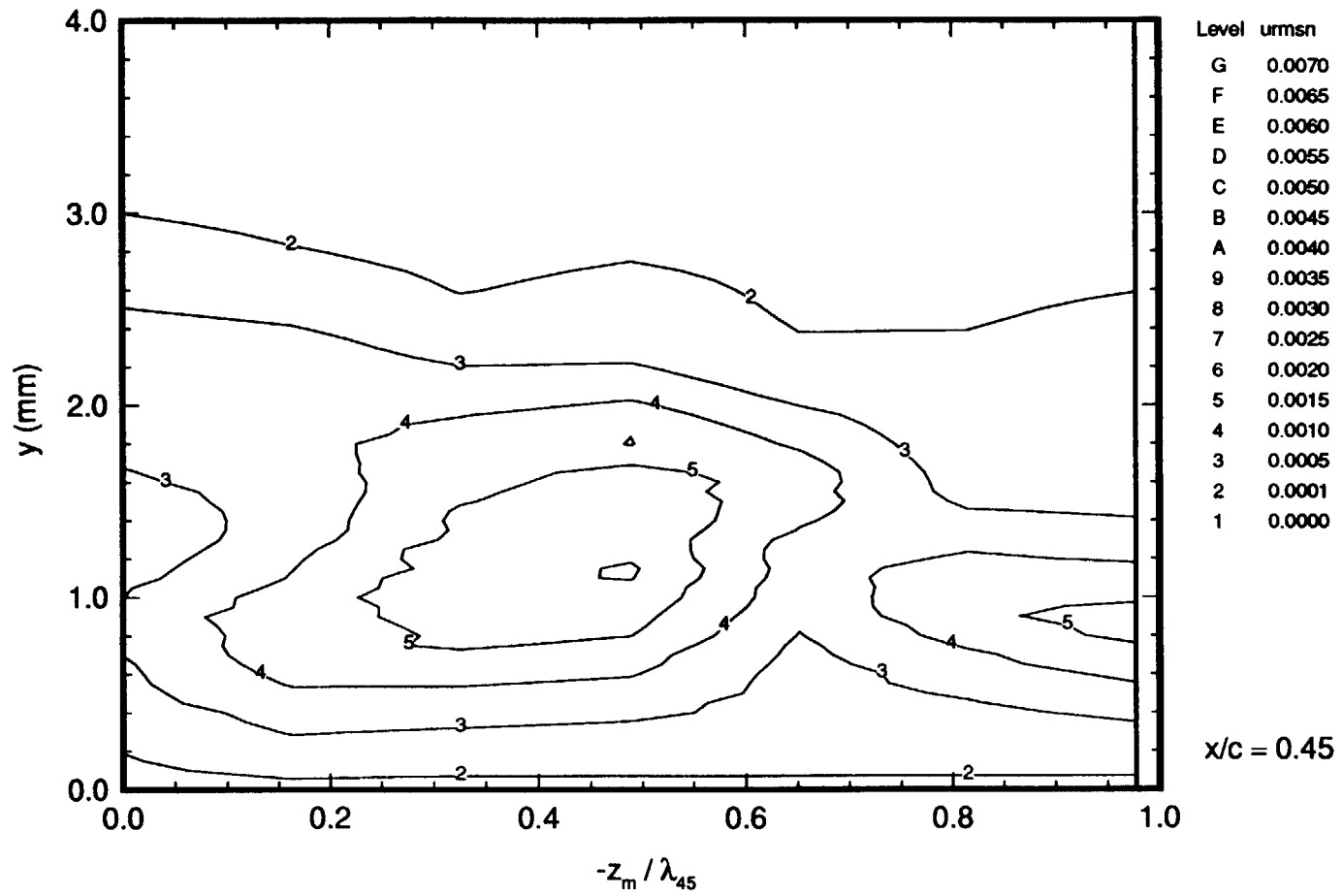


Figure 118. Travelling-Wave RMS-Velocity Contours for $f = 100$ Hz at $x/c = 0.45$, $\alpha = -4^\circ$, $R_c = 2.37 \times 10^6$.

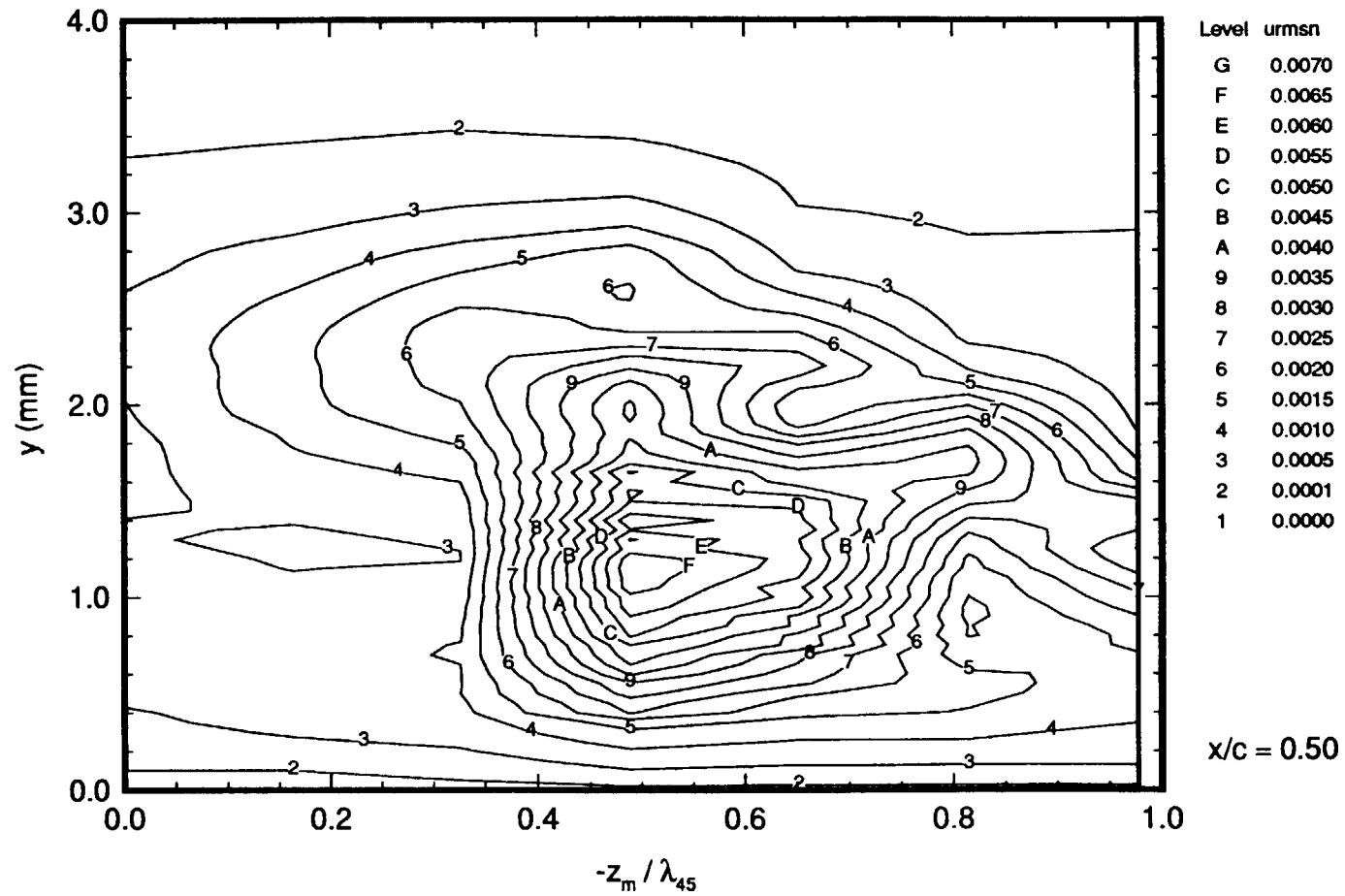


Figure 119. Travelling-Wave RMS-Velocity Contours for $f = 100$ Hz at $x/c = 0.50$, $\alpha = -4^\circ$, $R_c = 2.37 \times 10^6$.

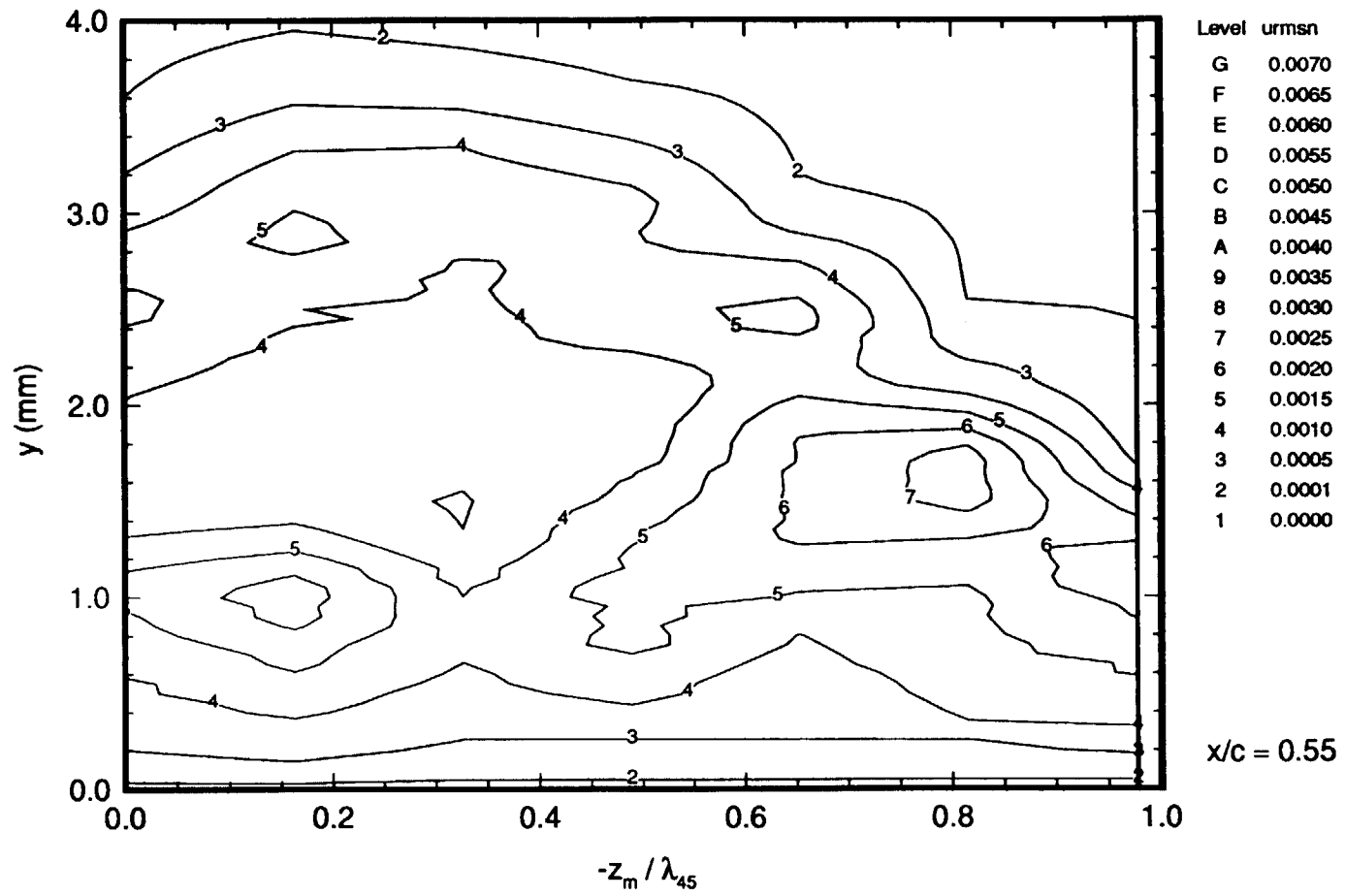


Figure 120. Travelling-Wave RMS-Velocity Contours for $f = 100$ Hz at $x/c = 0.55$, $\alpha = -4^\circ$, $R_c = 2.37 \times 10^6$.

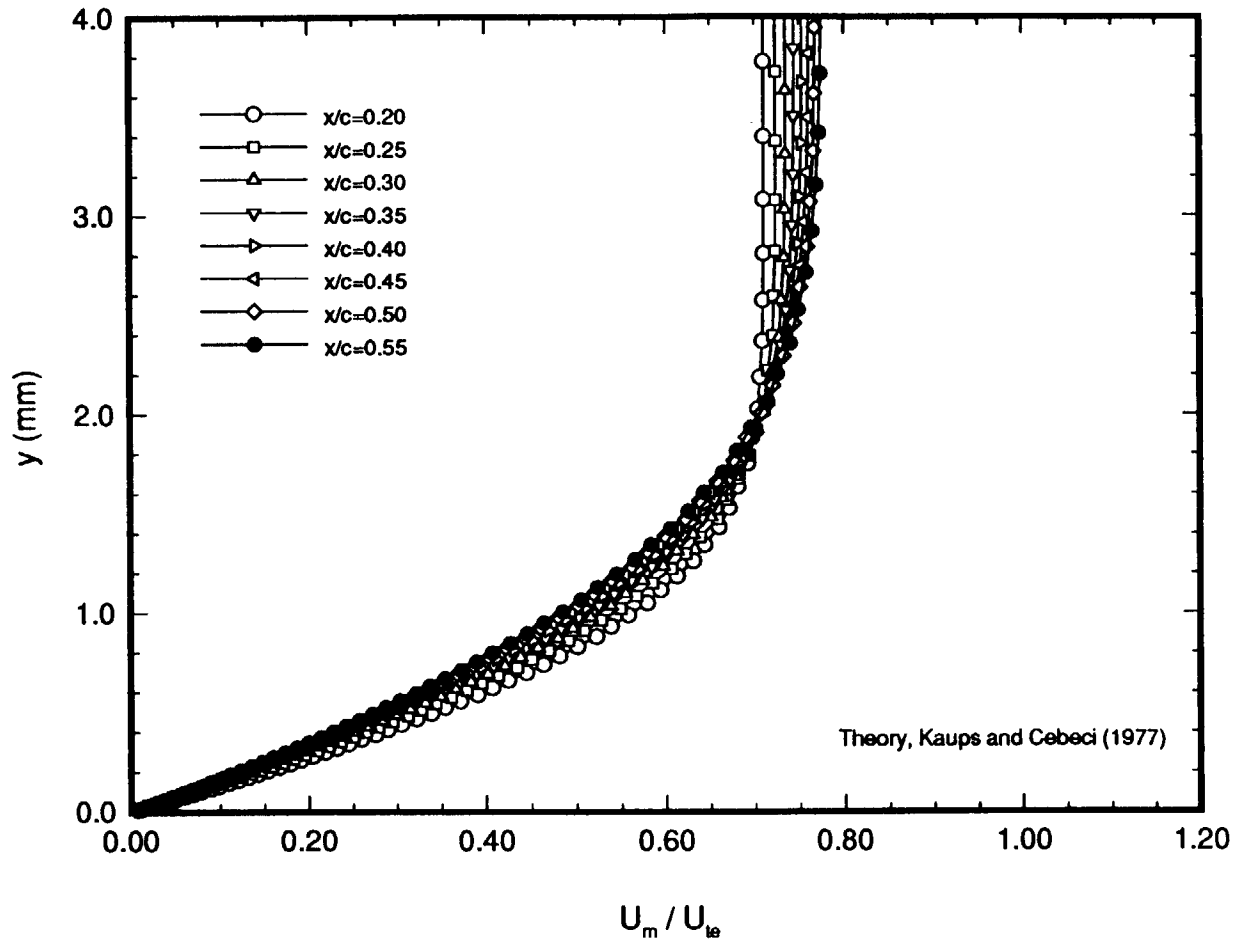


Figure 121. Theoretical Mean Chordwise-Velocity Profiles, $\alpha_{ref} = -5^\circ$, $R_c = 2.37 \times 10^6$.

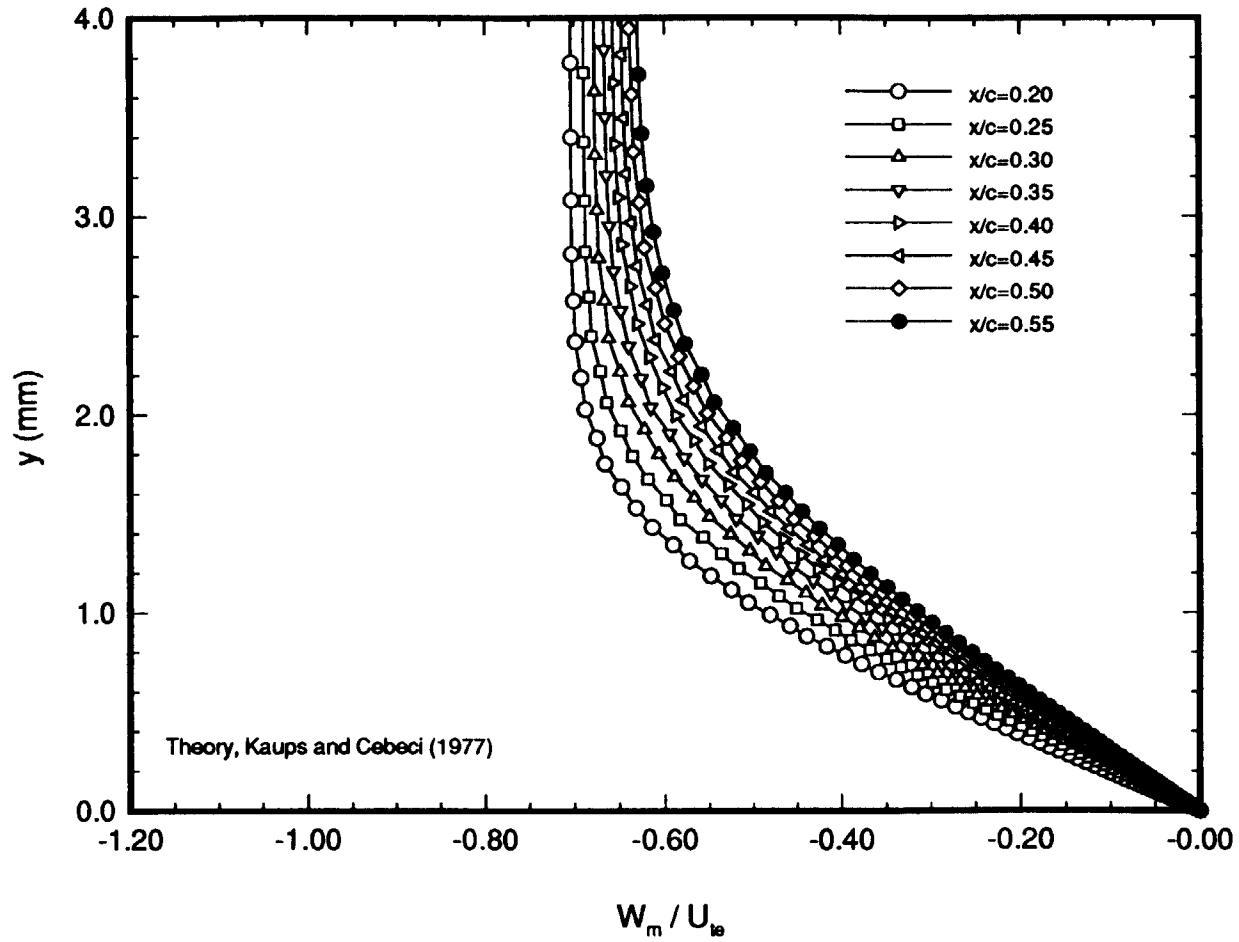


Figure 122. Theoretical Mean Spanwise-Velocity Profiles, $\alpha_{\text{ref}} = -5^\circ$, $R_c = 2.37 \times 10^6$.

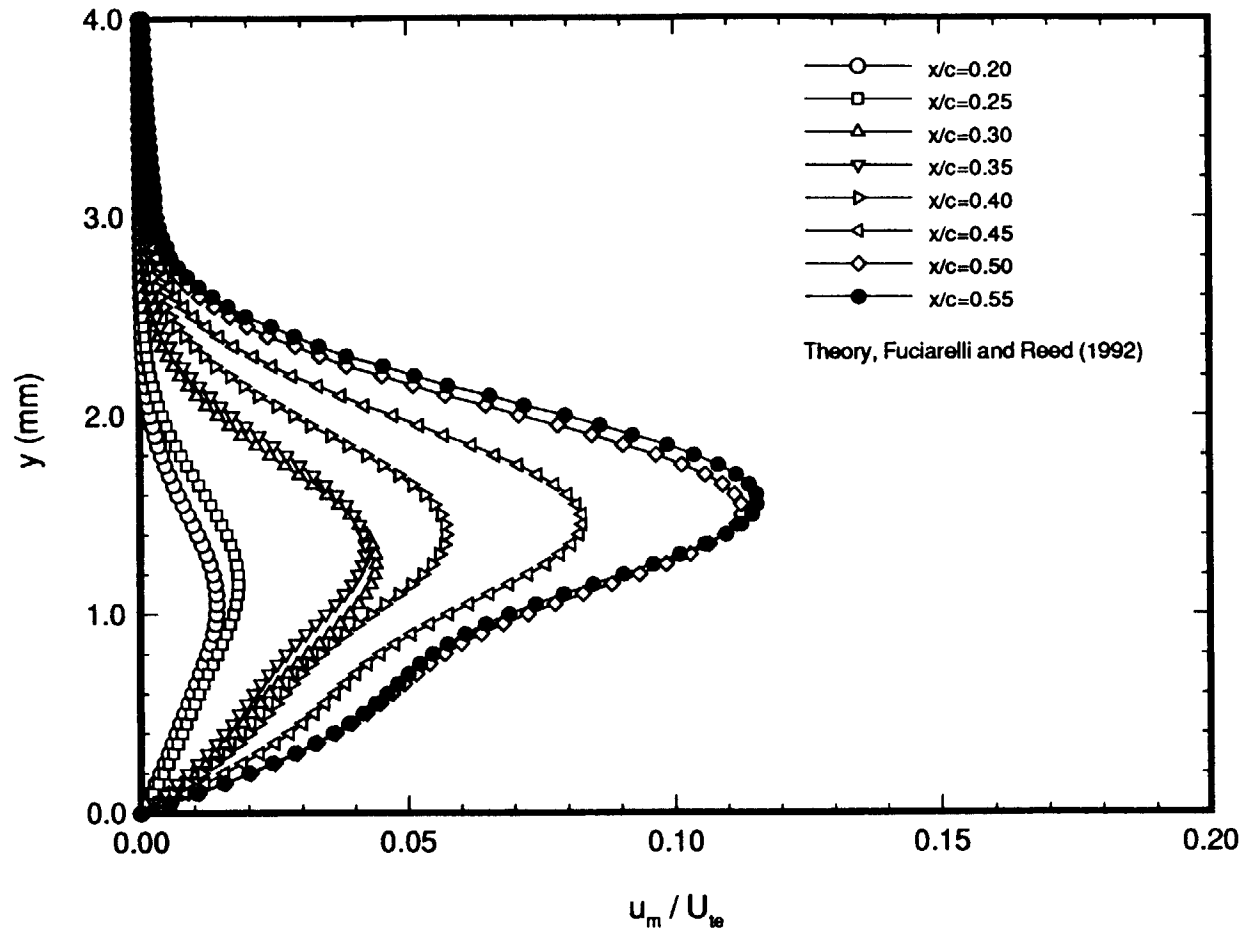


Figure 123. Theoretical Stationary Crossflow-Disturbance Velocity Profiles (Chordwise Component), $\alpha_{ref} = -5^\circ$, $R_c = 2.37 \times 10^6$.

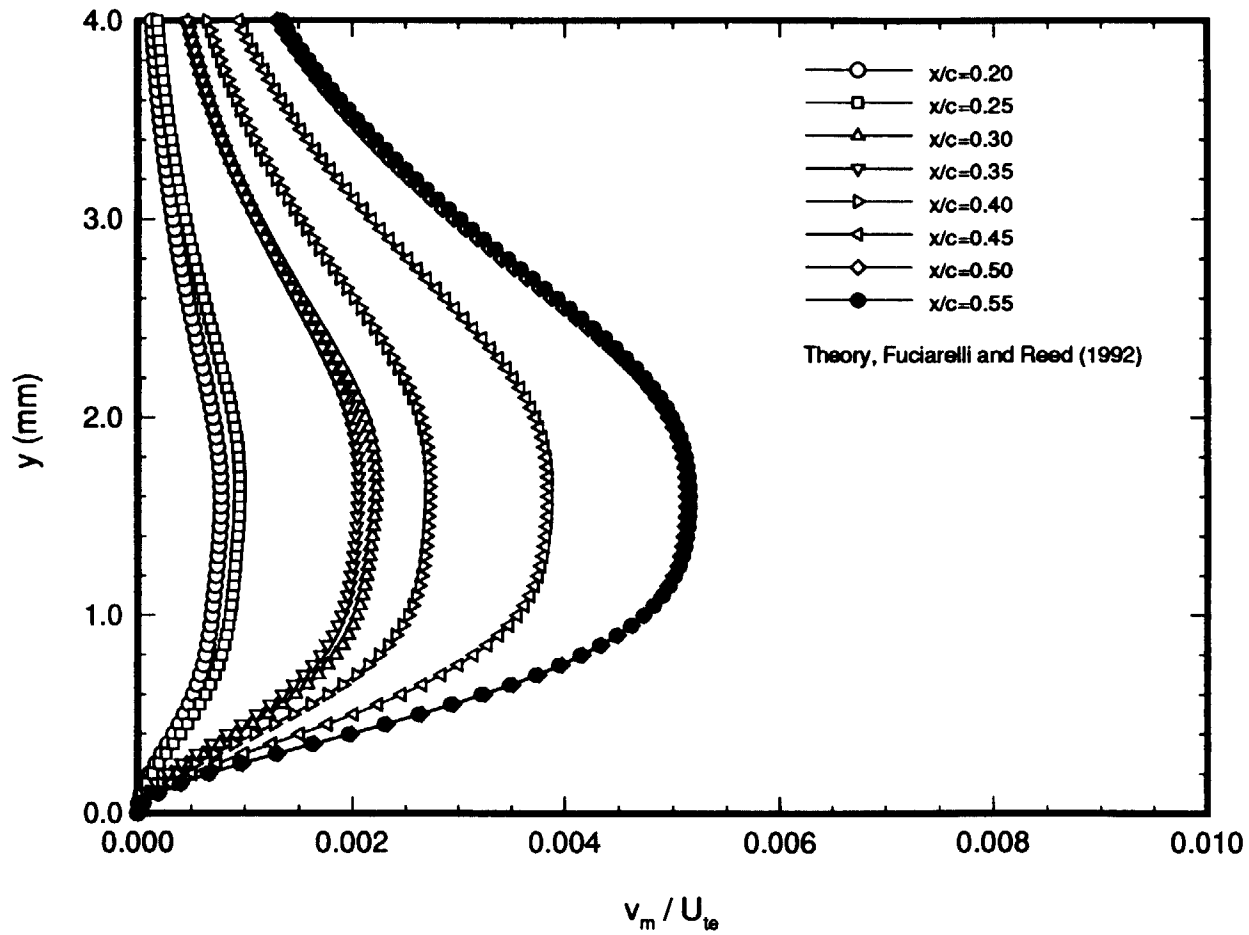


Figure 124. Theoretical Stationary Crossflow-Disturbance Velocity Profiles (Surface-Normal Component), $\alpha_{ref} = -5^\circ$, $R_c = 2.37 \times 10^6$.

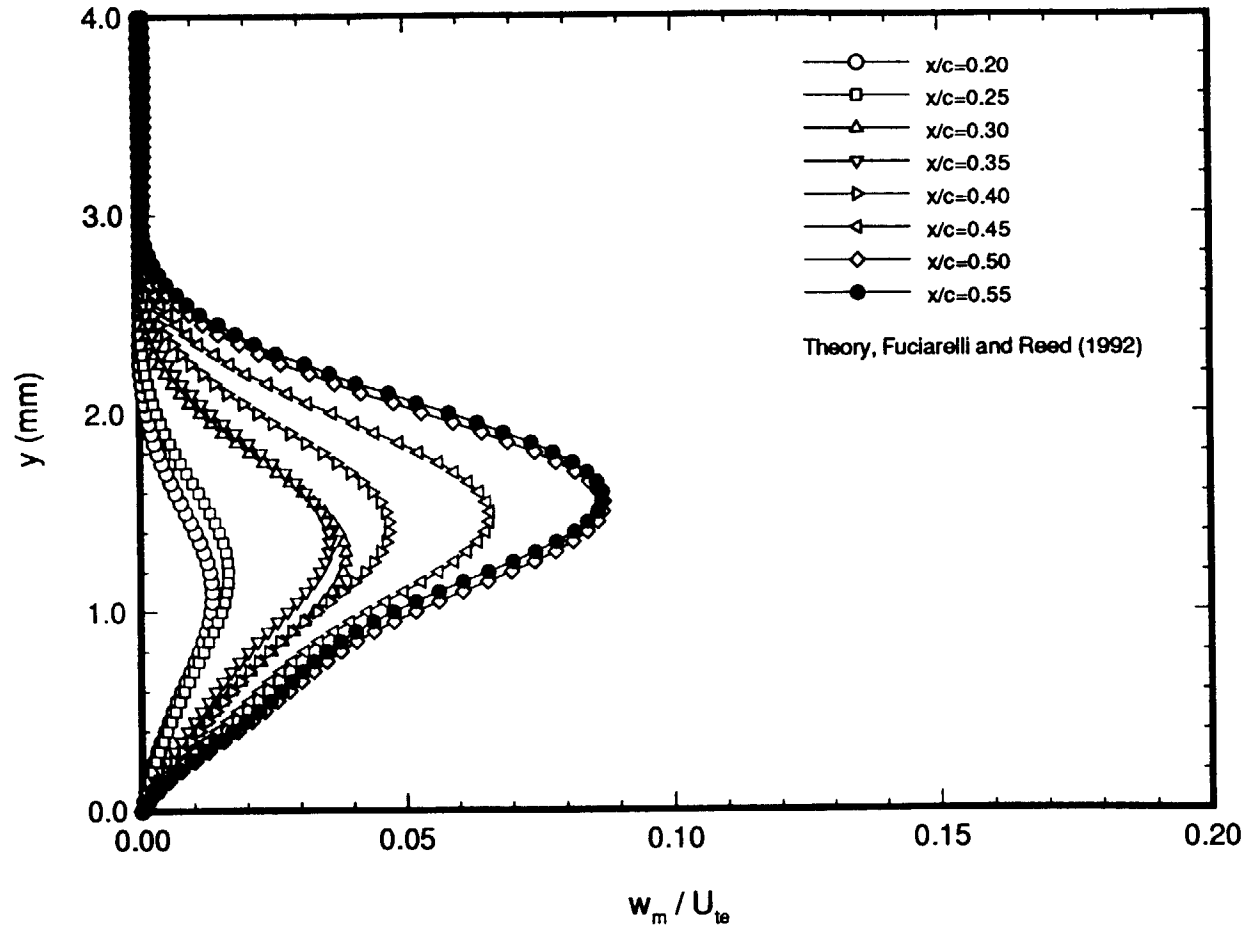


Figure 125. Theoretical Stationary Crossflow-Disturbance Velocity Profiles (Spanwise Component), $\alpha_{\text{ref}} = -5^\circ$, $R_c = 2.37 \times 10^6$.

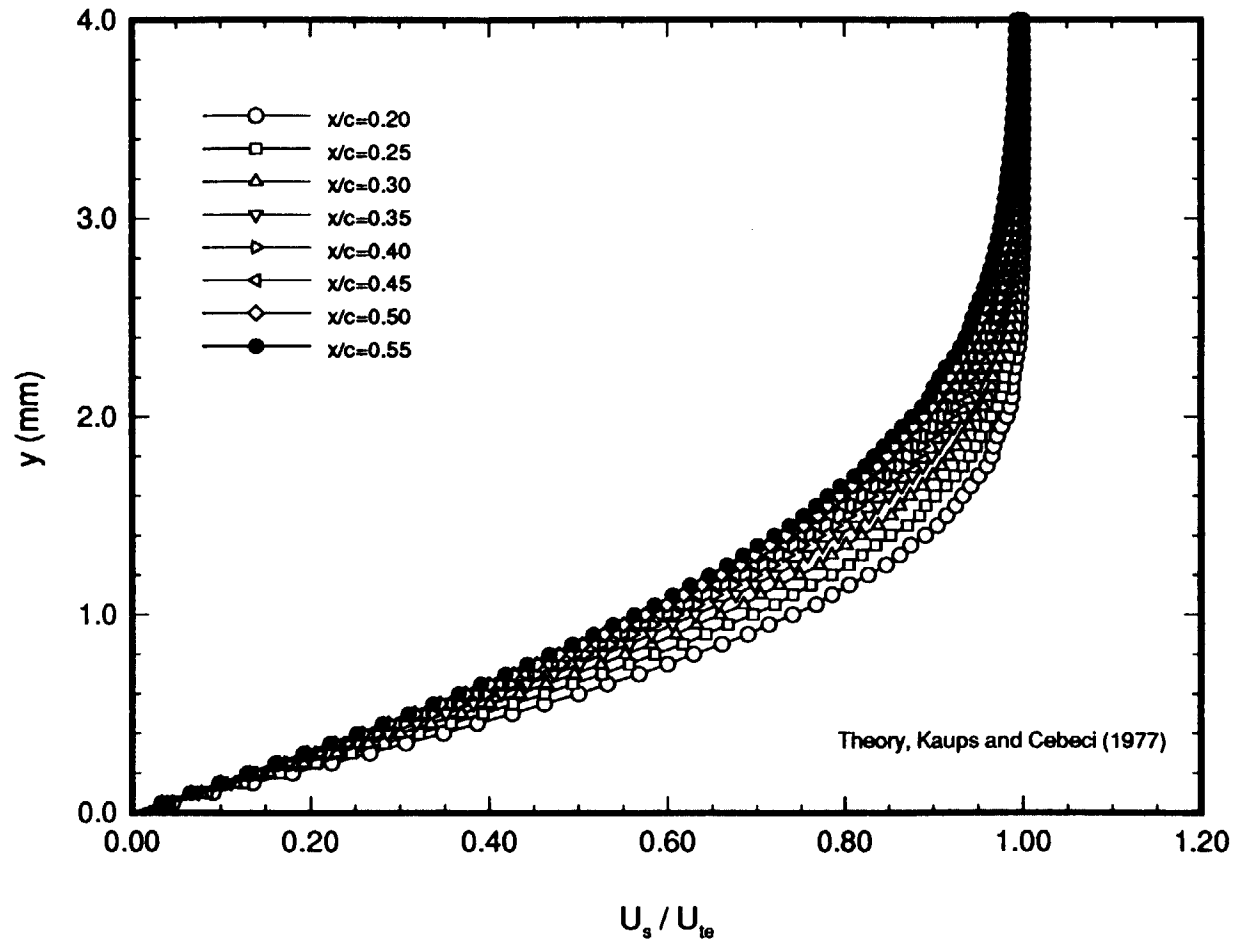


Figure 126. Theoretical Mean Streamwise-Velocity Profiles, $\alpha_{ref} = -5^\circ$, $R_c = 2.37 \times 10^6$.

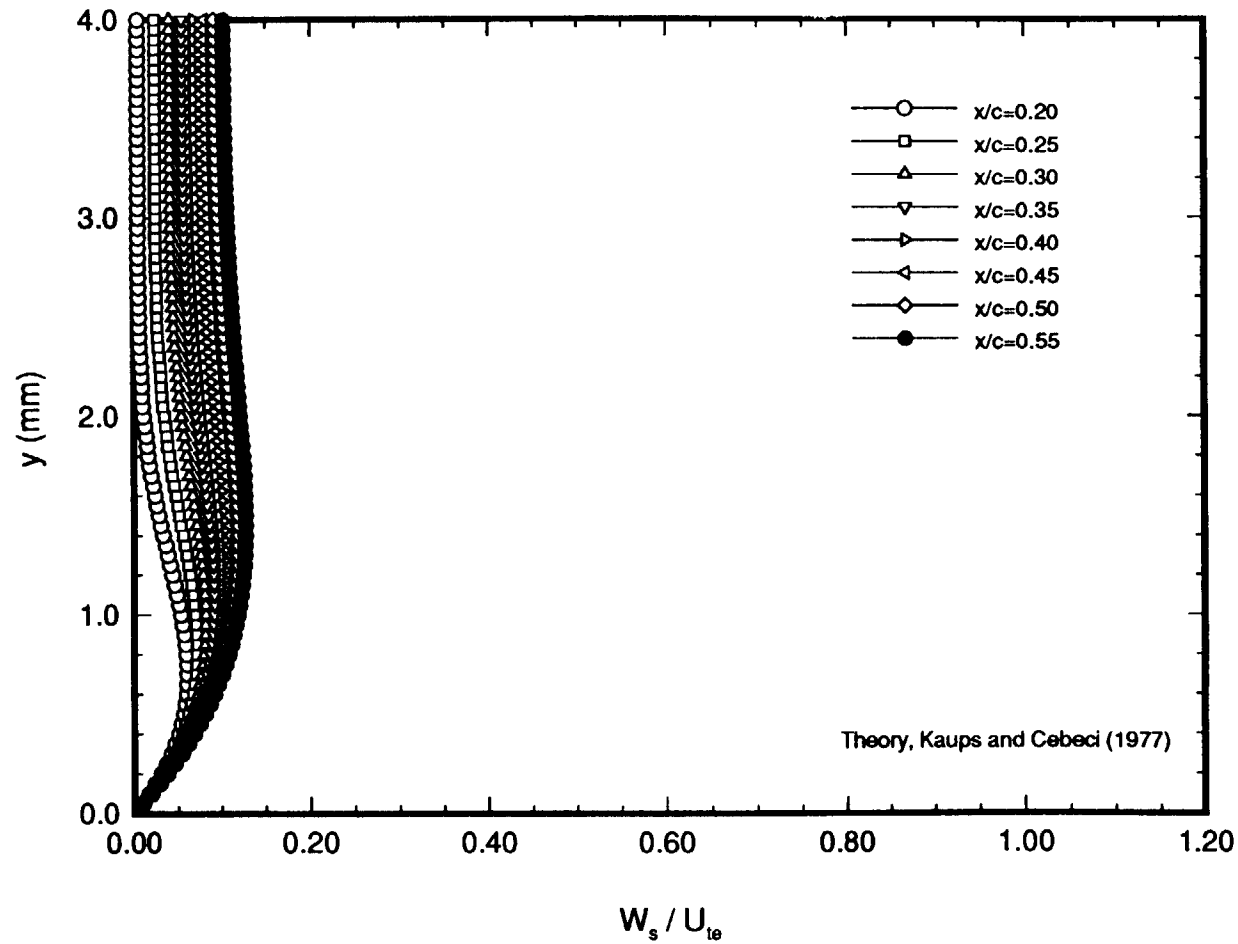


Figure 127. Theoretical Mean Cross-stream Velocity Profiles, $\alpha_{ref} = -5^\circ$, $R_c = 2.37 \times 10^6$.

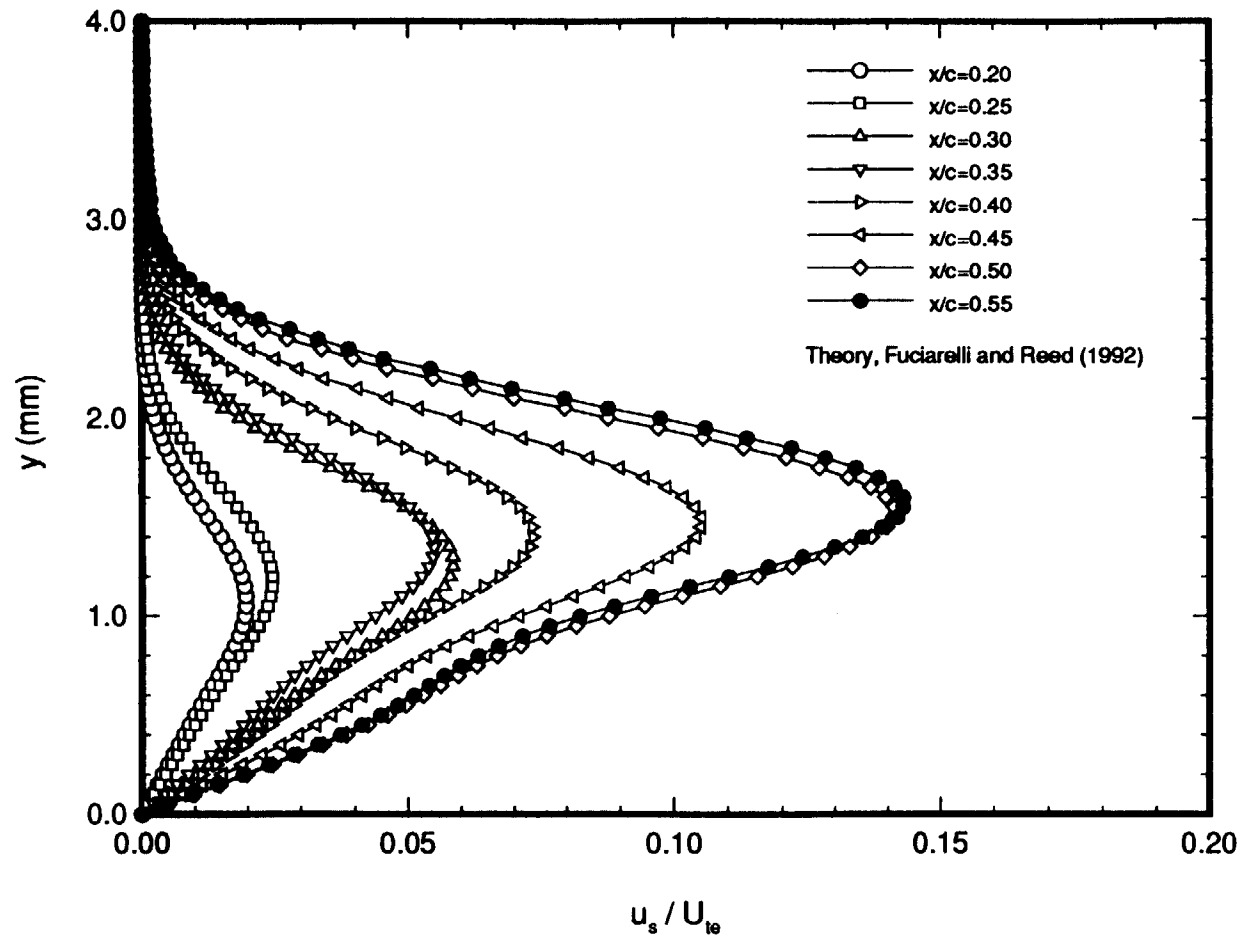


Figure 128. Theoretical Stationary Crossflow-Disturbance Velocity Profiles (Streamwise Component), $\alpha_{ref} = -5^\circ$, $R_c = 2.37 \times 10^6$.

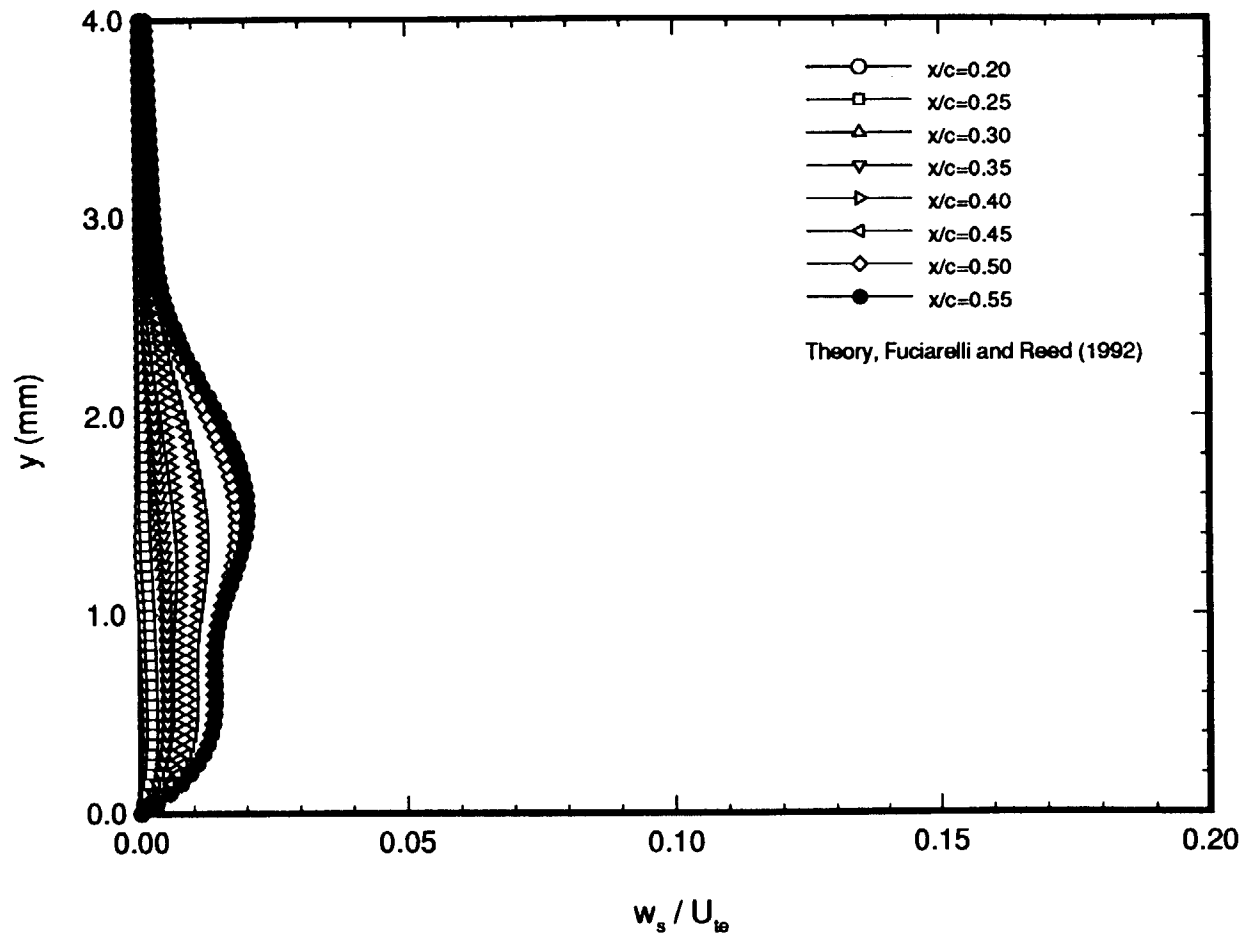


Figure 129. Theoretical Stationary Crossflow-Disturbance Velocity Profiles (Cross-stream Component), $\alpha_{ref} = -5^\circ$, $R_c = 2.37 \times 10^6$.

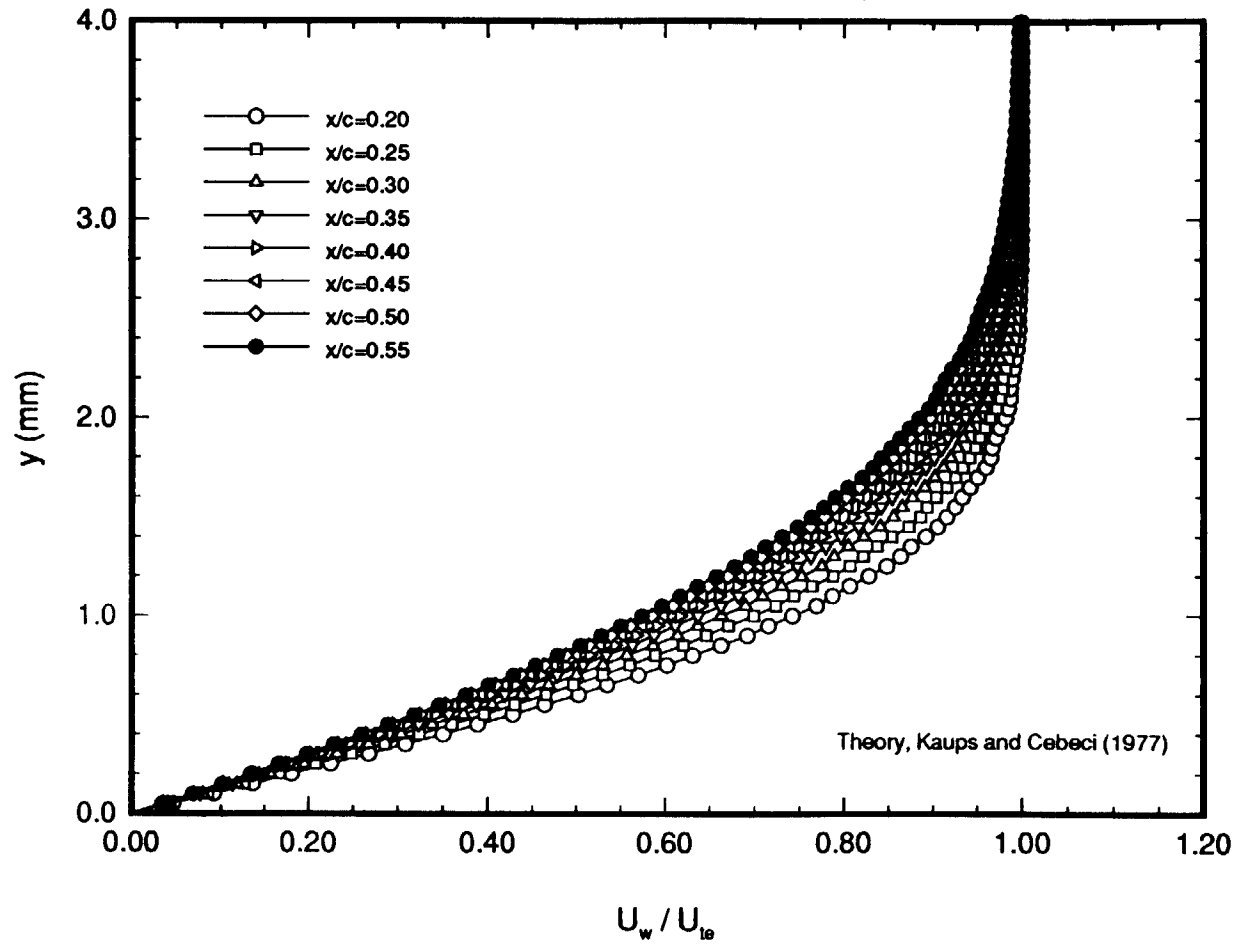


Figure 130. Theoretical Mean-Velocity Profiles Along the Vortex Axis, $\alpha_{ref} = -5^\circ$, $R_c = 2.37 \times 10^6$.

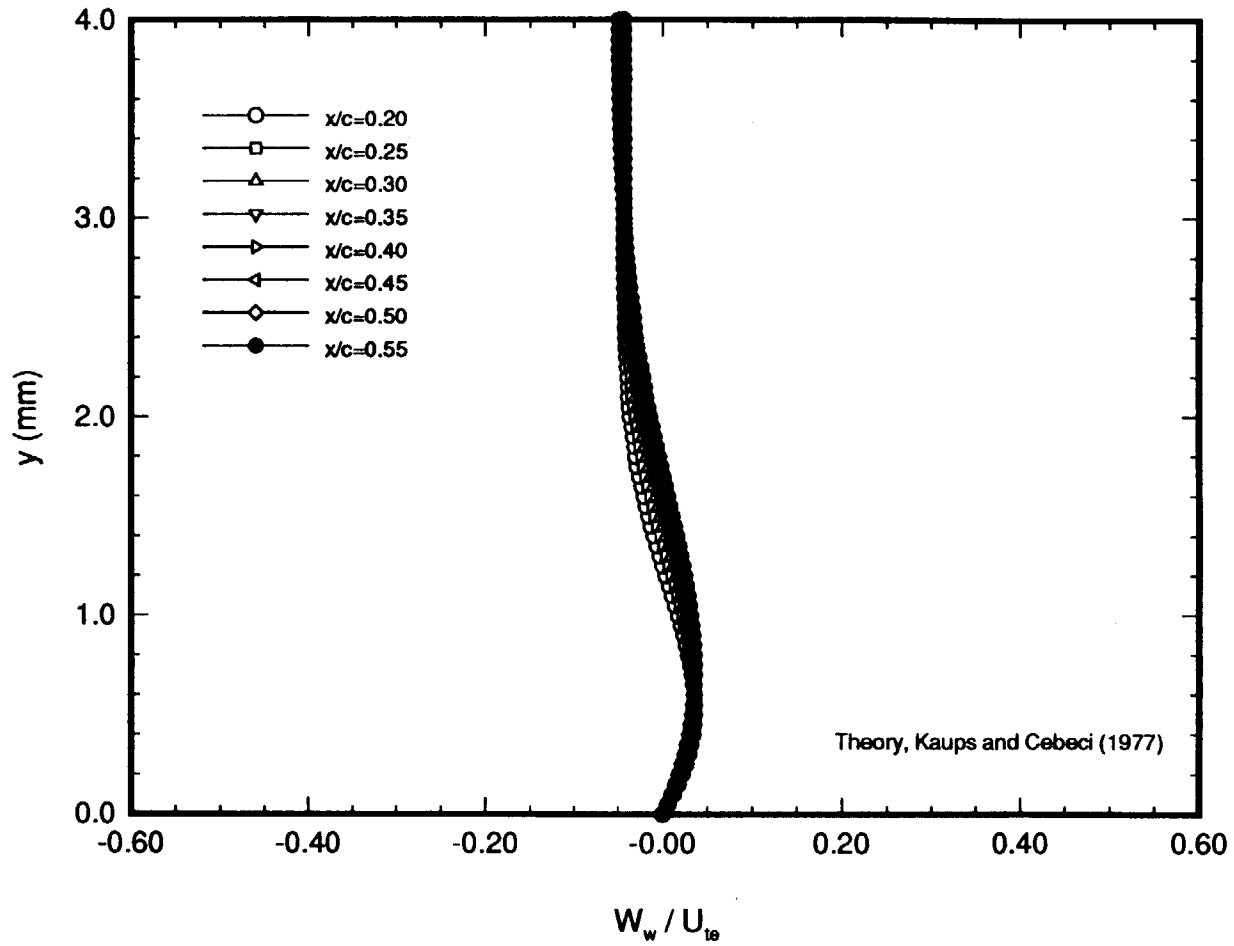


Figure 131. Theoretical Mean-Velocity Profiles Perpendicular to the Vortex Axis, $\alpha_{ref} = -5^\circ$, $R_c = 2.37 \times 10^6$.

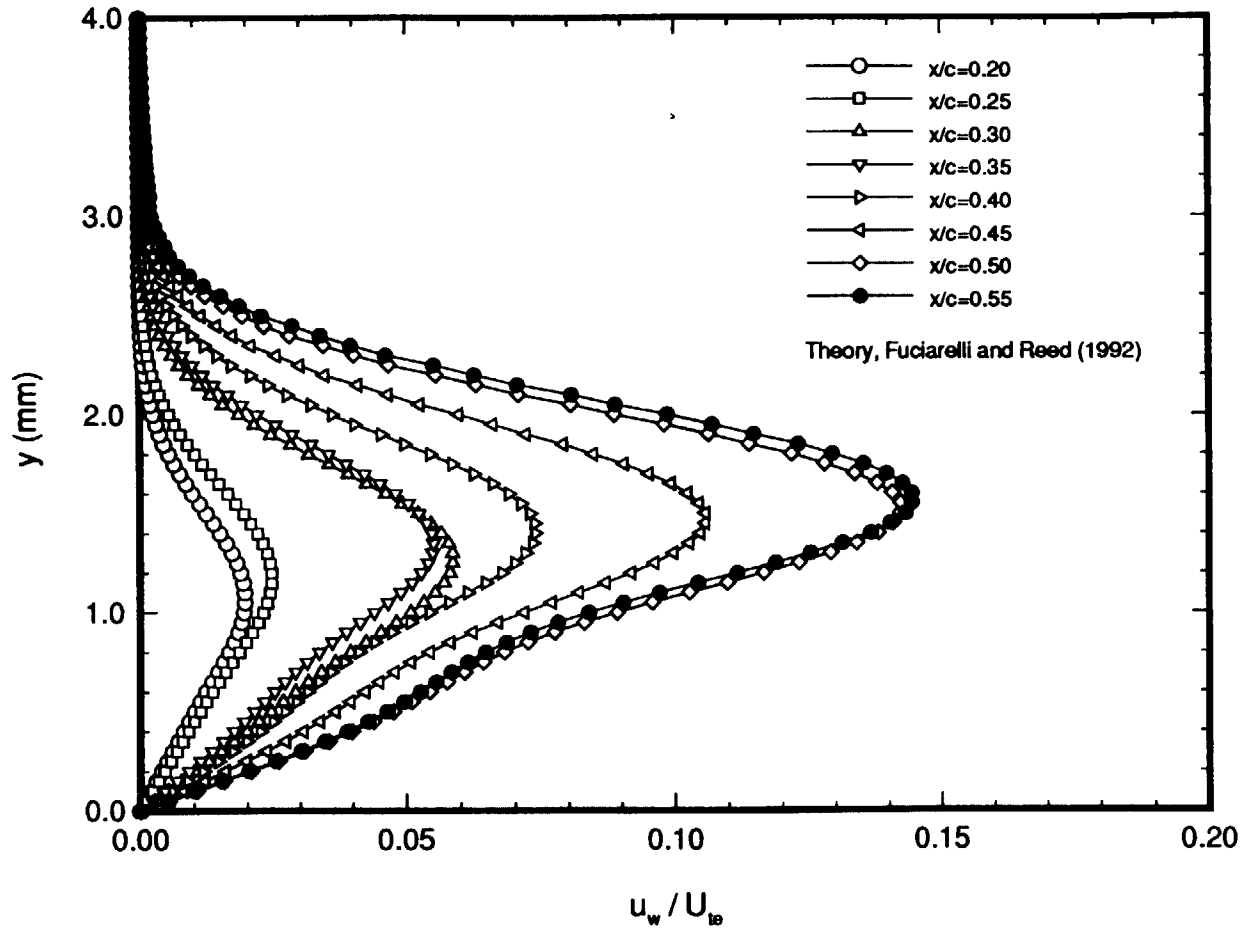


Figure 132. Theoretical Stationary Crossflow-Disturbance Velocity Profiles Along the Vortex Axis, $\alpha_{\text{ref}} = -5^\circ$, $R_c = 2.37 \times 10^6$.

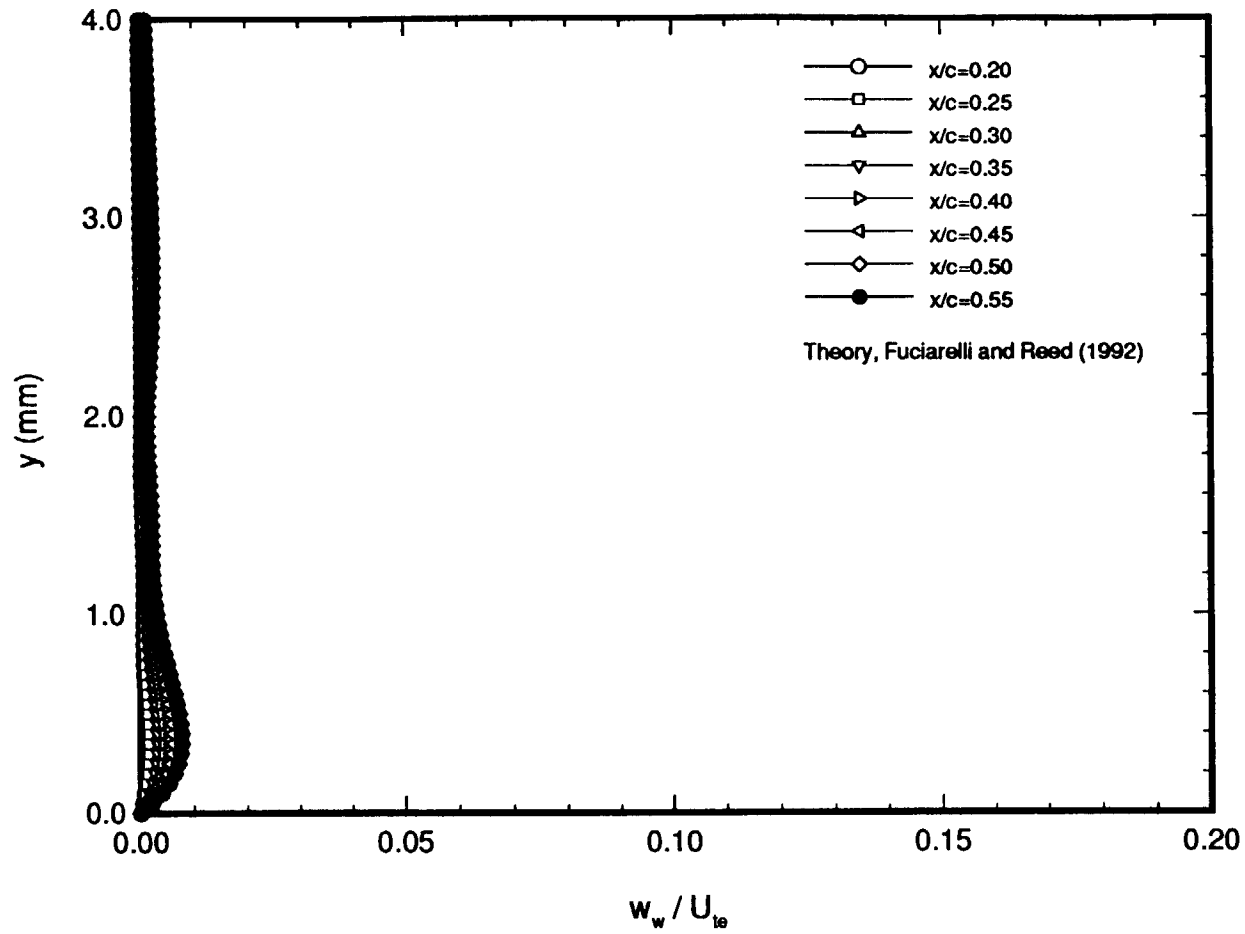


Figure 133. Theoretical Stationary Crossflow-Disturbance Velocity Profiles Perpendicular to the Vortex Axis, $\alpha_{\text{ref}} = -5^\circ$, $R_c = 2.37 \times 10^6$.

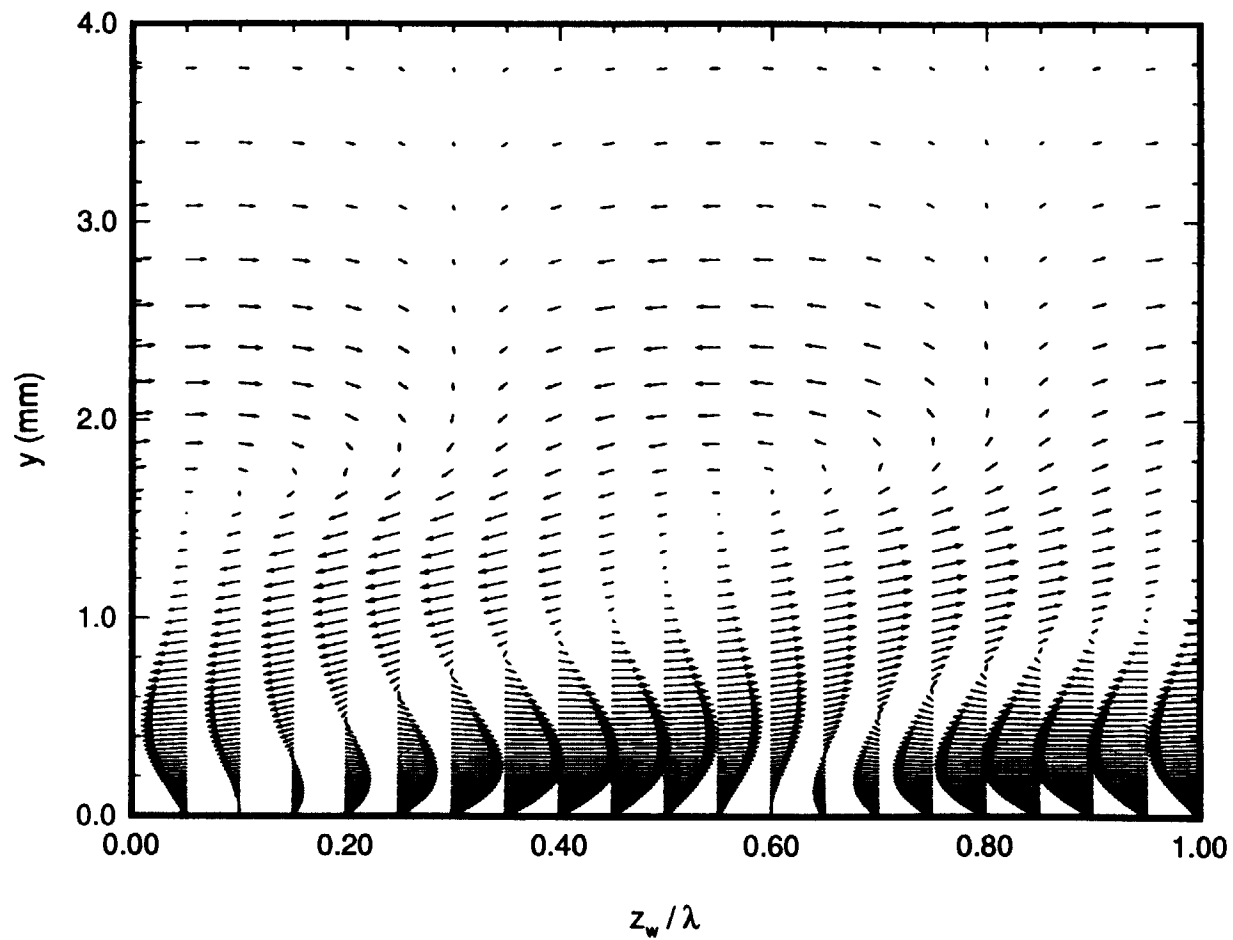


Figure 134. Theoretical Stationary Crossflow-Disturbance Velocity Vectors Across a Single Vortex Wavelength, $\alpha_{ref} = -5^\circ$, $R_c = 2.37 \times 10^6$.

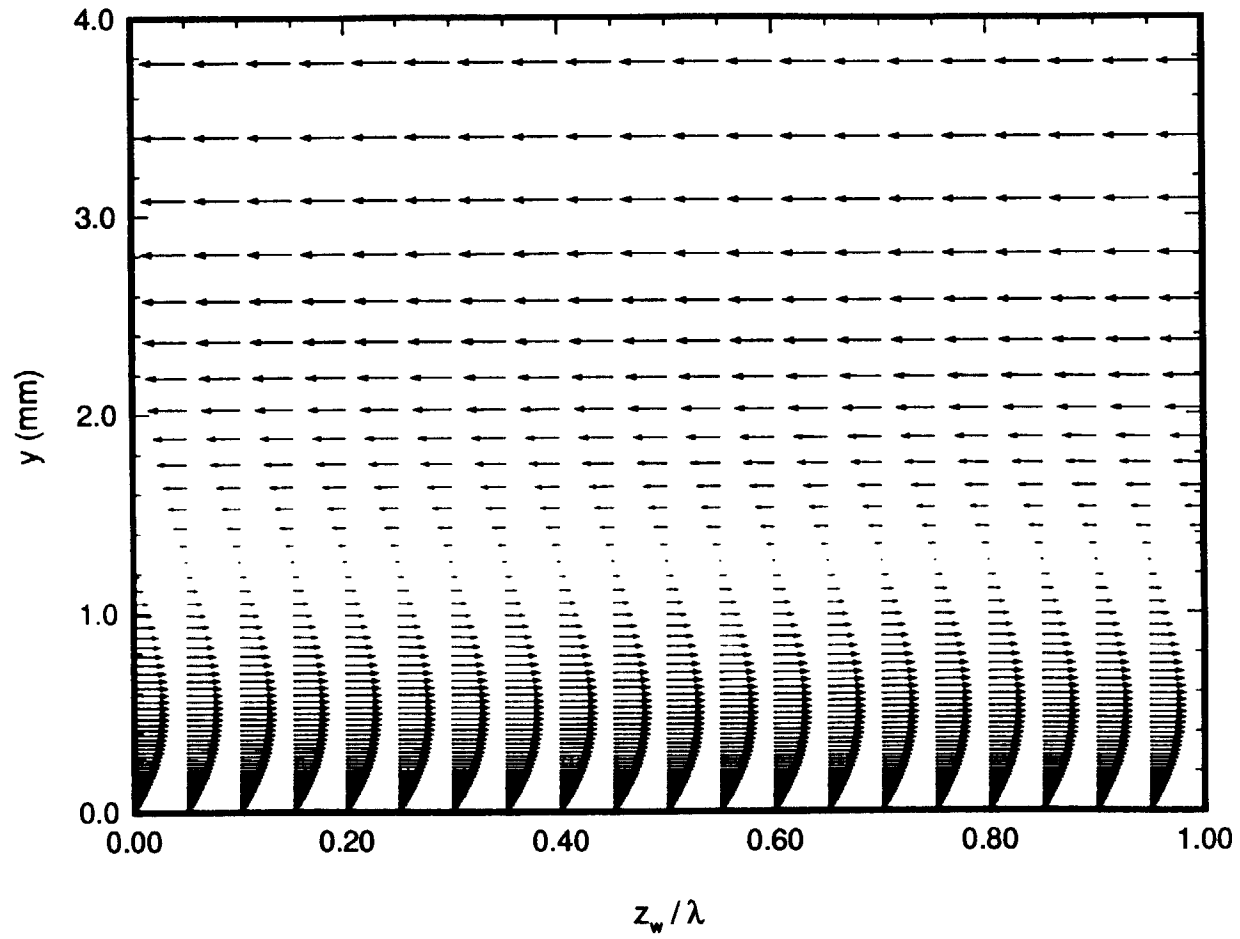


Figure 135. Theoretical Total Velocity Vectors (Disturbance Plus Mean Flow) Across a Single Vortex Wavelength, $\alpha_{ref} = -5^\circ$, $R_c = 2.37 \times 10^6$.

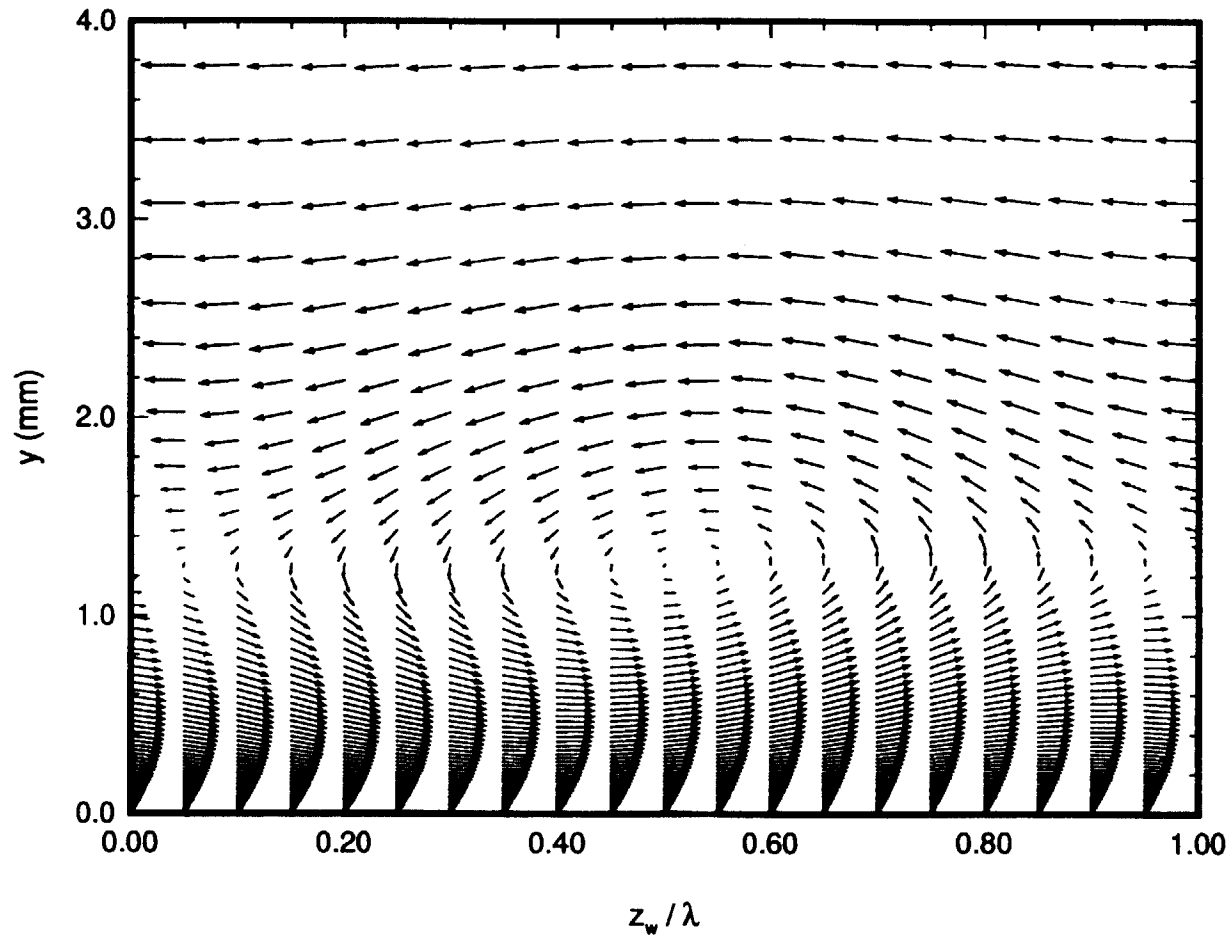


Figure 136. Theoretical Total Velocity Vectors (Disturbance Plus Mean Flow) Across a Single Vortex Wavelength With Normal Velocity Components Scaled by a Factor of 100, $\alpha_{ref} = -5^\circ$, $R_c = 2.37 \times 10^6$.

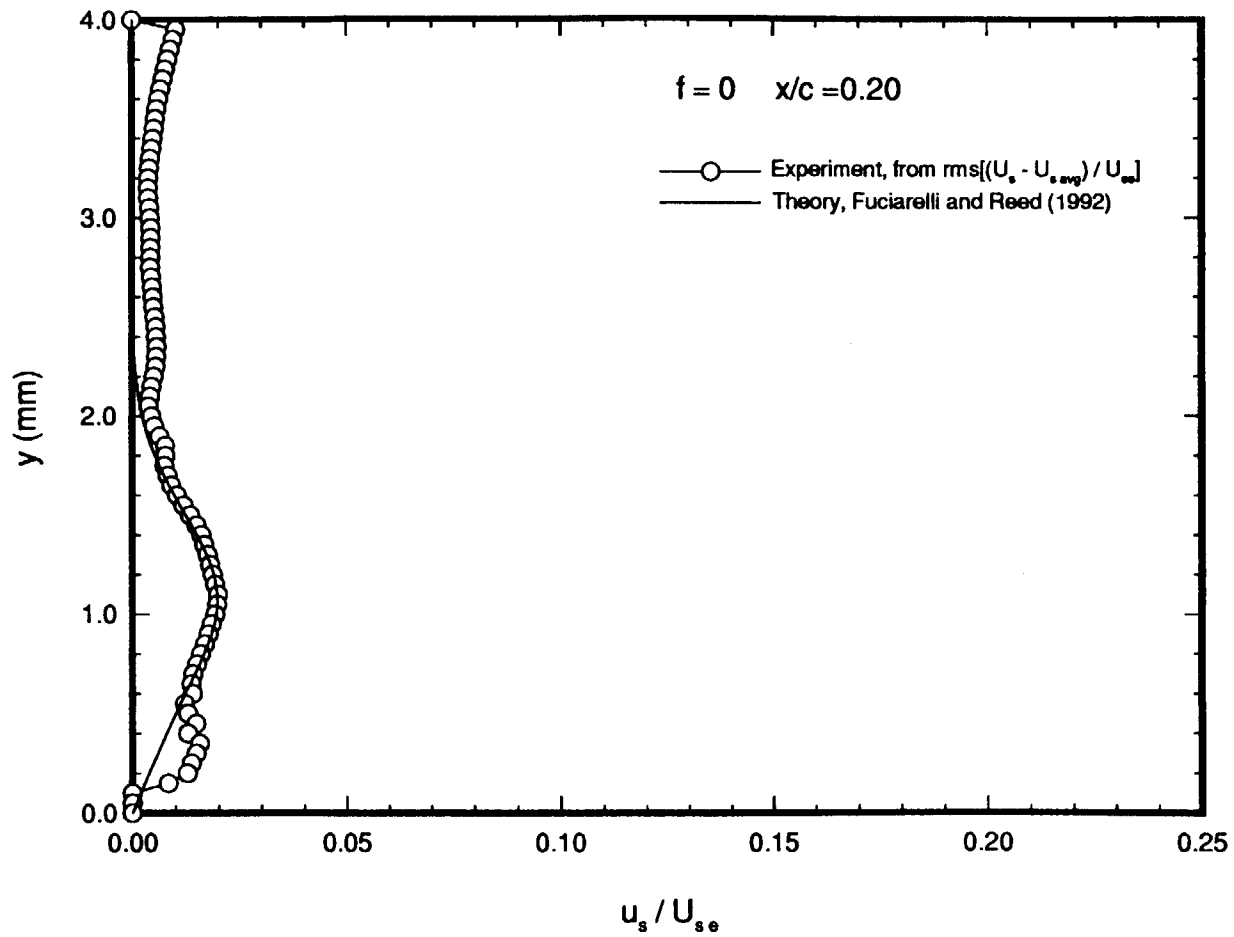


Figure 137. Comparison of Experimental Streamwise-Disturbance Velocity Profile Determined from $U_s - U_{s,\text{avg}}$ with Theoretical Eigenfunction, $x/c = 0.20$, $\alpha = -4^\circ$, $R_c = 2.37 \times 10^6$.

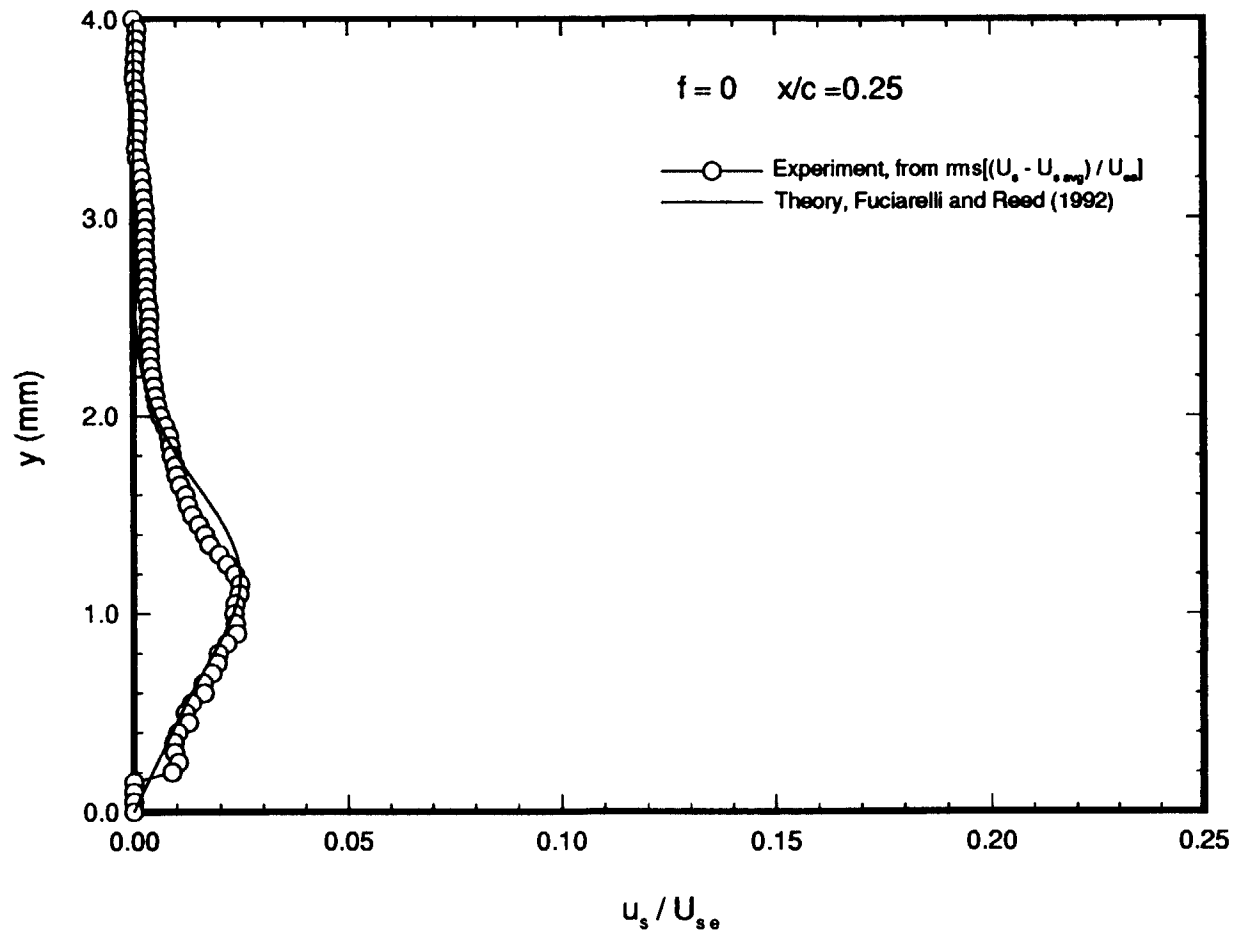


Figure 138. Comparison of Experimental Streamwise-Disturbance Velocity Profile Determined from $U_s - U_{s, \text{avg}}$ with Theoretical Eigenfunction, $x/c = 0.25$, $\alpha = -4^\circ$, $R_c = 2.37 \times 10^6$.

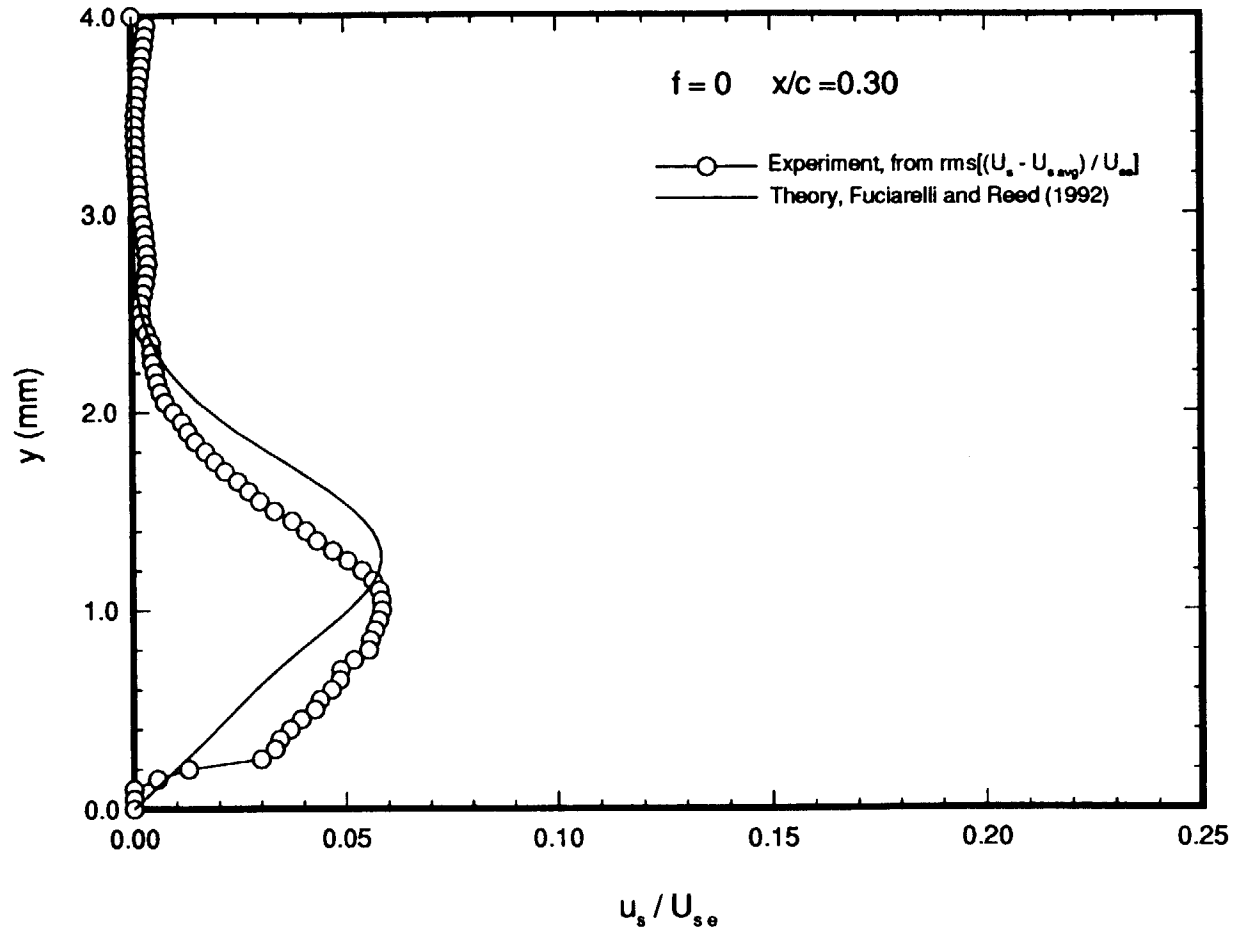


Figure 139. Comparison of Experimental Streamwise-Disturbance Velocity Profile Determined from $U_s - U_{s, \text{avg}}$ with Theoretical Eigenfunction, $x/c = 0.30$, $\alpha = -4^\circ$, $R_c = 2.37 \times 10^6$.

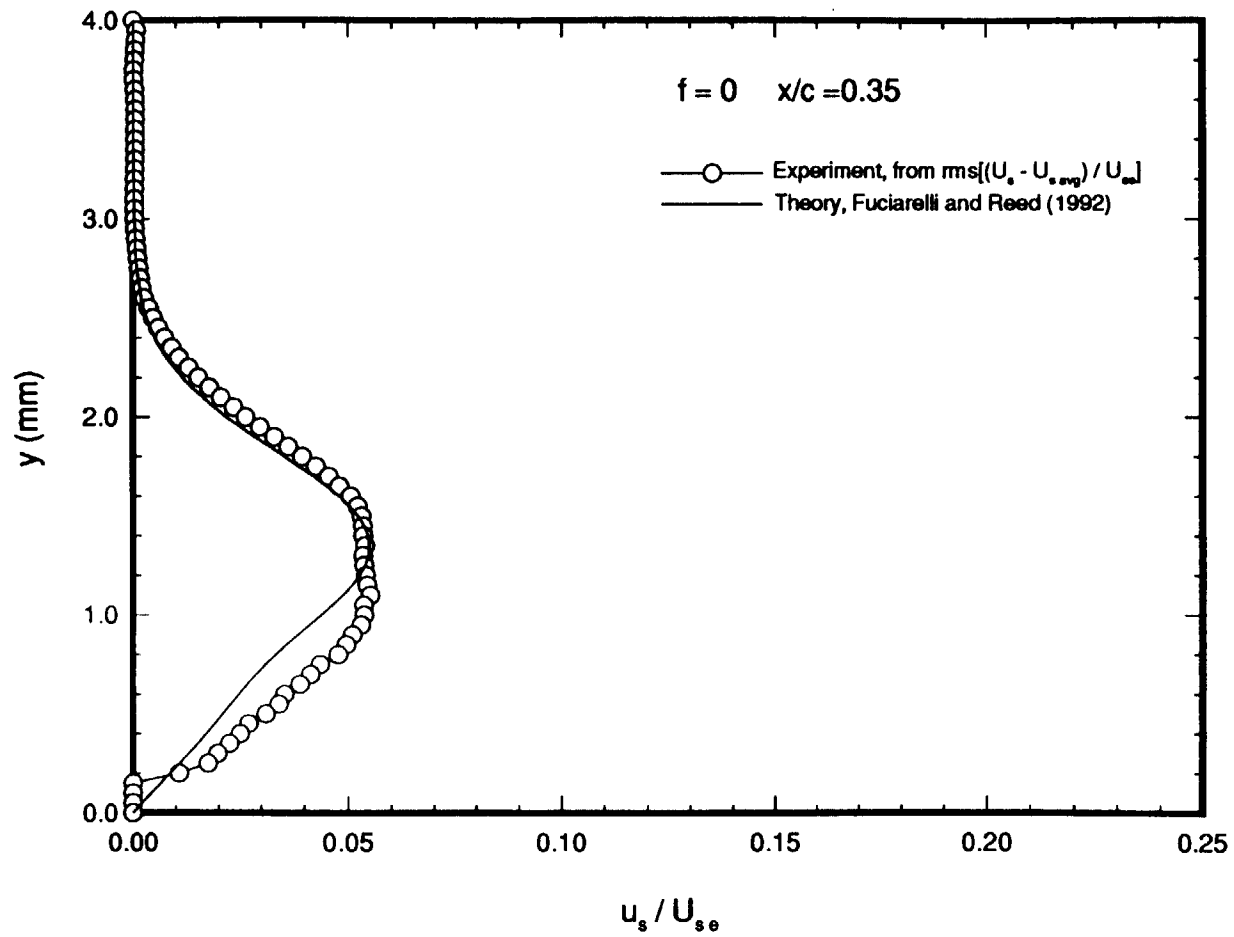


Figure 140. Comparison of Experimental Streamwise-Disturbance Velocity Profile Determined from $U_s - U_{s,avg}$ with Theoretical Eigenfunction, $x/c = 0.35$, $\alpha = -4^\circ$, $R_c = 2.37 \times 10^6$.

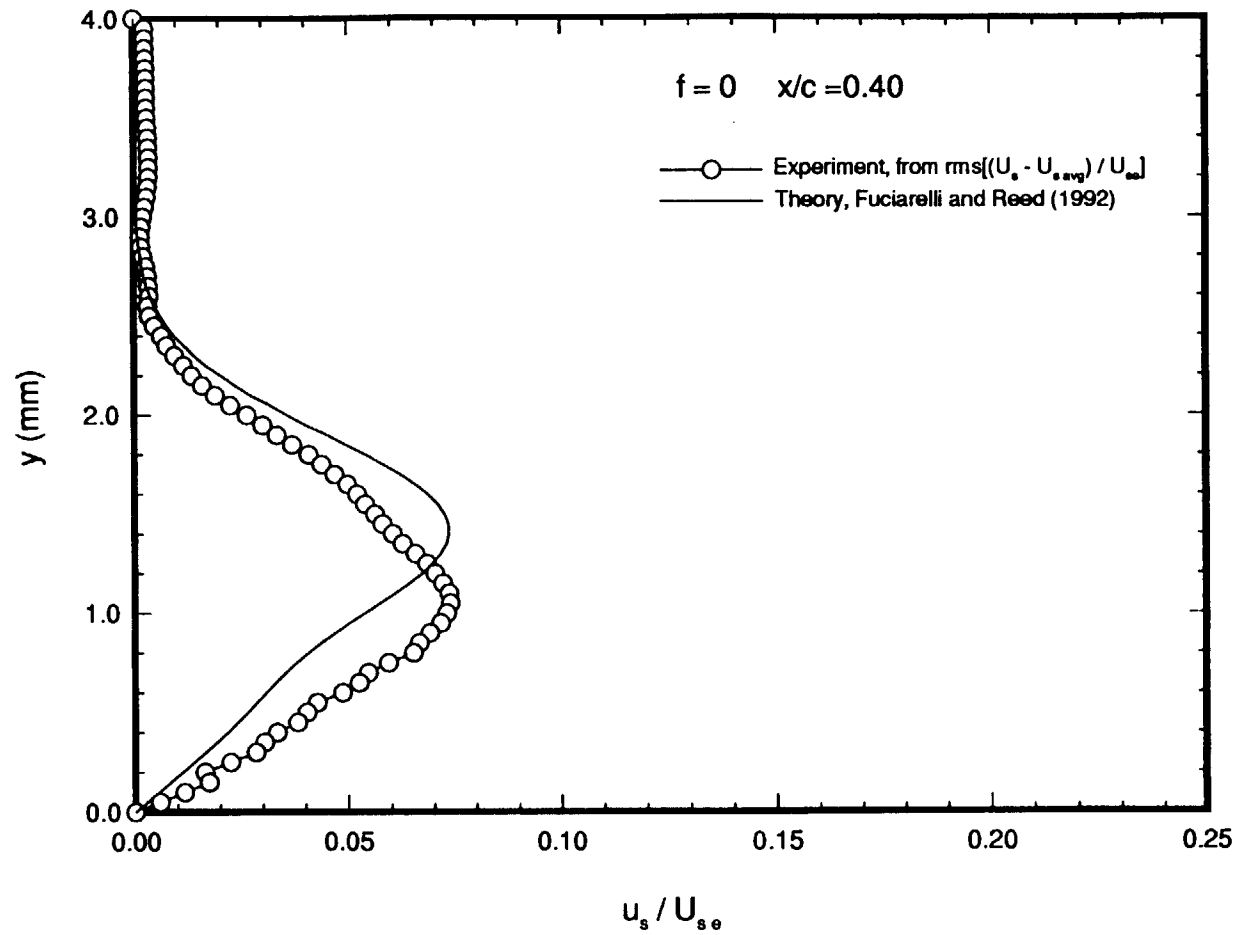


Figure 141. Comparison of Experimental Streamwise-Disturbance Velocity Profile Determined from $U_s - U_{s, \text{avg}}$ with Theoretical Eigenfunction, $x/c = 0.40$, $\alpha = -4^\circ$, $R_c = 2.37 \times 10^6$.

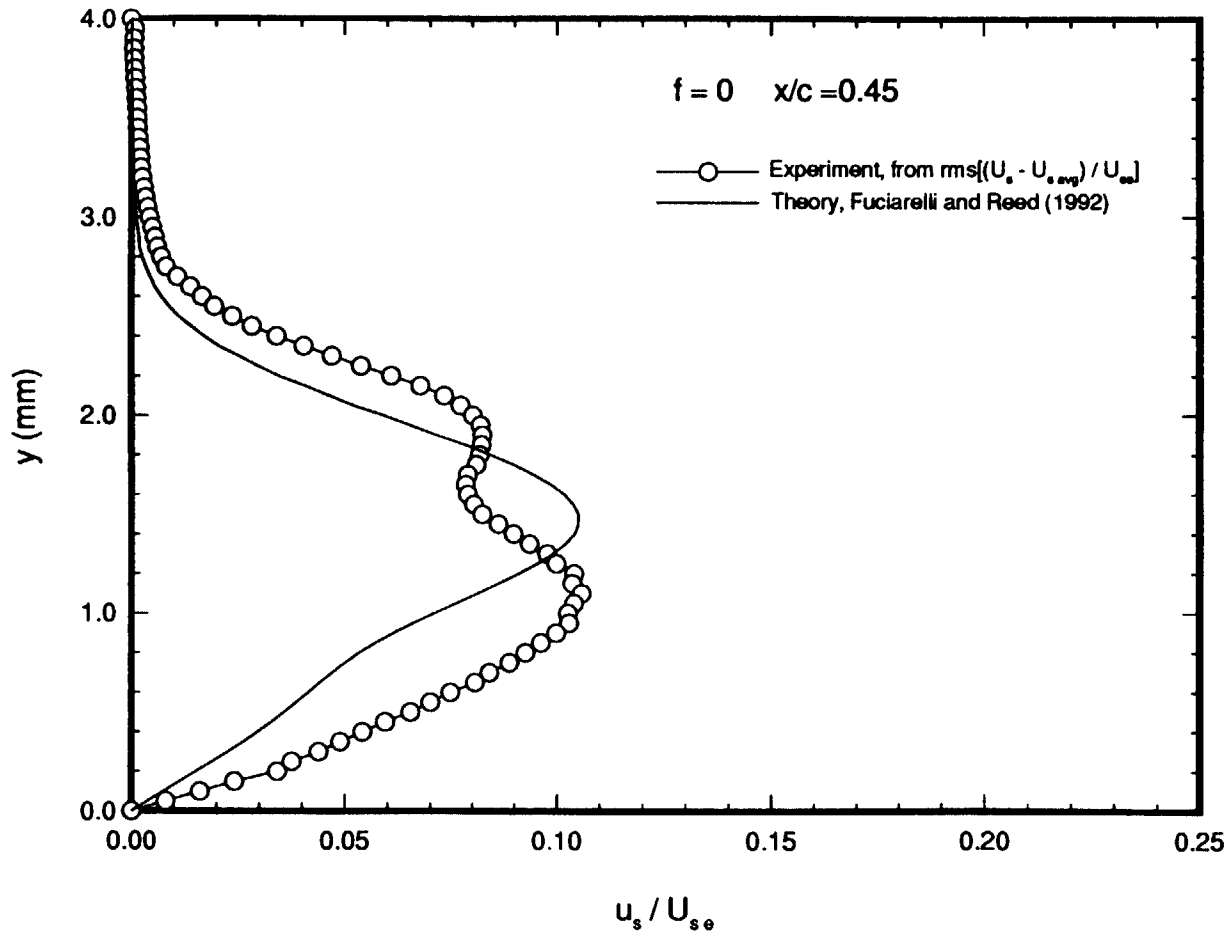


Figure 142. Comparison of Experimental Streamwise-Disturbance Velocity Profile Determined from $U_s - U_{s, \text{avg}}$ with Theoretical Eigenfunction, $x/c = 0.45$, $\alpha = -4^\circ$, $R_c = 2.37 \times 10^6$.

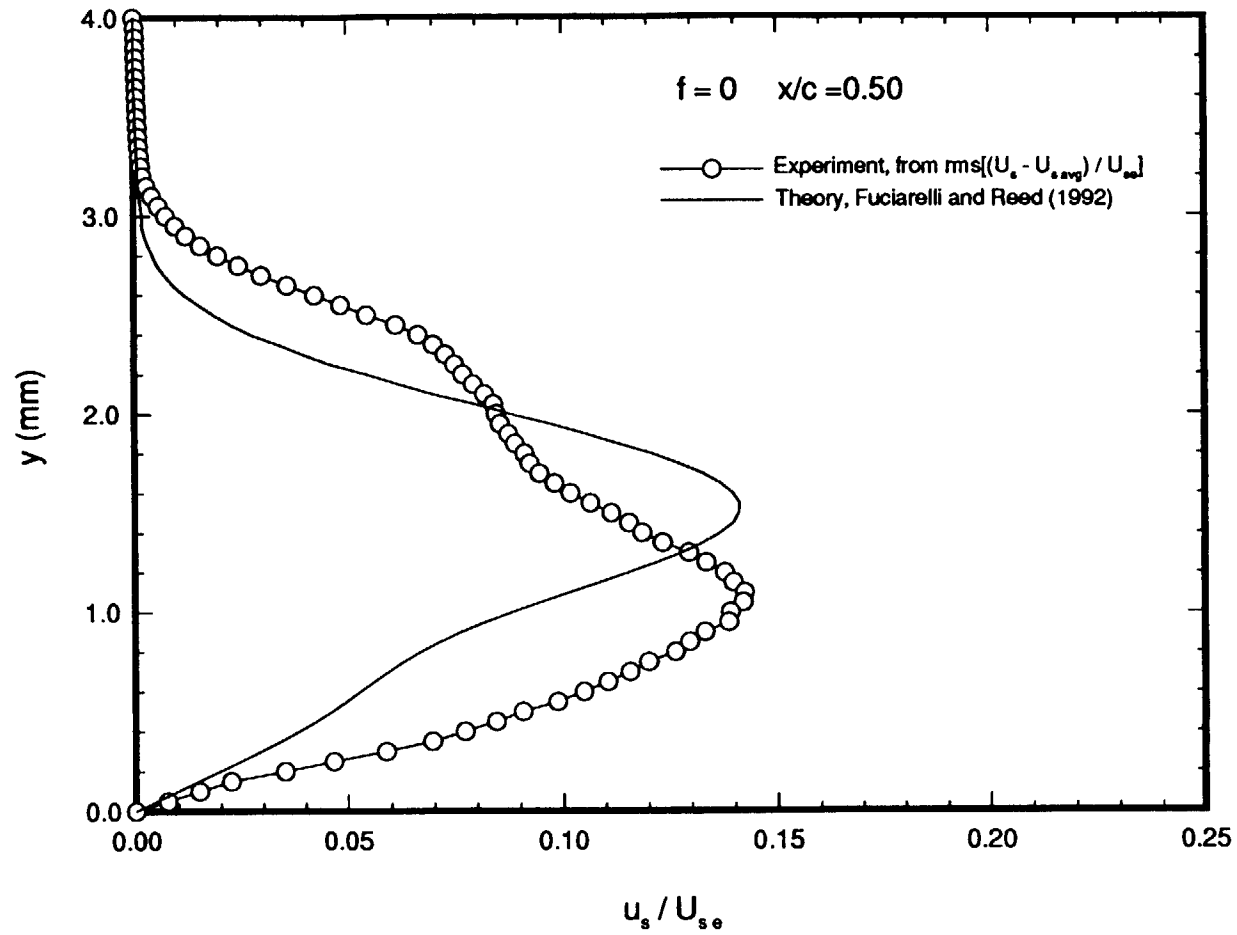


Figure 143. Comparison of Experimental Streamwise-Disturbance Velocity Profile Determined from $U_s - U_{s,\text{avg}}$ with Theoretical Eigenfunction, $x/c = 0.50$, $\alpha = -4^\circ$, $R_c = 2.37 \times 10^6$.

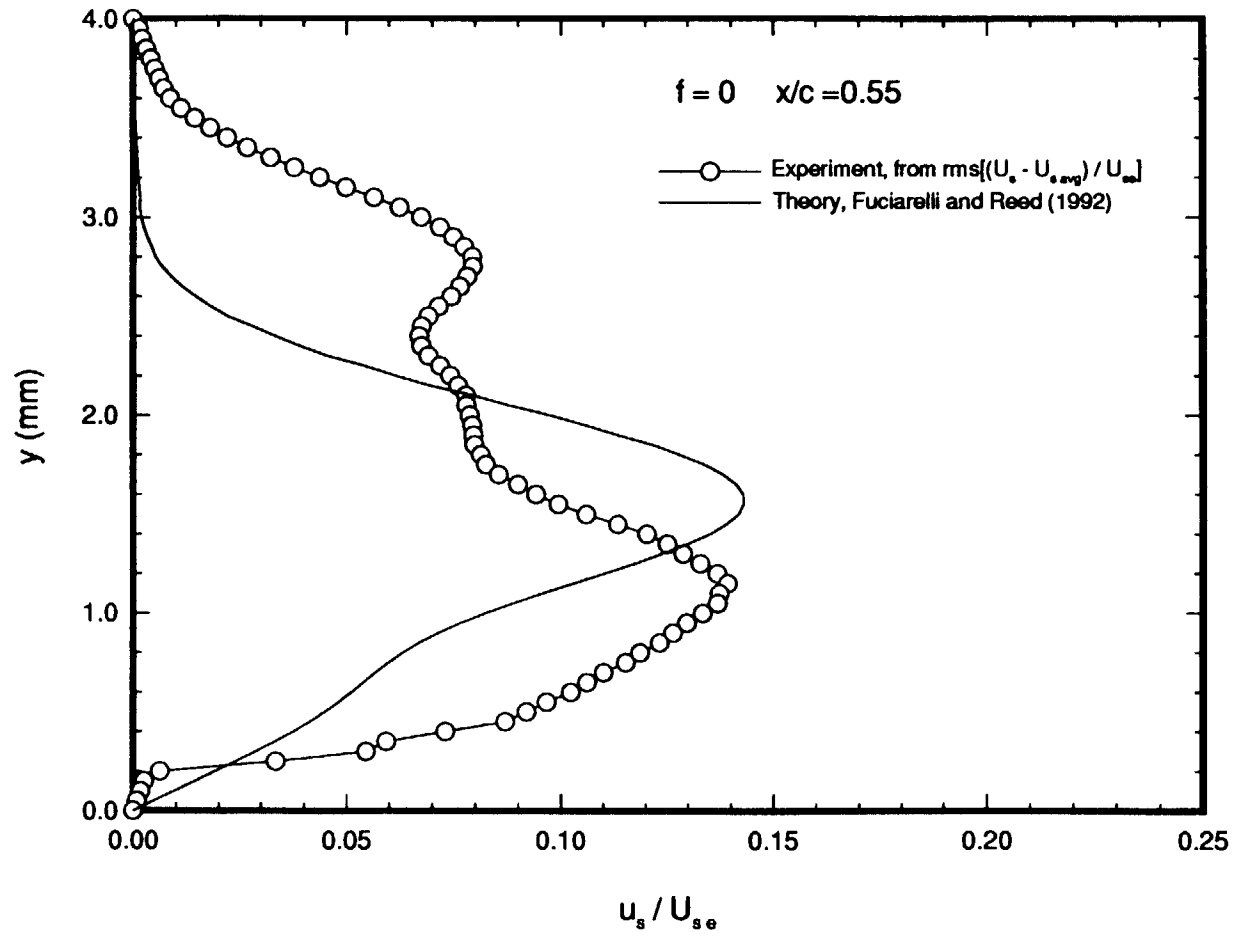


Figure 144. Comparison of Experimental Streamwise-Disturbance Velocity Profile Determined from $U_s - U_{s,avg}$ with Theoretical Eigenfunction, $x/c = 0.55$, $\alpha = -4^\circ$, $R_c = 2.37 \times 10^6$.

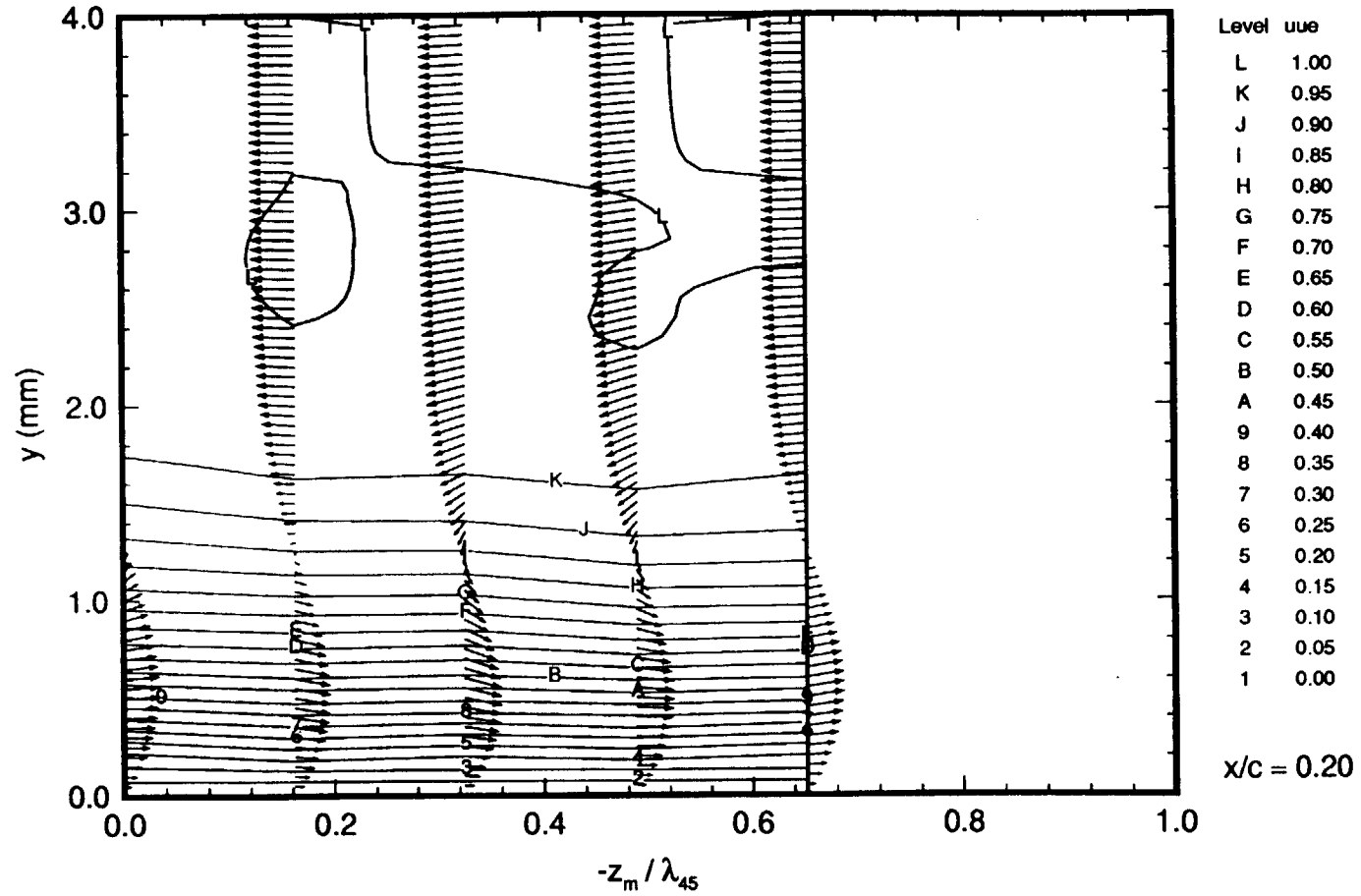


Figure 145. Comparison of Experimental Mean Streamwise-Velocity Contours with Theoretical Vortex Velocity-Vector Field, $x/c = 0.20$, $\alpha = -4^\circ$, $R_c = 2.37 \times 10^6$.

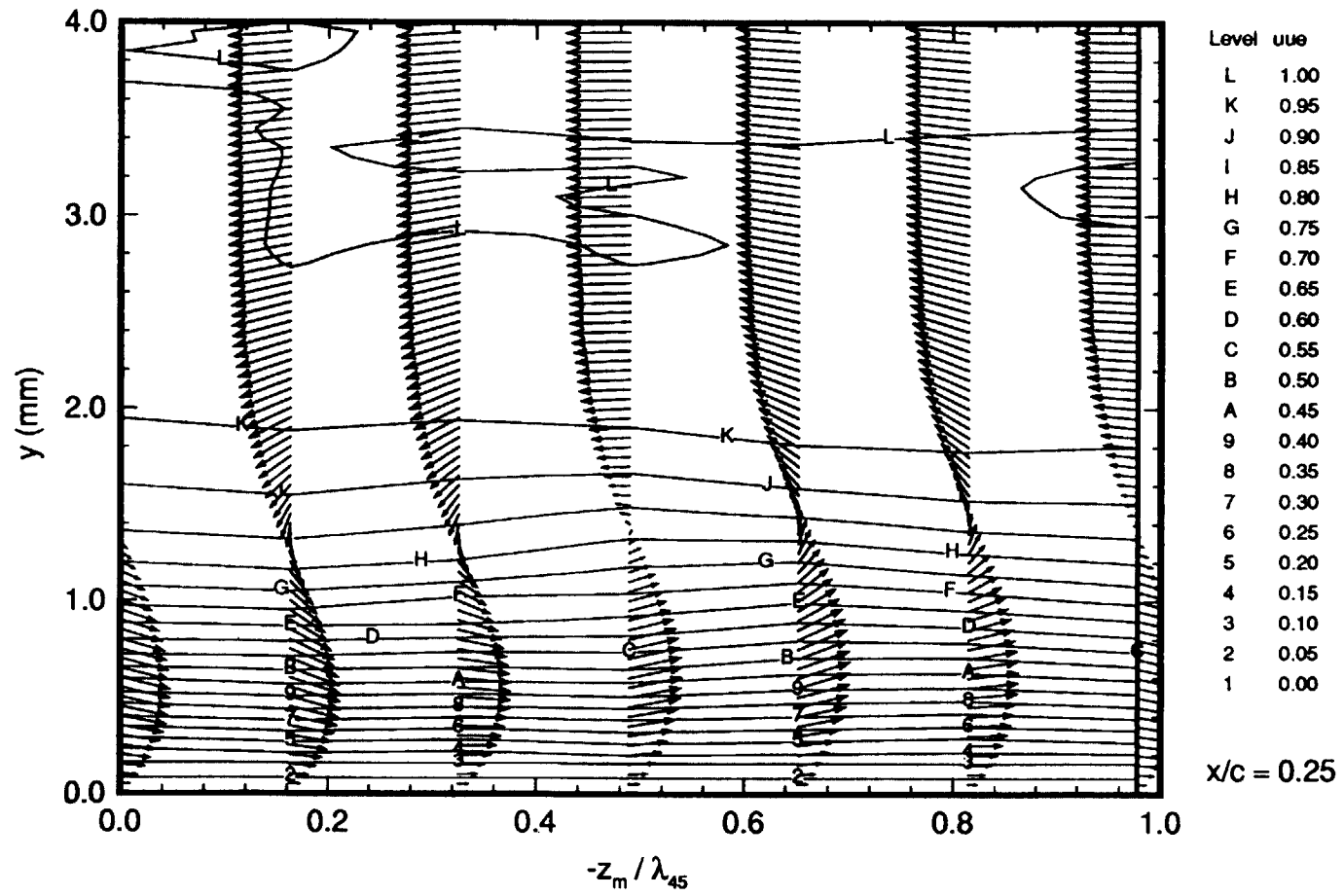


Figure 146. Comparison of Experimental Mean Streamwise-Velocity Contours with Theoretical Vortex Velocity-Vector Field, $x/c = 0.25$, $\alpha = -4^\circ$, $R_c = 2.37 \times 10^6$.

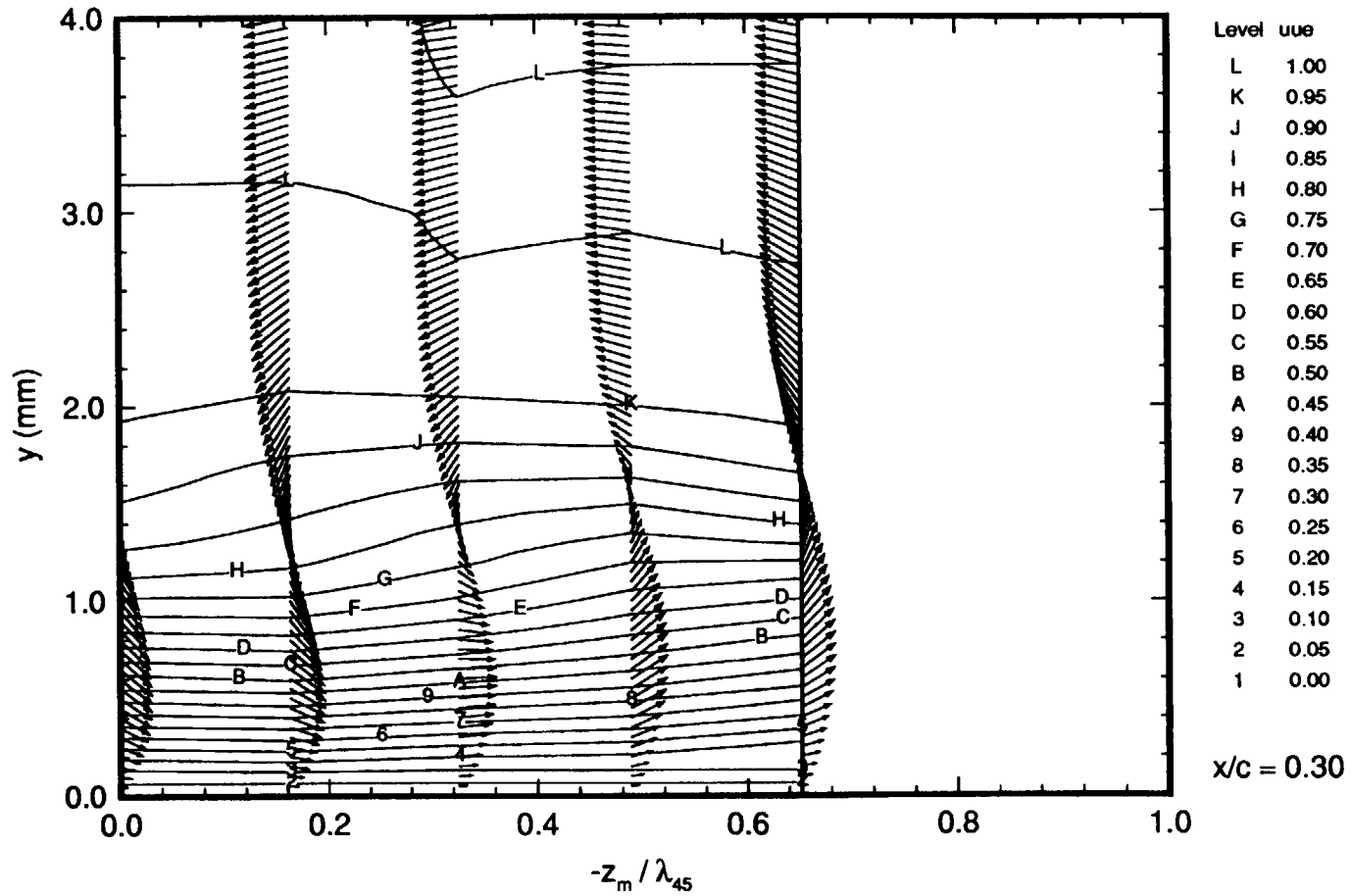


Figure 147. Comparison of Experimental Mean Streamwise-Velocity Contours with Theoretical Vortex Velocity-Vector Field, $x/c = 0.30$, $\alpha = -4^\circ$, $R_c = 2.37 \times 10^6$.

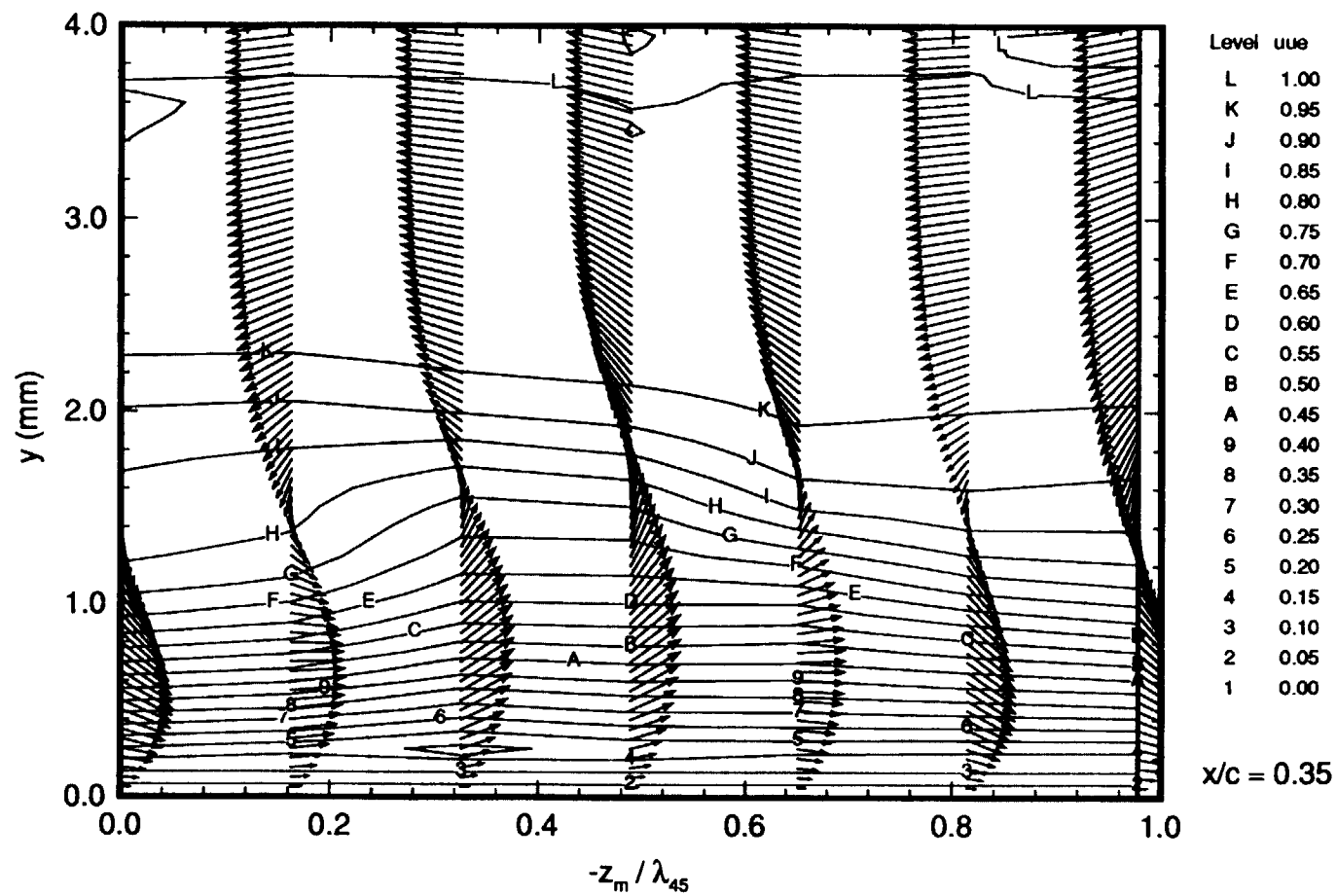


Figure 148. Comparison of Experimental Mean Streamwise-Velocity Contours with Theoretical Vortex Velocity-Vector Field, $x/c = 0.35$, $\alpha = -4^\circ$, $R_c = 2.37 \times 10^6$.

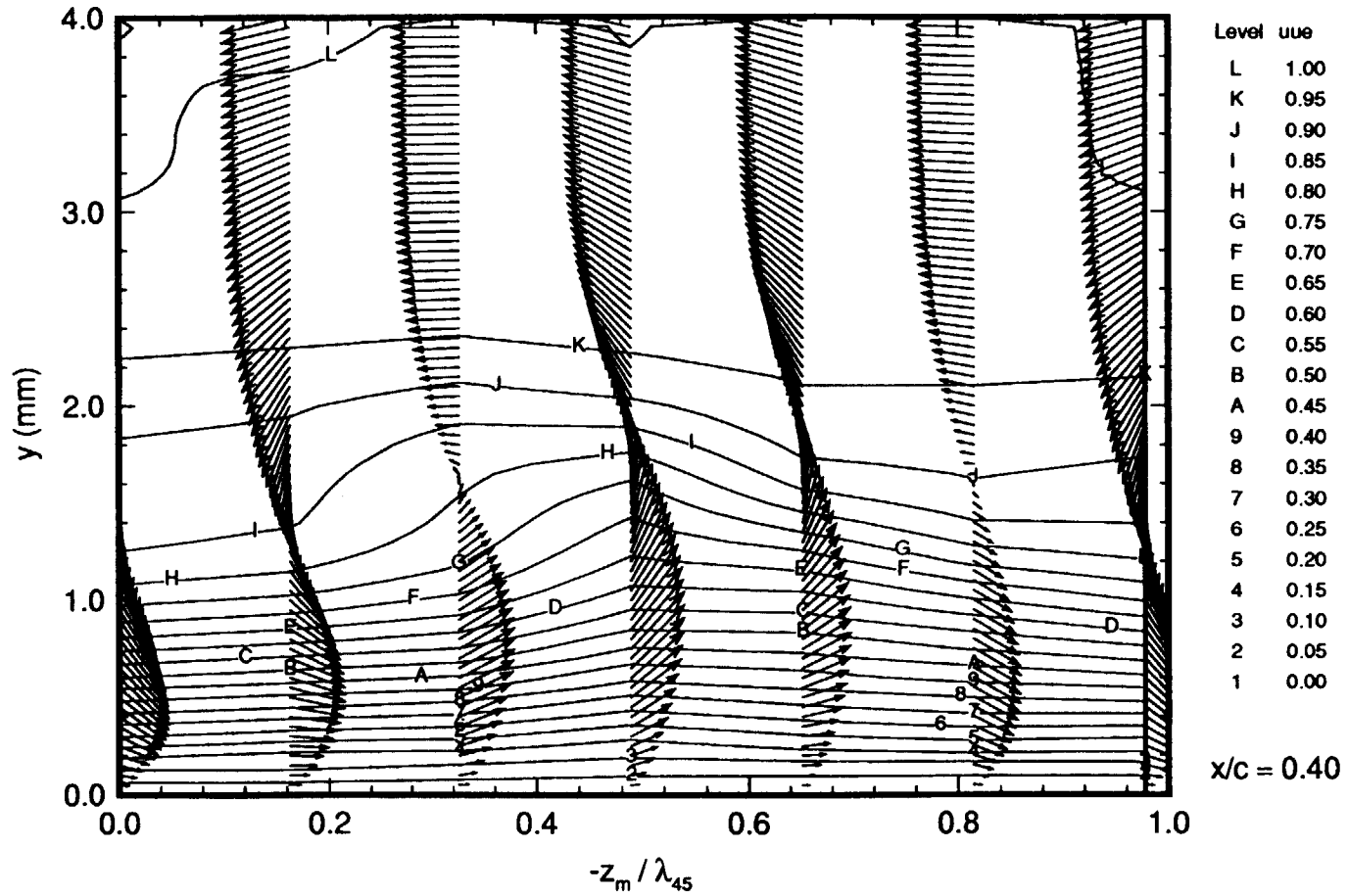


Figure 149. Comparison of Experimental Mean Streamwise-Velocity Contours with Theoretical Vortex Velocity-Vector Field, $x/c = 0.40$, $\alpha = -4^\circ$, $R_c = 2.37 \times 10^6$.

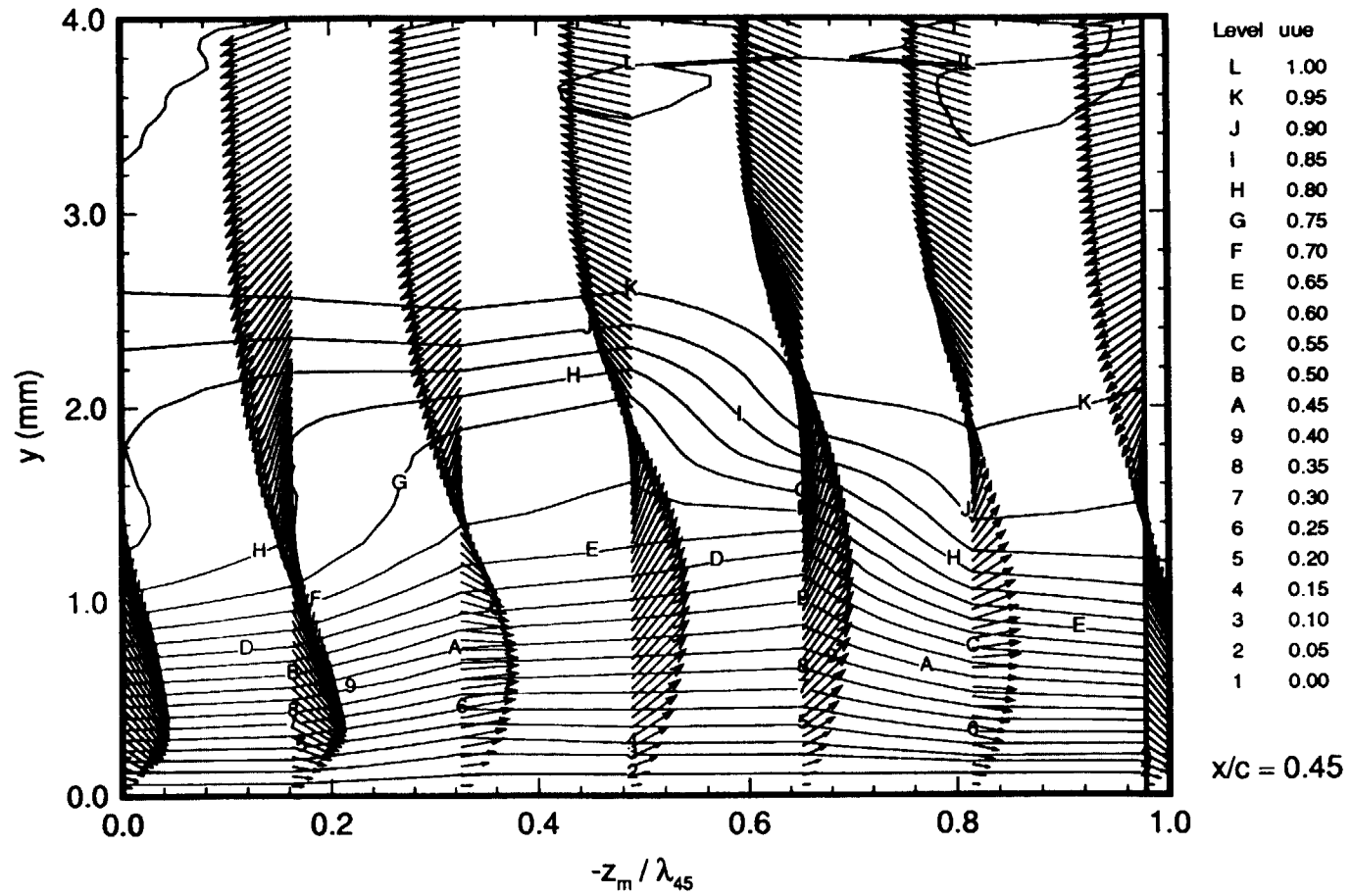


Figure 150. Comparison of Experimental Mean Streamwise-Velocity Contours with Theoretical Vortex Velocity-Vector Field, $x/c = 0.45$, $\alpha = -4^\circ$, $R_c = 2.37 \times 10^6$.

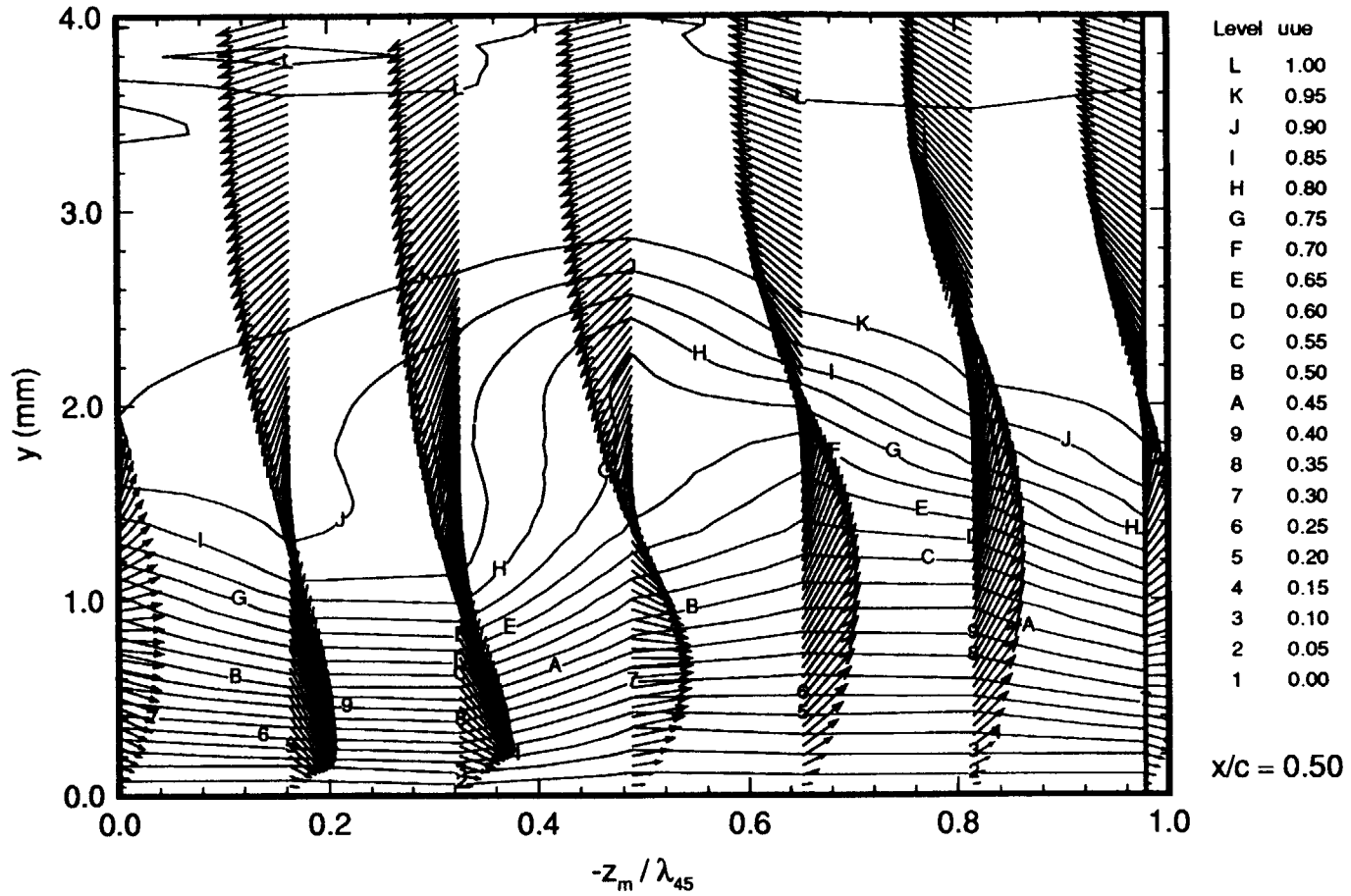


Figure 151. Comparison of Experimental Mean Streamwise-Velocity Contours with Theoretical Vortex Velocity-Vector Field, $x/c = 0.50$, $\alpha = -4^\circ$, $R_c = 2.37 \times 10^6$.

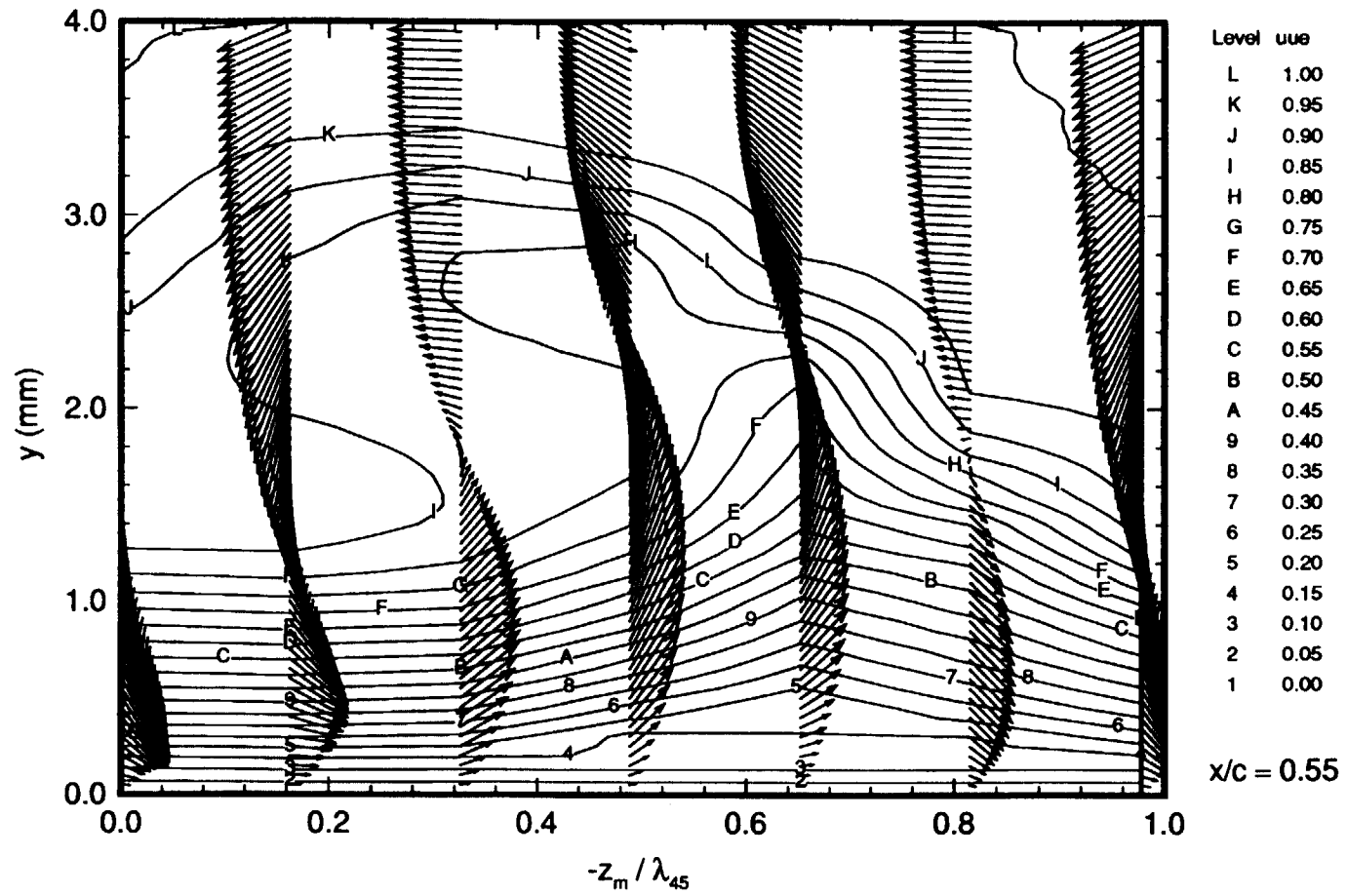


Figure 152. Comparison of Experimental Mean Streamwise-Velocity Contours with Theoretical Vortex Velocity-Vector Field, $x/c = 0.55$, $\alpha = -4^\circ$, $R_c = 2.37 \times 10^6$.

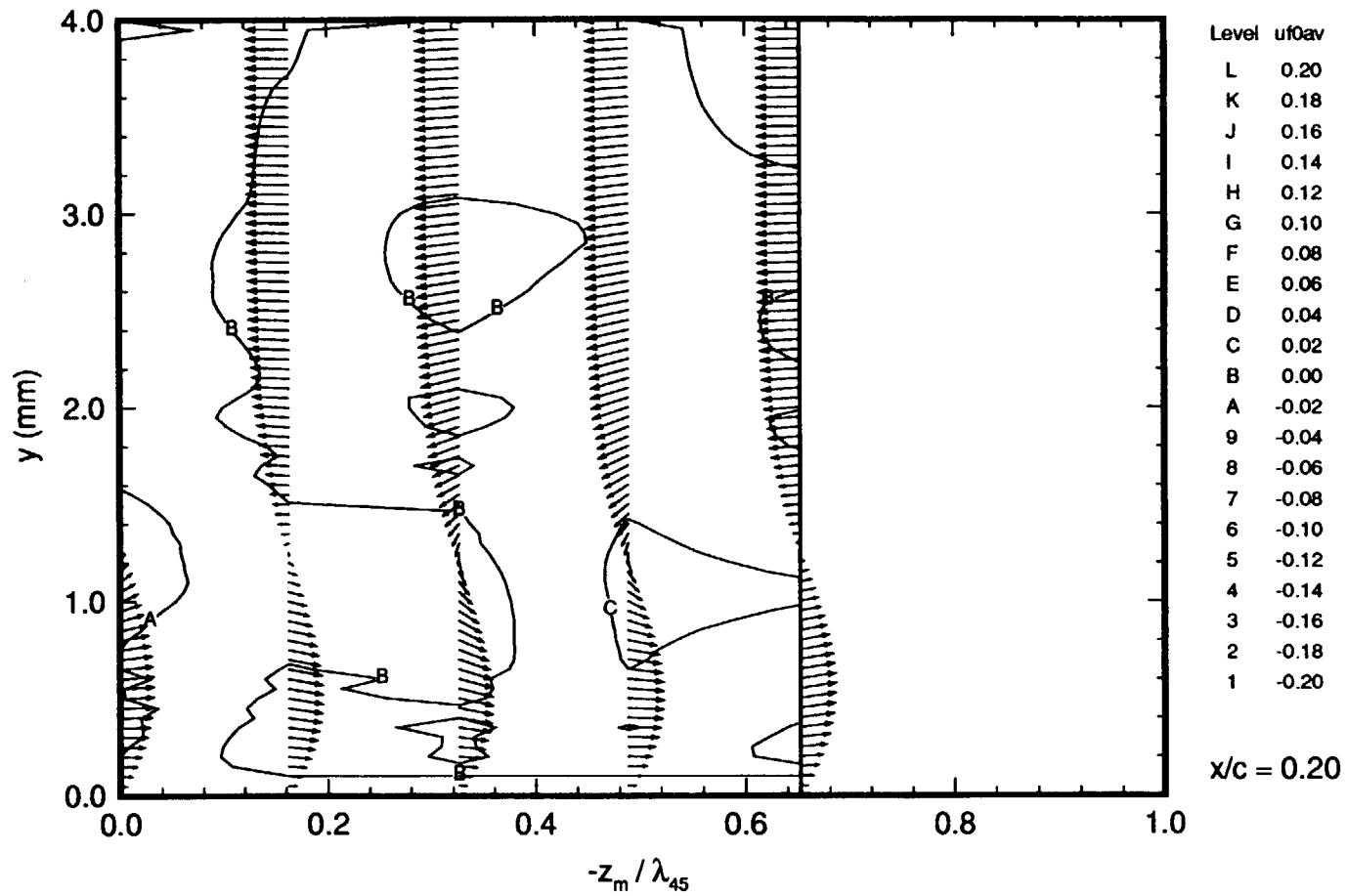


Figure 153. Comparison of Experimental Stationary Crossflow-Disturbance Velocity Contours with Theoretical Vortex Velocity-Vector Field, $x/c = 0.20$, $\alpha = -4^\circ$, $R_c = 2.37 \times 10^6$.

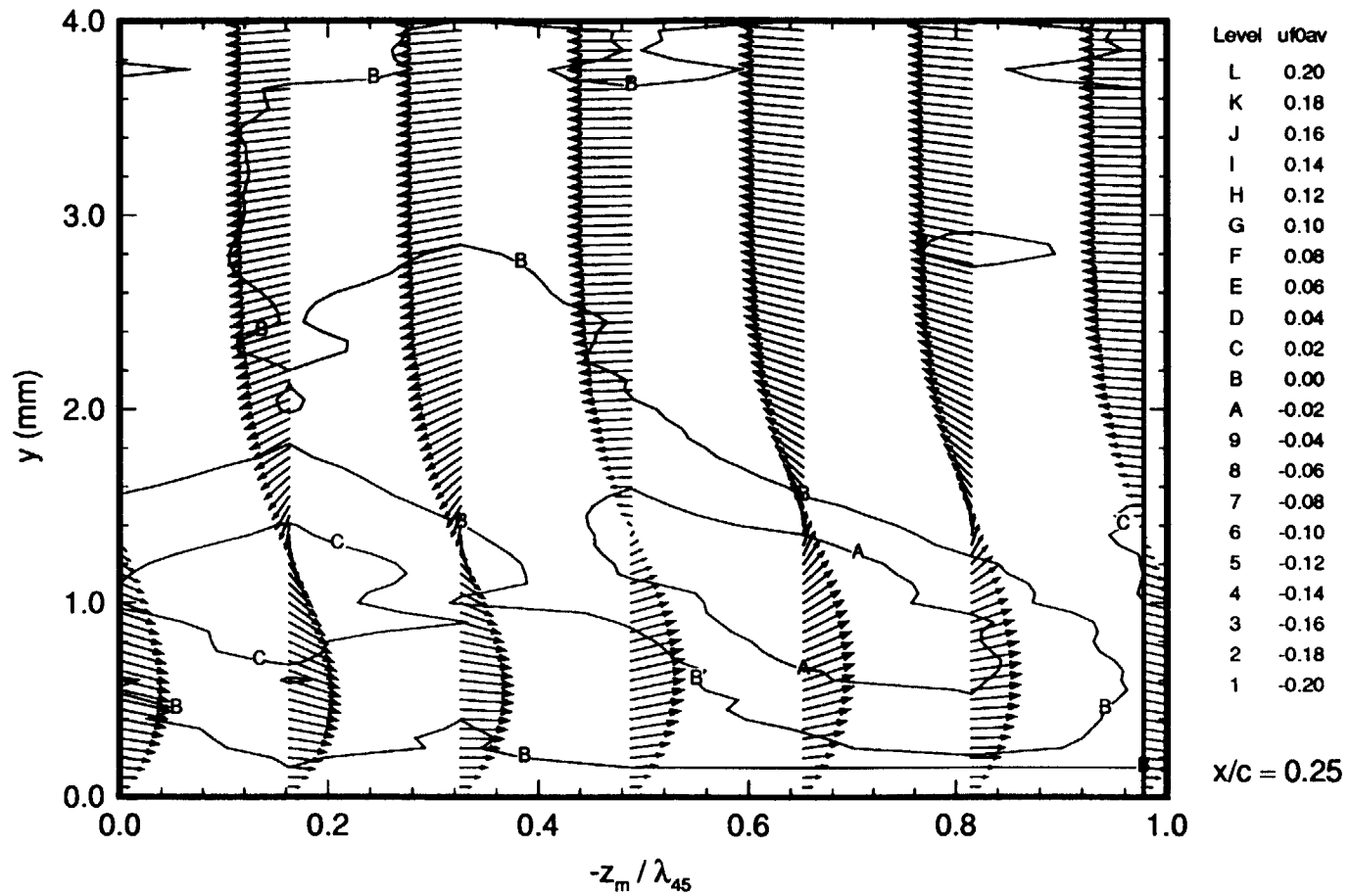


Figure 154. Comparison of Experimental Stationary Crossflow-Disturbance Velocity Contours with Theoretical Vortex Velocity-Vector Field, $x/c = 0.25$, $\alpha = -4^\circ$, $R_c = 2.37 \times 10^6$.

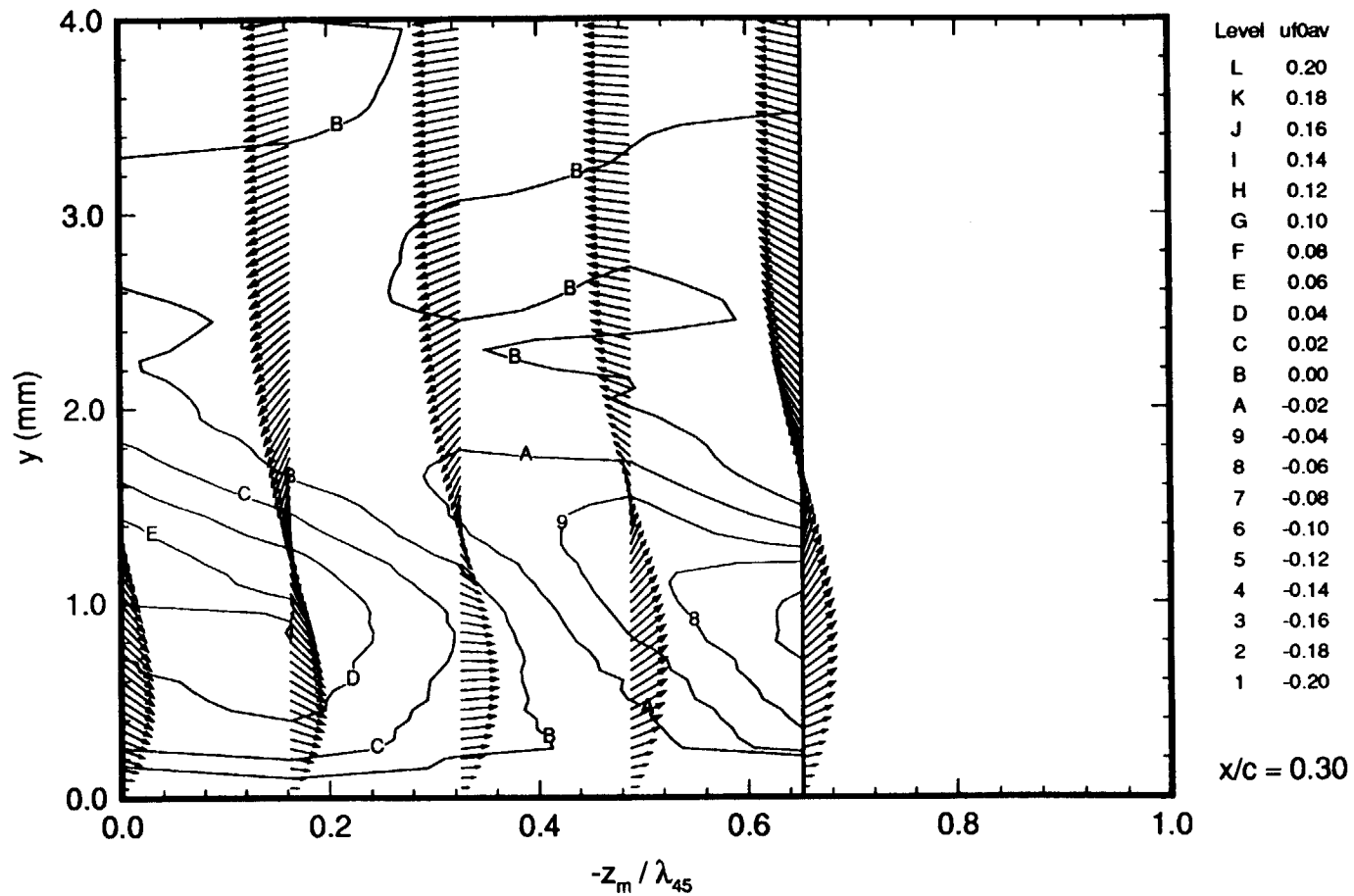


Figure 155. Comparison of Experimental Stationary Crossflow-Disturbance Velocity Contours with Theoretical Vortex Velocity-Vector Field, $x/c = 0.30$, $\alpha = -4^\circ$, $R_c = 2.37 \times 10^6$.

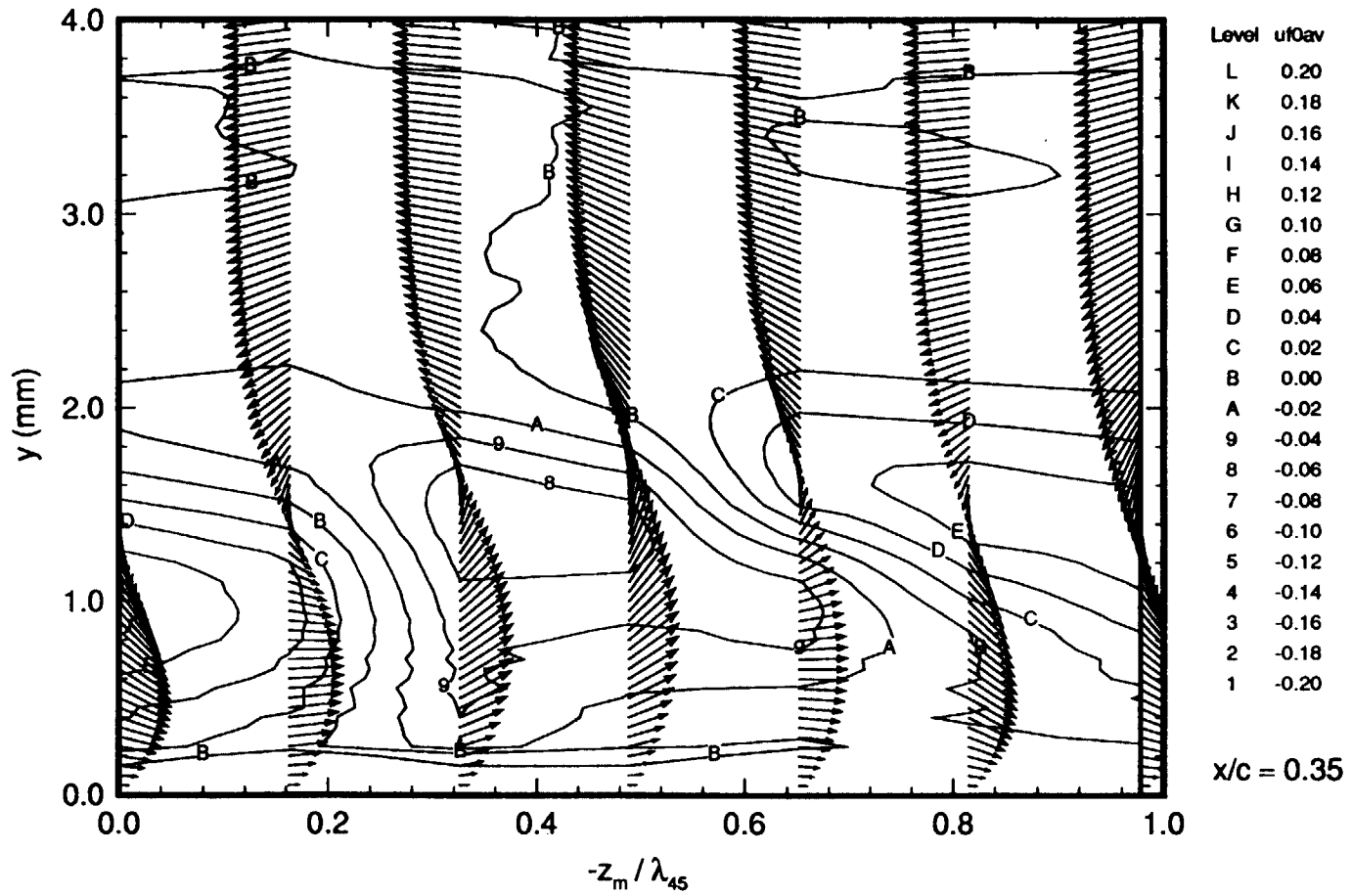


Figure 156. Comparison of Experimental Stationary Crossflow-Disturbance Velocity Contours with Theoretical Vortex Velocity-Vector Field, $x/c = 0.35$, $\alpha = -4^\circ$, $R_c = 2.37 \times 10^6$.

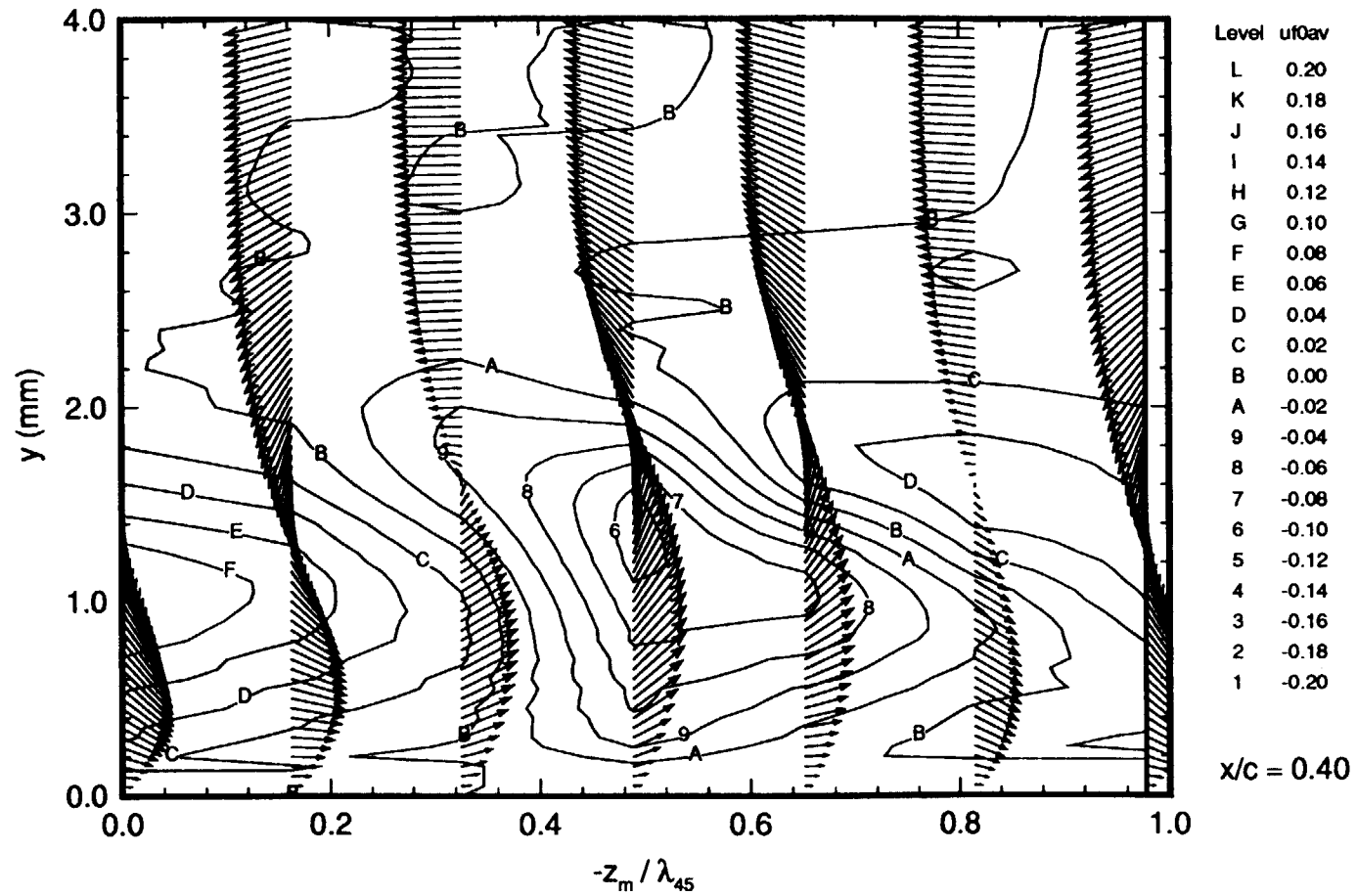


Figure 157. Comparison of Experimental Stationary Crossflow-Disturbance Velocity Contours with Theoretical Vortex Velocity-Vector Field, $x/c = 0.40$, $\alpha = -4^\circ$, $R_c = 2.37 \times 10^6$.

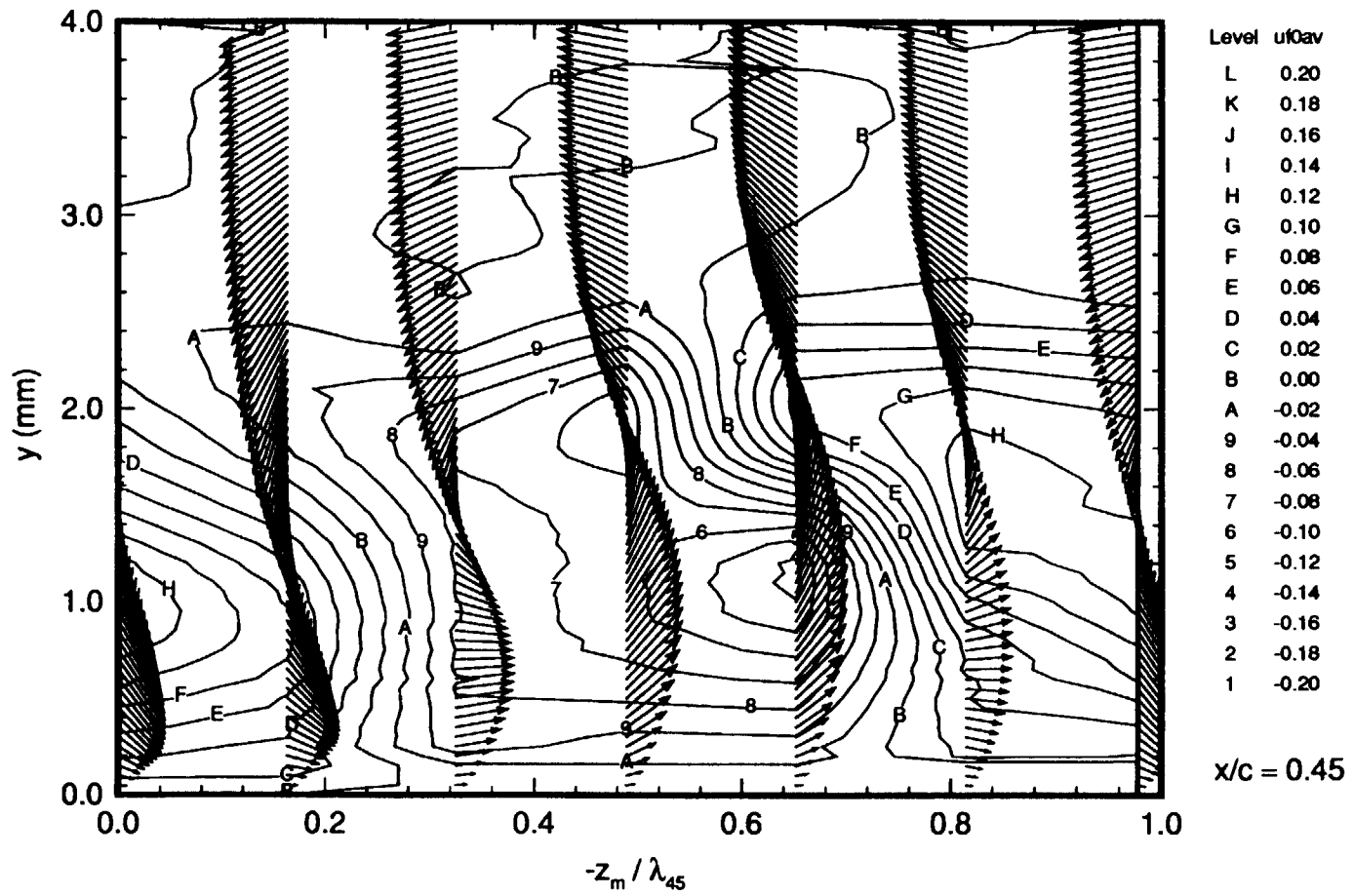


Figure 158. Comparison of Experimental Stationary Crossflow-Disturbance Velocity Contours with Theoretical Vortex Velocity-Vector Field, $x/c = 0.45$, $\alpha = -4^\circ$, $R_c = 2.37 \times 10^6$.

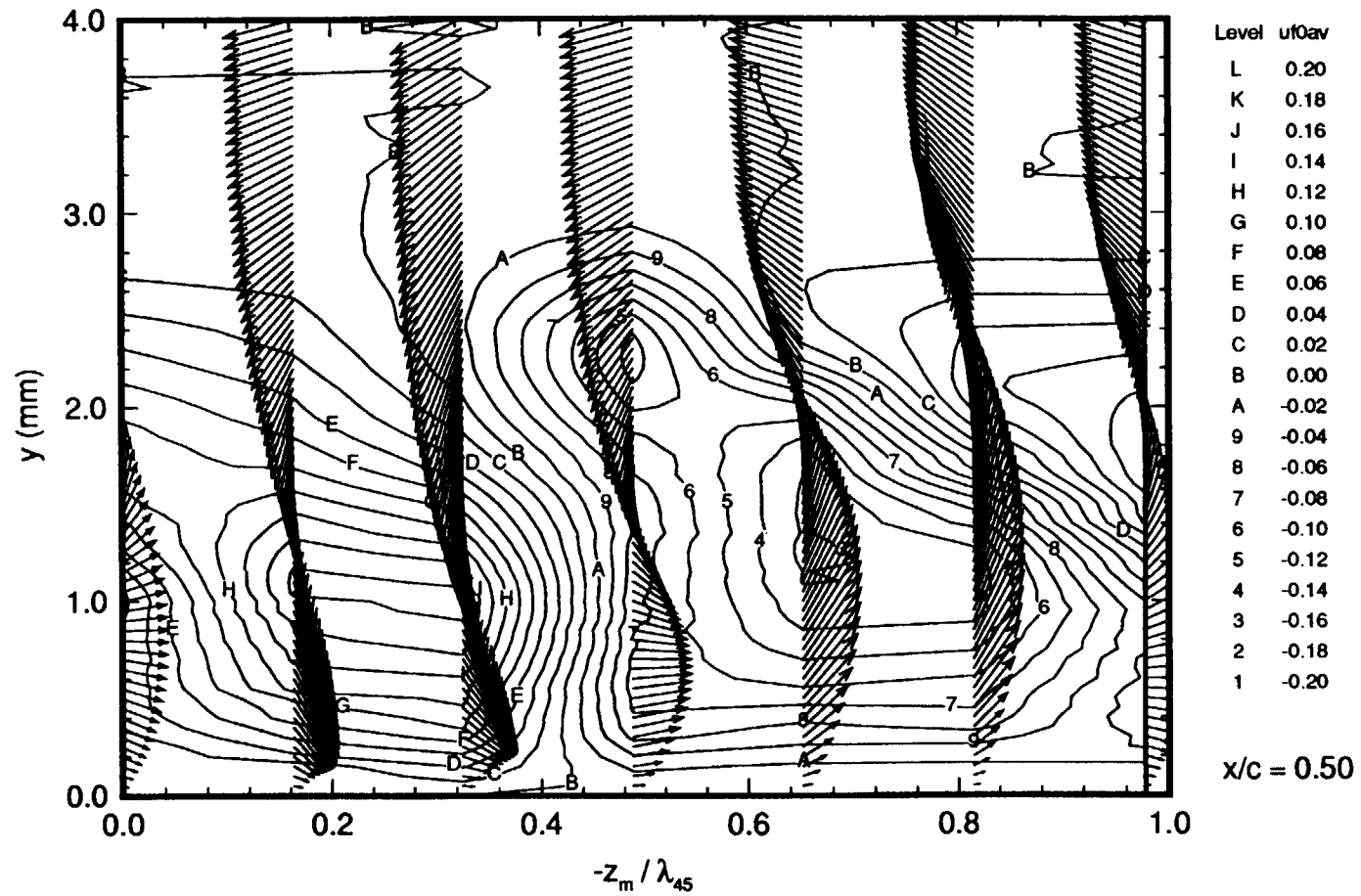


Figure 159. Comparison of Experimental Stationary Crossflow-Disturbance Velocity Contours with Theoretical Vortex Velocity-Vector Field, $x/c = 0.50$, $\alpha = -4^\circ$, $R_c = 2.37 \times 10^6$.

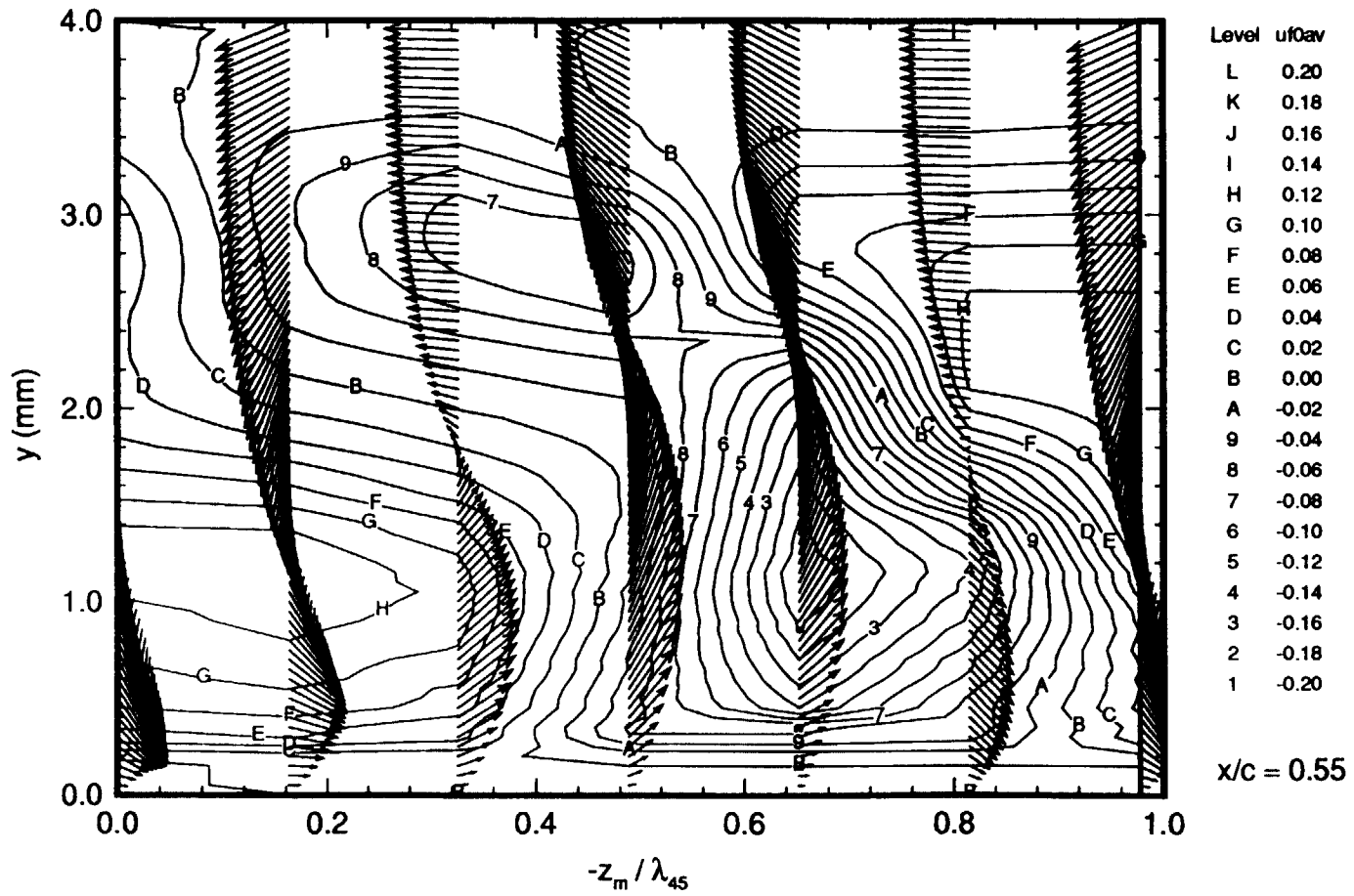


Figure 160. Comparison of Experimental Stationary Crossflow-Disturbance Velocity Contours with Theoretical Vortex Velocity-Vector Field, $x/c = 0.55$, $\alpha = -4^\circ$, $R_c = 2.37 \times 10^6$.

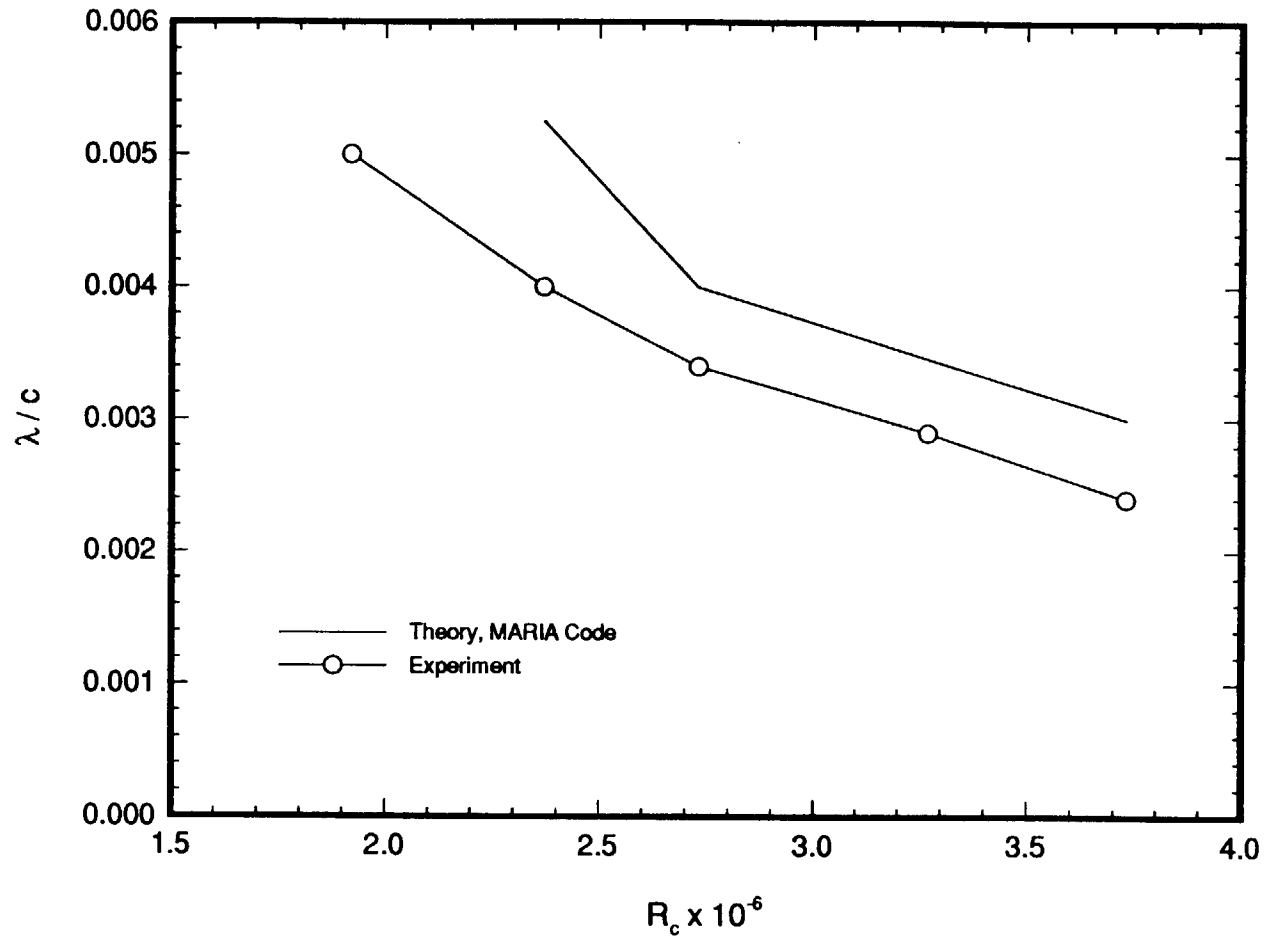


Figure 161. Comparison of Theoretical and Experimental Stationary Crossflow-Vortex Wavelengths, $\alpha = -4^\circ$, $R_c = 2.37 \times 10^6$.

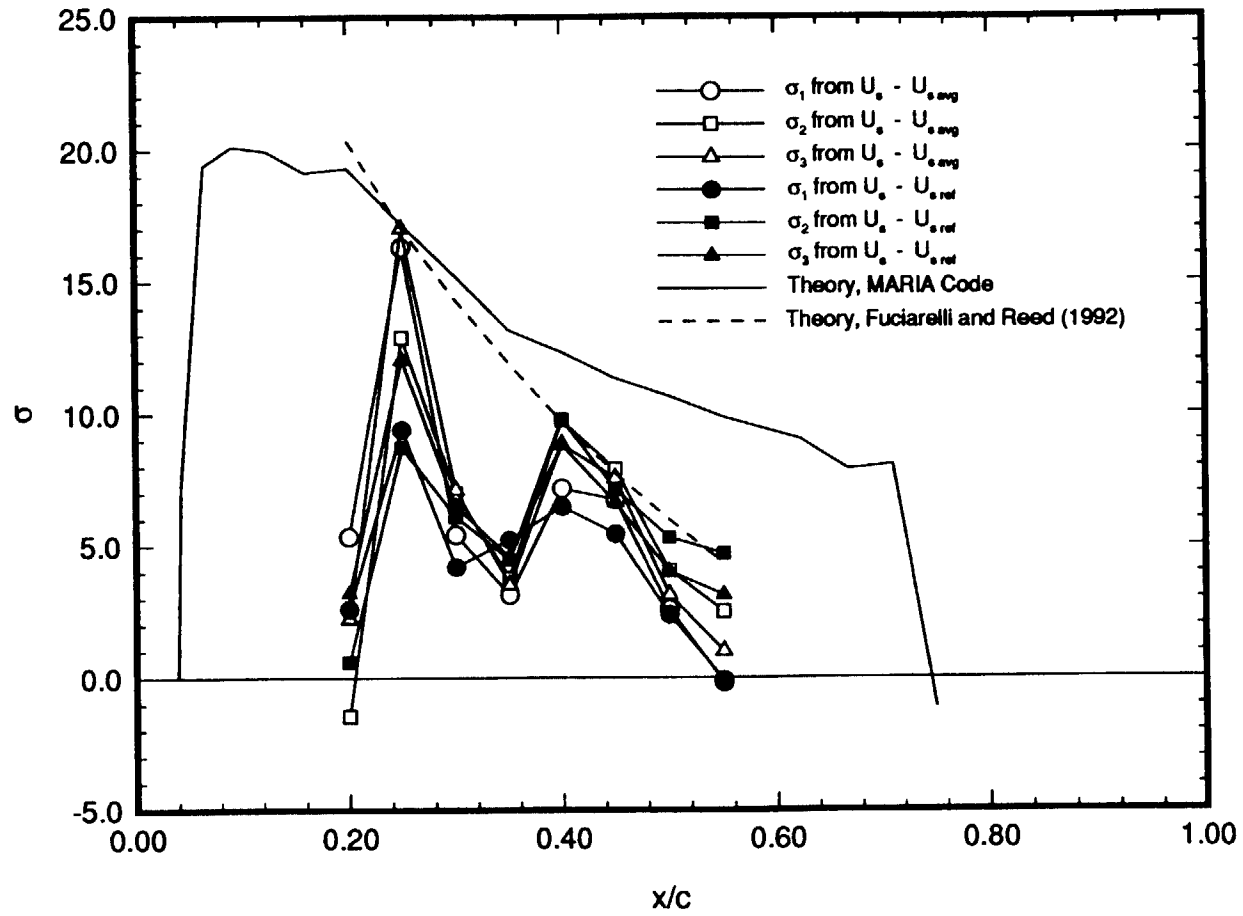


Figure 162. Comparison of Theoretical and Experimental Stationary Crossflow-Vortex Growth Rates, $\alpha = -4^\circ$, $R_c = 2.37 \times 10^6$.

Appendix A Relationships Between Coordinate Systems

Figure A1 shows a swept wing in a right-handed Cartesian coordinate system (x_m, y_m, z_m) where x_m is taken perpendicular to the wing leading edge, y_m is perpendicular to the wing-chord plane, and z_m is parallel to the wing leading edge. A positive wing sweep angle, Λ , is shown and the flow is from left to right. The boundary-layer edge velocity is given by

$$U_{te} = \sqrt{U_{me}^2 + W_{me}^2} \quad (\text{A } 1)$$

where $U_m(y) \geq 0$ and $W_m(y) \geq 0$ for attached flow. The angle of the boundary-layer edge velocity with respect to the z_m -axis is obtained as

$$\epsilon = \tan^{-1} \left(\frac{U_{me}}{W_{me}} \right) \quad (\text{A } 2)$$

and $0 \leq \epsilon \leq \frac{\pi}{2}$. The total wave number is given by

$$\alpha_T = \sqrt{\alpha_r^2 + \beta_r^2} \quad (\text{A } 3)$$

where α_r is the wave number in the x_m direction and β_r is the wave number in the z_m direction. The wave angle of the disturbance is then

$$\theta = \tan^{-1} \left(\frac{\alpha_r}{\beta_r} \right) \quad (\text{A } 4)$$

where $\theta > \pi/2$ for crossflow disturbances. And finally, the wave orientation angle with respect to the local boundary-layer edge velocity is obtained as

$$\psi = \theta - \epsilon \quad (\text{A } 5)$$

The model-oriented coordinates described above are obtained by rotation about the y_s -axis in the streamwise coordinate system (x_s, y_s, z_s) by the wing

sweep angle, Λ . Here x_s is parallel to the freestream velocity vector. The relationship between these two coordinate frames is given as

$$\begin{Bmatrix} z_m \\ x_m \end{Bmatrix} = \begin{bmatrix} \cos \Lambda & \sin \Lambda \\ -\sin \Lambda & \cos \Lambda \end{bmatrix} \begin{Bmatrix} z_s \\ x_s \end{Bmatrix} \quad (\text{A } 6)$$

or, inverting

$$\begin{Bmatrix} z_s \\ x_s \end{Bmatrix} = \begin{bmatrix} \cos \Lambda & -\sin \Lambda \\ \sin \Lambda & \cos \Lambda \end{bmatrix} \begin{Bmatrix} z_m \\ x_m \end{Bmatrix} \quad (\text{A } 7)$$

And, the relationship between the wave-oriented coordinate system (x_w, y_w, z_w) and the model coordinates is obtained as a rotation by the angle, θ , about the y_m -axis as

$$\begin{Bmatrix} z_w \\ x_w \end{Bmatrix} = \begin{bmatrix} \cos \theta & \sin \theta \\ -\sin \theta & \cos \theta \end{bmatrix} \begin{Bmatrix} z_m \\ x_m \end{Bmatrix} \quad (\text{A } 8)$$

Reed's left-handed coordinate system is shown in Figure A2 where the z -axes are all directed in the opposite directions from those in the right-handed systems above. Equations A1-A8 still apply, but all the rotations are taken in the opposite direction. In particular, the wing sweep angle, Λ , is now negative. Also, as consequence of this shift $W_m(y) \leq 0$ while $U_m(y) \geq 0$ for attached flow. The angle of the boundary-layer edge velocity vector with respect to the z_m -axis, ϵ , is now greater than $\pi/2$ and the crossflow wave orientation angle, θ , is less than $\pi/2$.

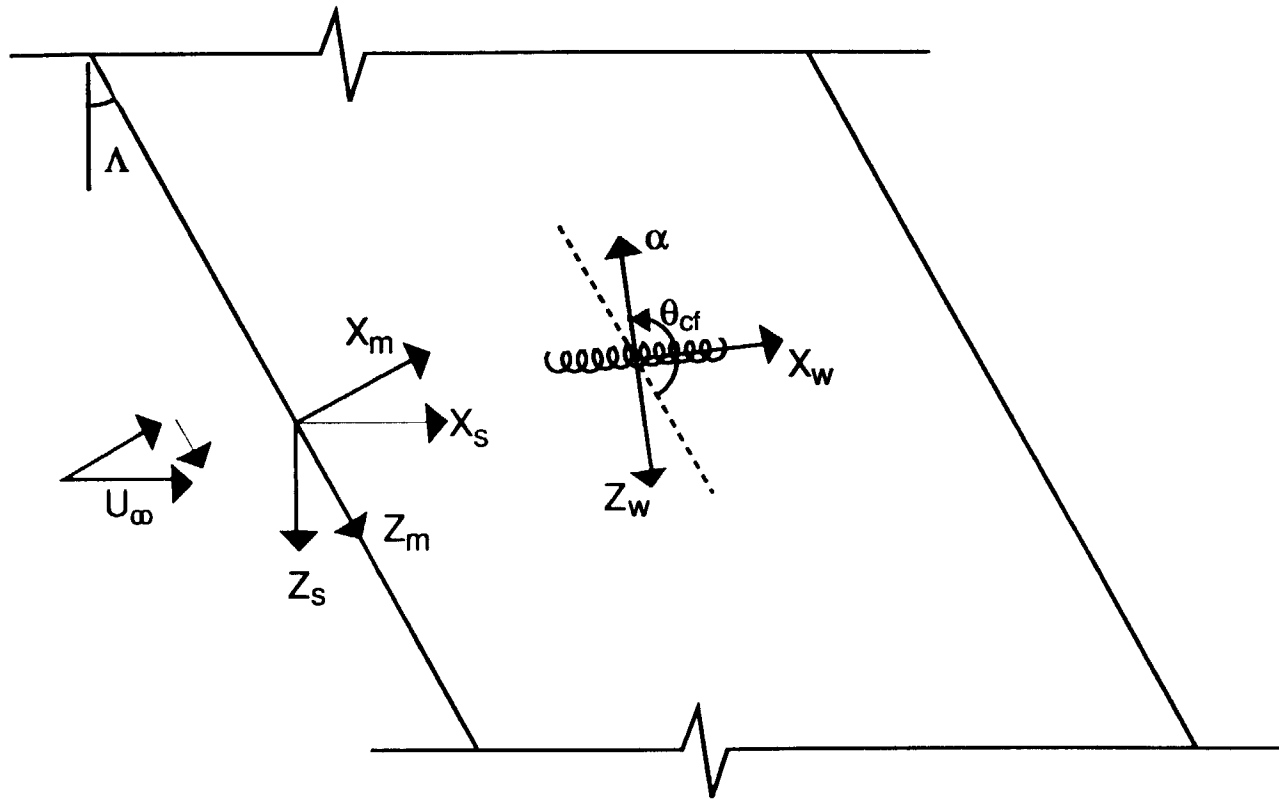


Figure A1. Coordinate System Relationships for a Swept Wing.

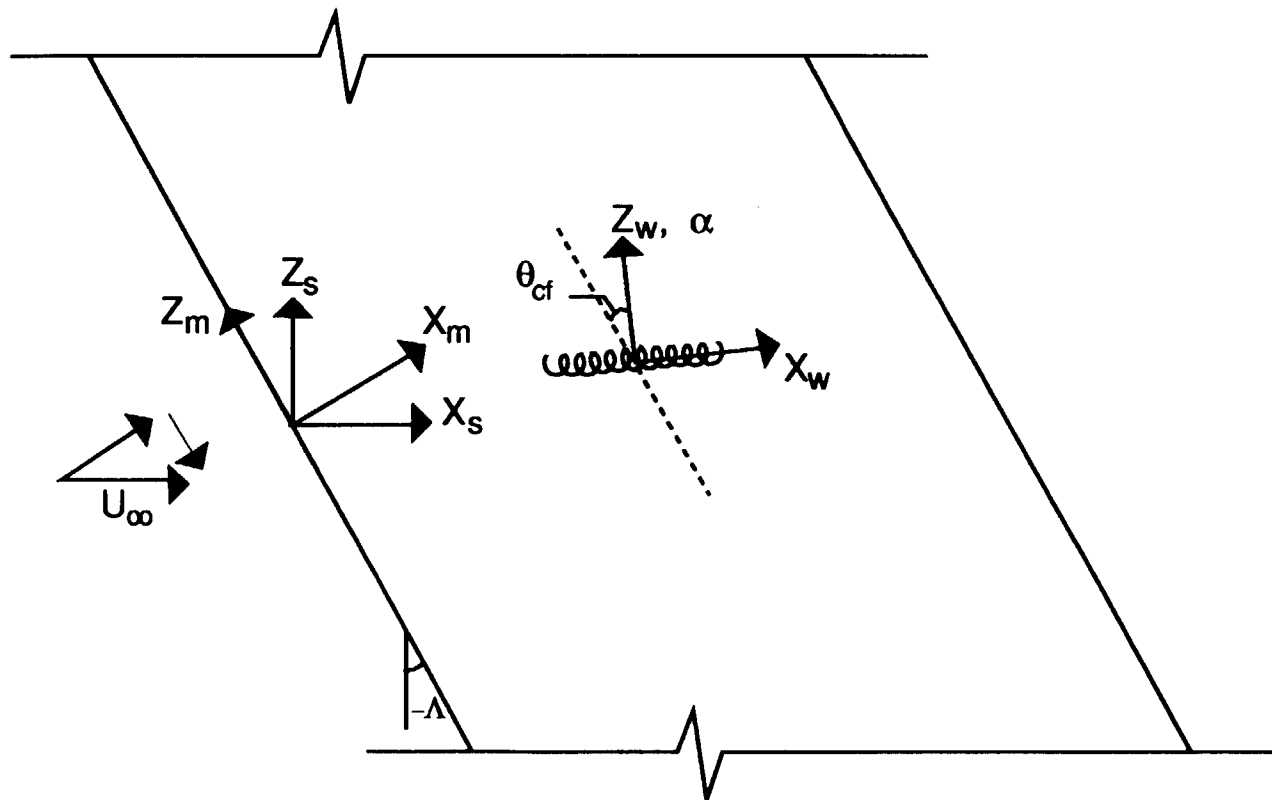


Figure A2. Left-Handed Coordinate Systems for a Swept Wing.

Appendix B Hot-Wire Signal Interpretation Procedure

The freestream and boundary-layer velocity measurements are performed using *Dantec* 55M01 constant-temperature anemometers equipped with 55M10 CTA standard bridges with bridge resistance ratios of 1:20. The hot-wires are *Dantec* type 55P15 miniature boundary-layer probes having 5- μm platinum-plated tungsten wires which are 1.25 mm in length. The probe tines are 8 mm long and are offset 3 mm from the probe axis. Standard 4-mm diameter probe supports are used. The three-dimensional traverse system (described in Chapter 3) is used to support and move the probes through the flow field. The traverse system is mounted external to the test section with only the probe-support sting extending through a sliding opening in the test-section wall. The sting consists of a composite element and an aluminum strut. The composite element is 5 mm thick, 0.425 m long, and its chord tapers from 64 mm at the base to 50 mm at the tip. The aluminum strut dimensions are 13 mm x 76 mm x 0.324 m. Both the steady-state and fluctuating hot-wire signals are sampled simultaneously using the 16-channel *MASSCOMP* 12-bit A/D converter which can sample at an aggregate rate of up to 1 MHz. The fluctuating voltage signal is narrow band-pass filtered using a *Spectral Dynamics* SD122 equipped with a 4-pole Butterworth tracking filter with ± 10 Hz passband.

The voltage response of a constant-temperature hot-wire anemometer can be assumed to have the form

$$E = F(\rho, U, T_0) \quad (\text{B } 1)$$

where ρ is the ambient air density, U is the velocity, T_0 is the total temperature, and E is the anemometer voltage response. Differentiating Equation B1 gives

$$dE = \frac{dF}{d\rho} d\rho + \frac{dF}{dU} dU + \frac{dF}{dT_0} dT_0 \quad (\text{B } 2)$$

Thus, a small voltage change is dependent on small changes in the density, velocity, and total temperature.

It is desirable to reduce the complexity of the functional relationship given in Equation B1. This can be accomplished by eliminating or at least minimizing the variations in ρ and T_0 so that the anemometer response depends solely on the velocity. The UWT has no heat exchanger system to maintain a desired tunnel temperature. The tunnel total temperature increases with test time until an equilibrium condition is achieved. For the present experiment the tunnel flow is preheated by operating the tunnel at the expected test condition for 45 minutes to 1 hour before hot-wire probe calibration. This provides sufficient time for the flow temperature to reach its equilibrium value. The air density depends on two factors — atmospheric pressure and flow temperature. To minimize atmospheric pressure effects the hot-wire calibrations are conducted before each data-acquisition run. These steps insure that $d\rho$ and dT_0 are nearly zero and can be neglected in Equation B2. Then, Equation B1 can be simplified to

$$E = f(U) \quad (\text{B } 3)$$

The hot-wire probes are calibrated in the UWT flow by varying the freestream velocity in steps across the range of velocities expected during the experiment. Typically twelve velocities are used for each calibration. Equation B3 is not actually used for probe calibration; instead,

$$U = g(E) \quad (\text{B } 4)$$

is used where $g(E)$ is a fourth-order least-squares curve fit to the calibration data. Then, $f(U)$ is determined as

$$E = f(U) = g^{-1}(E) \quad (\text{B } 5)$$

Differentiating Equation B3 gives

$$dE = \frac{df}{dU} dU = f' dU \quad (\text{B } 6)$$

Now we assume that

$$e = E + e' \quad (\text{B } 7)$$

and

$$u = U + u' \quad (\text{B } 8)$$

where e is made up of a steady (or DC) voltage, E , and a small fluctuating voltage, e' and u consists of a steady velocity, U , and a small fluctuating velocity, u' . Substituting Equations B7 and B8 into Equation B3 and expanding in a Taylor series while neglecting higher order terms (since e' and u' are assumed to be small) we obtain

$$E + e' = f(U + u') = f(U) + f'(U) u' \quad (\text{B } 9)$$

Subtracting Equation B3 from Equation B9 yields

$$e' = f'(U) u' \quad (\text{B } 10)$$

or solving for u' we obtain

$$u' = \frac{e'}{f'(U)} \quad (\text{B } 11)$$

Since u' and e' are small deviations from the steady values of U and E , we can apply Equation B11 not just at a single point in time but for $u'(t)$ and $e'(t)$ as functions of time while holding $f'(U)$ constant and then take the root mean square of these functions to get

$$u'_{rms} = \frac{e'_{rms}}{f'(U)} \quad (\text{B } 12)$$

which gives the rms velocity fluctuations as a function of the measured rms voltage output from the hot-wire anemometer circuit.

For boundary-layer velocity-profile measurements we desire the ratio of local velocity to the boundary-layer edge velocity. Two hot-wire probes are used for this measurement — one probe located in the boundary layer and the other in the external flow. Both probes are mounted on the traverse strut and moved together as the boundary-layer velocity profile is measured. The probe in the external flow is not located at the edge of the boundary layer but is, in fact, located approximately fifteen centimeters from the boundary-layer probe. During the traverse the two hot-wire probes move only about 4 mm. Over this distance the external flow probe detects only negligible variations in the velocity, but the boundary-layer probe sees the velocity decrease from the edge value down to near zero as the surface is approached. The boundary-layer velocity ratio cannot be obtained directly as the ratio

$$\frac{U_2}{U_1}$$

because U_1 is not at the boundary-layer edge. However, the desired velocity ratio is given by

$$\frac{U}{U_{se}} = \frac{\left(\frac{U_2}{U_1}\right)}{\left(\frac{U_2}{U_1}\right)_{y_{max}}} \quad (\text{B } 13)$$

where

$$\frac{U}{U_{se}}$$

is the boundary-layer velocity ratio, U_1 is the external flow velocity, and U_2 is the boundary-layer velocity. By scaling the measured velocity ratio,

$$\frac{U_2}{U_1}$$

in Equation B13 by the velocity ratio observed at the maximum distance from the surface we normalize the profile to unity at the boundary-layer edge. This accounts for the fact that the external-flow hot-wire probe is not at the boundary-layer edge.

Appendix C Error Analysis

Kline and McClintock (1953) discuss the effects of experimental measurement errors on computed data in various experimental situations. They discuss both single- and multiple-sample experiments, but their primary emphasis is on describing uncertainties in single-sample experiments. For multiple-sample experiments statistical methods can be used to establish both the mean values and variations from the mean. However, in single-sample experiments errors in the results computed from experimentally measured quantities can only be estimated. Kline and McClintock show that the uncertainty, w_R , for the computed result

$$R = R(v_1, v_2, v_3, \dots, v_n) \quad (\text{C } 1)$$

can be obtained as

$$w_R = \sqrt{\sum_{i=1}^n \left(\frac{\partial R}{\partial v_i} w_i \right)^2} \quad (\text{C } 2)$$

where v_i are the measured quantities used in the computation of R and w_i are the expected error ranges for the measured quantities.

In the present experiment the range of measured quantities is limited to static and dynamic pressures, pressure differentials, flow temperature, and hot-wire anemometer voltages. From these measured quantities the freestream velocity, the surface pressure coefficients, boundary-layer and edge velocities, and, most importantly, the boundary-layer velocity ratios are determined. The freestream velocity can be obtained from the incompressible Bernoulli equation and the perfect-gas equation of state as

$$U_\infty = \sqrt{\frac{2 q_\infty R T_\infty}{p_\infty}} \quad (\text{C } 3)$$

where U_∞ is the freestream velocity and the measured quantities are the dynamic pressure, q_∞ , the static pressure, p_∞ , and the static temperature, T_∞ , while R

is the gas constant from the equation of state. The surface pressure coefficient is given by

$$C_p = \frac{p - p_\infty}{q_\infty} = \frac{p_D}{q_\infty} \quad (\text{C } 4)$$

where C_p is the pressure coefficient and p is the local surface pressure. The boundary-layer and edge velocities are obtained from the hot-wire calibration functions

$$U = g(E) \quad (\text{C } 5)$$

while $f(U) = g^{-1}(E)$ is the inverse of the hot-wire calibration function.

Equation C2 can be applied to the Eq. C3-C5 to obtain uncertainty estimates for U_∞ , C_p , and U as

$$\frac{w_{U_\infty}}{U_\infty} = \sqrt{\left(\frac{w_{q_\infty}}{2q_\infty}\right)^2 + \left(\frac{w_{T_\infty}}{2T_\infty}\right)^2 + \left(\frac{w_{p_\infty}}{2p_\infty}\right)^2} \quad (\text{C } 6)$$

$$\frac{w_{C_p}}{C_p} = \sqrt{\left(\frac{w_{p_D}}{p_D}\right)^2 + \left(\frac{w_{q_\infty}}{q_\infty}\right)^2} \quad (\text{C } 7)$$

and

$$\frac{w_U}{U} = \sqrt{\left(\frac{w_E}{U \frac{df}{dU}}\right)^2} \quad (\text{C } 8)$$

Equations C6 and C7 can be straightforwardly applied because estimates of the uncertainties involved are easily obtained. However, Equation C8 is much more difficult to apply since an estimate of the uncertainty in the hot-wire anemometer voltage is much more difficult to ascertain. This difficulty can be overcome by recognizing that in the present experiment some of the hot-wire measurements can be considered as multiple-sample measurements while other measurements must be regarded as single-sample measurements.

The most important hot-wire measurements involve determining the boundary-layer velocity ratio given in Equation A12 as

$$U_R = \frac{U}{U_{se}} = \frac{\left(\frac{U_2}{U_1}\right)}{\left(\frac{U_2}{U_1}\right)_{y_{max}}} \quad (C 9)$$

where U_2 is the velocity indicated by the hot-wire probe inside the boundary layer and U_1 is the velocity indicated in the outer flow. U_2 and

$$\frac{U_2}{U_1}$$

must be regarded as single-sample measurements even though U_1 and U_2 are evaluated as time averages of repeated measurements taken at a frequency of $f_s = 1$ kHz over a 30 second interval. On the other hand, U_1 and

$$\left(\frac{U_2}{U_1}\right)_{y_{max}}$$

can be regarded as multiple-sample measurements and analyzed statistically since these two variables are measured repeatedly during a hot-wire survey of the boundary layer.

According to the instrument handbook the uncertainty in the measurement of q_∞ and p_∞ in Equation C6 is 0.08% of reading, but q_∞ is observed to oscillate due to a very low-frequency modulation of the fan controller at about 1% of reading. Thus, the expected uncertainties for q_∞ and p_∞ are taken as

$$w_{q_\infty} = 0.02 \text{ torr} \quad \text{at} \quad q_\infty = 2.00 \text{ torr}$$

and

$$w_{p_\infty} = 0.6 \text{ torr} \quad \text{at} \quad p_\infty = 720.0 \text{ torr}$$

Also, the thermocouple is found to be in error by

$$w_{T_\infty} = -1.5^\circ \text{K} \quad \text{at} \quad T_\infty = 309.0^\circ \text{K}$$

Substituting these uncertainties into Equation C6 gives

$$\frac{w_{U_{\infty}}}{U_{\infty}} = 0.6\%$$

If the uncertainty in C_p is evaluated at the maximum pressure point, then substituting

$$w_{p_D} = 0.02 \text{ torr at } p_D = q_{\infty} = 2.00 \text{ torr}$$

into Equation C7 yields

$$\frac{w_{C_P}}{C_P} = 1.4\%$$

The uncertainties in U_1 and

$$\left(\frac{U_2}{U_1}\right)_{y \max}$$

are evaluated statistically at each fractional chord measurement station. The standard deviation for U_1 is found to be between 1% and 3% of U_{s_e} for all of the measurement locations except $x/c = 0.55$ where it reached 5.56%. But, more importantly, the standard deviation in the velocity ratio is much smaller ranging from 0.15% to 1.38%.

An alternate method to estimate the error in the boundary-layer velocity ratio can be derived by using King's law as the calibration function for a constant-temperature hot wire

$$E^2 = A + BU^n \quad (\text{C } 10)$$

where we take $n = 1/2$. Or, solving for U

$$U = \left(\frac{E^2 - A}{B}\right)^2 \quad (\text{C } 11)$$

Strictly speaking, the calibration coefficients depend on the temperatures of the hot wire (T_w) and the flow (T_f) as

$$A = A_1 (T_w - T_f) \quad (\text{C } 12)$$

and

$$B = B_1 (T_w - T_f) \quad (\text{C } 13)$$

Now, suppose that the flow temperature changes from the calibration temperature giving,

$$A = \frac{A_c (T_w - T_f)}{(T_w - T_c)} \quad (\text{C } 14)$$

and

$$B = \frac{B_c (T_w - T_f)}{(T_w - T_c)} \quad (\text{C } 15)$$

where A_c and B_c are the values of A and B determined at the calibration temperature (T_c). Substituting Equations C14 and C15 into C11 for hot wires 1 and 2, and taking the ratio $\frac{U_2}{U_1}$ we obtain

$$\left(\frac{U_2}{U_1}\right)^{\frac{1}{2}} = \frac{B_{C1} E_2^2 - A_{C2} \left(\frac{T_w - T_f}{T_w - T_c}\right)}{B_{C2} E_1^2 - A_{C1} \left(\frac{T_w - T_f}{T_w - T_c}\right)} \quad (\text{C } 16)$$

But, if $T_f = T_c$ Equation C16 reduces to

$$\left(\frac{U_2}{U_1}\right)^{\frac{1}{2}} = \frac{B_{C1} E_2^2 - A_{C2}}{B_{C2} E_1^2 - A_{C1}} \quad (\text{C } 17)$$

An estimate of the error in $\frac{U_2}{U_1}$ is obtained by taking the ratio of Equations C16 and C17 and squaring the result. Doing so for a typical set of hot-wire calibration data with the maximum temperature shift taken to be $T_f - T_c = 4^\circ \text{C}$ we find that the effect of temperature drift is negligible at the boundary-layer edge, but it increases as U_2 is decreased. For most of the boundary layer, $0.25 \leq \frac{U_2}{U_1} \leq 1.0$ the error does not exceed 2.7%. The maximum error is 5.8% at the minimum velocity ratio of $\frac{U_2}{U_1} = 0.10$

References

- Arnal, D. 1989 Some transition problems in three-dimensional flows. In *Instability and Transition: Proceedings of the ICASE / NASA LaRC Workshop*. New York, Springer-Verlag, 1990.
- Arnal, D. and Aupoix, B. 1992 Hypersonic boundary layers: Transition and turbulence effects. In *ESA, Aerothermodynamics for Space Vehicles*, pp. 25–38.
- Arnal, D., Casalis, G., and Juillen, J. C. 1990 Experimental and theoretical analysis of natural transition on 'infinite' swept wing. In *Laminar-Turbulent Transition: Proceedings of the IUTAM Symposium, Toulouse, France, Sept. 11–15, 1989*. Berlin and New York, Springer-Verlag, 1990.
- Arnal, D. and Coustols, E. 1984 Application de critères bi et tridimensionnels au calcul de la transition et de la couche limite d'ailes en flèche. *AGARD CP No. 365, Paper No. 12*.
- Arnal, D., Coustols, E., and Jelliti, M. 1985 Transition en tridimensionnel et laminarisation de la couche limite sur une aile en flèche. *Colloq. Aérodyn. Appl. 22nd*, Lille, France.
- Arnal, D., Coustols, E., and Juillen, J. C. 1984 Experimental and theoretical study of transition phenomena on an infinite swept wing. *Rech. Aérop. No. 1984-4*.
- Arnal, D., Habiballah, M., and Coustols, E. 1984 Théorie de l'instabilité laminaire et critères de transition en écoulement bi- et tridimensionnel. *Réch. Aérop. No. 1984-2*.
- Arnal, D. and Juillen, J. C. 1987 Three-dimensional transition studies at ONERA/CERT. *AIAA Paper No. 87-1335*.
- Arnal, D., Juillen, J. C., and Casalis, G. 1991 The effects of wall suction on laminar-turbulent transition in three-dimensional flow. In *Boundary Layer Stability and Transition to Turbulence, ASME FED-Vol. 114*.
- Bacon, J. W. Jr., Tucker, V. L., and Pfenninger, W. 1959 Experiments on a 30° 12 per cent thick symmetrical laminar suction wing in the 5-ft x 7-ft University of Michigan tunnel. *Northrop Rep. NOR-59-328 (BLC-119)*.

- Balakumar, P. and Reed, H. L. 1991 Stability of three-dimensional supersonic boundary layers. *Phys. Fluids A* 3: 617–632.
- Berry, S. A., Dagenhart, J. R., Brooks, C. W. Jr., and Harris, C. D. 1990 Boundary-layer stability analysis of Langley Research Center 8-foot LFC experimental data. In *Research in Natural Laminar Flow and Laminar Flow Control*. NASA, Langley Res. Ctr., Hampton, VA.
- Berry, S. A., Dagenhart, J. R., Viken, J. K., and Yeaton, R. B. 1987 Boundary-layer stability analysis of NLF and LFC experimental data at subsonic and transonic speeds. *SAE Paper No. 87-1859*.
- Bassom, A. and Hall, P. 1990a On the interaction of stationary crossflow vortices and Tollmien-Schlichting waves in the boundary layer on a rotating disk. *NASA CR-181859*.
- Bassom, A. and Hall, P. 1990b Concerning the interaction of non-stationary crossflow vortices in a three-dimensional boundary layer. *NASA CR-182037*.
- Bassom, A. and Hall, P. 1990c Vortex instabilities in 3D boundary layers: The relationship between Görtler and crossflow vortices. *NASA CR-187456*.
- Bassom, A. and Hall, P. 1991 Vortex instabilities in three-dimensional boundary layers – The relationship between Görtler and crossflow vortices. *J. Fluid Mech.* 232: 647–680.
- Bieler, H. and Redeker, G. 1990 Entwicklung von transitionskriterien auf e sup n basis fuer dreidimensionale fluegelgrenzschichten (Development of transition criteria on the basis of e to the n power for three-dimensional wing boundary layers). In *DGLR, Flows with Separation*, pp. 103–116, Bonn, F. R. Germany.
- Bippes, H. 1989 Instability features appearing on swept wing configurations. In *Laminar-Turbulent Transition: Proceedings of the IUTAM Symposium*, Toulouse, France, Sept. 11–15, 1989. Berlin and New York, Springer-Verlag, 1990.
- Bippes, H. and Müller, B. 1990 Experimente zum umschlag laminar-turbulent am schiebenden fluegel (Experiments on the laminar-turbulent transition on swept wings). In *DGLR Flows with Separation*, pp. 3–16, Bonn, F. R. Germany.
- Bippes, H., Müller, B., and Wagner, M. 1991 Measurements and stability calculations of the disturbance growth in an unstable three-dimensional boundary layer. *Phys. of Fluids A* 3: 2371–2377.

- Boltz, F. W., Kenyon, G. C., and Allen, C. Q. 1960 Effects of sweep angle on the boundary layer stability characteristics of an untapered wing at low speeds. *NASA TN-D-338*.
- Brown, W. B. 1955 Extension of exact solution of the Orr-Sommerfeld stability equation to Reynolds numbers of 4000. *Northrop Rep. NAI-55-548 (BLC-78)*.
- Brown, W. B. 1959 Numerical calculation of the stability of crossflow profiles in laminar boundary layers on a rotating disk and on a swept wing and an exact calculation of the stability of the Blasius velocity profile. *Northrop Rep. NAI-59-5 (BLC-117)*.
- Brown, W. B. and Sayre, P. 1954 An exact solution of the Orr-Sommerfeld stability equation for low Reynolds numbers. *Northrop Rep. BLC-43*.
- Bushnell, D. M. and Malik, M. R. 1985 Application of stability theory to laminar flow control — progress and requirements. *Proc. Symp. Stab. of Time-Dependent and Spat. Varying Flow*, pp. 1–17. New York, Springer-Verlag.
- Choudahri, M. and Streett, C. L. 1990 Boundary layer receptivity phenomena in three-dimensional and high-speed boundary layers. *AIAA Paper No. 90-5258*.
- Collier, F. S. Jr., Bartlett, D. W., Wagner, R. D., Tat, V. V., and Anderson, B. T. 1989 Correlation of boundary layer stability analysis with flight transition data. In *Laminar-Turbulent Transition: Proceedings of the IUTAM Symposium*, Toulouse, France, Sept. 11–15, 1989. Berlin and New York, Springer-Verlag, 1990.
- Collier, F. S. Jr., Johnson, J. B., Rose, O. J., and Miller, D. S. 1990 Supersonic boundary-layer transition on the LaRC F-106 and DFRF F-15 aircraft. Part 1: Transition measurements and stability analysis. In *Research in Natural Laminar Flow and Laminar Flow Control*. NASA, Langley Res. Ctr., Hampton, VA.
- Collier, F. S. Jr. and Malik, M. R. 1990 Curvature effects on the stability of three-dimensional boundary layers. In *AGARD, Fluid Dynamics of Three-Dimensional Turbulent Shear Flows and Transition*.
- Creel, T. R., Malik, M. R., and Beckwith, I. E. 1990 Experimental and theoretical investigation of boundary-layer instability mechanisms on a swept leading edge at Mach 3.5. In *Research in Natural Laminar Flow and Laminar Flow*

- Control, Part 3*, pp. 981–995. NASA, Langley Res. Ctr., Hampton, VA.
- Dagenhart, J. R. 1981 Amplified crossflow disturbances in the laminar boundary layer on swept wings with suction. *NASA TP-1902*.
- Dunn, D. W. and Lin, C. C. 1955 On the stability of the laminar boundary layer in a compressible fluid. *J. Aeronaut. Sci.* 22: 455–77.
- El-Hady, N. M. 1980 On the stability of three-dimensional, compressible nonparallel boundary layers. *AIAA Paper No. 80-1374*.
- El-Hady, N. M. 1988 Evolution of resonant wave triads in three-dimensional boundary layers. *AIAA Paper No. 88-0405*.
- Eppler, R. and Somers, D. M. 1980 A computer program for the design and analysis of low-speed airfoils. *NASA TM 80210*.
- Fischer, T. M. 1991 A mathematical-physical model for describing transitional boundary layer flows. Volume 1: The linear and nonlinear disturbance differential equations. *ESA-TT-1242*.
- Fischer, T. M. and Dallmann, U. 1987 Theoretical investigation of secondary instability of three-dimensional boundary layer flows. *AIAA Paper No. 87-1338*.
- Fischer, T. M. and Dallmann, U. 1988 Theoretical investigation of secondary instability of three-dimensional boundary-layer flows with application to the DFVLR-F5 model wing. *DFVLR-FB-87-44*.
- Fischer, T. M. and Dallmann, U. 1991 Primary and secondary stability analysis of a three-dimensional boundary-layer flow. *Physics of Fluids A 3*: 2378–2391.
- Fuciarelli, D. A. and Reed, H. L. 1992 High-frequency breakdown of three-dimensional boundary-layer flows. *Physics of Fluids A* (submitted).
- Gault, D. E. 1960 An experimental investigation of boundary layer control for drag reduction of a swept-wing section at low speed and high Reynolds numbers. *NASA TN-D-320*.
- Gray, W. E. 1952 The effect of wing sweep on laminar flow. *RAE TM Aero 255*.
- Gregory, N., Stuart, J. T., and Walker, W. S. 1955 On the stability of three-dimensional boundary layers with application to the flow due to a rotating

- disk. *Philosophical Transactions of the Royal Society of London, Series A, No. 943, Vol. 248.*
- Harvey, W. D., Harris, C. D., and Brooks, C. W. Jr. 1989 Experimental transition and boundary-layer stability analysis for a slotted swept laminar flow control airfoil. *Fourth Symposium on Numerical and Physical Aspects of Aerodynamic Flows*. California State University, Long Beach, CA.
- Hefner, J. N. and Bushnell, D. M. 1979 Application of stability theory to laminar flow control. *AIAA Paper No. 79-1493.*
- Hefner, J. N. and Bushnell, D. M. 1980 Status of linear boundary layer stability theory and the e^N method, with emphasis on swept-wing applications. *NASA TP-1645.*
- Herbert, T. 1989 A code for linear stability analysis. In *Instability and Transition: Proceedings of the ICASE / NASA LaRC Workshop*. New York, Springer-Verlag, 1990.
- Herbert, T. 1991 Boundary-layer transition — Analysis and prediction revisited. *AIAA Paper No. 91-0737.*
- Horstmann, K.-H., Redeker, G., Quast, A., Dressler, U., and Bieler, H. 1990 Flight tests with a natural laminar flow glove on a transport aircraft. *AIAA Paper No. 90-3044.*
- Jaffe, N. A., Okamura, J. J., and Smith, A. M. O. 1970 Determination of spatial amplification factors and their application to predicting transition. *AIAA J. 8: 301-8.*
- Kachanov, Y. S. and Tararykin, O. I. 1989 The experimental investigation of stability and receptivity of a swept-wing flow. In *Laminar-Turbulent Transition: Proceedings of the IUTAM Symposium, Toulouse, France, Sept. 11-15, 1989*. Berlin and New York, Springer-Verlag, 1990.
- Kaups, K. and Cebeci, T. 1977 Compressible laminar boundary layers with suction on swept and tapered wings. *Journal of Aircraft, Vol. 14, No. 7.*
- King, R. A. 1991 Mach 3.5 boundary-layer transition on a cone at angle of attack. *AIAA Paper No. 91-1804.*
- Kline, S. J. and McClintock, F. A. 1953 Describing uncertainties in single-sample experiments. *Mech. Engr., Jan. 1953.*

- Kohama, Y., Ukaku, M., and Ohta, F. 1987 Boundary-layer transition on a swept cylinder. *Proc. Int. Conf. Fluid Mech.*, pp. 151–56. Beijing, Peking Univ. Press.
- Lee, C. C., Wusk, M. S., and Obara, C. J. 1990 Flight experiments studying the growth of the disturbances in the laminar boundary layer. *SAE Paper No. 90-1979*.
- Lees, L. and Lin, C. C. 1946 Investigation of the stability of the laminar boundary layer in a compressible fluid. *NACA TN-1115*.
- Lees, L. and Reshotko, E. 1962. Stability of the compressible laminar boundary layer. *J. Fluid Mech.* 12: 555–90.
- Lekoudis, S. G. 1979 Stability of three-dimensional compressible boundary layers over swept wings with suction. *AIAA Paper No. 79-1495*.
- Lekoudis, S. G. 1980 Resonant wave interactions on a swept wing. *AIAA J.* 18: 122–24.
- Lin, C. C. 1955 *The Theory of Hydrodynamic Stability*, pp. 75–82. London / New York, Cambridge Univ. Press.
- Lin, R.-S. 1992 Stationary crossflow instability on an infinite swept wing. Ph. D. Dissertation, Arizona State University, Tempe, AZ.
- Lin, R.-S. and Reed, H. L. 1992 Effect of curvature on stationary crossflow instability of a three-dimensional boundary layer. *AIAA J.* (accepted).
- Mack, L. M. 1965a Computation of the stability of the laminar compressible boundary layer. In *Methods in Computational Physics*, ed. B. Alder, 4: 247–99. New York, Academic.
- Mack, L. M. 1965b The stability of the compressible boundary layer according to a direct numerical solution. *AGARDograph No. 97*.
- Mack, L. M. 1969 Boundary-layer stability theory. *Jet Propul. Lab. Rep. 900-277, Rev. A*. Pasadena, CA.
- Mack, L. M. 1975 Linear stability theory and the problem of supersonic boundary-layer transition. *AIAA J.* 13: 278–89.
- Mack, L. M. 1977 Transition prediction and linear stability theory. *AGARD CP No.*

224, Paper No. 1.

- Mack, L. M. 1979 On the stability of the boundary layer on a transonic swept wing. *AIAA Paper No. 79-0264*.
- Mack, L. M. 1981 Compressible boundary-layer stability calculations for sweptback wings with suction. *AIAA J. 20: 363-69*.
- Mack, L. M. 1984 Boundary-layer linear stability theory. In *Special Course on Stability and Transition of Laminar Flows AGARD Rep. No. 709*, Von Karman Inst., Rhode-St.-Genese, Belg.
- Maddalon, D. V., Collier, F. S. Jr., Montoya, L. C., and Putnam, R. J. 1989 Transition flight experiments on a swept wing with suction. In *Laminar-Turbulent Transition: Proceedings of the IUTAM Symposium*, Toulouse, France, Sept. 11-15, 1989. Berlin and New York, Springer-Verlag, 1990.
- Malik, M. R. 1982 COSAL — a black box compressible stability analysis code for transition prediction in three dimensional boundary layers. *NASA CR-165952*.
- Malik, M. R. 1989 Group summary: Compressible stability and transition. In *Instability and Transition: Proceedings of the ICASE / NASA LaRC Workshop*. New York, Springer-Verlag, 1990.
- Malik, M. R. and Li, F. 1992 Three-dimensional boundary layer stability and transition. *SAE Paper No. 92-1991*.
- Malik, M. R. and Orszag, S. A. 1981 Efficient computation of the stability of three-dimensional compressible boundary layers. *AIAA Paper No. 81-1277*.
- Malik, M. R. and Poll, D. I. A. 1984 Effect of curvature on three-dimensional boundary layer stability. *AIAA Paper No. 84-1672*.
- Meyer, F. and Kleiser, L. 1988 Numerical simulation of the nonlinear evolution of a perturbation in a three dimensional boundary layer. In *DGLR, Flows with Separation*, pp. 39-40. Bonn, F. R. Germany.
- Meyer, F. 1990 Numerical simulation of transition in three-dimensional boundary layers. Ph. D. Thesis, Karlsruhe Univ., F. R. Germany.
- Meyer, F. and Kleiser, L. 1989 Numerical simulation of transition due to cross-flow instability. In *Laminar-Turbulent Transition: Proceedings of the IUTAM Symposium*, Toulouse, France, Sept. 11-15, 1989. Berlin and New York,

Springer-Verlag, 1990.

- Michel, R., Arnal, D., and Coustols, E. 1985 Stability calculations and transition criteria in two- or three-dimensional flows. In *Laminar-Turbulent Transition*, ed. V. V. Koslov, pp. 455–61, New York, Springer-Verlag.
- Michel, R., Arnal, D., Coustols, E., and Juillen, J. C. 1985 Experimental and theoretical studies of boundary-layer transition on a swept infinite wing. In *Laminar-Turbulent Transition*, ed. V. V. Koslov, pp. 553–61, New York, Springer-Verlag.
- Michel, R., Coustols, E., and Arnal, D. 1985 Calculs de transition dans les écoulements tridimensionnels. *Symp. Numer. Aspects Aerodyn. Flows*, Long Beach, CA.
- Morkovin, M. V. 1969 *Viscous Drag Reduction*, pages 1–31. New York, Plenum.
- Müller, B. 1989 Experimental study of the travelling waves in a three-dimensional boundary layer. In *Laminar-Turbulent Transition: Proceedings of the IUTAM Symposium*, Toulouse, France, Sept. 11–15, 1989. Berlin and New York, Springer-Verlag, 1990.
- Müller, B. Experimental investigation of cross-flow instability in the linear and non-linear stage of the transition region. *ESA-TT-1237*, Ph. D. Thesis, Karlsruhe Univ., F. R. Germany.
- Müller, B., Bippes, H., and Collier, F. S. Jr. 1989 The stability of a three dimensional laminar boundary layer over a swept flat plate. In *Instability and Transition: Proceedings of the ICASE / NASA LaRC Workshop*. New York, Springer-Verlag, 1990, Vol. 2, pp. 268–277.
- Nayfeh, A. H. 1980a Stability of three-dimensional boundary layers. *AIAA J.* 18(4): 406–16.
- Nayfeh, A. H. 1980b Three-dimensional stability of growing boundary layers. In *Laminar-Turbulent Transition*, ed. R. Eppler and H. Fasel, pp. 201–17. Berlin, Springer-Verlag.
- Nitschke-Kowsky, P. 1986 Experimental investigations on the stability and transition of three-dimensional boundary layers. *ESA-TT-1026 DFVLR-FB-86–24*.
- Nitschke-Kowsky, P. and Bippes, H. 1988 Instability and transition of a three-dimensional boundary layer on a swept flat plate. *Physics of Fluids* 31:

786–795.

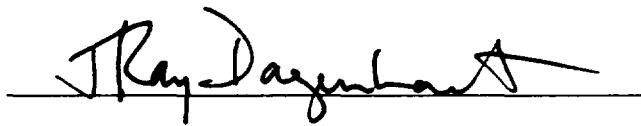
- Obara, C. J., Lee, C. C., and Vijgen, P. M. H. W. 1991 Analysis of flight-measured boundary-layer stability and transition data. *AIAA Paper No. 91–3282*.
- Obara, C. J., Vijgen, P. M. H. W., Lee, C. C., and Wusk, M. S. 1990 Boundary-layer stability analysis of flight-measured transition data. *SAE Paper No. 90–1809*.
- Owen, P. R. and Randall, D. J. 1952 Boundary-layer transition on the swept wing. *RAE TM Aero 277*.
- Padhye, A. R. and Nayfeh, A. H. 1981 Nonparallel stability of three-dimensional flows. *AIAA Paper No. 81-1281*.
- Parikh, P. G., Sullivan, P. P., and Bermingham, E., and Nagel, A. L. 1989 Stability of 3D wing boundary layer on a SST configuration. *AIAA Paper No. 89–0036*.
- Pfenninger, W. 1957 Experiments on a 30° 12% thick symmetrical laminar suction wing in the 5 x 7 foot Michigan tunnel. *Northrop Rep. NAI-57-317 (BLC-93)*.
- Pfenninger, W. 1977 Design considerations of large global range high subsonic speed LFC transport airplanes. In *Special Course on Concepts for Drag Reduction, AGARD Rep. No. 654*, Von Karman Inst., Rhode-St.-Genese, Belg.
- Pfenninger, W. and Bacon, J. W. Jr. 1961 About the development of swept laminar suction wings with full chord laminar flow. In *Boundary Layer and Flow Control*, ed. G. V. Lachmann, 2: 1007–32. New York, Pergamon.
- Poll, D. I. A. 1985 Some observations of the transition process on the windward face of a long yawed cylinder. *J. Fluid Mech.* 150: 329–56.
- Poll, D. I. A. 1989 The effect of isolated roughness elements on transition in attachment line flows. In *Laminar-Turbulent Transition: Proceedings of the IUTAM Symposium*, Toulouse, France, Sept. 11–15, 1989. Berlin and New York, Springer-Verlag, 1990.
- Reda, D. C. 1988 Liquid crystals for unsteady surface shear stress visualization. *AIAA Paper No. 88-3841CP*.
- Reed, H. L. 1988 Wave interactions in swept-wing flows. *Phys. Fluids* 30(11): 3419–26.

- Reed, H. L. and Lin, R.-S. 1987 Stability of three-dimensional boundary layers. *SAE Paper No. 87-1857*.
- Reed, H. L. and Nayfeh, A. H. 1982 Stability of compressible three-dimensional boundary-layer flows. *AIAA Paper No. 82-1009*.
- Reed, H. L. and Saric, W. S. 1989 Stability of three-dimensional boundary layers. *Ann. Rev. of Fluid Mech., Vol. 21, 1989*.
- Reed, H. L., Stuckert, G., and Balakumar, P. 1991 Stability of high-speed chemically reacting and three-dimensional boundary layers. In *Laminar-Turbulent Transition: Proceedings of the IUTAM Symposium*, Toulouse, France, Sept. 11-15, 1989. Berlin and New York, Springer-Verlag, 1990.
- Runyan, L. J., Bielak, G. W., Behbehani, R. A., Chen, A. W., and Rozendaal, R. A. 1990 The 757 NLF glove flight test results. In *Research in Natural Laminar Flow and Laminar Flow Control*. NASA, Langley Res. Ctr., Hampton, VA.
- Saric, W. S. 1989 Low-speed experiments: Requirements for stability measurements. In *Instability and Transition: Proceedings of the ICASE / NASA LaRC Workshop*. New York, Springer-Verlag, 1990.
- Saric, W. S. 1992a Laminar-turbulent transition: Fundamentals, lecture no. 4. In Special course on skin friction drag reduction, *AGARD Report No. 786, Von Karman Inst., Rhode-St.-Genese, Belg.*
- Saric, W. S. 1992b. The ASU transition research facility. *AIAA Paper No. 92-3910*.
- Saric, W. S., Takagi, S., and Mousseux, M. 1988 The ASU unsteady wind tunnel and fundamental requirements for freestream turbulence measurements. *AIAA Paper No. 88-0053*.
- Saric, W. S. and Yeates, L. G. 1985 Experiments on the stability of crossflow vortices in swept-wing flows. *AIAA Paper No. 85-0493*.
- Schlichting, H. (Kestin, J., translator) 1968 *Boundary-Layer Theory*. New York, McGraw-Hill Book Company.
- Singer, B. A., Meyer, F., and Kleiser, L. 1989 Nonlinear development of crossflow vortices. In *Instability and Transition: Proceedings of the ICASE / NASA LaRC Workshop*. New York, Springer-Verlag, 1990.

- Smith, A. M. O. and Gamberoni, N. 1956 Transition, pressure gradient, and stability theory. *Douglas Aircraft Company, Inc., ES 26388.*
- Somers, D. M. and Horstmann, K.-H. 1985 Design of a medium-speed natural-laminar-flow airfoil for commuter aircraft applications. *DFVLR-IB/29-85/26.*
- Spalart, P. R. 1989 Direct numerical study of crossflow instability. In *Laminar-Turbulent Transition: Proceedings of the IUTAM Symposium*, Toulouse, France. Berlin and New York, Springer-Verlag, 1990.
- Srokowski, A. J. and Orszag, S. A. 1977 Mass flow requirements for LFC wing design. *AIAA Paper No. 77-1222.*
- Stetson, K. F. 1989 Hypersonic boundary-layer transition. In *Second Joint Europe/U. S. Short Course in Hypersonics*. U. S. Air Force Academy, Colorado Springs, CO.
- Stevens, W. A., Goradia, S. H., and Braden, J. A. 1971 A mathematical model for two-dimensional multi-component airfoils in viscous flow. *NASA CR-1843.*
- Stuart, J. T. 1953 The basic theory of the stability of three-dimensional boundary layers. *ARC 15904.*
- Van Ingen, J. L. 1956 A suggested semi-empirical method for the calculation of the boundary-layer transition region. *Rep. Nos. VTH 71 and 74*, Dept. Aeronaut. Eng., Univ. Technol., Delft, Neth.
- Viken, J., Collier, F. S. Jr., Wagner, R. D., and Bartlett, D. W. 1989 On the stability of swept wing laminar boundary layers including curvature effects. In *Laminar-Turbulent Transition: Proceedings of the IUTAM Symposium*, Toulouse, France. Berlin and New York, Springer-Verlag, 1990.
- Waggoner, E. G., Campbell, R. L., Phillips, P. S., and Hallissy, J. B. 1990 Design and test of an NLF wing glove for the variable-sweep transition flight experiment. In *Research in Natural Laminar Flow and Laminar Flow Control*. NASA, Langley Res. Ctr., Hampton, VA.

Vita

J. Ray Dagenhart was born in [REDACTED]. He attended the public schools of Iredell County, NC. In 1973 he was awarded the Bachelor of Science Degree in Aerospace Engineering from North Carolina State University. He received the Master of Science Degree in Mechanical Engineering from the George Washington University in 1979. While an undergraduate at N. C. State he was a cooperative education student at NASA Wallops Flight Center. He was employed by Pratt and Whitney Aircraft Company for one year as an experimental engineer. In 1974 he joined the staff of NASA Langley Research Center in the Systems Engineering Division. In 1980 he became an experimental research engineer in the Aeronautics Directorate at NASA Langley. He has two children, Kimberly and Jeffrey Dagenhart, who live in York County, VA. He resides in Hampton, VA.

A handwritten signature in cursive script, reading "J. Ray Dagenhart", is written over a horizontal line.

PRECEDING PAGE BLANK NOT FILMED